



HAL
open science

Influence de la sollicitations hydriques sur le comportement mécanique du pisé: comportement au jeune âge

Parul Chauhan

► **To cite this version:**

Parul Chauhan. Influence de la sollicitations hydriques sur le comportement mécanique du pisé: comportement au jeune âge. Mechanics of materials [physics.class-ph]. Université Savoie Mont Blanc, 2021. English. NNT: 2021CHAMA007. tel-03600699

HAL Id: tel-03600699

<https://theses.hal.science/tel-03600699>

Submitted on 7 Mar 2022

HAL is a multi-disciplinary open access archive for the deposit and dissemination of scientific research documents, whether they are published or not. The documents may come from teaching and research institutions in France or abroad, or from public or private research centers.

L'archive ouverte pluridisciplinaire **HAL**, est destinée au dépôt et à la diffusion de documents scientifiques de niveau recherche, publiés ou non, émanant des établissements d'enseignement et de recherche français ou étrangers, des laboratoires publics ou privés.

THÈSE

Pour obtenir le grade de

DOCTEUR DE L'UNIVERSITÉ SAVOIE MONT BLANC

Spécialité : **Mécanique, génie mécanique, génie civil**

Arrêté ministériel : 25 Mai 2016

Présentée par

Parul CHAUHAN

Thèse dirigée par **Olivier PLE**, Pr, USMB
encadrée par **Noémie PRIME**, MdC, USMB

préparée au sein du **Laboratoire LOCIE**
dans l'**École Doctorale SISEO**

Influence of hydric solicitations on the mechanical behavior of rammed earth: early-age behavior

Influence des sollicitations hydriques sur le
comportement mécanique du pisé : comportement
au jeune âge

Thèse soutenue publiquement le **25 Février 2021**,
devant le jury composé de :

M. Domenico GALLIPOLI

Professeur des Universités, Università di Genova, Rapporteur

M. Arnaud PERROT

Maître de conférences HDR, Université de Bretagne-Sud, Rapporteur

M. Sofiane AMZIANE

Professeur des Universités, Université Clermont Auvergne, Examineur

M. Christopher BECKETT

Lecturer, University of Edinburgh, Examineur

M. Olivier PLE

Professeur des Universités, USMB, LOCIE, Directeur de thèse

Mme Noémie PRIME

Maître de conférences, USMB, LOCIE, Encadrant de thèse

Acknowledgements

Throughout the writing of this thesis, I have received a great deal of support and assistance. I want to acknowledge all the people who have helped me during this PhD journey.

I would like to express my sincere gratitude to my thesis supervisors Prof. Olivier PLÉ and Noémie PRIME, for providing continuous support and encouragement. Your valuable guidance and thought-provoking ideas helped me to continuously steer forward in the right direction and finish the thesis efficiently. I am also grateful to Prof. Simon WHEELER for accepting me for international mobility at the University of Glasgow and guiding me at the critical point of the thesis. I am thankful to the jury members for reading and reviewing my thesis and providing me with encouraging and constructive remarks.

I am thankful to Prof. Cino VIGGIANI for providing me with an opportunity to pursue higher education in France and for the consistent guidance and help during all these years. I am grateful to Prof. Sabatino CUOMO for supervising my master's thesis and helping me in obtaining this PhD project. I am wholeheartedly thankful to Prof. Vijay Shankar DOGRA for the support and guidance throughout these years. I am deeply indebted to you for helping me through every obstacle in life, whether personal or professional and for shaping my career into what it is today. I am also thankful to all my teachers in life, from school, NIT Hamirpur, and 3SR laboratory.

I would like to acknowledge all my colleagues in LOCIE laboratory. I really cherish the 3 years that I spent in this laboratory. I am thankful to Elio for the contribution to the thesis during his master's internship. I am really grateful to all my friends in LOCIE, especially Hasan, Amin, Taini, and Mathilde, for the wonderful memories and emotional support throughout the thesis. In the words of Hasan, we were a family across different borders. I am thankful to Hani for the deep philosophical discussions and for being an amazing friend. I am really thankful to Ritesh and Ankit for always being there for me during the good and the bad times. They are my Indian family in France. I could not have completed this thesis without their support.

Lastly, I am grateful to my parents and relatives, whose moral support and passionate encouragement made it possible for me to accomplish this journey. I am thankful to my mother for everything she has done for me. I owe everything that I have achieved in my life to her. I am grateful to my father for teaching me all the valuable lessons in life and guiding me on how to deal with difficult situations. I am thankful to my brother for always being there for me and helping me to achieve my goals.

Parul CHAUHAN

Abstract

Rammed earth construction provides an efficient alternative construction material to limit energy consumption and CO_2 emission. It possesses various characteristics of sustainable material, but its mechanical behavior is sensitive to humidity variations, which is a real difficulty for developing this construction technique. Thus, this study concerns the coupled hydro-mechanical behavior of rammed earth. This study is carried out using an experimental and numerical approach at both material and structural scales.

At the material scale, compression and shear testing were done at different suction conditions. The samples used were compacted using a technique of double-compaction. The results showed that the mechanical parameters improved with the suction state of rammed earth. Non-linearity in the failure envelope was observed over all the suction range, and thus a modified failure criterion was proposed. The intrinsic shear parameters were determined from saturated triaxial tests. From these tests, the expression of generalized effective stress for unsaturated soils was determined.

At the structural scale, the hydro-mechanical behavior of rammed earth columns was studied at non-uniform suction conditions. The columns were subjected to 1D natural convection drying, where the boundary conditions are representative of a real rammed earth wall. The drying phase kinetics were studied. The compressive testing of the columns was studied after the natural convection drying. The result showed that the strength and stiffness of the columns increased significantly within the first two weeks of drying. In addition to this, the consistency of the material changed from plastic to brittle with the increase in suction.

Coupled THM simulations of the drying phase and the compression testing were performed on the rammed earth columns using the finite element code called Code BRIGHT. The drying simulations were carried out using more realistic atmospheric boundary conditions. A good fitting with the experimental results was obtained for drying. For the compression simulations, a linear elastic-perfectly plastic mechanical constitutive model was used. The expression of generalized effective stress was introduced in the shear strength expression. The compressive strength obtained from the simulation was compared with the experimental results. A sensitivity analysis for the effective stress parameter on the compression strength was done.

Finally, a numerical case study was done to determine the drying period required for the walls to gain sufficient strength for subsequent floor construction. Two different configurations of walls were carried out at warm and cold environmental conditions while taking into account the safety criterion, inspired from the “Guide des bonnes pratiques”.

Résumé

La construction en pisé offre un matériau de construction alternatif efficace pour limiter la consommation d'énergie et les émissions de CO_2 . Il possède diverses caractéristiques de matériau durable, mais son comportement mécanique est sensible à l'eau et aux variations d'humidité, ce qui est une réelle difficulté pour développer cette technique aussi bien à la mise en œuvre qu'à la construction. Ainsi, cette étude concerne le comportement hydromécanique couplé du pisé. Cette étude est réalisée selon une approche expérimentale et numérique à la fois à l'échelle du matériau et d'éléments de structure.

À l'échelle du matériau, des fabrications puis des essais de compression et de cisaillement ont été effectués dans différentes conditions de succion. Les échantillons utilisés ont été compactés à l'aide d'une technique de double compactage statique. Les résultats ont montré que les paramètres mécaniques s'amélioraient avec l'état succion de pisé. Une non-linéarité dans l'enveloppe de rupture a été observée sur toute la plage de succion et ainsi un critère de rupture modifié a été proposé. Les paramètres de cisaillement intrinsèques ont été déterminés à partir d'essais triaxiaux saturés. À partir de ces tests, l'expression du stress effectif généralisé pour les sols non saturés a été déterminée.

À l'échelle structurelle, des éléments de structures ont été fabriqués puis testés, le comportement hydromécanique de ces colonnes de pisé a été étudié dans des conditions succion non uniformes. Les colonnes ont été soumises à un séchage par convection naturelle 1D où les conditions aux limites sont représentatives d'un véritable mur de pisé. La cinétique de la phase de séchage a été étudiée. L'essai de compression des colonnes a été étudié après le séchage par convection naturelle. Le résultat a montré que la résistance et la rigidité des colonnes augmentaient considérablement au cours des deux premières semaines de séchage. En plus de cela, la consistance du matériau est passée de plastique à fragile avec l'augmentation de la succion.

Des simulations THM couplées de la phase de séchage et des tests de compression ont été réalisées sur les colonnes de pisé en utilisant le code élément fini appelé Code BRIGHT. Les simulations de séchage ont été réalisées en utilisant des conditions aux limites atmosphériques plus réalistes. Un bon ajustement avec les résultats expérimentaux a été obtenu pour le séchage. Pour les simulations de compression, un modèle constitutif mécanique linéaire élastique parfaitement plastique a été utilisé.

L'expression de la contrainte effective généralisée a été introduite dans l'expression de la résistance au cisaillement. La résistance à la compression obtenue à partir de la simulation a été comparée aux résultats expérimentaux. Une analyse de sensibilité pour le paramètre de contrainte effective sur la résistance à la compression a été réalisée.

Enfin, une étude de cas numérique a été réalisée pour déterminer la période de séchage nécessaire pour que les murs acquièrent une résistance suffisante pour la construction ultérieure du plancher. Deux configurations de murs différentes ont été réalisées dans

des conditions ambiantes chaudes et froides en tenant compte des critères sécuritaires du guide des bonnes pratiques sur le pisé.

Contents

List of Figures	xi
List of Tables	xxi
1 Introduction	1
1.1 Earth as a construction material	1
1.2 Rammed earth	5
1.2.1 Advantages and limitation of earthen structures	6
1.3 Thesis objective and outline	8
2 Literature review	11
2.1 Key mechanical parameters	12
2.2 Factors influencing the mechanical characteristics	17
2.2.1 Sample geometry and scale	17
2.2.2 Granulometry	19
2.2.3 Clay content and nature	21
2.2.4 Dry density and method of compaction	23
2.3 Suction as a variable for describing water state	26
2.4 Modelling of Rammed earth	36
2.4.1 Damage models	36
2.4.2 Elasto-plasticity models	37
2.4.3 Coupled analysis	40
2.5 Conclusion	41
3 Hydro-mechanical behavior at material scale	43
3.1 Introduction	43

3.2	Geotechnical characterization of the material	44
3.2.1	Particle size distribution	44
3.2.1.1	Sieve Analysis	44
3.2.1.2	Sedimentation Analysis	45
3.2.2	Atterberg limits	45
3.2.3	Other characterization tests	48
3.3	Sample Preparation	50
3.3.1	Proctor compaction test	50
3.3.2	Double Compaction	52
3.4	Hydric conditions	57
3.4.1	Suction	57
3.4.2	Soil water retention curve (SWRC)	59
3.4.3	Control of suction	60
3.4.3.1	Liquid-vapor equilibrium method	60
3.4.3.2	Axis translation technique	61
3.4.4	Hydric properties of rammed earth	63
3.4.4.1	Soil water retention curve	63
3.4.4.2	Hydraulic conductivity	67
3.4.5	Conditioning of samples	68
3.5	Influence of suction on mechanical parameters	70
3.5.1	Unconfined compressive strength test	70
3.5.2	Direct shear tests: Influence of suction on shear parameters	75
3.5.3	Unsaturated triaxial tests	83
3.5.4	Intrinsic shear parameters	91
3.6	Towards constitutive modeling	97
3.7	Conclusion	103
4	Experiments and simulation at structural scale on columns	105
4.1	Introduction	105
4.2	Experimental study	106
4.2.1	Material	106
4.2.2	Experimental Protocol	107

4.2.2.1	Sample Preparation	109
4.2.2.2	Sensor calibration and layout	112
4.2.3	Results of the drying phase	116
4.2.4	Unconfined compression test on columns	122
4.2.4.1	Experimental procedure	122
4.2.4.2	Results of the compression test	123
4.3	Numerical analysis	131
4.3.1	Theoretical aspects of CODE_BRIGHT	131
4.3.1.1	Balance equations	132
4.3.1.2	Constitutive equations and equilibrium restrictions	134
4.3.2	Material parameters	142
4.3.2.1	Hydro-thermal parameters	142
4.3.2.2	Mechanical parameters	143
4.3.3	Numerical simulations of drying phase	145
4.3.3.1	Initial conditions and boundary conditions	146
4.3.3.2	Drying phase simulation results	147
4.3.4	Numerical simulations of compression phase	153
4.3.4.1	Initial state and boundary conditions	153
4.3.4.2	Compression phase simulation results	154
4.4	Conclusions and Perspective	165
5	Case study: THM coupled simulations of rammed earth walls	169
5.1	Introduction	169
5.2	General considerations for the simulations	170
5.2.1	Failure envelope	170
5.2.2	Environmental conditions	171
5.3	Single Wall	173
5.3.1	Compression of wall at compaction hydric state	174
5.3.2	Drying in warm conditions	175
5.3.3	Drying in cold conditions	178
5.4	Two walls joined at right angle	181
5.5	Conclusion and Perspective	186

6	Conclusions and perspectives	187
7	Synthèse	191
7.1	Etude expérimentale à l'échelle du matériau	192
7.1.1	Test de résistance à la compression non confiné (UCS)	195
7.1.2	Essai de cisaillement direct (DST)	195
7.1.3	Test triaxial non saturé	196
7.1.4	Test triaxial saturé	196
7.1.5	Vers une modélisation constitutive	197
7.2	Etude expérimentale à l'échelle structurelle sur colonnes	198
7.2.1	Comportement au séchage	198
7.2.2	Comportement de compression	198
7.3	Simulation du comportement de séchage et de compression des colonnes de pisé	199
7.3.1	Simulation de phase de séchage	200
7.3.2	Simulation de phase de compression	200
7.4	Étude de cas: simulations couplées THM de murs en pisé	201
	Appendices	202
	Bibliography	214

List of Figures

1.1	A world map showing the different areas of earthen architecture and UNESCO world heritage sites (Source: CRATerre/ENSAG)	2
1.2	The classification of the earth construction process by Hamard et al. 2016 [1]. W_m is the manufacturing water content, W_{OP} is optimum water content, W_p and W_l are the plastic and liquid limit of soil	2
1.3	The construction process of wattle and daub technique (a) and house made with this technique in Miltenberg, Germany (b)	3
1.4	Construction of a cob wall (a) and a modern cob house in Ottery St. Mary, United Kingdom (b) (Source: Wikipedia)	3
1.5	Manufactured adobe bricks (a) and wall construction using adobe bricks (b)	4
1.6	A compressed earth block using mechanical press (a) and center of earth architecture building made from CEBs in Mopti, Mali (b)	4
1.7	A scheme for construction of rammed earth wall in layers [2]	5
1.8	A rammed earth wall made in LOCIE laboratory (a) and Château de Reyrieux made from rammed earth (b) in France (Photo: Auroville, earth institute)	6
2.1	The results of characteristic compressive strength (f') and dry density for different rammed earth soil type [3].	13
2.2	The rammed earth wall studied (left) and the loading pattern and the failure mechanism for the wall from Jaquin, 2006 [4]	14
2.3	Experimental setup for the compression testing of the wallettes (left) and Load-displacement curve (right) from Bui et al. 2014 [5].	15
2.4	Fracture surface on the wallette due to differential settlement between loaded and unloaded zone [5].	15
2.5	Experimental results of axial compression test (left) and diagonal compression test (right) on wallettes from Miccoli et al. 2015 [6]	16

2.6	Different scales of study including wall scale, a representative element scale and material scale (CEB) from Bui et al. 2009 [7].	18
2.7	Reloading modulus of elasticity variation with preload stress for the three scales of study by Bui et al. 2009 [7]	19
2.8	Particle size distribution of different soil mixes [3] and limit envelopes according to Houben et al. 1994 [8]	20
2.9	Particle size distribution of tested material [9] and upper and lower bounds according to Houben et al. 1994 [8] represented as BS1377-Min and BS1377-Max	20
2.10	Evolution of compressive strength with drying age for soils having different clay content	21
2.11	Variation of unconfined compressive strength with clay content (modified after Helson et al. 2017 [10])	22
2.12	Damage and plasticity behavior for different soils at different storage humidity	22
2.13	Relationship between compressive strength and Young modulus for different soils	23
2.14	Variation of compressive strength with dry density for different types of soil after [11]	24
2.15	Evolution of compressive strength with dry density for traditional adobe and pressed adobe blocs (PABs)[12]	24
2.16	Determination of OMC using vibrating hammer test by Jaquin et al. 2009 [13]	25
2.17	Comparison of dry density between the standard Proctor test (a) and specific Proctor method (b) [14].	25
2.18	Variation of compressive strength (fc) and secant modulus (E) with moisture content for different soils studied from Bui et al. 2014 [15]	27
2.19	Comparison of the unconfined compressive strengths of mixes 5-1-4 and 7-1-2 against humidity and temperature [16].	28
2.20	Variation of compressive strength and Young's modulus with relative humidity from Champire et al. 2016 [9]	28
2.21	Results of the triaxial tests on rammed earth samples carried under constant water content conditions from Jaquin et al. 2009 [13].	30
2.22	Variation of compressive strength with suction for the unstabilised soil from Bui et al. 2014 [15] and Jaquin et al. 2009 [13]	31
2.23	Variation of compressive strength with suction from Gerard et al. 2015 [14]	31

2.24	Variation of peak compressive strength and Young's modulus with total suction from Bruno et al. 2017 [17]	32
2.25	Variation of tensile strength from Brazilian test (from Jaquin et al. 2008 [18].	33
2.26	Variation of tensile strength with suction from Gerard et al. 2015 [14]	33
2.27	Young's modulus and residual strain shown as function of stress level at different humidity conditions from Champiré et al. 2016[9]	34
2.28	Evolution of Young's modulus and residual strain with increasing stress state for samples conditioned at different relative humidities and tested at different confining pressures from Xu et al. 2017 [19].	34
2.29	Variation of Poisson's ratio with moisture content for different soils studied from Bui et al. 2014 [15]	35
2.30	Comparison of the experimental and the numerical results for wallettes under axial compression (from Bui et al. 2014 [5]).	37
2.31	Mohr-Coulomb and Drucker-Prager yield surface in the isometric principal stress space	39
2.32	Experimental and modelling results of unconfined compressive strength at different suction states from Francois et al. 2017 [20].	39
2.33	Mohr circles at failure in terms of effective stress for UCS (left) and indirect tensile strength test (right) at different initial suction conditions [14]	40
3.1	Particle size distribution and the guidelines by Houben et al. 1994[8]	46
3.2	Casagrande test for liquid limit determination	47
3.3	Casagrande's Plasticity chart for the classification of fine grained soils	47
3.4	Triangular classification of fine grained soils	48
3.5	Activity of soil studied based on the clay fraction and plasticity index	49
3.6	Results of normal Proctor test and 80% and 100% saturation lines	51
3.7	Process of cylindrical specimen preparation using the static double compaction technique	54
3.8	Mold (a) used for preparation of prismatic samples (b)	54
3.9	The dry density variation of a doubly compacted sample across the height	55
3.10	Force-displacement curve during compaction for both stages of loading for sample at 10.8% water content	56
3.11	Air-water interface of a partially saturated soil [21]	58
3.12	Different suction zones corresponding to the soil water retention curve [22]	59

3.13	A scheme representing the relative humidity boxes which contains the salt solution and rammed earth samples	62
3.14	Use of axis translation technique to avoid metastable states (left) Atmospheric conditions; (right) axis translation (after Marinho et al. 2009 [23]) .	62
3.15	Scheme of pressure plate device [21]	63
3.16	Variation of water content with time when the soil samples were move between different relative humidity boxes	64
3.17	Soil water retention curve plotted from Liquid vapor equilibrium method for both sorption and desorption phases	65
3.18	Testing of the samples in the pressure plate device and pressure regulation system	66
3.19	Soil water retention curve using the results of pressure plate test and saline solution method (desorption phase)	67
3.20	Cylindrical specimens (a) and Prismatic specimens (b) placed in RH box for suction equalization	68
3.21	Moisture content variation (average of 3 samples) with time during the suction equilibration in humidity controlled boxes for samples of UCS test directly placed in RH boxes after manufacture	69
3.22	Scheme of different tests including the number of tests and hydric states .	70
3.23	Variation of compressive strength with suction, samples compressed with unload-reload cycles shown in circular marking	71
3.24	Axial stress-deformation curve during unconfined compressive strength test for 3 samples conditioned at 39 MPa suction including testing with unload-reload cycles	72
3.25	Variation of initial tangent modulus E_{tan} with suction conditions	73
3.26	Variation of E_{sec} with Axial stress to UCS ratio for different suction conditions	74
3.27	Variation of residual strain after unloading with Axial stress to UCS ratio for different suction conditions	74
3.28	Schematic representation of the Casagrande shear box showing the different components (modified from celtest.com)	76
3.29	Shear stress vs shear deformation curve during the direct shear tests for samples at suction 153.4 MPa, RH = 32.8%	77
3.30	Mohr-Coulomb failure envelope for samples conditioned at different suction conditions for series 1,2, and 3	79
3.31	Variation of apparent cohesion (a) and friction angle (b) from direct shear tests shown with error bars from results of 3 series of tests	80

3.32	Variation of shear strength with suction at a constant normal stress of 0.139 MPa (a), 0.278 MPa (b), and 0.417 MPa (c), and 0.556 MPa (d)	82
3.33	The experimental setup and the various components of triaxial test	84
3.34	Variation of deviator stress versus axial strain during shear stage of triaxial test for samples conditioned at 23.4 MPa suction and 84.34% RH	86
3.35	Mohr circles at failure for samples conditioned at 23.4 MPa suction and 84.34% RH	87
3.36	Comparison of the variation of deviator stress with axial strain for samples conditioned at suction values of 3.8 MPa (a) and 331.3 MPa (b)	88
3.37	Variation of apparent cohesion (a) and apparent friction angle (b) with suction states determined from the unsaturated triaxial tests	89
3.38	Results of UCS, DST, and unsaturated triaxial test in $\tau - \sigma_n$ plane for all suction states	90
3.39	Variation of confining stress, back pressure, and back volume during the saturation phase for sample (a) and the zoomed-in view of B-check during saturation (b)	92
3.40	Variation of back volume with the square root of time during the consolidation phase of the CU triaxial test	93
3.41	Variation of deviatoric stress (a) and pore water pressure (b) for 4 saturated samples at $\sigma'_3 = 100$ kPa, 200 kPa, 300 kPa, and 1500 kPa in the shear phase	95
3.42	Failure envelope from 4 consolidated undrained triaxial test to determine intrinsic shear parameters	96
3.43	Non-linear failure envelope plotted for $s = 205.2$ MPa and $RH = 22.51\%$ using the results of UCS, DST and unsaturated triaxial test	98
3.44	Failure envelope plotted for all suction states including the saturated state. For the unsaturated states, net normal stress is defined as $\sigma_n = \sigma - u_a$ and for the saturated state as $\sigma_n = \sigma - u_w$ as $u_a = u_w$	98
3.45	Determination of expression for χ_s using saturated triaxial test and Mohr circles from unsaturated triaxial test and UCS ($\sigma_3 = 0$) using the methodology of Gerard et al .2015 [14]	100
3.46	Determination of relation between χ and S_l in normal scale (a) and log-log scale (b)	101
4.1	Particle size distribution of the soil used for manufacturing columns along with the limit range specified by Houben et al. 1994 [8]	107
4.2	Depiction of the samples as a volume representative of the rammed earth wall along with the dimensions and slenderness ratio	108

4.3	Experimental plan depicting the different samples, duration of drying after which they are tested and the loading type	109
4.4	Different steps for the preparation of prismatic rammed earth columns	111
4.5	Figure depicting the different compaction layers and the placement of SHT sensors	111
4.6	Samples left for drying in an indoor environment	111
4.7	The SHT75 sensor used to relative humidity and temperature measurement	112
4.8	The RH-tolerance at 25 °C (a) and temperature tolerance for the SHT sensor (taken from sensirion.com)	113
4.9	Calibration curve with regards to temperature and relative humidity for all the sensors	115
4.10	Placement of sensors in the middle of rammed earth layer along with the plastic protection membrane (a) and Sensor layout (b)	116
4.11	Variation of relative humidity vs time for sample 6 (a), 7 (b), and 8 (c), which are to be compressed after 13, 31, and 62 days of drying respectively	117
4.12	Variation of relative humidity with distance from the edge of drying face at different duration of drying for sample 8	119
4.13	Variation of average water content with time for sample 4: 1D drying and sample 9: drying from all sides	120
4.14	Variation of RH with time showing the raw measured data (a), (b), and (c) along with the corrected data (d), (e), and (f) for samples 6,7, and 8 respectively	121
4.15	Experimental setup for unconfined compression test	123
4.16	Axial stress-strain curve for samples after 0 (a), 13 (b) days of drying with and without unload-reload cycles	125
4.17	Axial stress-strain curve for samples after 31(a) and 62 (b) days of drying with and without unload-reload cycles	126
4.18	Axial stress-strain curves for samples loaded until failure (a) and with unload-reload cycles (b) at different drying duration	127
4.19	Axial stress-strain curve for sample 9 which is fully dried after 30 days without unload-reload cycles	128
4.20	Variation of compressive strength and RH (sample 8) with duration of drying for samples with (sample 5-8) and without (sample 1-4) unload-reload cycles	129
4.21	Variation of tangent modulus of elasticity with duration of drying for samples with and without unload-reload cycles	130

4.22	Yield surface for Drucker-Prager plasticity model in p'q space (a) and in principal stress space (b)	139
4.23	The coupling between the thermal, hydric and mechanical analysis shown as the effect of T/H/M (shown in horizontal) on the T/H/M (shown in vertical)	141
4.24	Soil water retention curve obtained from pressure plate and saline solution method using Van-Genuchten fitting parameters	142
4.25	Relative hydraulic conductivity as a function of liquid degree of saturation using Mualem model [24]	143
4.26	The geometrical 3D model of the problem (right) and the 2D mesh composition (left)	145
4.27	Isochrones of suction (a) and liquid degree of saturation (b) across the width of rammed earth column	149
4.28	Comparison of experimental and simulation results for relative humidity	150
4.29	Comparison of experimental and simulation results for water content	151
4.30	Comparison of experimental and simulation results for global average water content	152
4.31	Initial hydric state (for 62 days of drying) for the compression phase (left) and mechanical boundary conditions for the compression of rammed earth columns (right)	153
4.32	Suction distribution (a) and comparison of the compression test conducted without any drying phase i.e. 0 days with the simulation results (b)	155
4.33	Suction distribution (a) and comparison of the compression test conducted after 13 days of drying period with the simulation results (b)	156
4.34	Suction distribution (a) and comparison of the compression test conducted after 31 days of drying period with the simulation results (b)	157
4.35	Suction distribution (a) and comparison of the compression test conducted after 62 days of drying period with the simulation results (b)	158
4.36	Comparison of the compressive strength for samples tested without unload-reload cycles and the simulation results at different duration of drying	160
4.37	Comparison of the compressive strength for samples tested at the same hydric state but at different geometry, granulometry, scale, compaction method	161
4.38	The variation of χ - S_l (a) and $\text{Log } \chi$ - $\text{Log } S_l$ (b) for $\alpha = 1.8127$ and $\alpha = 2.0035$	163
4.39	The variation of compressive strength for the sensitivity analysis performed on the effective stress parameter χ	164

5.1	The ultimate failure envelope and safety failure envelope in p' - q plane . . .	171
5.2	The weather data related to temperature and relative humidity for Le Bouget-du-Lac (year 2019) taken from meteoblue.com	171
5.3	The geometrical model (3D) of the problem (left) and the 2D mesh composition (right) showing the drying direction and loading	173
5.4	Stress path for single wall at the critical point due to vertical stress at top starting from optimum compaction hydric state	174
5.5	The stress path in p' - q plane for the critical point in the wall at different duration of drying in warm environmental conditions	176
5.6	Suction (a) and degree of saturation (b) variation across the width of rammed earth wall at 0, 30, 60, 90, and 120 days of drying period in warm environmental conditions	177
5.7	The stress path in p' - q plane for the critical point in the wall at different duration of drying in cold environmental conditions	178
5.8	Suction (a) and degree of saturation (b) variation across the width of rammed earth wall at 0, 30, 60, 90, 120, 150, and 180 days of drying period in cold environmental conditions	179
5.9	Comparison of suction evolution at the critical point (at the center) for warm and cold environmental conditions	180
5.10	3D model of the 2 walls showing the boundary conditions and direction of drying	181
5.11	The 2D mesh composition of the model in XZ plane (top view)	182
5.12	The stress path in p' - q plane for the critical point in the wall at different duration of drying in warm environmental conditions	183
5.13	Suction distribution across the width of rammed wall after 240 days of drying period	183
5.14	Suction (a) and degree of saturation (b) variation across the diagonal of rammed column formed at the junction of 2 walls at different drying period in warm environmental conditions	184
7.1	Méthodologie du travail de thèse	193
A.1	Axial stress vs deformation curve for the unconfined compressive strength test conducted at different initial suction states	203
A.2	Determination of initial Young's modulus and secant modulus for the unconfined compressive strength test conducted at different initial suction states	204

B.1	Shear stress vs shear deformation curve during the direct shear tests for all samples of series 1	205
B.2	Shear stress vs shear deformation curve during the direct shear tests for all samples of series 2	206
B.3	Shear stress vs shear deformation curve during the direct shear tests for all samples of series 3	207
C.1	Deviator stress vs axial strain curve for all samples tested in the unsaturated triaxial tests (Unconsolidated undrained) at 7 different initial suction states	208
D.1	Relative humidity calibration factors for SHT sensors 0-4	209
D.2	Relative humidity calibration factors for SHT sensors 5-9	210
D.3	Temperature calibration factors for SHT sensors 0-4	211
D.4	Temperature calibration factors for SHT sensors 5-9	212
E.1	Plan and elevation of the 2 floor building (ground floor+1) taken from GBP Pisé, 2018 [25] for the estimation of vertical stress	213

List of Tables

2.1	Range of different mechanical parameters in compression from literature . . .	13
2.2	Dry density and OMC from different experimental campaigns on rammed earth	26
3.1	Activity of different clay minerals	48
3.2	Cation exchange capacity and specific surface area of different clay minerals	50
3.3	Average dry density and standard deviation from the average for cylindrical and prismatic samples (Instron machine was more accurate than HM machine)	56
3.4	Different saline solutions, their solubility at 25 °C, the relative humidity, and corresponding suction imposed	61
3.5	Hydraulic conductivity test results	68
3.6	Normal load and stress applied in various series for a particular suction state	75
3.7	Values of the parameter σ_c corresponding to each suction state	97
4.1	Compressive strength, tangent modulus, axial strain at failure for all samples	124
4.2	Independent variables (unknowns) summary	135
4.3	Constitutive equations and equilibrium restrictions	135
4.4	Synthesis of hydraulic, thermal, and mechanical parameters required for the THM coupled modelling	141
4.5	Various material parameters used for THM coupled problem and the method of determination of these parameters, where ‘Exp’ represents determined experimentally, ‘C’ represents that the classical or default value is chosen, and ‘L’ represents taken from literature	144
4.6	The details of the samples studied including the shape, size, method of compaction and granulometry	161
5.1	Synthesis of parameters in two different environmental conditions	172

Chapter 1

Introduction

This chapter provides an overview of different earth construction techniques and mainly focusing on rammed earth. The various advantages of using rammed earth as a sustainable construction material will be discussed. Despite having numerous advantages, there are few drawbacks in using this material for construction. Thus in order to have a better understanding of rammed earth from a mechanical point of view will help to overcome the drawbacks, and this serves as a motivation for the current study. Finally, the objectives of the current study will be highlighted along with the outline of the different chapters.

1.1 Earth as a construction material

Earth is one of the oldest construction material and has been used to build houses, monuments, temples, churches etc. According to Schroeder et al. 2012 [26], the first use of earth as a building material can be dated back to 10000 BC in the eastern Mediterranean and Mesopotamia. In these archaeological constructions, mixtures of locally excavated sand, gravel, and clay were used [27][28]. There are also numerous historical monuments made from earth construction around the globe. A few examples include Potala Palace in Tibet, Ben-Haddou in Ouarzazate (Morocco), the temple of Ramses II at Gournah, Great wall of China, Alhambra palace of Granada (Spain) etc. Even today, earth construction exists throughout the world, and it is the primary process of construction for some countries. Around 30% of the world population still lives in buildings of earthen construction. The worldwide use of earth construction and various UNESCO world heritage sites have been shown in figure 1.1. In most countries of the world, it is possible to compact earth using either sophisticated or primitive tools for building construction. The range of the technical, constructional and architectural possibilities of earth is extremely wide [29]. Earthen construction is being used not only in developing countries but also in developed countries because of its sustainable properties.

The basis of earth construction implies using locally available material. Since the earth composition is different in different places, the construction techniques have been

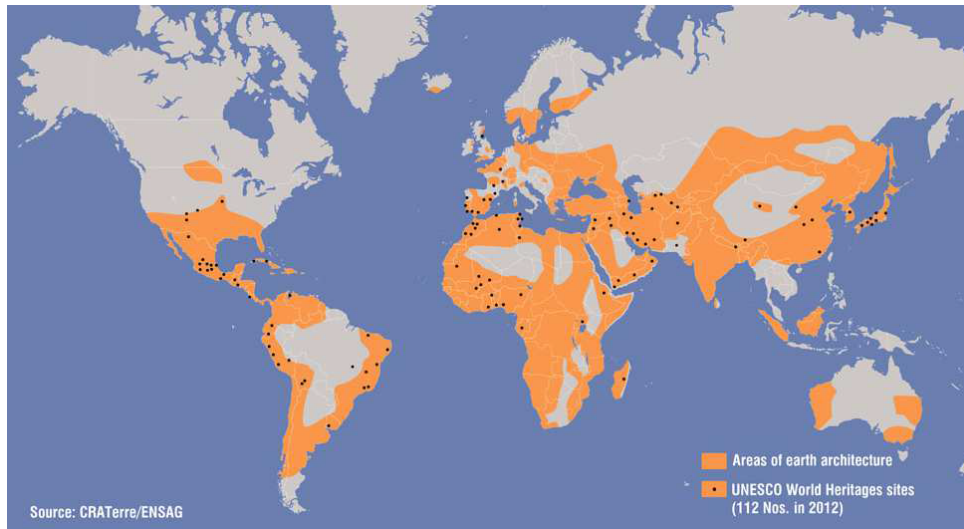


Figure 1.1: A world map showing the different areas of earthen architecture and UNESCO world heritage sites (Source: CRATerre/ENSAG)

evolving with time. There are different techniques for earthen construction based on the method of compaction, moisture content, drying of material, the composition of soil etc. The various construction techniques used are: wattle and daub, cob, adobe, compressed earth bloc, and rammed earth. The distinction between these techniques according to the classification proposed by Hamard et al. 2016 [1] is shown in figure 1.2. This classification was based on three criteria:

- Water content of the mixture
- Implementation either as masonry unit, monolithic wall or infilling
- Structural role, i.e. load-bearing or non-load bearing walls

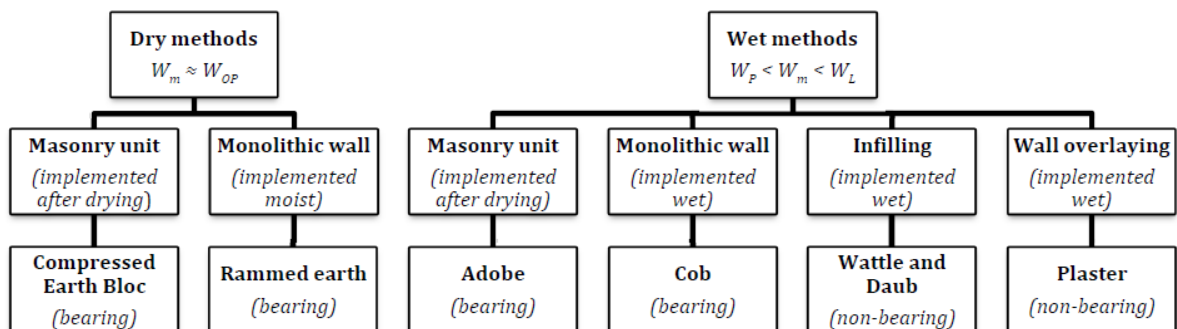


Figure 1.2: The classification of the earth construction process by Hamard et al. 2016 [1]. W_m is the manufacturing water content, W_{OP} is optimum water content, W_p and W_l are the plastic and liquid limit of soil

Wattle and Daub: It is perhaps one of oldest earth construction technique and has been used for over 6000 years. It consists of two parts: wattle and daub. Wattle is the woven lattice of timber elements acting as a load-bearing frame. Daub or mud is the clayey earth which is put on the wattle to cover the entire surface. It does not serve any structural function. The earth used is mixed with straw or other vegetable fibers to prevent shrinkage upon drying. This technique is used for non load-bearing walls which can be either external walls or partition walls of thickness 8-20 cm. The construction process and an example of this construction are shown in figure 1.3.

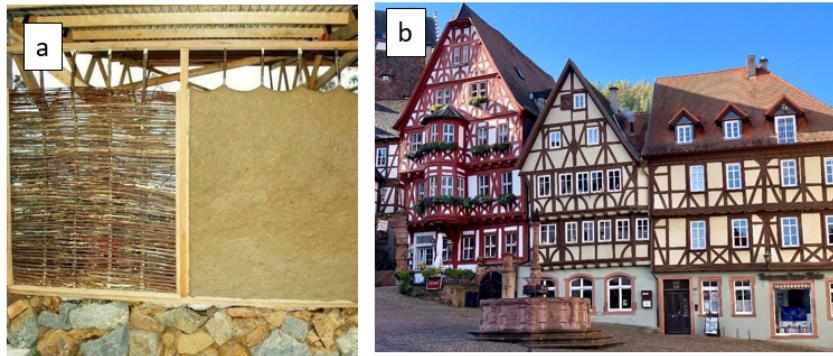


Figure 1.3: The construction process of wattle and daub technique (a) and house made with this technique in Miltenberg, Germany (b)

Cob: It is one of simplest earth construction technique which does not require many tools or a form-work. It usually consists of a wet mixture of clay, sand and organic fibers such as straw or reed, which is molded by hand without any form-work to construct a wall. A plaster made out of lime and sand is used sometimes to windproof the exterior walls from wind damage. Since the cob mixture is applied in a wet state, the mechanical strength of this material is low and it settles under its own weight which limits the height of the wall. Thus cob walls are constructed in multiple layers of monolithic units called lifts. A new lift is constructed after allowing the last lift to dry for around two weeks to gain sufficient strength. The construction of a cob wall and a modern house made with cob is shown in figure 1.4.

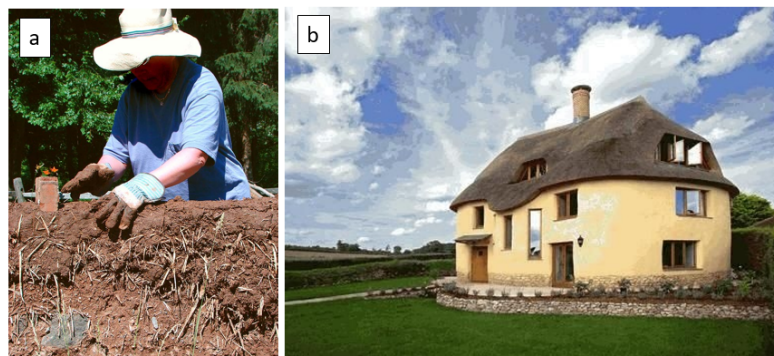


Figure 1.4: Construction of a cob wall (a) and a modern cob house in Ottery St. Mary, United Kingdom (b) (Source: Wikipedia)

Adobe: It is a construction technique that consists of pouring a wet mixture of clayey soil and straw are made inside a mold with dimensions similar to conventional bricks. These are left to dry in the sun for days and are used as masonry units. Straw or other fibers helps to reduce the shrinkage and serves as a reinforcement. The same earth is used as a mortar. Sometimes additives such as asphalt emulsions are added to waterproof the adobe bricks. A mixture of cement and lime can also be used, although it increases the cost of construction. An example of a construction of the wall with adobe bricks is shown in figure 1.5.



Figure 1.5: Manufactured adobe bricks (a) and wall construction using adobe bricks (b)

Compressed earth blocks (CEB): It is a relatively modern construction technique which is an improved form of traditional adobe construction. This method involves pressing a moist mixture of soil to obtain higher density than adobe bricks. The obtained earth blocks are heavier and mechanically more resistant. The compaction pressure can be applied either manually or by using a mechanical press which reduces the original soil volume by half. The blocks are assembled into walls using standard masonry technique. The mortar can be a slurry made of the same soil, or a cement mortar can be used for higher strength. Figure 1.6 shows the manufacturing of Compressed earth blocks and an example of a building using this technique.

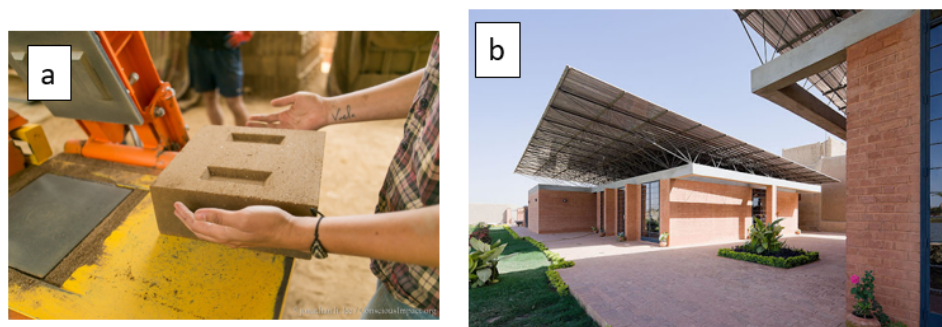


Figure 1.6: A compressed earth block using mechanical press (a) and center of earth architecture building made from CEBs in Mopti, Mali (b)

1.2 Rammed earth

Rammed earth is a construction technique by which dense load-bearing walls can be made by the dynamical compaction of moist soil in layers between removable shuttering or form-works. It is an ancient technique, but the interest in this has been revived due to its sustainable characteristics.

Rammed earth can be used for the construction of foundation, floors and walls. The construction process begins with a temporary frame called form-works. It consists of 2 parallel frames which are clamped together to hold them in position during the compaction process. Wood or plywood form-works were used in traditional construction practice. These form-works should be sufficiently braced in order to maintain the desired shape and dimensions during the construction of the wall. Nowadays, metallic frameworks are used, which allows to input higher compaction energy.

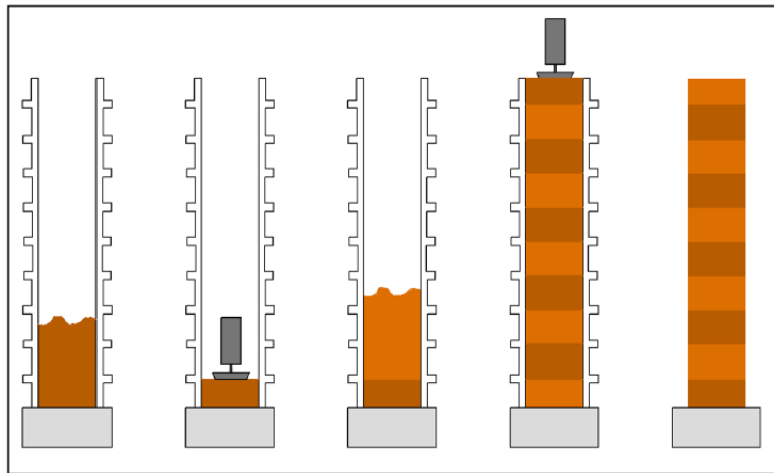


Figure 1.7: A scheme for construction of rammed earth wall in layers [2]

The process of construction of a rammed earth wall is shown in figure 1.7. The moist soil is poured in layers of about 10-15 cm into the temporary form-work and compacted using either manually using a tamper or mechanically using a pneumatic rammer. The thickness of the rammed earth wall is around 45-50 cm. After the compaction process is complete, the thickness of each layer is around 6-10 cm [5]. In this way, a layer of rammed earth is formed. This process of compaction is continued until reaching the top level of the form-work. Rammed earth has sufficient strength and stability to not collapse under its own weight, and the form-works can thus be removed immediately after the compaction process. The part of the wall is allowed to dry for sufficient duration to gain strength, and then another form-work can be placed over it to continue the compaction process until the desired height of the wall is achieved. Rammed earth is generally founded on a base made from stones and pebbles of about 50 cm height [30] in order to avoid the damping effect from the ground. In modern construction, the base is usually made of concrete. An example of a rammed earth wall and a house is shown in figure 1.8.

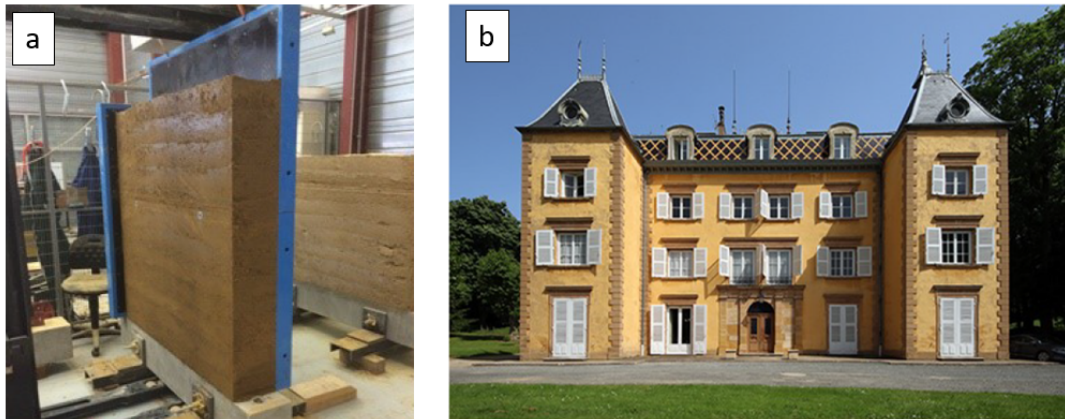


Figure 1.8: A rammed earth wall made in LOCIE laboratory (a) and Château de Reyrieux made from rammed earth (b) in France (Photo: Auroville, earth institute)

There are two different types of rammed earth: unstabilized and stabilized rammed earth. When the clay is the only binder material, it is termed as unstabilized rammed earth or simply rammed earth. When additional binding agents such as cement or lime is added to the soil mix, it is termed as stabilized rammed earth. Stabilization increases the mechanical strength and durability of rammed earth. It reduces the susceptibility to water erosion. It also decreases the permeability of the soil and thus the ability of moisture to pass through the wall. Stabilization reduces the potential of the material to be recycled and also increases the construction cost due to an increase in the embodied energy [5][31]. Thus stabilized rammed earth has reduced environmental and cost benefits. This study will focus only on unstabilized rammed earth and will be labelled as rammed earth in the manuscript.

1.2.1 Advantages and limitation of earthen structures

The building sector is responsible for more than 40% of the total emission of greenhouse gases, and it contributes to the high levels of pollution. According to ADEME 2015, the amount of waste from the building sector was around 44% of the total waste in France. This waste is usually not recyclable and is disposed of in landfills leading to loss of land and pollution. Thus there is a necessity of alternative construction material which has more eco-friendly characteristics compared to concrete and steel. Earthen materials provide a viable solution to this problem since earth is available in abundance and can be sourced at the construction site. It reduces the consumption of natural resources not only during the construction but also during its lifetime. Thus earthen construction such as rammed earth represents a sound alternative to conventional construction techniques, from both energetic and mineral resources point of view and, thus, exactly fulfills the criteria for the urgent and intense ecological transitions needed for the sustainability of society. It has numerous characteristics as a sustainable construction material, and the various advantages have been mentioned below:

1. Reduction of embodied energy: Embodied energy is the total energy consumed by all the processes associated with the production of building, from mining and processing of natural resources to manufacturing and transportation. The embodied energy required for an earthen material is around 1% of the energy needed for construction with cement-based materials [32]. Morel et al. 2001 [33], studied the environmental benefits of construction using local materials. A comparison was made between the energy consumed by a rammed earth house and a concrete house. It was found that rammed earth consumes less energy (70 GJ) compared to the concrete house (239 GJ).
2. Hygro-regulator effect: Earthen construction leads to the reduction of operational energy due to the hygro-regulator effects. In atmospheric conditions where the relative humidity is high, earthen walls absorb moisture due to the presence of clay particles. When the relative humidity of the surrounding atmosphere becomes low, this absorbed vapor is released back. Thus it helps in maintaining the hygroscopic conditions and reduce the need for air-conditioning.
3. Thermo-regulator effect: It also reduces the operational energy due to the thermo-regulatory effects. The hygro-regulatory effects discussed above also impact the average temperature inside the earthen building. During the hottest hours of the day, evaporation takes place in the earth mass which is an endothermic process which, requires heat and thus reduces the temperature of the surrounding. Similarly, during the cold hours of the day, condensation takes place in the earth mass, which is an exothermic process releasing heat and thus raises the temperature.
4. Recycling or demolition of building: The recycling and the demolition of the building also contribute to a significant amount of energy consumption [2]. The amount of waste generated from construction and demolition of a building is responsible for filling between 13-30% of the total landfills around the world [34]. For raw earth construction, recycling is not a problem because the same earth can be reused for construction activity and does not need any landfills for its storage. This advantage is lost if the earth is stabilized using chemical binders.

In addition to these advantages, earth construction has several other benefits such as acoustic insulation properties, fire resistance etc.

Limitations of earthen materials

Despite the numerous advantages of the earth with regards to sustainability, various limitations hinders the widespread use of earthen materials such as rammed earth for construction. One of the biggest limitations of using an earthen material is its sensitivity to water which makes its use challenging to be generalized. Indeed, moisture ingress induces changes in the consistency of the earth from solid to plastic. This leads to a change in the mechanical strength and rigidity. When earthen structures are present in a dry climate, they are durable which can be seen from different historical monuments which are still in

well-preserved conditions. On the other hand, in wet climatic conditions, durability and stability decrease, especially for unstabilized earth. Rainfall can cause surface erosion and capillarity from the ground surface leads to an increase in saturation and thus decrease in the strength and rigidity. These unfavorable humid pathologies lead to different problems and uncertainties in the stability of earthen buildings. Different measures can be followed to avoid these problems such as overhanging roofs and protective foundations. Despite that, the changes in relative humidity during typical working environment cannot be avoided. During the lifespan of the building, the ambient conditions are continuously evolving, which affects the mechanical performance. Thus the lack of characterization of this hydric influence is a major disadvantage for its direct practical application.

Another drawback that the earthen construction faces are the lack of technical guidelines and codal provisions. Although some countries have their own set of guidelines and standards, there are uncertainties in the design methodologies. In addition, there is a lack of coherence between guidelines from different countries. This is partly because of different environmental conditions in these countries which makes it difficult to be generalized. There is a lack of standardized procedures for the determination of mechanical parameters in the laboratory. Some of the procedures used are from concrete or soil mechanics which are not suitable since it does not take into account the properties specific to earthen materials.

1.3 Thesis objective and outline

As discussed in the previous section, the earthen materials such as rammed earth have numerous advantages to be used as a sustainable construction material. Despite having these advantages, it suffers from a sensitivity to water which limits its use in the mainstream market. The main objective of this study is to emphasize the use of rammed earth for energy-efficient construction since it is an eco-sustainable material. This will help to have a better understanding of the hydro-mechanical behavior of rammed earth. This hydro-mechanical coupling is essential to be understood and quantified both for new construction and preservation of historical buildings and monuments, which are very relevant nowadays. The various aspects that will be studied in the thesis are mentioned as follows:

- An extensive experimental campaign will be carried out at a material scale on rammed earth to study the hydro-mechanical behavior. The tests will be carried out at different hydric conditions. This will help us to understand the variation of various key mechanical parameters with the hydric state.
- To study the hydro-mechanical behavior at a structural scale, an experimental campaign will be done on representative columns. The columns will be subjected to drying for different durations and then mechanically tested to study the variation of strength and stiffness parameters.

- From the experimental campaign conducted at the material scale, suitable parameters will be chosen and adapted in a constitutive model for performing finite element modelling. Using the concepts of unsaturated soil mechanics, the hydro-mechanical coupled modelling will be taken into account. The objective will be to reproduce the results of experiments on columns with non-uniform hydric states using numerical modelling.
- A numerical case study will be done performed on rammed earth walls with different orientations. The early age drying behavior of walls will be studied. The objective will be to determine the drying period required after the preparation of a wall in order to construct another floor above it. In this way, a very important practical problem in rammed earth construction will be analyzed.

This thesis is divided into six chapters, a brief outline is discussed below:

Chapter 1 (*Introduction*): This chapter highlights the use of earth as a construction material using different techniques, particularly rammed earth. The various advantages and limitations of earthen materials are discussed. Finally, the main objectives of this thesis are highlighted.

Chapter 2 (*Literature review*): This chapter presents the detailed literature review of the experimentation performed on rammed earth. The various factors influencing the mechanical parameters will be studied, especially the hydric influence. The various studies done on the constitutive modelling taking into account the hydric influence are presented.

Chapter 3 (*Hydro-mechanical behavior at material scale*): This chapter includes the experimental campaign at material scale to study the hydro-mechanical behavior. The various characterization tests, method of compaction of samples, method of control of hydric conditions, the variation of mechanical parameters with the hydric state are presented in detail.

Chapter 4 (*Experiments and simulation at structural scale on columns*): The hydro-mechanical behavior of representative rammed earth columns is investigated. The first part of this chapter includes the drying behavior and the compression characteristics of the rammed earth columns. The second part includes the hydro-mechanical coupled finite element method simulations of the drying phase and the compression results. Finally, a comparison of the experimental and simulation results is presented.

Chapter 5 (*Case study on rammed earth walls*): In this chapter, a numerical case study is performed on rammed earth walls to study the early age drying behavior. The drying period required for subsequent floor constructions in different environmental conditions is determined to answer a practical issue in rammed earth construction.

Chapter 6 (*Conclusions and perspectives*): This chapter presents the key findings of the thesis and proposals for future research work.

Chapter 2

Literature review

In the past centuries, earth has been employed for construction purposes using various traditional construction techniques such as rammed earth, daub, adobe, and cob. Due to the advent of technology and availability of powerful machinery earth can now be developed using modern construction techniques such as compressed earth blocks (CEB), prefabricated rammed earth, casted earth etc. The present work focuses on the use of rammed earth as a construction material.

Until a few years ago, the design rules of rammed earth constructions were based on empirical relations and physical properties of soil which did not take into account the hydro-mechanical coupling. Recently, this material has been analyzed using the concepts of soil mechanics, in particular using unsaturated soil mechanics theories, since rammed earth is basically a compacted soil existing in an unsaturated state. Jaquin et al. 2009 [13] discussed the unsaturated characteristics of rammed earth. Rammed earth samples were prepared at the optimum moisture content, and after undergoing significant drying, it leads to lower water contents and provides additional strength. Gallipoli et al. 2014 [32] underlined the role of unsaturated soil mechanics in rammed earth construction. Indeed, until recently rammed earth construction was considered as ‘weak masonry’ rather than a porous continuum. Gulkan et al. 2004 [35] studied the earthquake damage of rammed earth building which was due to loss in cohesive strength, which was better explained by porous continuum models rather than masonry models. This highlights the need for research in the interface between structural engineering and geotechnical engineering to better understand and predict the behavior of earthen structures.

In this section, a bibliography synthesis of the key mechanical parameters of rammed earth mechanical such as the compressive strength, tensile strength, modulus of elasticity is presented. The various factors influencing the mechanical behavior are discussed in detail, especially the water influence. Finally, a brief discussion is presented on the constitutive modelling of rammed earth and coupled hydro-mechanical analysis to take into account the unsaturated behavior of rammed earth.

2.1 Key mechanical parameters

Rammed earth has been used as a construction material for centuries, yet the scientific characterization of the earth is very recent. There are very few guidelines and standards for testing of this material. The design guide by Walker et al. 2005 [36] for the construction of rammed earth structure indicates that the most widely used indicator of strength is compressive strength. It depends on several factors such as moisture content, compaction energy, sample geometry, and, dry density based on the optimum moisture content. According to New Zealand standard NZS:1998 [37] for rammed earth to be used as a construction material, it should have a minimum characteristic compressive strength of 1.3 MPa. The Australian Earth Building Handbook [38] recommends the design value of compressive strength in the range of 0.4 to 0.6 MPa. Whereas, New Mexico code, 2001 [39], suggests a range of 1-2 MPa for the characteristic compressive strength. It is worth noting that although this value is low when compared to other construction materials such as bricks or concrete, the typical downward pressure of a single storey building made of earth is of the order 0.1 MPa.

Concerning the value of Young's modulus, there are no coherent design standards. The recommend design value of Young's modulus is 150 MPa from the New Zealand standards and 500 MPa from the Australian handbook. No recommendation for Young's modulus was provided in the New Mexico code. Thus in this part, the discussion about the strength and stiffness characteristics at both material and structural scale in the literature has been presented.

Material Scale

Various testing programs for the experimental characterization of the mechanical parameters of rammed earth has been done at material scale. Several studies have been carried out to analyze the mechanical behavior and evaluate its compressive strength (R_c) and elastic modulus. The tangential Young's modulus (E_{tan}) is evaluated from the initial linear part of the stress-strain curve. Hall et al. 2004 [3] performed compressive strength test on 10 cm cubic rammed earth samples (figure 2.1) with different particle size distribution. The samples before testing were cured for a minimum of 28 days at a temperature of 20 °C and relative humidity (RH) of 75 %. It was observed that only a few samples exceeded the threshold of minimum compressive strength = 1.3 MPa mentioned in NZS:1998 [37].

Lilley et al. 1995 [40] also performed the compressive strength testing on 15 cm rammed earth cubes of different soils in a British Standard concrete cube test machine at ages of 24 hours, 7 days, and, 28 days. The dry density of samples was between 1970 to 2110 kg/m³, and the compressive strength obtained after 28 days of curing was around 1.8-2 MPa.

Maniatidis et al. 2007 [41] determined the unconfined compressive strength on cylindrical samples of 10 cm diameter and 20 cm high. The average compressive strength obtained was 2.46 MPa (coefficient of variation of 6.42%) with an initial tangent modulus

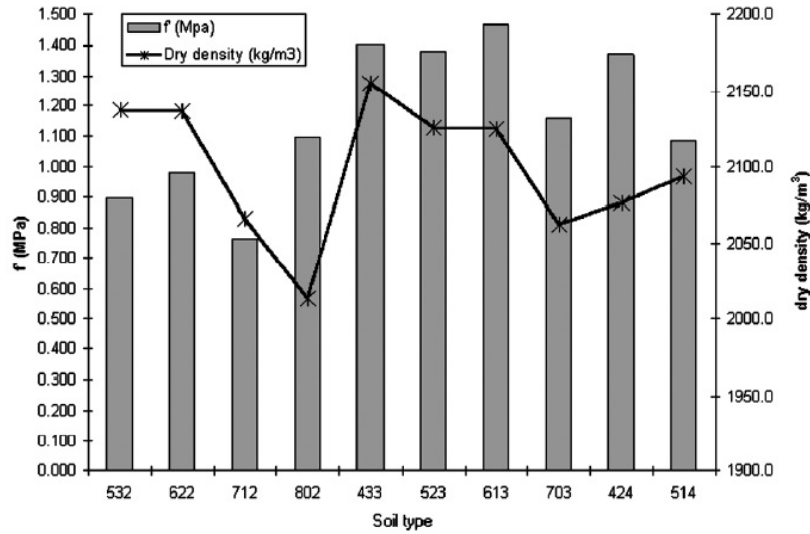


Figure 2.1: The results of characteristic compressive strength (f') and dry density for different rammed earth soil type [3].

of 160 MPa.

Table 2.1 shows the different mechanical parameters in compression found in the literature. These different results will be discussed in the further sections. A discrepancy for the value of compressive strength is observed. A significant degree of dispersion is also found in the value of Young's modulus. These dispersions can be due to difference in the soil, the method followed, dry density after compaction, scale and geometry of samples, workmanship etc. Besides, it is essential to note that the compressive strength is also dependent on the hydric state at which the samples are conditioned. The difference in the ambient atmospheric conditions in the literature mentioned above can lead to a discrepancy in the results.

Table 2.1: Range of different mechanical parameters in compression from literature

Specimen size	R_c (MPa)	ρ_d (kg/m^3)	Slenderness ratio	E_{tan} (MPa)	Reference
$10 * 10 * 10 \text{ cm}^3$	0.75-1.5	2020-2160	1	-	Hall et al. 2004 [3]
$15 * 15 * 15 \text{ cm}^3$	1.8-2	1970-2110	1	-	Lilley et al. 1995 [40]
$\phi = 30 \text{ cm}, H = 60 \text{ cm}$	1.9	1850	2	160	Maniatidis, 2008 [42]
$30 * 30 * 60 \text{ cm}^3$	0.62-0.97	1760-2027	2	60-70	
$\phi = 10 \text{ cm}, H = 20 \text{ cm}$	2.46	1850	2	205	Maniatidis, 2007 [41]
$100 * 100 * 30 \text{ cm}^3$	0.6-0.7	-	3.3	60	Jaquin et al. 2006 [4]
$40 * 40 * 65 \text{ cm}^3$	1	1820-1980	1	100	Bui et al. 2009 [7]
$\phi = 16 \text{ cm}, H = 30 \text{ cm}$	1.7-2.1	1920	1.87	460-540	Bui et al. 2014 [5]
$46 * 31 * 13 \text{ cm}^3$	6.56	-	0.42	71	Piattoni et al. 2011 [43]
$25 * 15 * 13 \text{ cm}^3$	2.55	-	0.87	131	

Structural scale testing

It is vital to understand that test at the material scale is not sufficient to understand fully the behavior of rammed earth. The scale and geometry effects lead to a difference in mechanical behavior. In addition, rammed earth is compacted in layers which is harder to reproduce at the material scale. Thus, in order to have a better idea of the behavior of in-situ rammed earth walls, various authors have conducted compression and shear testing at a structural scale on wallettes.

Jaquin 2006 [4] tested 5 rammed earth walls of size $100 \times 100 \times 30 \text{ cm}^3$. The walls after compaction at optimum conditions were left to dry in the ambient condition for 14 days. The loading on the walls was applied across the whole width, and the load was spread using timber of size $6 \text{ cm} \times 30 \text{ cm}$ (figure 2.2). The failure stress was determined while the displacements were not recorded. Diagonal cracking was observed in walls, and the peak stress obtained was between 0.6 and 0.7 MPa. It is to be noted that the walls were not allowed to dry fully and reach quasi-static water content. The failure stress obtained was thus less than 1 MPa and is lower than the values observed in other studies mentioned in table 2.1.

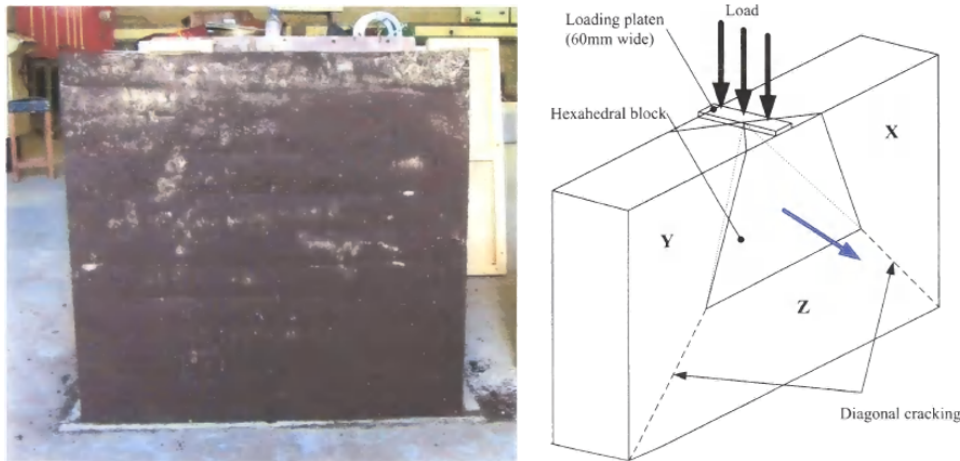


Figure 2.2: The rammed earth wall studied (left) and the loading pattern and the failure mechanism for the wall from Jaquin, 2006 [4]

Bui et al. 2014 [5], conducted compression test by applying concentrated loads on $(30 \times 30) \text{ cm}^2$ surface at the middle of two wallettes of size $(100 \times 100 \times 30) \text{ cm}^3$ (figure 2.3). Before testing the wallettes were subjected to drying for 148 and 155 days to ensure stable water content ($1.8 \pm 0.2\%$). The mean failure load of 112 kN, corresponding to a displacement of 4.5 mm from the central point of the wallettes was obtained (figure 2.3). The maximum normal stress in the wallettes was 1.22 MPa at the loaded zone, whereas the mean compressive strength of the cylindrical specimens for the same soil was 1.9 MPa. It was pointed out that slenderness of wall was greater than two that can induce buckling and could decrease the failure stress. Also, the real compressive strength of wallette could be less than the cylindrical specimens.

It was observed that the zone under loading had a greater settlement and under-

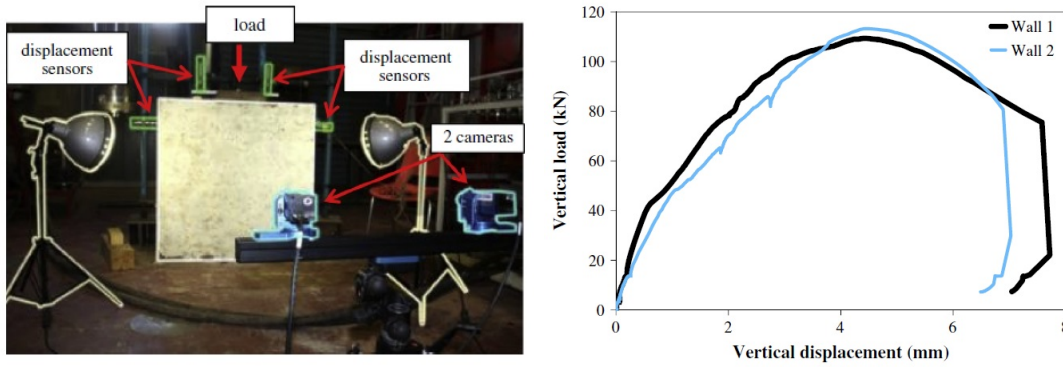


Figure 2.3: Experimental setup for the compression testing of the wallettes (left) and Load-displacement curve (right) from Bui et al. 2014 [5].

went failure. A quasi-vertical failure surface was formed due to the differential settlement between the loaded and unloaded zone (figure 2.4). To study this behavior, it is essential to determine the shear strength of rammed earth wallettes. Shear strength is required to check the punching strength of rammed earth walls, such as beam placed on rammed earth wall and vertical ties in anti-seismic devices. Also, it is mobilised due to wind loading and seismic conditions, which causes stability issues. The shear strength was analytically determined using apparent values of cohesion and friction angle (Mohr-coulomb theory). They identified the value of the shear parameters $c = 0.14f_c$ and $\phi = 51^\circ$. Thus, for rammed earth with compressive strength in the range of 1-3MPa, cohesion is about 0.14-0.42 MPa. These values were found to be coherent with Jaquin et al. 2008 [18]. These parameters are apparent, in the sense that they vary with the humidity condition in the earth and do not characterize the material intrinsically. These effects will be dealt with later in the text.

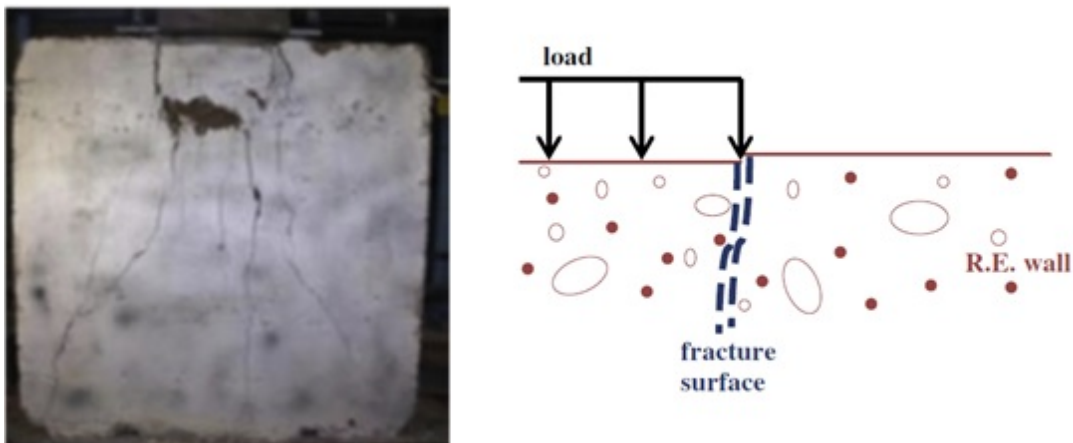


Figure 2.4: Fracture surface on the wallette due to differential settlement between loaded and unloaded zone [5].

The compressive strength and shear strength for the wallettes was also determined by Miccoli et al. 2015 [6]. They conducted axial compression, and diagonal compression test on stabilized rammed earth wallettes of dimensions $50 \times 50 \times 11 \text{ cm}^3$. Before

testing the samples were dried in a climate room with a temperature of 23 °C and relative humidity of 50 %. Five compression tests were carried under displacement control. The axial stress-strain curves highlighted non-linear behavior under compression, starting at low-stress levels (Figure 2.5a). Compressive strength showed relatively low scattering and varied from 3.3 MPa to 3.9 MPa while elasticity modulus showed high scattering and varied from 2844 MPa to 5048 MPa (2.5a). Five diagonal compression tests were carried under force control. Rammed earth wallettes exhibited early peak shear stress followed by shear hardening (2.5b). Both shear strength and shear modulus showed relatively high scattering, shear strength varied from 0.54 MPa to 0.83 MPa and shear modulus varied from 1260 MPa to 2146 MPa. Cracks were observed in the interface between the layers suggesting that in this stress state rammed earth should be considered anisotropic. The values of strength and stiffness obtained from these test were significantly higher due to the stabilization of earth. It has a direct effect on increasing the mechanical performance leading to a high value of compressive strength and Young's modulus.

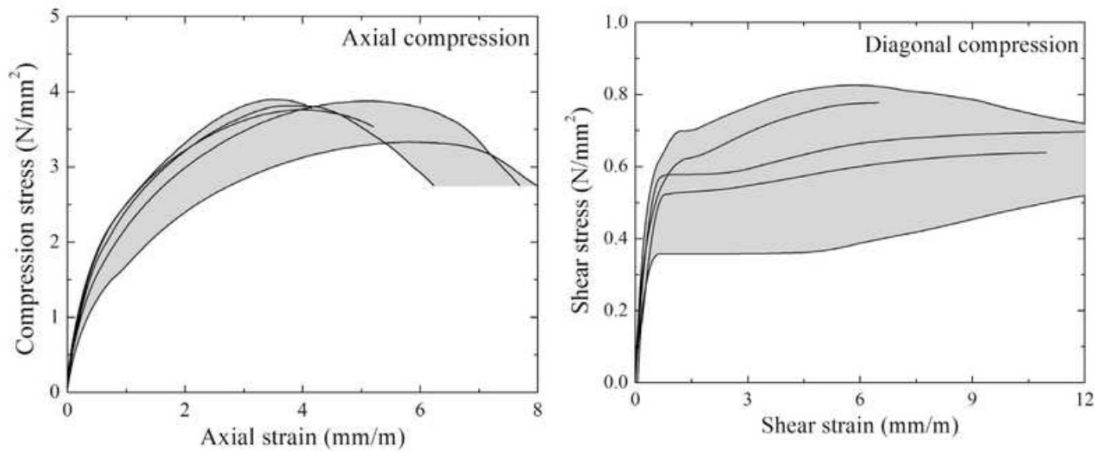


Figure 2.5: Experimental results of axial compression test (left) and diagonal compression test (right) on wallettes from Miccoli et al. 2015 [6]

The shear strength parameters were determined by El Nabouch et al. 2018,[44] at large scale. Direct shear tests were performed in a tailored shear box (length = width = 49 cm and height = 45cm) to test representative samples. A drying period of one month was chosen, which led to a water content of 4-6%. The samples were tested so that the horizontal shear plane was at the middle of the layer and at the interface. The apparent cohesion and apparent friction angle obtained at the interface of the layer ($c = 24.7$ kPa and $\phi = 32.9^\circ$) was lower than in the middle of the layer ($c = 30$ kPa and $\phi = 35.3^\circ$). The direct shear test was also done in a Casagrande box on samples that were taken from the wall, which was at quasi-dry state (2-2.5% water content). The apparent cohesion and apparent friction angle were significantly higher for the small samples since the water content was lower. Also, the specimen size could have also affected the results. It is pretty evident that there is a great dispersion in the evaluation of mechanical characteristics in the literature. There are various factors which affect these parameters, and thus it is very important to discuss them for studying the mechanical behavior.

2.2 Factors influencing the mechanical characteristics

In the previous section, the mechanical parameters of rammed earth were discussed. It was found that there is a discrepancy in the value of these parameters in the literature. It is because there are multiple factors which affect the mechanical strength of rammed earth related to the method of compaction, sample geometry, the composition of soil, nature of clay, soil structure, and hydric state. In this section, these factors will be discussed in detail.

2.2.1 Sample geometry and scale

The geometry of the samples used for studying mechanical characteristics can significantly affect the value of compressive strength. Maniatidis et al. 2008 [42] studied prismatic samples (60 cm x 30 cm x 30 cm) and cylindrical samples ($H = 60$ cm and $\phi = 30$ cm) which were stacked at different heights and then compressed. Before compression, the samples were dried in ambient laboratory conditions for 4 to 6 weeks. Comparison of the prismatic samples with the cylindrical ones with the same height shows that the cylindrical sample had 50 % higher compressive strength compared to the equivalent prismatic sample. It was suggested that it could be due to the localized and less effective compaction of the material at the corners of the prismatic specimen. It seems thus that it is preferable to use a cylindrical sample to determine more representative characteristics.

In addition to the geometry, slenderness ratio of the sample also significantly affects the compressive strength. Slenderness ratio (SLR) is defined as the ratio between the height and width (for prismatic samples) or diameter (for cylindrical samples). There is an increase in the compressive strength of material for lower slenderness ratio. It is because of the more significant boundary effect, which leads to additional friction between the loading platen and the sample top and bottom surfaces. This leads to additional confinement which results in increased strength. Piattoni et al. 2011 [43] studied the compressive strength of rammed earth blocs with a slenderness ratio of 0.42 and 0.87 and compared it with a wall of slenderness ratio of 1.26. The compressive strength decreased with the increasing slenderness ratio, from 6.56 MPa for $SLR = 0.42$, 2.55 MPa for $SLR = 0.87$ to 1 MPa for wall with $SLR = 1.26$. Ciancio et al. 2012 [45] concluded that for a cylindrical sample with slenderness ratio equal to 2, the effect of boundary condition is negligible on the computation of compressive strength if measurements are done in the central third of the sample. Also, several studies have shown that for a slenderness ratio of about 2, the compressive strength does not depend on the geometry and depends only on the material used and method followed [46][47]. In addition, the slenderness ratio of 2 avoids buckling effects. Thus, for conducting a compressive strength test on earthen material, a slenderness ratio of 2 with cylindrical geometry is generally recommended.

In addition to the sample's geometry, the scale at which the study of mechanical

behavior is carried out is also important. Maniatidis et al. 2007 [41] performed small scale compression test on cylindrical sample of height = 20 cm and diameter (ϕ) = 10cm, which were compacted using modified Proctor test and cured at 65 % RH and 20 °C for four weeks. There was significant variation in material performance between small scale specimen and samples closer to the size of the walls. The strength of the cylindrical sample with 30 cm diameter was found to be 23 % lower than the 10 cm diameter sample. The reduction in strength and stiffness was attributed to higher gravel content according to the weak link theory.

Mechanical characteristics was also determined by Bui et al. 2009 [7] on three different experimental scales (figure 2.6).

- Wall scale
- Representative Volume Element (RVE) scale
- Compressed earth blocs (CEBs) scale

This study was done on full-scale in-situ walls, on a column which is manufactured in the same process as the in-situ wall which is representative of the actual wall conditions and at material scale on equivalent CEBs which facilitates laboratory test procedures. The elastic modulus of rammed earth was determined at these three different test scales. Figure 2.7 shows the comparison of modulus of elasticity at three different scales. The results calculated from equivalent CEBs were close to the rammed earth RVEs tested in the laboratory. At the wall scale, the in-situ dynamic measurements gave higher results than the other two approaches.

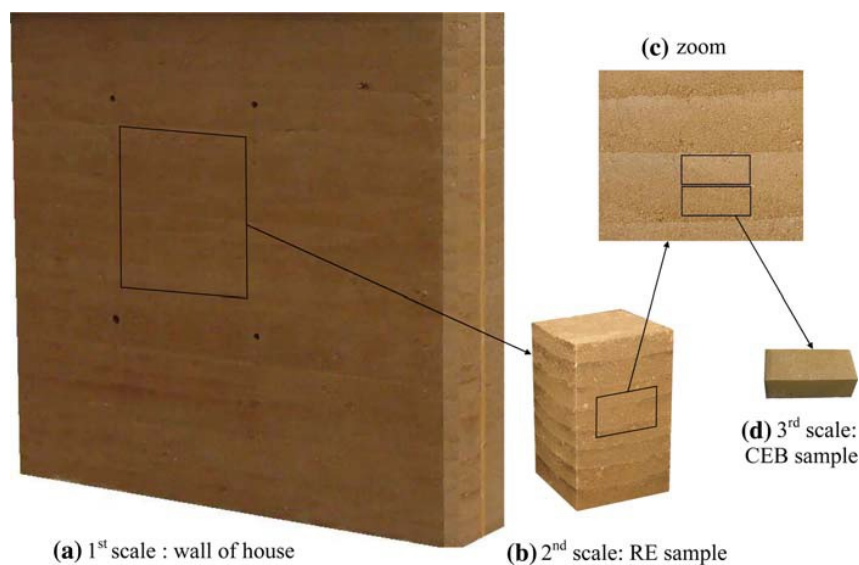


Figure 2.6: Different scales of study including wall scale, a representative element scale and material scale (CEB) from Bui et al. 2009 [7].

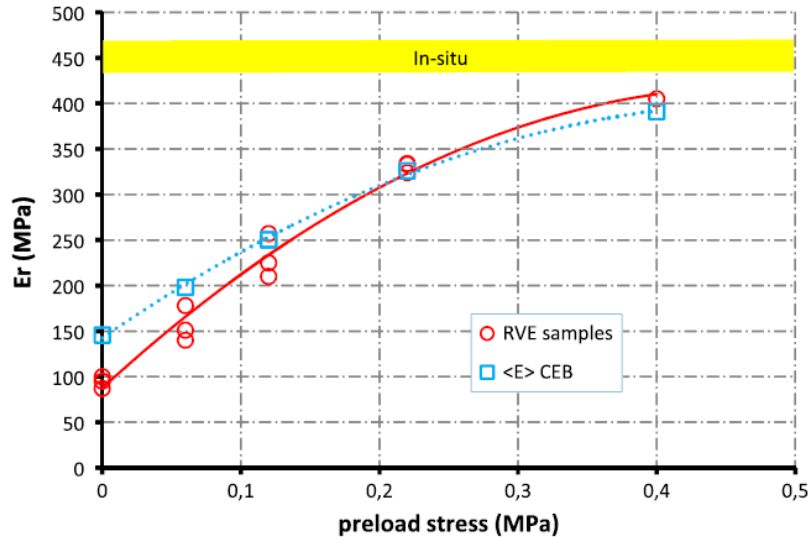


Figure 2.7: Reloading modulus of elasticity variation with preload stress for the three scales of study by Bui et al. 2009 [7]

2.2.2 Granulometry

A very important question is whether a particular soil can be considered suitable to be used as a rammed earth construction material or not. The earth which is used for construction is generally sandy loam subsoil. The topsoil is unsuitable for rammed earth as it contains organic matter. The quantity of this soil must be limited to 1-2 % if allowed at all [48].

Further, the granulometry a key factor for the suitability of the soil as rammed earth material. The particle size distribution curve is obtained from a combination of dry and wet sieving, and sedimentometry. The composition of rammed earth soil is analogous to concrete. It contains an inert aggregate fraction (sand and gravel) and a binding agent (silt and clay). The relative proportions of gravels, silts, sand, and clay providing a well-graded material are more suitable for construction as it makes it possible to reach a high degree of imbrication of grains.

Houben et al. 1994 [8] suggested a range of particle size distribution for the soil to be suitable for rammed earth construction purposes (figure 2.8). It means that if the particle size distribution of the soil is within the envelope proposed, the soil can be used as rammed earth material. It is the most well-known guideline related to the granulometry of the soil.

However, there is evidence in the literature that granulometry is not sufficient for the suitability of soil. Ciancio et al. 2013 [49] highlighted that it is not always recommended to predict the mechanical performance of rammed earth only on the basis of soil properties. Hall et al. 2004 [3] studied the compressive strength of 10 different soil mixes corresponding to the particle size distribution parameters suggested (figure 2.8). It was found out that only 4 out of 10 samples had sufficient compressive strength of 1.3

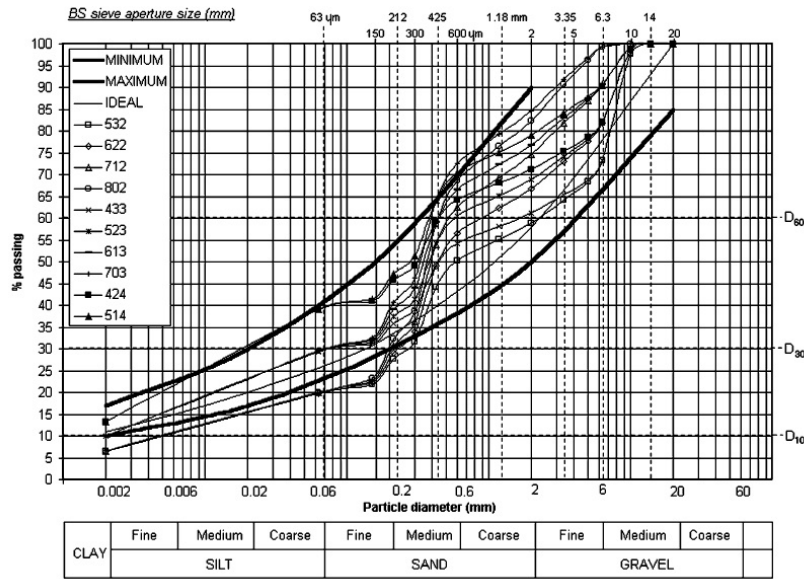


Figure 2.8: Particle size distribution of different soil mixes [3] and limit envelopes according to Houben et al. 1994 [8]

MPa according to NZS:1998 [37] standards.

Other studies such as Champire et al. 2016 [9] studied three different soils (labelled as STR, CRA, and ALX) which came from old rammed earth buildings. The particle size distribution curve (figure 2.9) shows that the soils were not in the envelope proposed by Houben et al. 1994 [8]. They concluded that granulometry cannot be solely used as a criterion for suitability of soil as rammed earth material. It was suggested that nature of clay is useful in addition to amount of clay, which is characterized by granulometry.

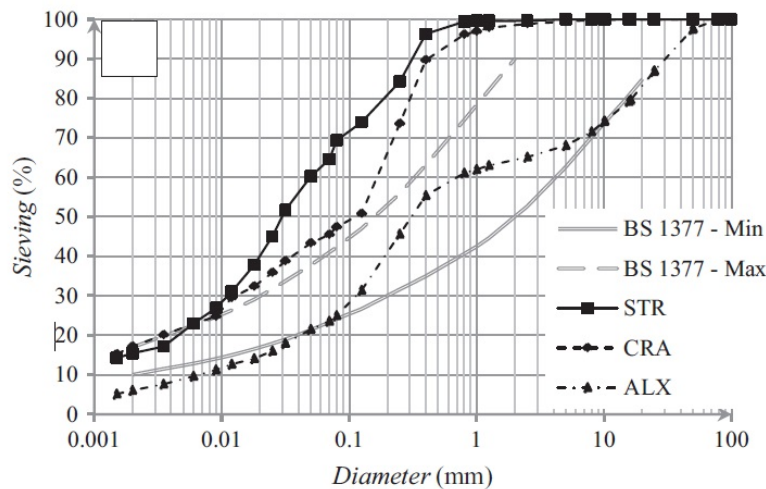


Figure 2.9: Particle size distribution of tested material [9] and upper and lower bounds according to Houben et al. 1994 [8] represented as BS1377-Min and BS1377-Max

2.2.3 Clay content and nature

A large proportion of clay, especially swelling clays, is not recommended. Volumetric variations due to shrinkage under drying are unwanted as it generates cracks which have an impact on the global deformation of rammed earth structures. The addition of a small quantity of sand or gravel could have a positive impact on the reduction of shrinkage [20].

Lilley et al. 1995 [40] conducted compressive strength tests on cubes with soil mixes with different clay contents. Figure 2.10 shows the difference in compressive strength at different ages of drying (24 hours, 7 days, and 28 days). The strength of the soils after 28 days reduced by 14 % of their strength at 7 days. It was highlighted that this decrease in cube strength was due to the shrinkage cracks upon drying, which weakens the soil having a higher percentage of clays.

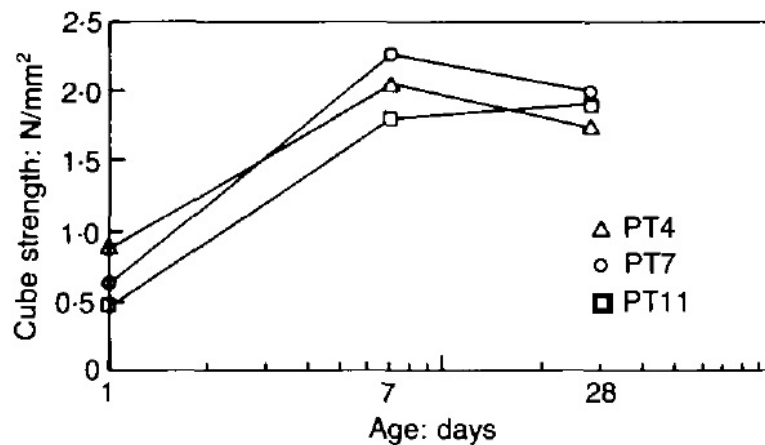


Figure 2.10: Evolution of compressive strength with drying age for soils having different clay content

Helson et al. [10] studied the effect of clay content on the compressive strength for two different stabilised soils. Figure 2.11 shows that the unconfined compressive strength increases with clay content until reaching an optimum percentage of clay and then decreases.

Champiré et al. 2016 [9] highlighted that the activity of clays has a much more significant impact on the mechanical behavior of compacted earth in comparison to the quantity of clay. This is true provided that the amount of clay in the cohesive matrix is sufficient to provide cohesion. The activity of clay which depends on the mineralogical nature is defined as the ratio of plasticity index to the percentage of soil finer than $2 \mu\text{m}$ and the amount of clay is quantified from the particle size distribution curve.

The particle size distribution of the three soils studied (STR, CRA, and ALX) is shown in figure 2.9. The amount of clays (particles lower than $2 \mu\text{m}$) was equal to 15% for STR, 16% for CRA and 8% for ALX. The activity of clay was qualitatively linked to the Methylene Blue Value (MBV). Higher the MBV value, more active is the soil. The soil

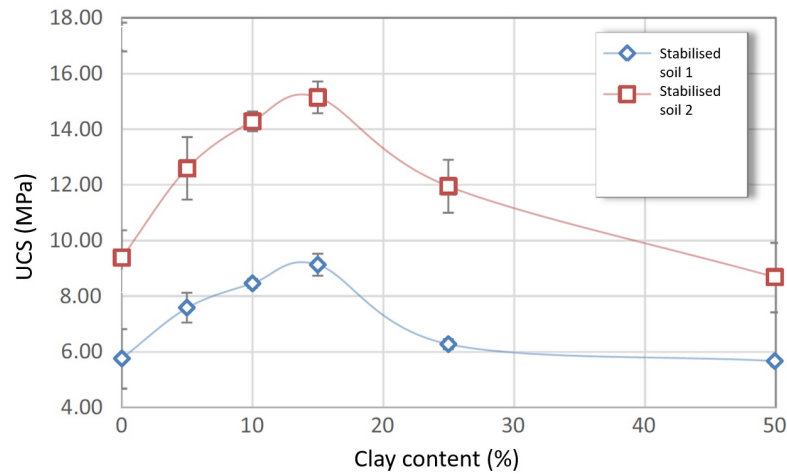


Figure 2.11: Variation of unconfined compressive strength with clay content (modified after Helson et al. 2017 [10])

CRA was most active soil ($MBV = 2.7$) amongst the three, whereas STR ($MBV = 1$) and ALX ($MBV = 0.8$) have similar activity. The damage which is related to the degradation of stiffness (E) and plasticity behavior represented by the residual strain (ϵ_{res}) at the end of each loading cycle is shown in figure 2.12 for the different soils. The soil with more active clay (CRA) showed very high irreversible plastic strains and almost no damage at all. In comparison, the other two soils (STR and ALX), which were less active showed significant damage and lower irreversible plastic strains.

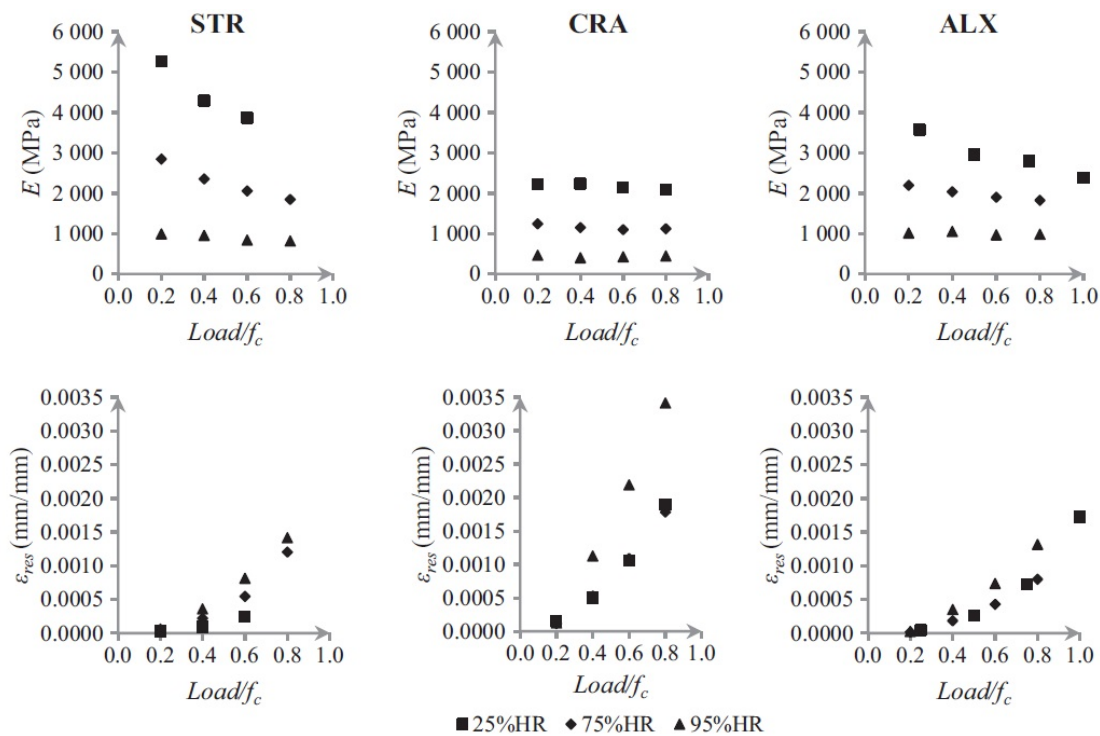


Figure 2.12: Damage and plasticity behavior for different soils at different storage humidity

Figure 2.13 shows the strength to stiffness relationship for the different soils studied by Champiré et al. 2016 [9]. Soils with similar activity values showed a similar relationship, whereas the soil with higher activity exhibits a higher strength to stiffness ratio.

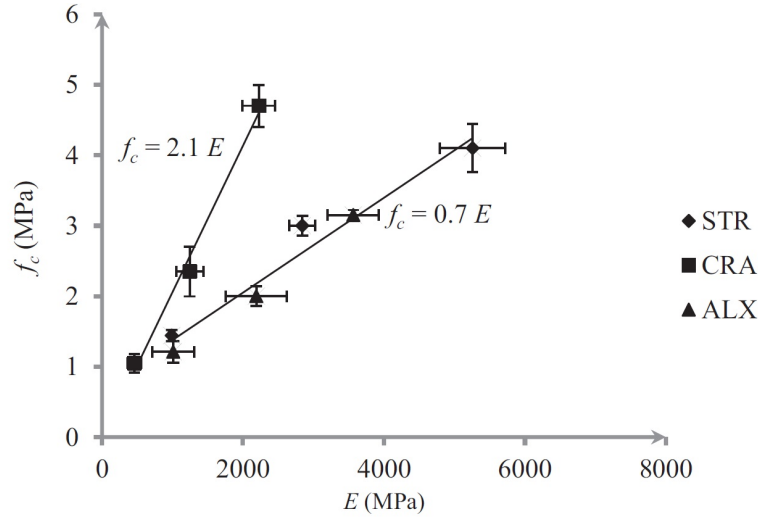


Figure 2.13: Relationship between compressive strength and Young modulus for different soils

2.2.4 Dry density and method of compaction

Dry density is one of the main parameter influencing the strength of rammed earth. The dry density is dependent on the granulometry, which we already discussed, moisture content during compaction, the energy input for compaction, and the type of compaction (static or dynamic) [50]. The dry density value for different earth structures usually ranges from 1700 kg/m^3 to 2200 kg/m^3 [8].

Various authors studied the variation of compressive strength with the dry density obtained after compaction. Morel et al. 2007 [11] studied the compressive strength of compressed earth blocs (CEBs) for unstabilised soil and soil stabilised with cement. Figure 2.14 shows that the compressive strength increases with increase in dry density.

Kouakou et al. 2009 [12] studied the unconfined compressive strength of two types of Adobe material: Traditional adobe blocs and Pressed adobe blocs (PABs). For both types of adobes, the compressive strength increased with the dry density (figure 2.15).

In order to achieve the maximum dry density, it is important to determine the optimum moisture content (OMC) and the appropriate method of compaction for determination of OMC. Different compaction techniques have been used in the literature such as ‘standard’ Proctor test using 2.5 kg rammer and ‘modified’ Proctor tests using 4.5 kg rammer (BS 1377-4, 1990), vibrating hammer generally used for granular soils, heavy manual compaction test etc.

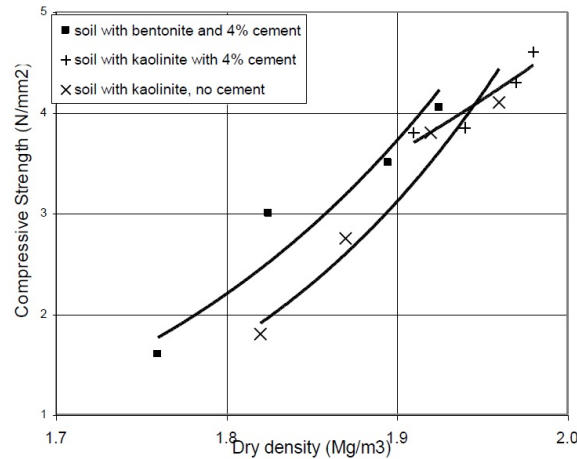


Figure 2.14: Variation of compressive strength with dry density for different types of soil after [11]

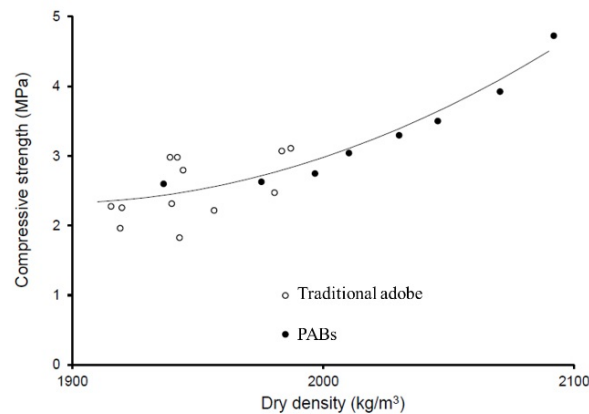


Figure 2.15: Evolution of compressive strength with dry density for traditional adobe and pressed adobe blocs (PABs)[12]

Jaquin et al. 2009 [13] used vibrating hammer test to determine the optimum moisture content (figure 2.16). Burroughs, 2010 [51] used modified Proctor test as the compaction effort applied provides a greater simulation of compaction to on-site ramming. Beckett et al. 2012 [16] used the Light Proctor test for optimum moisture determination in accordance with British Standard BS 1377- Part4: Compaction following the work of Hall et al. 2004 [3].

Gerard et al. 2015 [14] determined the optimum compaction conditions using a specific Proctor method. Dynamical compaction of soil in layers imparting greater compaction energy than standard Proctor was done at different moisture contents. The compaction of each layer was achieved when the handle of the hammer (2.5 kg) “rings” when dropped over the compacted soil. These samples were further tested in uniaxial loading condition to obtain the uniaxial compressive strength and dry density in function of compaction water content. Based on the compressive strength value, the optimum conditions of compaction ($OMC = 8\%$ and $\rho_d = 2000 \text{ kg/m}^3$) were chosen (figure 2.17b).

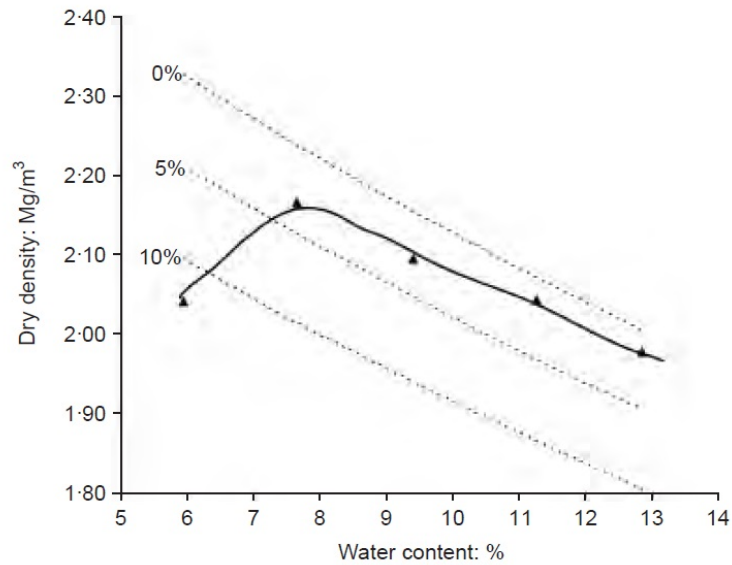
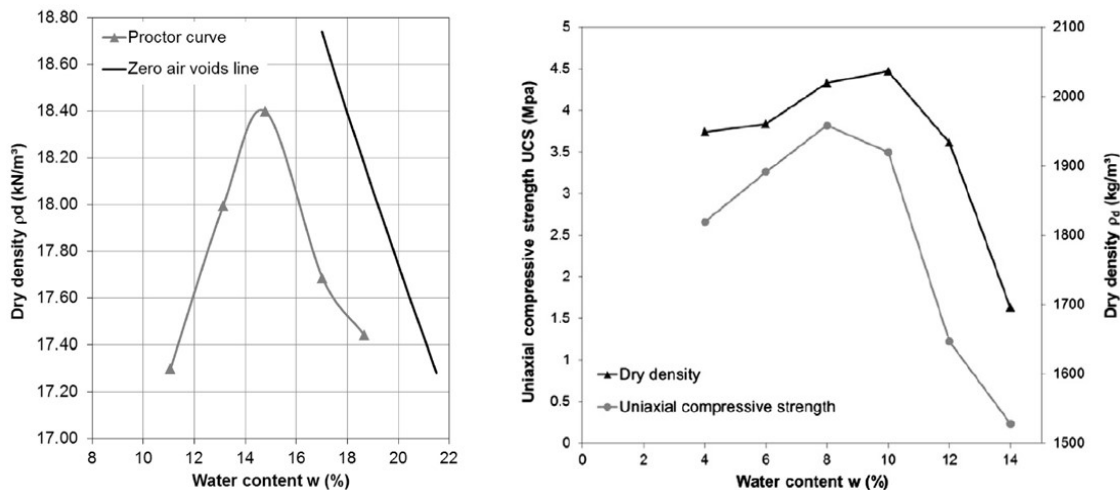


Figure 2.16: Determination of OMC using vibrating hammer test by Jaquin et al. 2009 [13]

This kind of specific Proctor provides a much denser sample as compared to standard Proctor where the maximum dry density reached was 1840 kg/m^3 (figure 2.17a). The comparison of dry density between these two methods has been shown in figure 2.17b.



(a) Standard Proctor curve of the soil (b) Uniaxial compressive strength and dry density as studied as a function of compaction water content

Figure 2.17: Comparison of dry density between the standard Proctor test (a) and specific Proctor method (b) [14].

The different methods of compaction used in the literature to determine the optimum moisture content for maximum dry density have been summarized in Table 2.2. Thus different methods have been used in the literature to determine the optimum conditions with the objective is to reach the dry density of rammed earth walls.

Table 2.2: Dry density and OMC from different experimental campaigns on rammed earth

Reference	Dry density (kg/m^3)	OMC (%)	Method of compaction
Hall et al. 2004 [3]	2020-2160	8	Light Proctor
Maniatidis et al. 2008 [42]	1850	12.5	Modified Proctor
Bui et al. 2008 [7]	1900	10	Pneumatic Rammer
Jaquin et al. 2009 [13]	2017-2061	12	Vibrating hammer
Beckett et al. 2012 [16]	1918.1-1947.5	12	Light Proctor
Gerard et al. 2015 [14]	2000	8	Specific Proctor
Martinez, 2015 [52]	2100	10.1	Standard Proctor
Champiré et al. 2016 [9]	1950-1980	9-11	Double Compaction

When rammed earth wall is prepared at the optimum compaction conditions, it undergoes drying, which leads to an increase in the strength of the wall. Conversely, when it is subjected to wetting (e.g. rainfall or inundation), a reduction in strength is observed. A rammed earth wall is subjected to changing humidity conditions during its lifetime, which leads to change in the hydric state of the wall. As the hydric state of the wall is evolving continuously, the mechanical behavior and other properties are affected. This hydric influence on mechanical characteristics is the main topic of study for the current research. The literature on the hydric influence is discussed in detail in the next section.

2.3 Suction as a variable for describing water state

For conventional construction material such as concrete, the study of strength parameters is acceptable without the regulation of relative humidity. However, for earthen materials such as rammed earth, mechanical behavior is strongly affected because of the interaction of soil particles (mainly clay) with the water molecules. The moisture plays a role in the cohesion of earthen materials, and thus it is necessary to study this water influence on the mechanical behavior [53]. Different authors have studied the influence of moisture on the strength and stiffness characteristics of rammed earth.

Compressive strength and Stiffness

Bui et al. 2014 [15] conducted unconfined compressive strength (UCS) test at a wide range of moisture contents which varied from wet state (11%) after compaction to dry state in normal atmospheric conditions (1-2%). The influence of moisture on the mechanical characteristics of rammed earth considering 5 different soils (with lime stabilization, i.e. soil B and E, and without lime stabilization, i.e. soil A, C, and D) was done. Compressive strength tests were conducted with unload-reload cycles, and secant modulus was determined for stress levels between 0 and 20% of maximum stress. The compressive strength decreased (from 2 MPa to 0.1 MPa) with increasing moisture content. However, when the moisture content was below 4%, it was found that the compressive strength did not change much with the decrease in the water content for sandy soil A, and stabilized soil B and E. In contrast, a decrease of 10 % in strength

was observed for clayey soils C and D (according to French Standard NF P 11-300)(figure 2.18). Secant modulus varied in a similar manner with water content (figure 2.18).

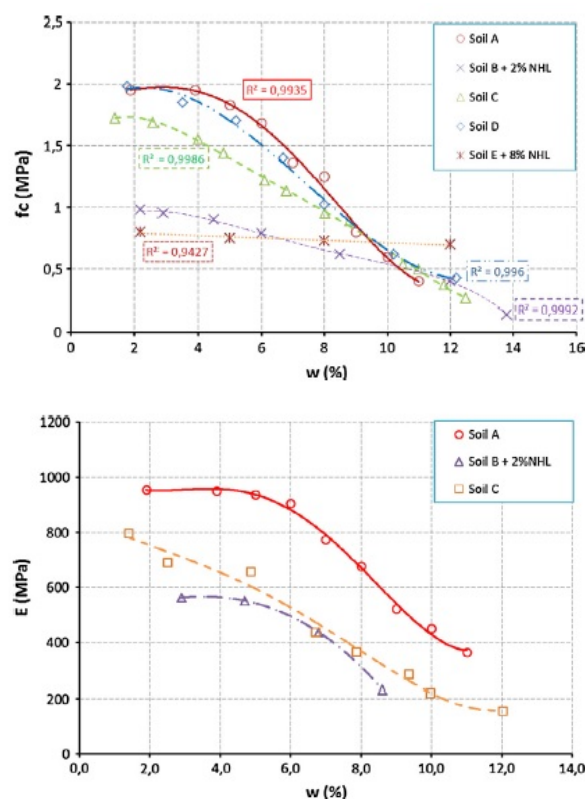


Figure 2.18: Variation of compressive strength (f_c) and secant modulus (E) with moisture content for different soils studied from Bui et al. 2014 [15]

Beckett et al. 2012 [16] studied the effect of humidity and temperature conditions on the unconfined compressive strength of rammed earth using two soil mixes. They were represented as 5-1-4 containing 50% sand, 10% gravels and 40% silty clay and 7-1-2 containing 70% sand, 10% gravels and 20% silty clay. Soil mixes have maximum and minimum clay content, respectively, necessary for rammed earth (as suggested by Houben and Guillaud 1996 [8]) to determine the role of clay in strength determination. Both soil mixes contain minimum gravel content to reduce the risk of over-sized particle affecting the results. Cubic samples of 100 mm were prepared by compaction in layers at optimum water content determined by light proctor test. Unconfined compression test was conducted on both mixes conditioned at different temperature and humidity values (15, 20, 30, 40 °C and 30, 50, 70 and 90%). It was found that for two different types of soil studied; the compressive strength is predominantly dependent on relative humidity than temperature(Figure 2.19).

Champire et al. [9] performed unconfined compressive strength test with and without unload-reload cycles on 3 different types of earth, conditioned at 3 different relative humidities. The samples were cored from compressed earth blocs extracted from existing rammed earth buildings. The three soil mixes contain 15%, 16% and 8% clay respectively and having a different level of activity. It was observed that both compressive

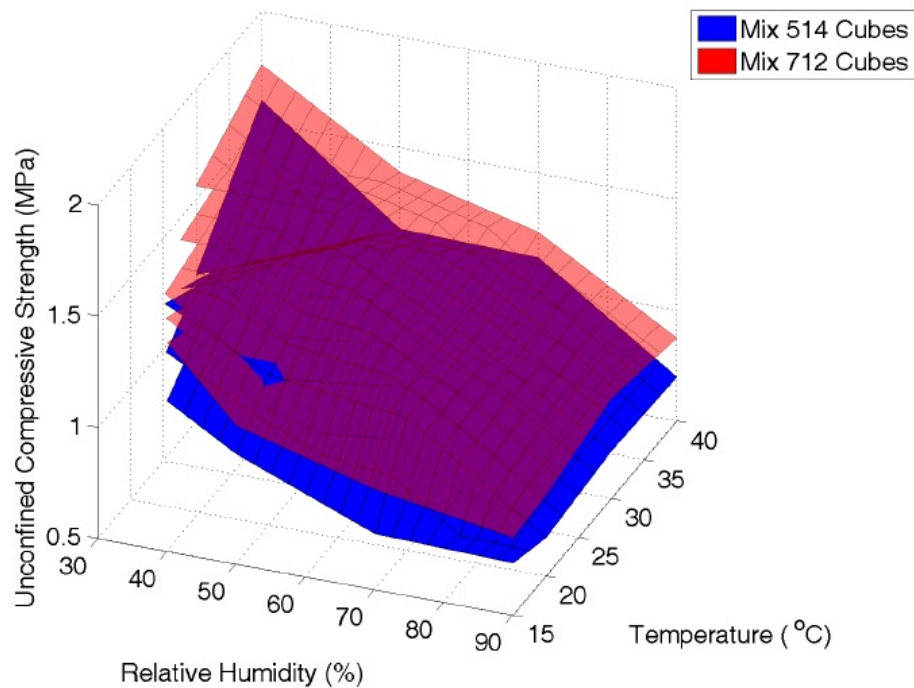


Figure 2.19: Comparison of the unconfined compressive strengths of mixes 5-1-4 and 7-1-2 against humidity and temperature [16].

strength and initial Young's modulus decreased with increasing water content (Figure 2.20). This behavior has also been observed in various studies [13][15][54][55][56]. The reduction of compressive strength and Young's modulus ranges from 25% to 50% with the change in relative humidity from 25% to 75%. Whereas, the change in absolute moisture content is less than 0.5%. This is due to the retention behavior of the soil.

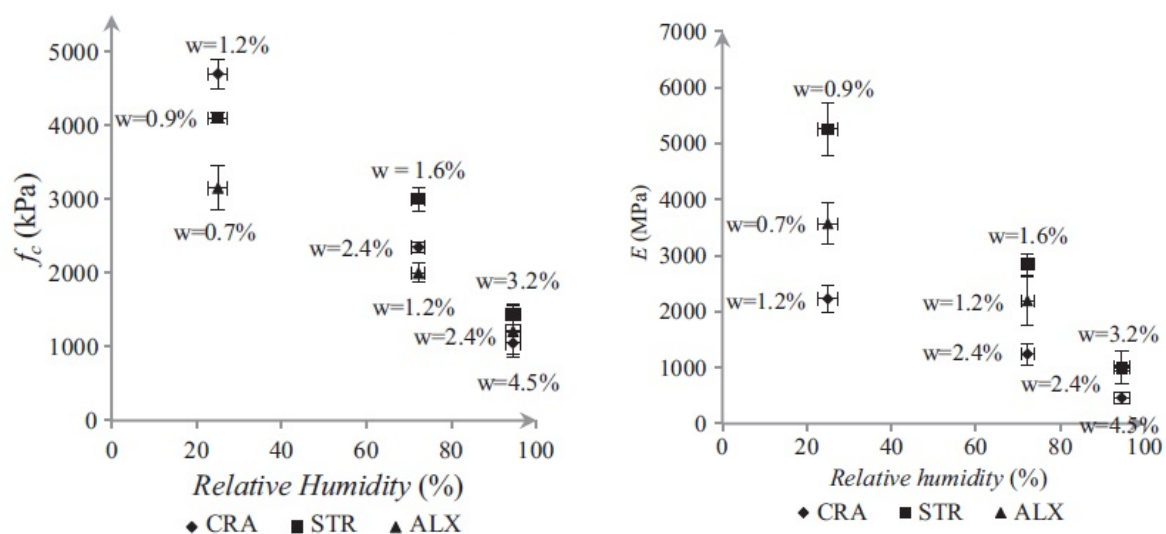


Figure 2.20: Variation of compressive strength and Young's modulus with relative humidity from Champire et al. 2016 [9]

Various authors studied the hydric influence on the mechanical parameters in terms of water content or relative humidity. Unfortunately, water content and relative humidity are not state variables and consequently, cannot account for objective behavior. Olivier et al. 1995 [57] first initiated the use of suction as a parameter to study the hydric influence on compacted earth material. In unsaturated soil mechanics, suction is one of the most important state variables to represent the hydric state. Suction (s) is defined as the difference of air pressure (u_a) and water pressure (u_w) i.e. $s = u_a - u_w$. It can be linked with the relative humidity of the pore air through Kelvin's equation which is defined as:

$$s = -\frac{\rho_w \cdot R \cdot T}{M_w} \ln(RH) \quad (2.1)$$

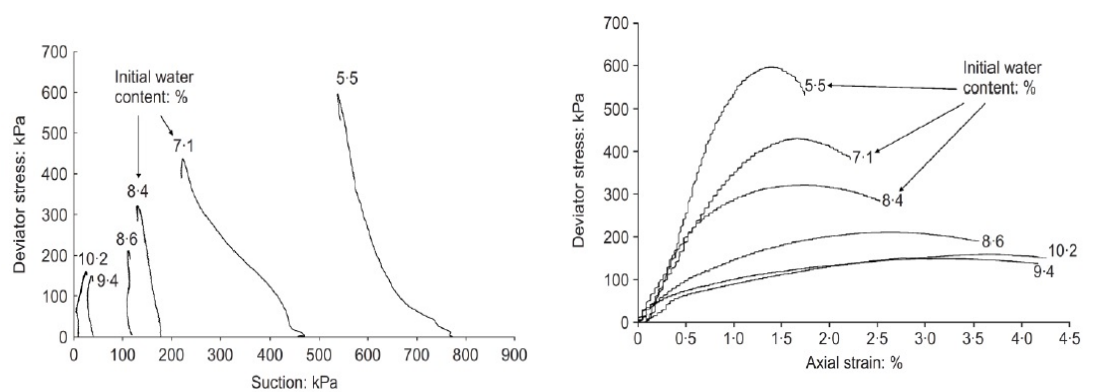
where, s is the suction defined as difference of pore air pressure (u_a) and pore water pressure (u_w) at a given temperature T (in Kelvin, K), R is universal gas constant ($R = 8.3143 \text{ J/mol/K}$), M_w is the molar mass of water ($M_w = 0.018 \text{ Kg/mol}$), ρ_w is the bulk density of water ($\rho_w = 1000 \text{ Kg/m}^3$) and RH is the relative humidity, which is defined as the ratio of partial vapor pressure P in the considered atmosphere and the saturation vapor pressure P_o at a particular temperature ($T = 298 \text{ K}$).

The water content or degree of saturation can be related to suction using the soil water retention curve (SWRC). The SWRC represents a fundamental constitutive relationship in unsaturated soil mechanics to define the affinity of the porous medium with water. The water retention curve is thus essential to characterize since the retention and mechanical behavior are interconnected. Different techniques have been used for plotting the retention curve. Gerard et al. 2015 [14] used the saline solution method which imposes different suction to obtain the SWRC. Bui et al. 2014 [5] used filter paper method to obtain the relationship between water content and suction.

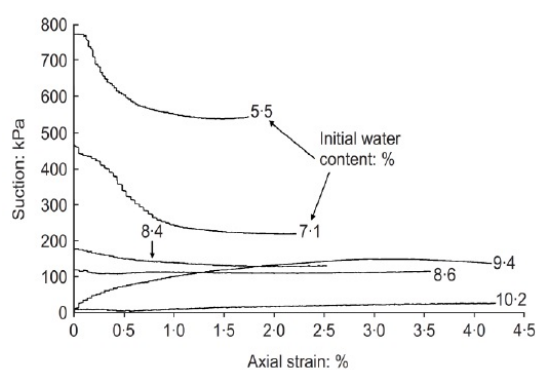
The change in the mechanical strength with the hydric state can be explained by the change of suction in the porous medium. Rammed earth derives its strength from two parts. A part of strength is due to the interlocking between the particles due to frictional resistance induced by the compaction process [58]. Also, in addition, there is a part of strength because of suction induced cohesion due to partial saturation of the earth which contributes a major part of the resistance [13][59][60][61][62][63][64][65][66][67][68][26].

Thus, the mechanical behaviour of rammed earth is strongly affected by the suction state of the wall. The increase of apparent cohesion with suction is not unlimited. When the soil completely dries out has no apparent cohesion due to suction as no water is present [13]. However, this situation is unrealistic since a real rammed earth wall is never completely dry, and even in an oven-dry state in the laboratory, there is still presence of adsorbed water. Toll et al. 1990 [69] has shown that for unsaturated soils, strength increases with suction but as soil completely dries out, the additional strength peaks and then vanishes.

Jaquin et al. 2009 [13] studied the influence of variation of suction on the compressive strength and stiffness of rammed earth. They performed a series of triaxial compressive strength test on samples prepared in Proctor split compaction mould and air-dried to different suction values. The samples were axially compressed at constant water content conditions. The suction was measured at the top of the sample continuously during the test using a high-capacity tensiometer. A link between suction and both strength and stiffness was observed. Increase in strength with suction state was observed (Figure 2.21a). Suction seems to decrease for tests in the lower water content range (5.5-8.4 %), whereas suction increases for tests at higher water content (9.4-10.2 %). Stiffness studies indicated that wetter samples have greater ductility, whereas the behavior of drier samples is more brittle in nature (Figure 2.21b). Figure 2.21c shows that the rate of suction change decreases with axial strain. During the shearing of samples at constant water content conditions, samples with initially low suction showed an increase in suction, whereas samples having higher initial suction showed a decrease in suction. This suggests that there exists a unique water content-suction relationship at critical state.



(a) Plots of suction against deviator stress (b) Plots of axial strain against deviator stress



(c) Plots of axial strain against suction

Figure 2.21: Results of the triaxial tests on rammed earth samples carried under constant water content conditions from Jaquin et al. 2009 [13].

The results from Bui et al. 2014 [15] and Jaquin et al. 2009 [13] were correlated and represented as the variation of compressive strength and suction (figure 2.22). It was found that the compressive strength is linearly correlated to suction in logarithmic

scale even though the material composition is different from each other for the four soils studied. However, it was pointed out that, in order to validate this result, analysis should be carried out on a large number of soils of different types.

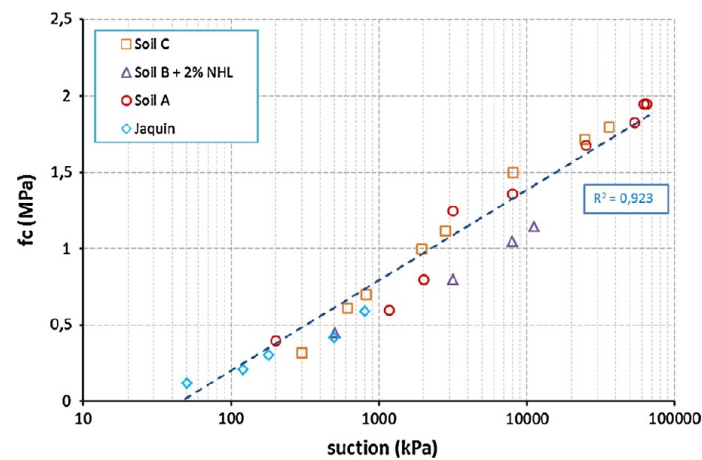


Figure 2.22: Variation of compressive strength with suction for the unstabilised soil from Bui et al. 2014 [15] and Jaquin et al. 2009 [13]

Gerard 2015 [14], studied the ability of Belgian clayey silt to develop sufficient mechanical strength under variable relative humidity conditions to be used as an unstabilized rammed earth construction material. The evolution of the strength as a function of atmospheric relative humidity was characterized through Uniaxial compression test. Suction was imposed using saturated saline solutions of different salts. Following conclusions were drawn: Unconfined compressive strength increased with suction. In addition, with increase in suction, brittleness also increases, i.e. dryer is the material, more brittle it is. Upon saturation, the compressive strength is almost zero, and the behavior is very ductile, highlighting the contribution of suction-induced cohesion on strength. The Unconfined compression strength was correlated linearly to logarithm of suction (Figure 2.23) similar to the results obtained by Bui et al. 2014 [15].

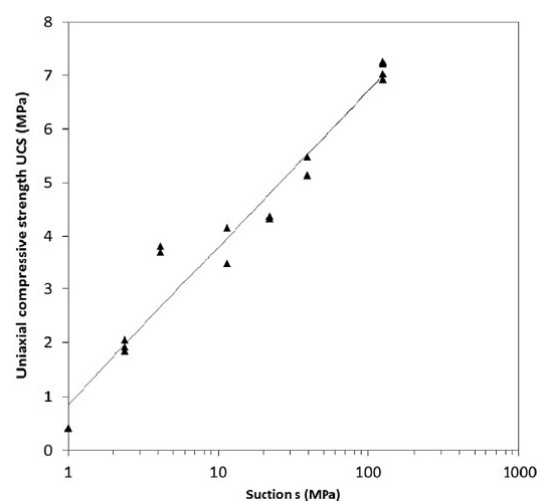


Figure 2.23: Variation of compressive strength with suction from Gerard et al. 2015 [14]

Bruno et al. 2017 [17] performed a study in context to hypercompacted raw earth, which was compacted to three compaction pressures of 25, 50, and 100 MPa. These samples after compaction at optimum moisture content were subjected to different relative humidity conditions to impose suction values of 7, 36, 66, 112, and 190 MPa. In addition, to determine Young's modulus, the samples were subjected to 5 unload-reload cycles. Figure 2.24 shows that, in general, Young's modulus and compressive strength increases as total suction increases from 7 MPa to 112 MPa tending towards a constant value with further increase in total suction. This behavior of tending towards a constant value of the mechanical parameters with increasing suction is justified according to the meniscus model of Fisher et al. 1926 [59] which shows that the additional cohesion due to capillary effects increase with suction asymptotically towards a constant value.

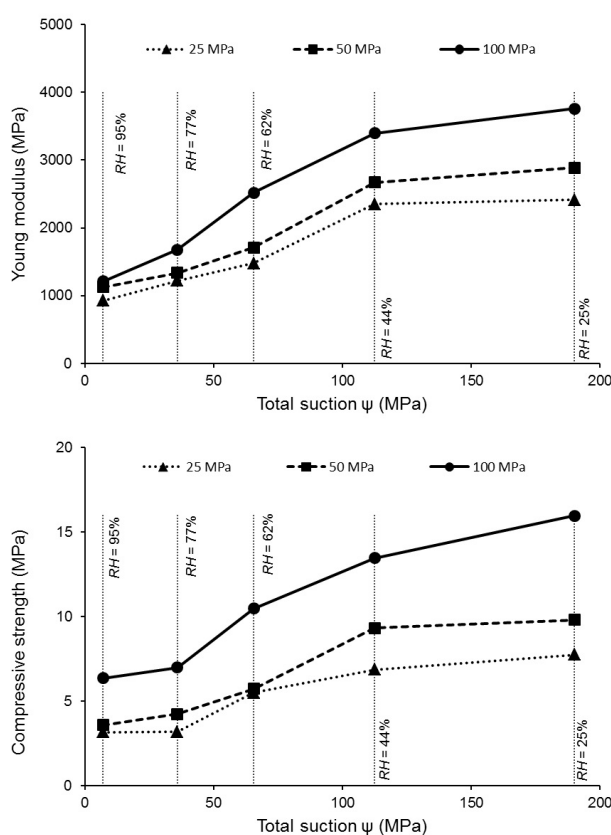


Figure 2.24: Variation of peak compressive strength and Young's modulus with total suction from Bruno et al. 2017 [17]

Tensile strength

Various studies have been done on the compressive behavior of rammed earth but only a few focus on the influence of suction on tensile strength. Jaquin et al. 2008 [18], determined the tensile strength using the modified Brazilian test on two soil mixes A (more coarse particle) and B (more fine particles). This test is generally used for tensile strength testing in rock and involves compressive loading on cylindrical specimen across the diameter. As the suction increases, the tensile strength increases, indicating suction as a source of tensile strength. Comparison on the basis of particle size distribution for

the tensile strength shows that at same tensile strength, more water content was retained in mix B which contains more finer particles than mix A (Figure 2.25).

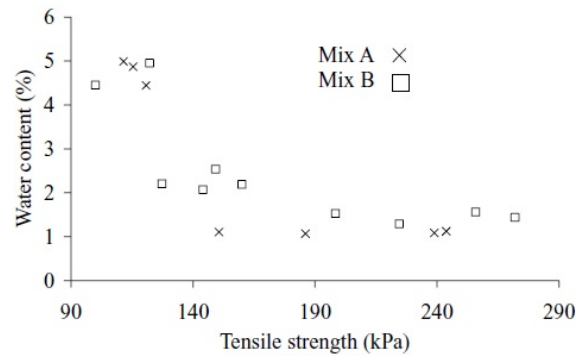


Figure 2.25: Variation of tensile strength from Brazilian test (from Jaquin et al. 2008 [18]).

The indirect tensile strength was also studied by Gerard et al. 2015 [14] using the Brazilian test. In the saturated conditions, the indirect tensile strength was almost zero, and it increases with suction. The indirect tensile strength was correlated linearly to the logarithm of suction, as shown in figure 2.26. Thus it follows the same trend of variation with suction as the compressive strength (figure 2.23).

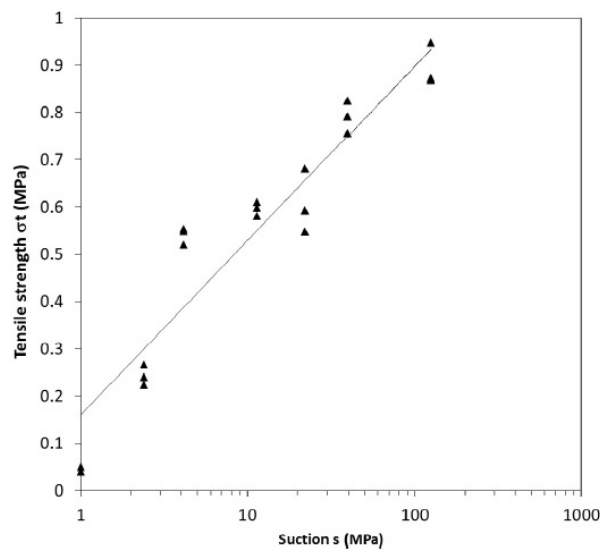


Figure 2.26: Variation of tensile strength with suction from Gerard et al. 2015 [14]

Damage and plasticity

In the previous discussion we have seen that suction affects the strength and stiffness of rammed earth. In addition to that, suction has a significant influence on the plastic strain- ing and mechanical damage. Champiré et al. 2016 [9] observed that relative humidity (or suction) appears to affect plasticity which was characterized by residual deformation and damage which was characterized by a drop in Young's Modulus (figure 2.27). The damage was significantly greater for samples conditioned at higher suction states, whereas plastic

behavior was more prominent at lower suction states. It was concluded that the earth exhibits a complex mechanical behavior which combines elasto-plasticity and damage, each one evolving with the ambient climatic conditions.

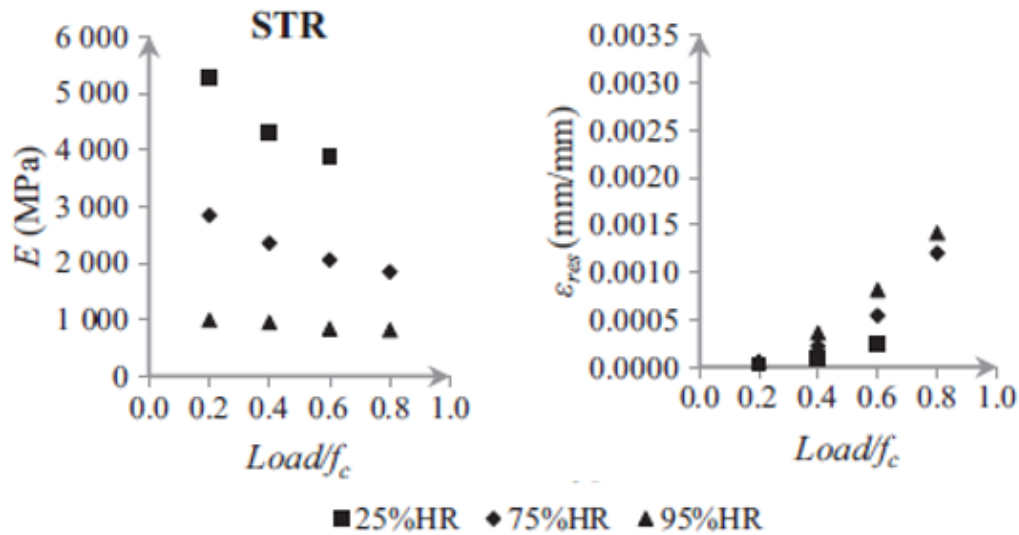


Figure 2.27: Young's modulus and residual strain shown as function of stress level at different humidity conditions from Champiré et al. 2016[9]

Similar results were observed by Xu et al. 2017 [19]. Triaxial tests were performed on compacted on rammed earth (labelled as CRA) at 2 different confining pressures of 100 kPa and 600 kPa conditioned at different humidity conditions. The degradation of Young's modulus with the increase in applied stress, i.e. damage (figure 2.28) was observed. Damage was higher for samples conditioned at higher suction states. Similarly, strong irreversible strains were observed at lower suction state.

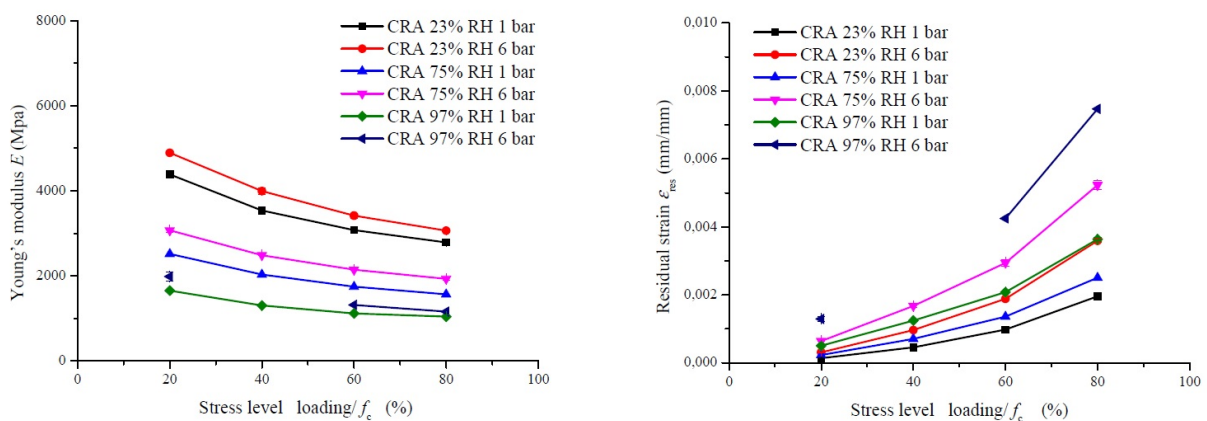


Figure 2.28: Evolution of Young's modulus and residual strain with increasing stress state for samples conditioned at different relative humidities and tested at different confining pressures from Xu et al. 2017 [19].

Poisson's ratio

The variation of Poisson's ratio with moisture content was studied Bui et al. 2014 [15]. In dry state i.e. less than 4% water content, the value of Poisson's ratio was 0.2 ± 0.02 . This value increased to 0.37 ± 0.01 for wet samples at higher water content (figure 2.29). The increase in the value is justified as for saturated samples, the Poisson's ratio approaches to 0.5.

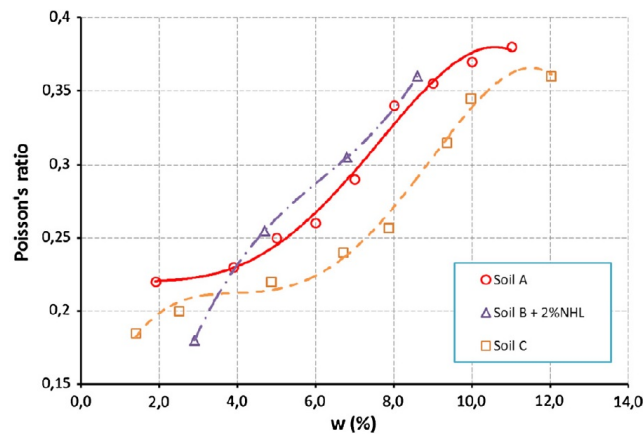


Figure 2.29: Variation of Poisson's ratio with moisture content for different soils studied from Bui et al. 2014 [15]

Champiré et al. 2016 [9] also studied the volumetric behavior during the unload-reload cycles to determine the Poisson's ratio at different humidity conditions. This study was done for relative humidity ranging from 25% to 95% and corresponding water content varying from 1% to 4.5%. It was observed that the value of Poisson's ratio varied between 0.15 and 0.2. It was concluded that the hypothesis of constant Poisson's ratio was valid for the humidity range studied. Thus a constant value of Poisson's ratio can be taken unless the relative humidity is closer to 100%.

2.4 Modelling of Rammed earth

Numerous studies have been carried out related to the experimental characterization of rammed earth at different scales, including the material scale and wall scale. On the other hand, there are few studies carried out on the coupled hydro-mechanical modelling of rammed earth. These studies have used elasto-plastic constitutive models and damage models for prediction of the mechanical behavior of rammed earth.

2.4.1 Damage models

Rammed earth in dry state behaves as a quasi-brittle material. Damage models are more suitable for the constitutive modeling of quasi-brittle materials such as concrete. When earthen material is subjected to mechanical loading or environmental conditions, microscopic defects and cracks can develop. The distributed defects in the material are responsible not only for crack initiation and final fracture but also induced deterioration or damage such as a reduction of strength and stiffness (Zhang et al. 2010 [70]). This behavior can be studied by the use of a damage model which can represent the change in material properties and its failure due to initiation of damage, its growth and propagation. The damage models require the definition of an appropriate damage variable to represent the macroscopic effects of microscopic cracks. If the damage is assumed isotropic, a scalar damage variable can be used, and for anisotropic damage, a tensor damage variable is required. Also, a constitutive equation, including damage variable to describe the mechanical behavior is required. The different damage models can be isotropic elastic damage model, elastoplastic damage model, and elasto-viscoplastic damage model.

The most commonly used isotropic damage model is Mazars model [71], generally used for concrete. The constitutive relationship between stress and strain in Mazars model is given by the following relationship, which is based on generalized Hooke's law:

$$\boldsymbol{\sigma} = (1 - D)\mathbf{E}\boldsymbol{\epsilon}^e \quad (2.2)$$

where, \mathbf{E} is Hooke matrix, $\boldsymbol{\epsilon}^e$ is the elastic strain, and D is the scalar damage variable which varies between 0 and 1. D is defined as a combination of two damaging modes defined by D_c and D_t which also varies between 0 and 1 depending on the state of damage in compression and tension respectively.

$$D = \alpha_c D_c + \alpha_t D_t \quad (2.3)$$

where, α_c and α_t are weight coefficients depending on the principal strains.

Bui et al. 2014 [5] used damage model to simulated the mechanical behavior of rammed earth wallettes under compression loading by taking into account the complex behavior of rammed earth, i.e. non-linearity, cracking and damage. This study used

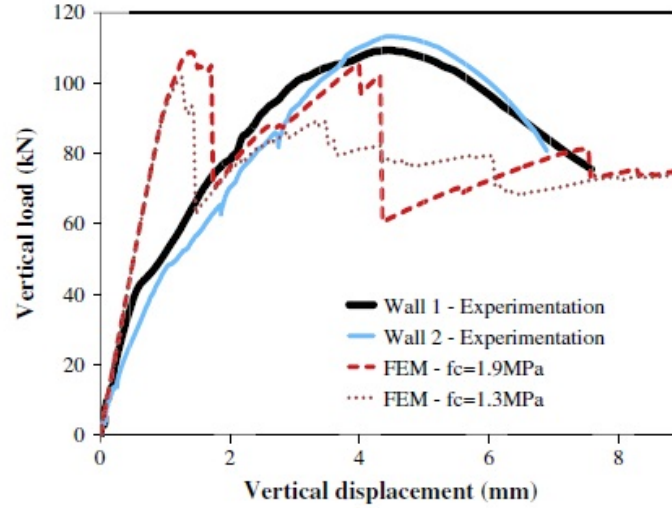


Figure 2.30: Comparison of the experimental and the numerical results for wallettes under axial compression (from Bui et al. 2014 [5]).

Mazar's model which is an isotropic nonlinear damage model. It can identify the gradual degradation in stiffness caused by micro-cracks. The wallettes analyzed were considered homogeneous and isotropic. The numerical model could reproduce the initial stiffness in compression and the strength, but could not predict the behavior once the cracking begins, and stiffness decreased (figure 2.30). It is a common limitation of Mazar's model as it can reproduce the maximal load but not the behavior curve. On the other hand, the Mazar's model cannot reproduce the behavior cycles, which is not suitable in the case of drying/humidification cycles as in the case of earthquakes.

2.4.2 Elasto-plasticity models

Another approach for constitutive modeling of rammed earth is the elastoplasticity framework. This approach is more adapted to represent the behavior of the post-peak phase as rammed earth is not perfectly brittle. Rammed earth can show significant ductility, especially at higher moisture conditions. The assumption of elasto-plasticity is that for small strain conditions, the total strain can be decomposed into elastic ($d\epsilon^e$) and plastic ($d\epsilon^p$) strain (equation 2.4).

$$d\epsilon = d\epsilon^e + d\epsilon^p \quad (2.4)$$

The elastic deformations in the soil are generally computed using the linear Hooke's law:

$$d\epsilon^e = \left(\frac{1+\nu}{E}\right)\boldsymbol{\sigma} - \left(\frac{\nu}{E}\right)tr(\boldsymbol{\sigma})\mathbf{I}_d \quad (2.5)$$

where, E is the Young's modulus, ν is the Poisson's ratio, and \mathbf{I}_d is the identity tensor.

E and ν are the parameters of this elastic model.

Apart from the linear elastic Hooke's law, other models have been used to model elasticity in rammed earth. Francois et al. 2017 [20] used a non-linear hypoelastic law to determine the elastic component of strain. Hypoelasticity is generally used to model materials that exhibit non-linear, but reversible stress-strain behavior even at small strains. The strain in the material depends only on the stress applied and not on the rate or history of loading. The stress is a non-linear function of strain even when the strains are small. The Young's modulus (E) was taken as a function of mean effective stress through a hyperbolic function:

$$E = E_{ref} \left(\frac{p'}{p'_{ref}} \right)^{n_e} \quad (2.6)$$

where, p' is the mean effective stress, E_{ref} is the reference Young's modulus at the reference mean effective stress p'_{ref} , and n_e is a material parameter. By using mean effective stress in the expression of elastic modulus, the effect of suction on the stiffness was taken into account.

Concerning plasticity, there are numerous models used for geomaterials such as Mohr-Coulomb, Drucker-Prager, and Cam-Clay model. Mohr-Coulomb model is an elastic-perfectly plastic model used to model soil behavior. It uses two parameters which define the failure criterion, i.e. cohesion (c) and friction angle (ϕ). In addition, it uses a parameter to describe the flow rule, i.e. dilatancy angle (ψ) coming from the non-associative flow rule to model the irreversible change in volume due to shearing. Since it is a perfectly plastic model, it does not include strain hardening or softening effects. The Mohr-Coulomb yield surface in the principal stress space is shown in figure 2.31. The simplification of Mohr-Coulomb model where the hexagonal shape of the failure surface is changed with a circle is the Drucker-Prager model (figure 2.31). In simple 3D space, the hexagonal failure cone is replaced by a simple cone in Drucker-Prager failure model. It uses the same parameters to define the failure criterion.

Drucker-Prager model was used by Francois et al. 2017 [20] to model the plasticity. The Drucker-Prager failure surface can be expressed as:

$$f = q - M \left(p' + \frac{c'}{\tan\phi'} \right) \quad (2.7)$$

where, $M = 6\sin\phi' / (3 - \sin\phi')$, p' and q are the mean effective stress and deviatoric stress, c' and ϕ' are the cohesion and friction angle respectively.

The plastic strains are determined using the plastic multiplier $d\lambda$ and plastic potential g :

$$d\epsilon^p = d\lambda \frac{\partial g}{\partial \sigma} \quad (2.8)$$

The plastic potential g can be expressed as: $g = q - M'p' = 0$, with $M' = 6\sin\psi / (3 - \sin\psi)$ where ψ is the dilatancy angle.

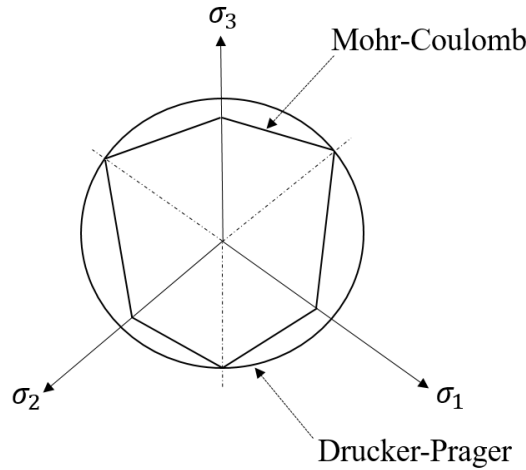


Figure 2.31: Mohr-Coulomb and Drucker-Prager yield surface in the isometric principal stress space

Figure 2.32 shows the results of the simulation for the unconfined compressive strength tests at different initial suction states. The non-linear elasto-perfectly plastic model used was able to predict the effect of suction on the strength and stiffness. However, the sudden transition from elastic to perfectly plastic is not consistent with the experimental observations. It is a known drawback of classic elasto-plastic models.

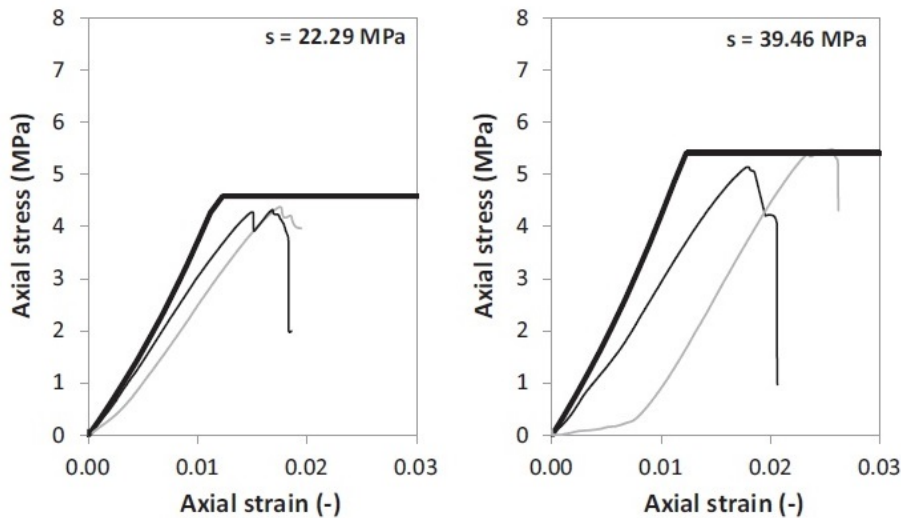


Figure 2.32: Experimental and modelling results of unconfined compressive strength at different suction states from Francois et al. 2017 [20].

In addition to these models, there is Cam-Clay model which uses the strain hardening theory of plasticity to formulate the stress-strain model. It is based on critical state and generally used for normally consolidated or lightly overconsolidated soils.

Finally, for the constitutive modelling of unsaturated soil, it is essential to incorporate the effect of suction on the failure criterion. Thus the approach which has been used in literature to do a coupled analysis is discussed in the next part.

2.4.3 Coupled analysis

The link between the mechanical behavior and the hydraulic conditions can be considered by an approach that takes into account the hydro-mechanical coupling. As rammed earth is present in an unsaturated state, soil suction has a significant effect on the stress state and thus the mechanical behavior. In unsaturated soil mechanics, the stress state of a porous medium can be represented by two independent stress variables such as net vertical stress ($\sigma - u_a$) and matric suction ($u_a - u_w$) which are measurable and have an experimental significance. On the other hand, an approach which uses single effective stress to define the stress state can also be used. Effective stress is the stress which is being transferred by grain to grain contact and responsible for the mobilization of shear strength in the soil. In order to represent the results of tests at different suction conditions in a single stress framework, Bishop's generalized effective stress can be used:

$$\sigma'_{ij} = \sigma_{ij} + \chi s \delta_{ij} \quad (2.9)$$

where, σ' is the effective stress tensor, σ is the net stress tensor, s is the suction, δ_{ij} is the Kronecker delta ($\delta_{ij}=0$ if $i \neq j$, else = 1) and χ is the effective stress parameter which is a function of degree of saturation.

It helped to obtain a unique failure criterion by including the effect of water retention on strength directly in the stress definition. To define the unified failure criterion, the intrinsic strength parameters: effective cohesion (c') and effective friction angle (ϕ') were determined by Gerard et al. 2015 [14]. Consolidated and undrained (CU) triaxial tests at different confining pressures were performed on saturated samples. The value of cohesion and friction angle obtained was 6.2 kPa and 36.5° respectively. Using these values, a Mohr-Coulomb failure criterion was drawn. This unified failure criterion and the various unconfined compressive strength and indirect tensile strength tests represented as their Mohr circle at failure state are shown in figure 2.33. The test which were carried out in saturated conditions did not fit well with the failure envelope. Otherwise, a decent fitting of the experimental data with the proposed unified failure criterion was observed.

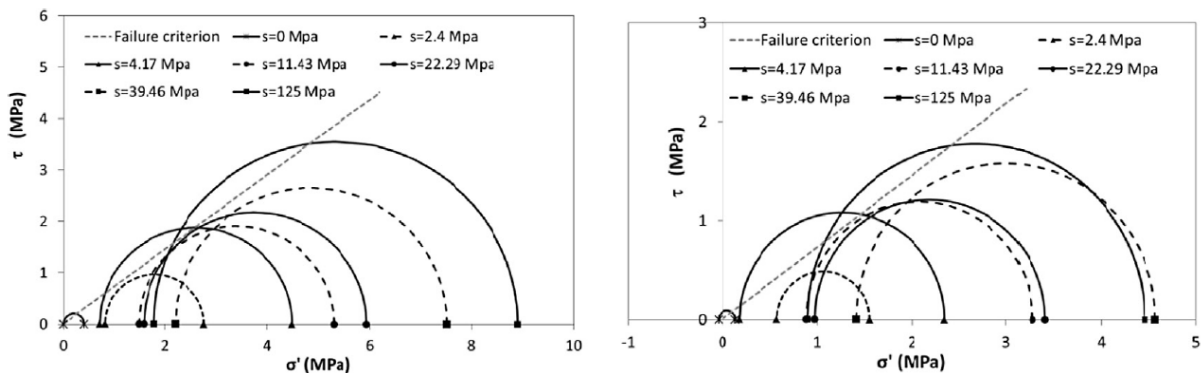


Figure 2.33: Mohr circles at failure in terms of effective stress for UCS (left) and indirect tensile strength test (right) at different initial suction conditions [14]

2.5 Conclusion

In this chapter, the bibliographic review of the various experimental and numerical studies carried out on rammed earth was presented. Firstly various key mechanical parameters from an engineering point of view were discussed. Compressive strength was the most widely used indicator of strength for the construction of rammed earth structure. The different standards and guidelines indicated that the minimum compressive strength should be in the range of 1-2 MPa.

Various studies on the compressive strength and stiffness behavior indicated that there were discrepancies in the values of compressive strength and Young's modulus. These dispersions in the results was attributed to various influencing factors such as granulometry, nature of clay, method of compaction, scale and geometry of samples. It was concluded that a cylindrical sample with a slenderness of 2 was preferable to determine the mechanical characteristics of rammed earth. In addition to the sample's geometry, the scale at which study is carried out influenced the results. The different methods of compaction for the determination of optimum conditions were discussed. It was decided that the material scale experimental campaign in this study will be carried out on cylindrical samples with a slenderness ratio of around 2. The optimum compaction condition will be determined from the standard Proctor test. In addition, the samples will be compacted by a double compaction process to produce samples with more homogeneity of density to achieve a dry density representative of an in-situ wall. For the structural scale, compression testing will be performed on columns representative of rammed earth wall. These columns will be compacted in layers by dynamic compaction as in a real wall.

One of the most important factors influencing the mechanical behavior is the hydric state of the rammed earth. When a rammed earth wall undergoes drying, there is increase in strength, and conversely when it is subjected to wetting, there is reduction in strength. Different authors studied this influence on the mechanical characteristics in terms of water content and relative humidity of the samples. Since rammed earth is an unsaturated compacted soil, suction can be used as a parameter to study the hydric influence. Suction is an important state variable in unsaturated soil mechanics. Suction was related to water content in terms of soil water retention curve. The soil water retention curve was obtained using different methods such as filter paper technique and saline solution method but for higher values of suction. Thus it was decided that in this study, the retention curve will be plotted using the saline solutions method for higher suction values and pressure plate method for lower suction values. Various studies were carried out on the variation of compressive strength, Young's modulus, tensile strength with suction. Only a few studies focused on the determination of shear strength and shear parameters such as cohesion and friction angle and none on its variation with suction. Thus in the present study, an extensive experimental program will be carried out to understand the variation of mechanical parameters with suction. Unconfined compressive strength test, direct shear test, unsaturated triaxial test will be performed to study the variation of

compressive strength, Young's modulus, shear strength, apparent cohesion and friction angle with suction. In addition, saturated triaxial test will be done to determine the intrinsic values of cohesion and friction angle.

Numerous studies were carried out on the experimental characterization but a few on the coupled hydro-mechanical modelling of rammed earth. To take into account the unsaturated nature of rammed earth, the stress state can be represented using an effective stress approach. The most commonly used stress framework is Bishop's generalized effective stress which takes into account the effect of water retention directly in the stress definition. For the constitutive modelling, damage and elasto-plastic models were used. It was highlighted that rammed earth has a fragile behavior which is more prominent in dry state for which damage models are more suitable. On the other hand, rammed earth has a ductile behavior which is more relevant in wet state for which elasto-plastic models are preferred. Finally, in this study, the coupled hydro-mechanical modelling will be done by using a linear elastic-perfectly plastic model with Drucker-Prager failure criterion.

Chapter 3

Hydro-mechanical behavior at material scale

3.1 Introduction

The objective of this chapter is to investigate the effect of suction on different mechanical parameters which will help to define a constitutive hydro-mechanical model able to quantify the main features of the rammed earth material. For this purpose, we chose to adopt the concepts of unsaturated soil mechanics, in which many constitutive developments already exist and could be applied to our material. The work presented in this chapter gathers, in one hand, the presentation of subsequent hydro-mechanical tests led at the material scale and on the other hand analysis of the results of the experimental campaign which can be a step forward towards coupled modeling.

Firstly, the geotechnical description of the rammed earth used in this work is presented including the basic characterization tests, the manufacture of the specimens, which are representative of the compacted structure element, and the different hydric conditions applied.

In the next section, the extensive experimental campaign aiming to highlight the suction influence on mechanical characteristics is presented. Unconfined compressive strength, Young's modulus, and shear parameters (cohesion and friction angle) are analyzed through unconfined compression tests, direct shear tests and triaxial tests as underlined in the literature review. The shear parameters are studied since they are essential parameters in soil mechanics, although very few studies about rammed earth focus on it. Intrinsic shear parameters which are independent of suction state are evaluated by performing saturated triaxial tests.

Based on this experimental analysis, the final section proposes a synthesis of these hydro-mechanical tests, which can help to obtain a coupled constitutive model able to predict the coupled hydro-mechanical behavior.

3.2 Geotechnical characterization of the material

The material used in this study was procured from an existing construction site at La Roche Condrieu in Auvergne-Rhone Alpes region of France. Thus the soil is an appropriate material for the study as rammed earth.

3.2.1 Particle size distribution

Since the soil is to be used for small scale (material scale) testing, it was first sieved through 5 mm sieve, in order to have a representative size of grains considering the chosen size of samples. The percentage of different size of particles in a given dry sample of soil was determined using the particle size analysis, which is carried out in two stages:

- Sieve Analysis
- Sedimentation Analysis

Sieve analysis is completed by sedimentation analysis when 10% of the mass of soil is finer than 63 μm . Since rammed earth soil is well graded, it consists of mostly all sizes of particles, and thus both the stages of particle size analysis were performed. Wet sieving of the soil was done to dislodge the small particles stuck on the particles bigger than 5 mm size. The soil is further oven-dried which is used for the dry sieve analysis.

3.2.1.1 Sieve Analysis

Sieve analysis is carried out for soil fraction which is retained over 80 μm sieve, i.e. for soil particles having size greater than 80 μm . The sieves are designated by the size of the aperture of the square in mm. Different sieves were arranged one over each other in descending order of their size having a maximum size of aperture at the top and minimum size of aperture at the bottom. 1 kg of oven-dried sample of soil was placed over the topmost sieve, and sieving was done for at least 15 min. Dry weight of the particle retained over each sieve was noted and used to find the corresponding percentage (%) finer:

$$\% \text{ finer} = 100 - \text{cumulative } \% \text{ retained}$$

The different sieve sizes used were 80 μm , 100 μm , 200 μm , 400 μm , 630 μm , 1.25 mm. We recall that the greater size is 5 mm since all the material has been sieved at 5 mm in order to have Representative Elementary Volume while compacting decimetric samples. The result of this analysis is shown in figure 3.1 and labelled sieve analysis.

3.2.1.2 Sedimentation Analysis

Sedimentation analysis was carried out for soil fractions passing through 80 μm sieve. It is based on Stoke's law and assumes the particle to be spherical. Soil fractions which are smaller than 0.2 μm cannot be analyzed with sedimentation analysis since Brownian motion sets up due to which settlement does not take place, and Stoke's law is not valid. It is done by placing a hydrometer inside a soil suspension and noting density of the suspension at different time intervals to compute the percentage finer.

Using the results of both the analysis, the particle size distribution curve is shown in figure 3.1. It shows that it contains 11% gravel, 30% sand, 52% silt, and 7% clay. In addition to the particle size distribution curve of the soil studied, a range of maximum and minimum distribution curves proposed by Houben et al. 1994 [8] is also plotted. From figure 3.1, it can be seen that the distribution curve is not enclosed within this spindle. This spindle provides a criterion to identify suitable soils for rammed earth construction purposes based on the shape of the particle size distribution curve. As seen in the literature review, it is known that these specifications are often not followed by rammed earth and that, particle size distribution is not the only determining parameter for suitability of soil as rammed earth. This soil is well-graded and close from the range proposed by Houben et al. 1994 [8]. Notably, the percentage of clay of 7%, although in the low range of this recommendation, is consistent with those found in the literature [49][9].

3.2.2 Atterberg limits

Consistency of a soil is the ease with which it can be deformed and denotes the degree of firmness varying with the water content. Atterberg defined 4 stages of consistency:

- Solid stage of consistency
- Semi-solid stage of consistency
- Plastic stage of consistency
- Liquid stage of consistency

A Consistency limit or Atterberg limit is defined as the water content at which soil passes from one stage of consistency to another.

- Liquid limit (w_l) is defined as the minimum water content at which soil is in the liquid stage of consistency. At this water content, the soil passed from the liquid state of consistency to plastic state of consistency.

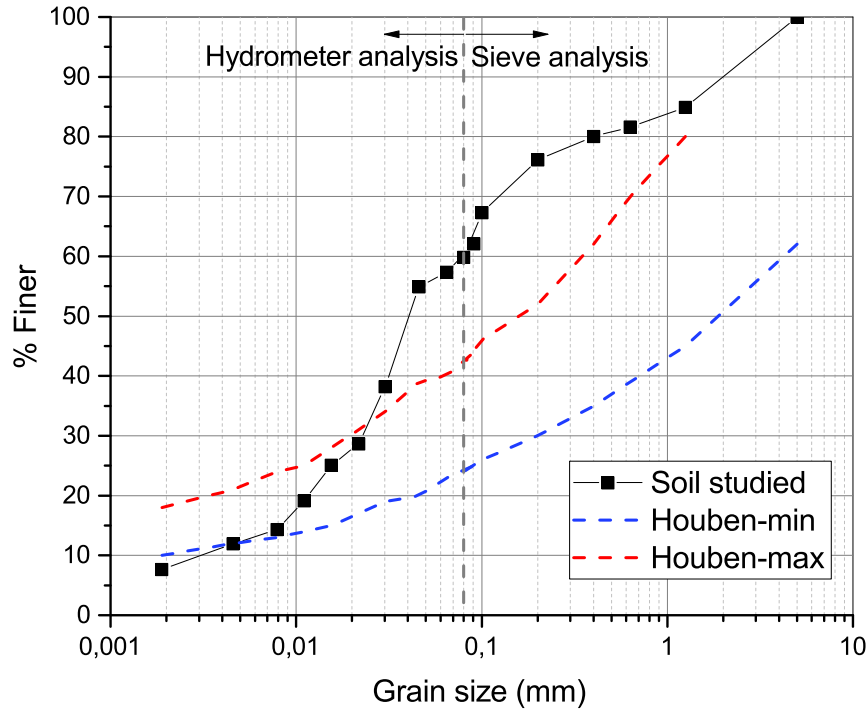


Figure 3.1: Particle size distribution and the guidelines by Houben et al. 1994[8]

- Plastic limit (w_p) is defined as the minimum water content at which soil is in plastic state of consistency. At this water content, the soil passes from plastic state of consistency to semi-solid state of consistency.

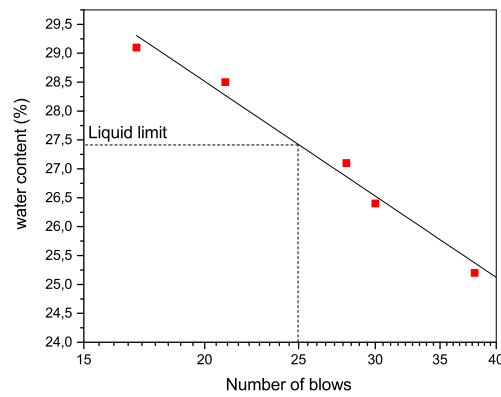
Liquid limit (w_l) was evaluated using Casagrande Tool (figure 3.2a) according to the French standard NF P 94-051, 1993 [72]. Soil was first sieved through 400 μm sieve and then mixed at a certain water content. The soil is placed in the soil cup and cut by a groove of 10 mm. Soil cup is allowed to fall freely over the rubber base from a height of 10 mm, and the number of blows required to flow the soil together is noted. The test was carried out for five different water content, and the result of the test is expressed in terms of Flow curve (figure 3.2b) which represents the water content and the corresponding number of blows on a logarithmic scale. At the liquid limit, the groove must be closed over a length of 10 mm after the application of 25 blows. The liquid limit was evaluated to be $w_l = 27.42\%$.

Plastic limit (w_p) was determined as the minimum water content at which soil begins to crumble or crack when rolled into a thread of 3 mm diameter. The plastic limit (w_p) was evaluated equal to 16.39%.

Plasticity index (I_p) gives the range of consistency in which the soil exhibits plastic properties and is the numerical difference between liquid limit and plastic limit: $I_p = w_l - w_p = 11.03\%$.



(a) Moist soil grooved in the Casagrande Tool



(b) Flow curve showing the water content and the corresponding number of blows in \log_{10} scale

Figure 3.2: Casagrande test for liquid limit determination

The soil is termed as fine-grained soil since it has more than 35% particles passing 80 μm sieve. Casagrande defined an A-line in order to separate inorganic clays from silt and organic soils. The A-line represents the relationship between the plasticity index and liquid limit of soil.

$$I_p = 0.73(w_l - 20) \quad (3.1)$$

According to Casagrande's Plasticity chart, the soil is classified as inorganic clay (lies above A-line) of low plasticity ($w_l < 30\%$) (figure 3.3). According to the triangular classification for fine-grained soils, it is classified as silty loam (figure 3.4).

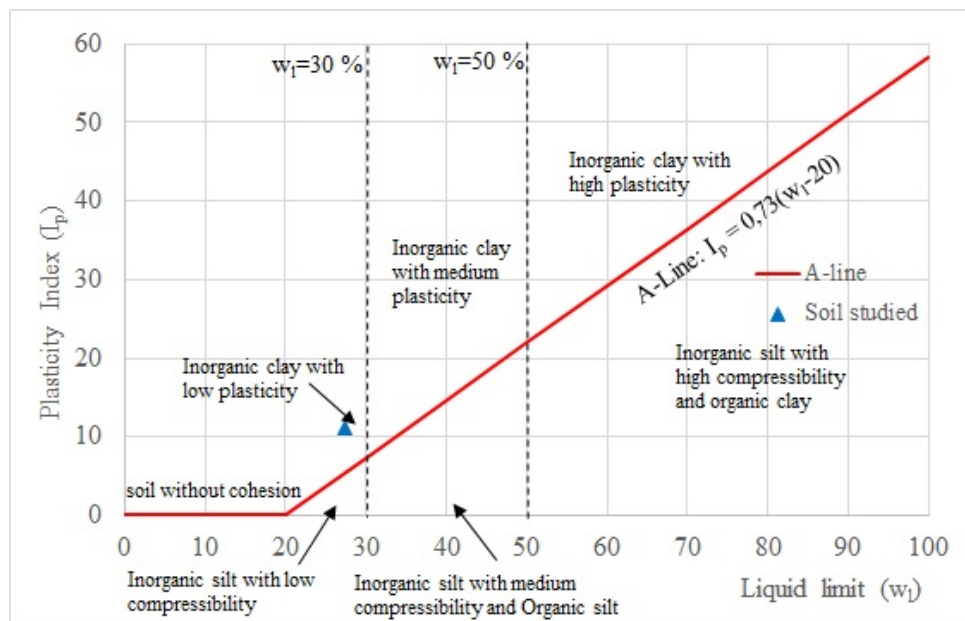


Figure 3.3: Casagrande's Plasticity chart for the classification of fine grained soils

According to the French Classification of soils GTR (Guide de Terrassements

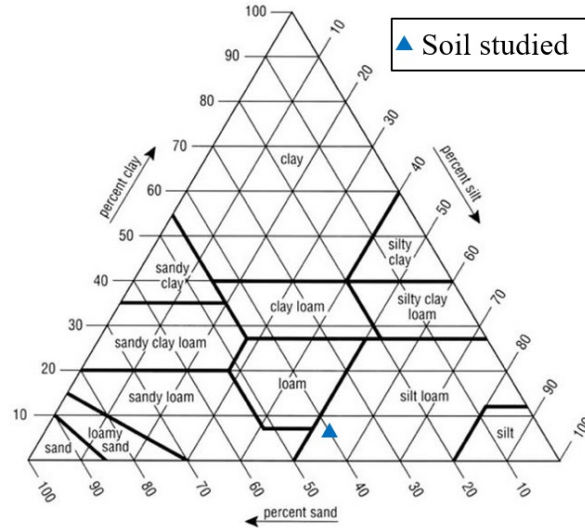


Figure 3.4: Triangular classification of fine grained soils

Routier) for fine-grained soils (i.e. more than 35% of grains passing $80 \mu\text{m}$ and no grain size over 50mm), it is classified as A1, i.e. low plastic silt ($I_p < 12\%$). It means that the soil has low plasticity.

3.2.3 Other characterization tests

In order to finely characterize the clay, the activity (A_c) of soil is determined which is a parameter used to indicate the compressibility of soil (swelling or shrinkage of soil with a change in water content). Activity is a characteristic of soil that depends principally on the mineralogical nature of clay as shown for example, in table 3.1 for various clay minerals. It is defined as the ratio of Plasticity index (I_p) of the soil to the percentage of the particles finer than $2 \mu\text{m}$ (f), i.e. the clay size.

$$A_c = \frac{I_p}{f} \quad (3.2)$$

The activity was found equal to 1.44 and is in the active range ($1.25 < A_c < 2.0$) and can be considered as slightly active soil (figure 3.5).

Table 3.1: Activity of different clay minerals

Mineral	Activity
Montmorillonite	1-7
Illite	0.5-1
Kaolinite	0.5

In order to determine the behavior of clay in the soil, a few samples were sent to ISTERre in Grenoble to measure the cation exchange capacity (CEC) and the specific surface area (S_{sp}).

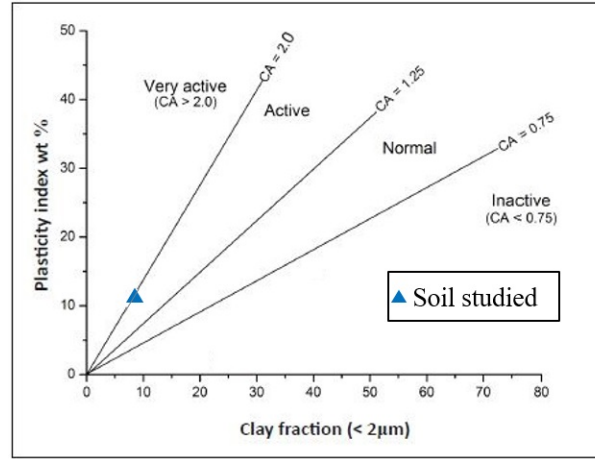


Figure 3.5: Activity of soil studied based on the clay fraction and plasticity index

Cation exchange capacity (CEC) is a measure of the ability of soil to retain and exchange cations which are retained on negatively charged sites that are found on the surface of particles of clay. The cation exchange capacity (CEC) of 2.6 cmol/kg at a pH of 7.63, which is considered to be a very low value ($\text{CEC} < 9 \text{ cmol/kg}$). Therefore, the soil has a low retention capacity.

The specific surface area (S_{sp}) measurement is based on the Brunauer, Emmett and Teller theory (BET) which determines the specific surface due to the physical adsorption of a gas (dinitrogen) on a solid surface. The adsorbed gas molecules have a tendency to form a thin layer which covers the entire surface of the solid. The surface of the solid will be calculated from the section and the number of gas molecules (known) constituting the monolayer. The volume of adsorbed gas is calculated from the following formula:

$$v = V_{mono}c \frac{P_A/P_{A,sat}}{(1 - P_A/P_{A,sat})(1 - P_A/P_{A,sat} + cP_A/P_{A,sat})} \quad (3.3)$$

where,

P_A : partial pressure of adsorbate at equilibrium;

$P_{A,sat}$: saturated vapor pressure of the adsorbate at the experiment temperature;

v : volume of gas adsorbed per gram of adsorbent;

V_{mono} : volume corresponding to a monolayer of adsorbed molecules;

c : BET constant, which is characteristic of the interaction between the adsorbate and the adsorbent.

The total surface area (S_t) of the sample material was determined from the following expression:

$$S_t = \frac{v_m N s}{V_{mono}} \quad (3.4)$$

where, s is the cross-sectional area of adsorbed gas molecules and N is the Avogadro's number (6.02×10^{23} molecules/mol).

The Specific surface area was further evaluated from total surface area and mass of sample (m) from the following expression:

$$S_{sp} = \frac{S_t}{m} \quad (3.5)$$

The Specific surface area (S_{sp}) equal to $14.7m^2/g$ was obtained. It is difficult to determine the nature of the clays containing in this soil based to CEC and S_{sp} measurements because of the heterogeneity of the soil, but we can predict that this soil contains very low percentage or absence of clays which have a swelling character (such as smectite and vermiculite) since these minerals have a very high specific surface and CEC (Table 3.2). Thus, this soil is representative of building construction since it has low activity.

Table 3.2: Cation exchange capacity and specific surface area of different clay minerals

Mineral	Specific surface area (S_{sp})	CEC $cmol/kg$
Kaolinite	10-30	5-15
Illite	100-175	10-40
Smectite	700-800	80-150
Vermiculite	760	100-150
Chlorite	100-175	10-40

3.3 Sample Preparation

For sample preparation, the determination of optimum moisture content at which compaction is carried out is very important. In this part, the optimum conditions are determined from normal Proctor test, and sample preparation using a technique of static double compaction is discussed. The various advantages of using static double compaction in comparison to classical dynamic compaction are mentioned. The energy imparted to the soil during compaction in standard Proctor and static double compaction is compared. Finally, the dry density achieved from these two methods is compared to the in-situ walls.

3.3.1 Proctor compaction test

In order to determine the water content to be achieved for optimum compaction, normal Proctor test was done. The optimum Proctor water content is determined by carrying out a series of dynamic compaction on a soil mass whose water content varies from one sample to another. It is then possible to determine the optimum water content by comparing the evolution of dry density after compaction. The normal Proctor test was carried out by using automatic compaction device recommended in the French Standard NF P 94-093, 1999 [73] and EN 13 286-2 [74].

- Water was added to air-dried soil to bring its water content to about 9% and mixed thoroughly.
- This mixed soil was compacted in a normal Proctor mold in 3 layers using 25 blows each. Compaction in each layer consisted of 5 sequences of 5 blows distributed in the mold.
- The mass of soil is measured and a part of the soil is taken for water content determination. The dry density (ρ_d) is calculated from the following expression:

$$\rho_d = \frac{\rho}{1 + w} \text{ with } \rho = \frac{m}{V_{mold}} \quad (3.6)$$

where, w is the water content, ρ is the bulk density, m is the mass of soil in the mold and V_{mold} is the volume of mold.

- The water content is increased gradually and measured posteriori, and the compaction process was repeated until the mass of compacted soil in the mold decreases, i.e. the dry density decreases.

The compaction curve is plotted in figure 3.6 to obtain the relationship between water content and dry density. A range of optimum moisture content (11.8%-13.4%) to obtain the maximum dry density was observed, and finally, optimum moisture content of 12.5% was chosen for the preparation of the soil. The maximum dry density obtained was around 1905 kg/m^3 .

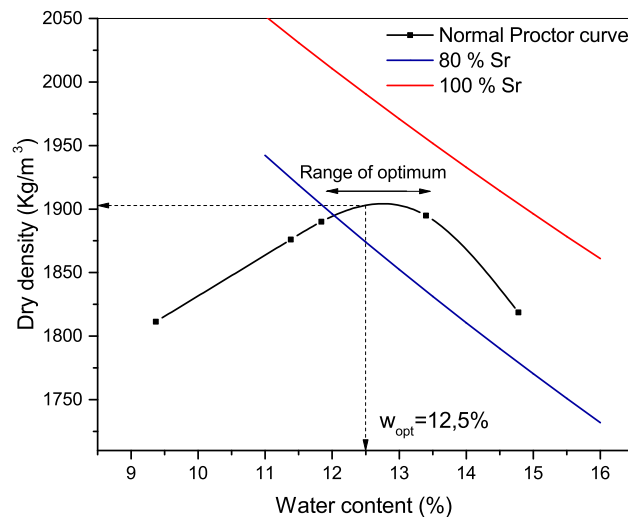


Figure 3.6: Results of normal Proctor test and 80% and 100% saturation lines

In addition, a line showing the relationship between the water content and dry density of the compacted soil at constant degree of saturation termed as saturation line

(equation 3.7), is plotted at 80% and 100% degree of saturation. Usually, the optimum compaction condition state passes through 85% to 95% saturation line.

$$\rho_d = \frac{G\rho_w}{1 + \frac{wG}{S}} \quad (3.7)$$

where, ρ_d is the dry density of soil, ρ_w is the density of water, w is the water content, G is the specific gravity of soil taken as 2.65, and S is the degree of saturation.

The energy imparted to the soil sample during the Proctor compaction can be determined using the following expression [73]:

$$E = \frac{HmgN_1N_2}{V_{mold}} = \frac{0.305 * 2.405 * 9.81 * 3 * 25}{0.000948} = 569kJ/m^3 \quad (3.8)$$

where,

H : Height of free fall of hammer = 0.305 m

m : mass of hammer = 2.405 kg

N_1 : Number of layers = 3

N_2 : Number of blows in each layer = 25

V_{mold} : Volume of mold = 0.000948 m^3

3.3.2 Double Compaction

During the compaction process of rammed earth, there is a density gradient in the soil layers. The soil is denser at the top and looser at the bottom of the layer. As there is heterogeneity in the sample, it adds an additional difficulty in the interpretation of hydro-mechanical experiment results, since the dry density of soil is an important parameter controlling the mechanical behavior as seen in the literature review. In addition, the objective of this study is to understand in detail the hydric influence on mechanical characteristics. Thus, it is very important to control the other influencing parameters such as the dry density of compacted soil. In this regard, a method of static double compaction in which compression is applied simultaneously at both ends of the sample was used. Double compaction has been used as a method of sample preparation to study the behavior of rammed earth by various authors in the literature[75][17].

A hollow cylindrical stainless steel mold was used, with an outside diameter 13 cm, an inside diameter of 5 cm and a height of 25 cm. The thickness of 4 cm of the mold steel was chosen to resist the lateral pressure developed by the material (itself having a diameter of 5 cm) during the compaction process. 4 lateral handles are attached to mold in order to facilitate holding and turning of the mold. A cylindrical sample of diameter 5 cm and a height of about 10 cm was obtained from the compaction process. This gives a slenderness ratio of about 2. This value of slenderness ratio is recommended in the literature [46][47][45] as discussed in the literature review part. In addition, it prevents

from buckling during compression. Cylindrical samples were prepared using this mold with the static double compaction method. A final static compaction pressure of 5 MPa was chosen, as it is the classical pressure for compressed earth blocs (CEBs)

Following are the steps for the preparation of specimen using the static double compaction process and the illustration of each stage is given in figure 3.7.

1. Firstly, the soil which is sieved at 5 mm was mixed thoroughly at an optimum moisture content of 12.5% and left for water content equalization for at least 24 hours in a sealed container.
2. Two cylindrical disks of 5 cm diameter and 1 cm height are inserted at the bottom of the mold. These cylindrical disks are used to facilitate the insertion of cylindrical piston once the mold is turned.
3. Around 425 g of wet soil estimated to obtain the desired dry density and height of the sample is poured inside the mold (1).
4. A cylindrical piston labelled A (diameter 5 cm and height 12.5 cm) in figure 3.7 is inserted at the top and pressed manually to be at least 1 cm inside the mold (2). The piston is rotated about the vertical axis to confirm that the piston is not getting stuck and is vertical in orientation. If the piston is not vertical, there can be abrasion between the piston and the inside of the mold, which can completely halt the process and damage the mold.
5. Firstly 80% of the total compaction pressure, i.e. 4 MPa is applied at a displacement rate of 2 mm/s. The first stage of compression can be seen in (2) to (3) in the figure 3.7.
6. The specimen is unloaded and the 2 cylindrical disks at the bottom of the mold are removed by holding the complete assembly up. Then the mold is carefully rotated so that the piston A is now at the bottom of the mold assembly.
7. Another piston B (diameter 5 cm and height 12.5 cm) is inserted from the top in the gap that was created before by the cylindrical disks (4).
8. The loading plate is made to come in contact with the piston B and 100% of the total compaction pressure, i.e. 5 MPa is applied from the top at a displacement rate of 1 mm/s (5).
9. The double compaction process is complete. In order to remove the sample from the mold, the piston B is removed. In order to create a gap at the bottom of mold, the mold is placed on a mechanical nut, diameter of which is less than 5 cm. This assembly is pressed downwards, and the piston B is inserted at the bottom (6).
10. In order to move the mold downwards and not compress the specimen, another hollow cylindrical mold of inside diameter 10 cm is placed at the top of the assembly.

11. This assembly is loaded very slowly from the top until both the pistons A and B are inside the mold, and they gradually push the sample outside of the mold (7,8).
12. In this way, a cylindrical sample of diameter 5 cm and height of about 10 cm is obtained (9).

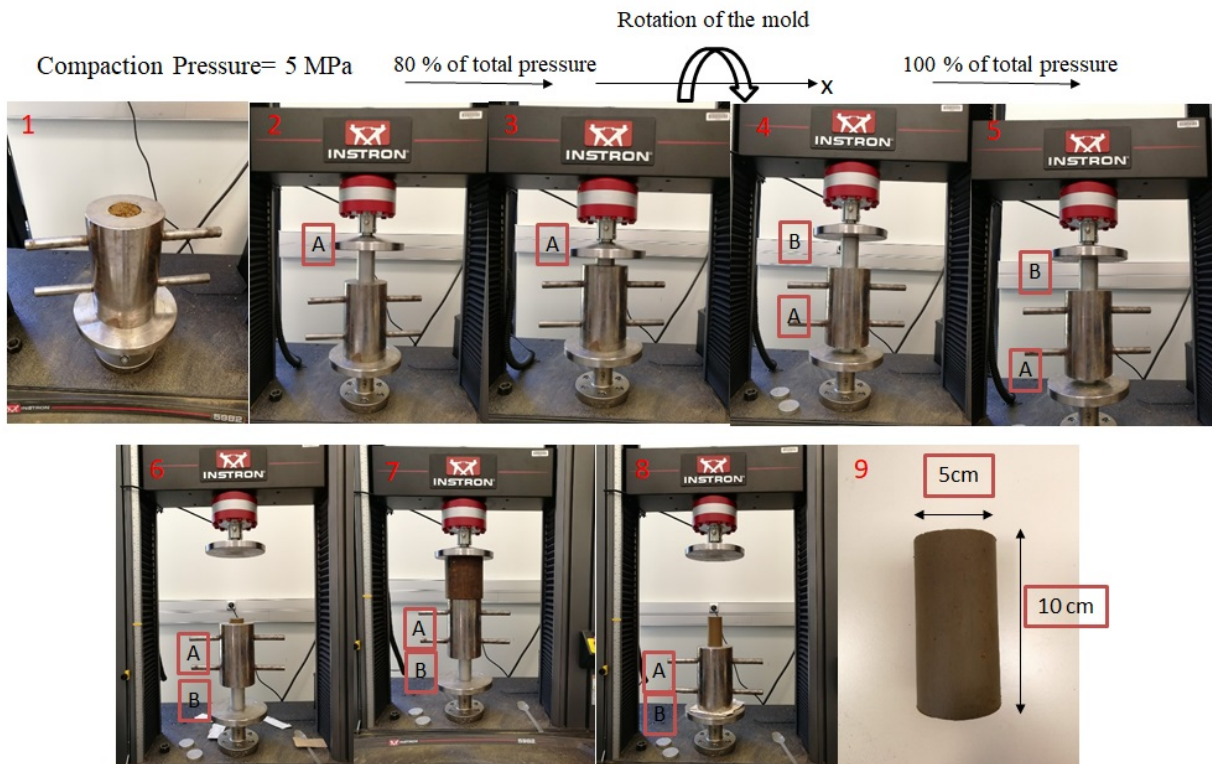


Figure 3.7: Process of cylindrical specimen preparation using the static double compaction technique

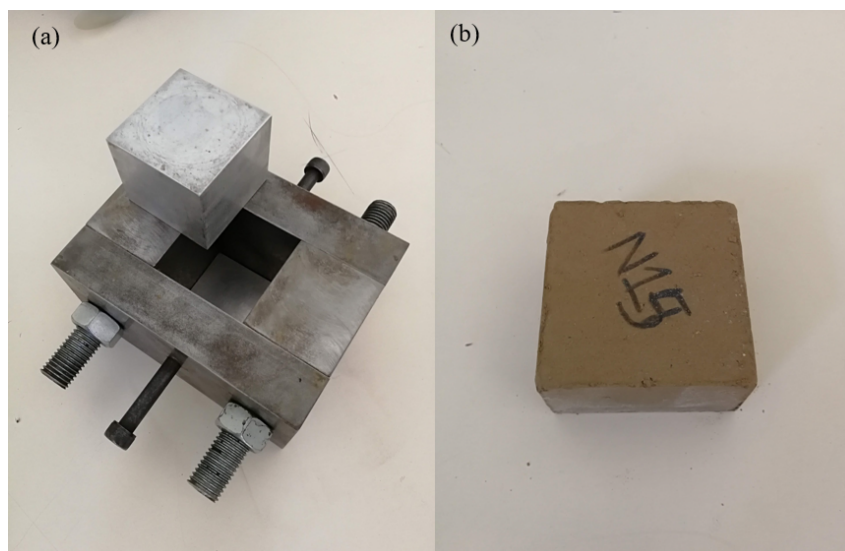


Figure 3.8: Mold (a) used for preparation of prismatic samples (b)

The cylindrical samples were prepared in order to be tested mechanically. For the unconfined compressive strength (UCS) test and triaxial test, 49 (24+25) cylindrical samples were prepared using this mold with the static double compaction method. A similar method of double compaction with same compaction pressure of 5 MPa was used to prepare prismatic specimens (60 mm x 60 mm with height of 30 mm) for performing Direct shear tests (DST). A total of 63 samples were prepared this way. Samples of these dimensions were tested considering the mechanical capacity of the shear device. The prismatic samples were prepared using a home-made mold which is shown in figure 3.8.

The method of static double compaction has various advantages with regards to the classical dynamical compaction in regards to testing at experimental scale.

- This method gives a sample with more homogeneous density in contrast to the classical dynamical compaction, where a gradient of density is observed, the earth layer being denser at top and looser at bottom. In order to study the effectiveness of double compaction in the cylindrical specimens, which are about 10 cm in height, a test cylindrical sample was prepared and cut into 5 pieces of 15-20 mm thickness. The dry density was measured for each part (figure 3.9). A maximum difference of 3% was observed in the dry density. This gives an insight that the double compaction is sufficient for cylindrical specimens. In addition, for the prismatic samples, the height is about 3 cm, and thus it was assumed that the double compaction is more effective in this case.

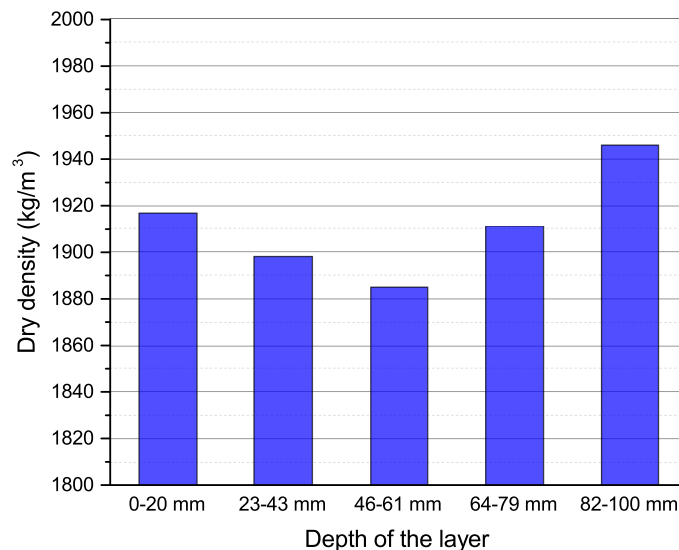


Figure 3.9: The dry density variation of a doubly compacted sample across the height

- The samples were prepared with very good repeatability. The mean dry density and standard deviation from mean for each group of samples is shown in table 3.3. A maximum standard deviation from mean of 1.74% was observed for prismatic

samples. For samples made from dynamical compaction a standard deviation as high as 11% can be observed [76].

Table 3.3: Average dry density and standard deviation from the average for cylindrical and prismatic samples (Instron machine was more accurate than HM machine)

Samples	Dimensions (mm)	Number	Avg. ρ_d (kg/m^3)	SD (%)	Machine
Cylindrical (UCS)	$\phi=50$, H = 100	24	1855	1.26	HM
Prismatic (DST)	60 x 60 x 30	63	1906	1.74	Instron
Cylindrical (triaxial)	$\phi=50$, H = 100	25	1910	0.36	Instron

These values of dry density lie within the range of dry density for earthen structures ($1700 \text{ kg}/m^3$ to $2200 \text{ kg}/m^3$ [36]). Thus, even though the method of compaction differs from the actual method of compaction in the field, it is a material which is representative of rammed earth.

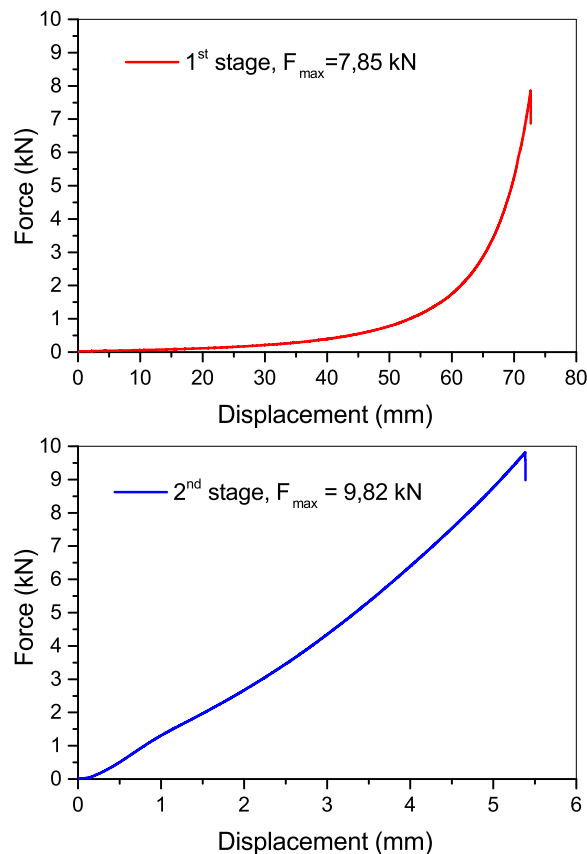


Figure 3.10: Force-displacement curve during compaction for both stages of loading for sample at 10.8% water content

The specimens were compacted statically in two stages following the method of double compaction. In the first stage a load of 7.85 kN was applied corresponding to 4 MPa pressure and in the second stage a load of 9.82 KN was applied corresponding to

5 MPa pressure (figure 3.10). The static compaction energy was evaluated through the following integral formula using the force-displacement curve.

$$W = \int F.du \quad (3.9)$$

The energy of compaction in the double compaction method (at the proctor optimum) is about 476 kJ/m^3 , and for standard Proctor, the energy is about 569 kJ/m^3 . Still, the dry density is the most important parameter influencing the strength properties [55], and the objective is to approach the dry density as in a rammed earth wall (dry density for rammed earth wall of the studied soil is about 1900 kg/m^3). Thus the optimum moisture content obtained from the standard Proctor can be used for the method of double compaction. In addition, it can be observed that energy imparted in Proctor test is higher compared to static double compaction to obtain the same dry density. Thus, it can be said that static compaction process is more energy-efficient probably due to the higher energy loss during the impact of falling weight in the Proctor test [75][77].

3.4 Hydric conditions

The cylindrical samples and prismatic samples were prepared in order to test them mechanically when submitted to different uniform hydric conditions. This part presents how these hydric solicitations are obtained.

As explained in the literature review, suction is one of the key parameters to quantify the hydric state of unsaturated soil. Thus, in this section, firstly the definition of suction and the retention behavior of soil is presented. In addition, it is necessary to control the suction state of rammed earth samples before mechanical testing. For this, the different methods to control the suction, such as Liquid-vapor equilibrium and axis translation method are presented. Finally, the hydric properties of the rammed earth studied, and the conditioning of rammed earth samples before testing is discussed.

3.4.1 Suction

Total suction quantifies the thermodynamic potential of the pore water in the soil in comparison to the reference potential of free water. Free water is defined as water containing no dissolved solute, under no external force other than gravity, no interaction with other phases leading to curvature in the air-water interface. The various factors that lead to the reduction of the potential of pore water are:

- Capillary effects: due to the presence of air-water interface.
- Osmotic effects: due to the dissolved solutes in the soil pore water.

- Short-range adsorption: due to the electrical and Van der Waal forces in the vicinity of solid-liquid interface.

The capillary effects are unique to the unsaturated soils, which includes the curvature of the air-water interface and the associated negative pore water pressure. The osmotic effects and the short-range adsorption occurs under both saturated and unsaturated conditions.

Suction due to the combined effect of capillarity and short-range adsorption is termed as matric suction (s_m). The suction arising from the osmotic effects due to dissolve solutes in the pore water is termed as osmotic suction (s_o). Total suction (s) is the algebraic sum of matric and osmotic suction.

$$s = s_m + s_o \quad (3.10)$$

The air-water interface existing in partially saturated soil is shown in figure 3.11. The water present in the surface experiences different forces in comparison to water present in the bulk region. In the bulk region, the water molecule is under the effect of neighbouring water molecules equally from all directions leading to zero net force. Whereas, water molecule at the surface is affected only by the water molecules under the surface, leading to a net inward force. This leads to the water surface being under tension and a curved meniscus. The difference in the air pressure (u_a) on the concave side of the meniscus and lower water pressure (u_w) on the convex side of the meniscus is termed as matric suction. Here the short-range adsorption effects are neglected since they are relevant at very low values of water content when the adsorbed pore water is primarily in the form of thin films coating the particle surface.

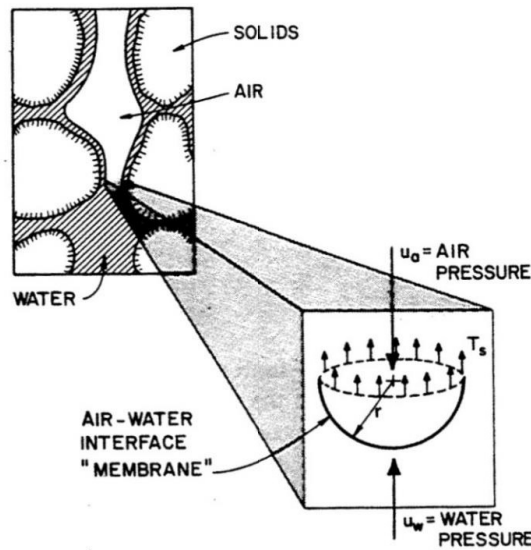


Figure 3.11: Air-water interface of a partially saturated soil [21]

The height above the water table until which the soil remains in saturated state is governed by the size of pore and the difference between air and water pressure. The

free-body diagram is shown in the expanded view (figure 3.11), where, r is the radius of idealized sphere representing the bottom of the air channel, T_s is the surface tension in the membrane. Based on the vertical force equilibrium at the air-water interface, the matric suction can be evaluated using Jurin's law of capillary rise:

$$s_m = u_a - u_w = \frac{2T_s}{r} \quad (3.11)$$

Osmotic suction in clay is due to the chemical activity of the soil leading to forces on the water molecules. Generally, distilled water is used for sample preparation and in tests which include the exchange of pore water. This leads to osmotic part of the suction to be zero, and the total suction can, in fact, be taken equal to the matric suction.

3.4.2 Soil water retention curve (SWRC)

The soil water retention curve (SWRC) represents a fundamental constitutive relationship in unsaturated soil mechanics and is used to define the affinity with water of a porous media. Soil water retention curve describes the thermodynamic potential of soil pore water as a function of amount of the water adsorbed in the soil system. Specifically, it describes the relationship between the soil suction and water content (gravimetric or volumetric) or degree of saturation of the porous media. It is also called 'sorption behaviour' when relative humidity is used instead of suction. The SWRC has three different suction regimes or zones, as shown in figure 3.12.

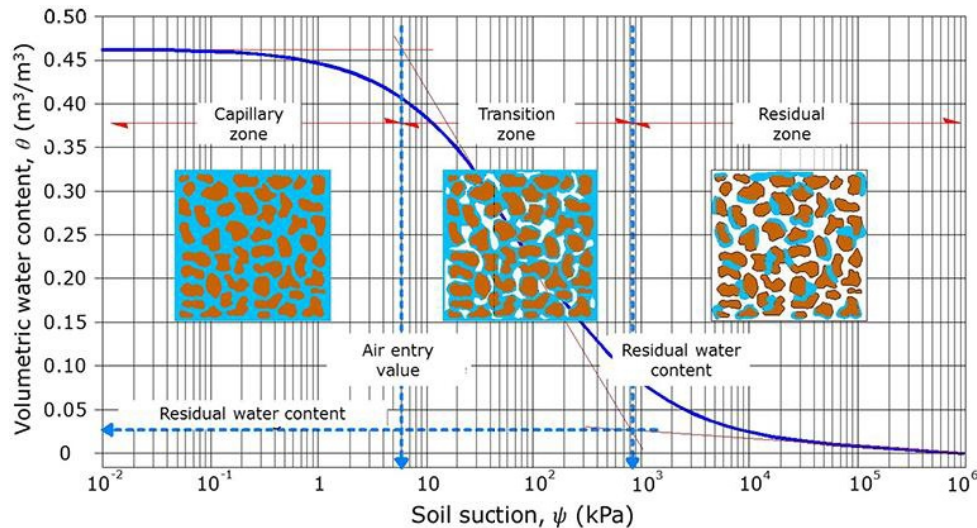


Figure 3.12: Different suction zones corresponding to the soil water retention curve [22]

- Capillary zone: It is a zone present in saturated state and ends at the air-entry pressure value, which is defined as the value of matric suction at which the air enters the biggest pore of the soil. In this zone of relatively high water content and corresponding low suction values, capillarity is the main mechanism for pore water

retention. It is governed by the particle and pore structure, and the distribution of pores.

- **Transition zone:** In this zone, the water is displaced due to entry of air and is not saturated. This zone is defined between the air-entry and the residual conditions, where pore water becomes discontinuous. The transition between the low suction zone where capillarity is the main retention mechanism and high suction zone where short-range adsorption is the main mechanism is dependent on the type of soil. For fine-grained soils such as clay, a significant amount of water is retained due to high specific surface of the particles. Whereas for coarser soils such as sand, capillarity is majorly responsible for water retention and very low amount of water is retained in the high suction regime.
- **Residual zone:** In this section, the increase of suction does not produce significant changes in the water content. As water is scarce, it does not flow between pores, and its removal only occurs by evaporation. This zone is characterized by relatively low value of water content and corresponding high values of suction, where the pore water is present in the form of thin films over the soil particles. The main mechanism of pore water retention is short-range adsorption which is governed by the properties of soil particles.

The retention behavior of soils is significantly affected by particle and pore size distribution, clay content and mineralogy, density of soil.

3.4.3 Control of suction

The main objective of the work is to study the effect of hydric conditions (suction states) on the mechanical behavior of rammed earth. Thus, it is imperative to control the suction of specimens before testing. Rammed earth structures during their lifetime are subjected to changes in suction due to the changing atmospheric humidity conditions. After fabrication at the optimum water content, it is subjected to drying. Thus, in this study, after specimen preparation at optimum conditions, the samples will be subjected to different suction conditions (different relative humidities) before testing mechanically. Two different methods were used for the control of suction state based on the range of suction for which these methods are valid [78].

- **Liquid-vapor equilibrium method:** used for high values of suction (3-350 MPa).
- **Axis-translation technique:** used for lower values of suction (0-1.5 MPa).

3.4.3.1 Liquid-vapor equilibrium method

In liquid-vapor equilibrium method, the relative humidity of the atmosphere is controlled and imposed around the specimen. This method is realised by using saline solutions. The

saturated aqueous solution of different salts (table 3.4) are used to control the relative humidity of the air around the samples from 9% to 97.3%. Based on the difference of relative humidity between the ambient conditions of the surrounding air and the specimen, water exchanges take place by means of vapor transfer up to the equilibrium of the pore relative humidity. The relationship between the equilibrium of relative humidity of the pore air and the suction imposed on the specimen is based on Kelvin's thermodynamic equilibrium:

$$s = -\frac{\rho_w \cdot R \cdot T}{M_w} \ln(RH) \quad (3.12)$$

where, s is the suction at a given temperature T (in Kelvin, K), R is universal gas constant ($R = 8.3143 \text{ J/mol/K}$), M_w is the molar mass of water ($M_w = 0.018 \text{ Kg/mol}$), ρ_w is the bulk density of water ($\rho_w = 1000 \text{ Kg/m}^3$) and RH is the relative humidity, which is defined as the ratio of partial vapor pressure P in the considered atmosphere and the saturation vapor pressure P_o at temperature ($T = 298 \text{ K}$).

Table 3.4: Different saline solutions, their solubility at 25 °C, the relative humidity, and corresponding suction imposed

Salt	<i>KOH</i>	<i>CH₃CO₂K</i>	<i>MgCl₂</i>	<i>NaBr</i>	<i>NaCl</i>	<i>KCl</i>	<i>K₂SO₄</i>
RH (%)	9	22.51	32.8	57.6	75.3	84.34	97.3
Solubility at 25 °C (g/100 ml)	121	268.6	56	94.6	36	35.54	12
Suction (MPa)	331.3	205.3	153.4	75.9	39	23.4	3.8

In order to impose different suction conditions, relative humidity boxes with aqueous solutions were made for all the salts mentioned in table 3.4. The scheme of the relative humidity controlled boxes is shown in figure 3.13. At the base of the box, saturated solutions of the salt is poured, and inverted plastic cups are placed in the solutions so that the top of the plastic cup is at a level higher than the aqueous solution. A plastic mesh is placed at the top of the plastic cups to place the rammed earth specimens. This box was closed and sealed to create ambient conditions which will impose suction on the specimens.

The rammed earth specimens before being placed inside the RH boxes were covered with a paper which allows only the transfer of liquid vapor and not the liquid. This was done so that, if the specimen gets in contact with the aqueous solution, it does not absorb the liquid directly. This ensures that the transfer between the specimen and surrounding air only takes place by means of vapor transfer.

3.4.3.2 Axis translation technique

In order to control suction in the lower range, axis translation technique is used, which involves measurement of the pressure differential across a high air-entry ceramic disk. It

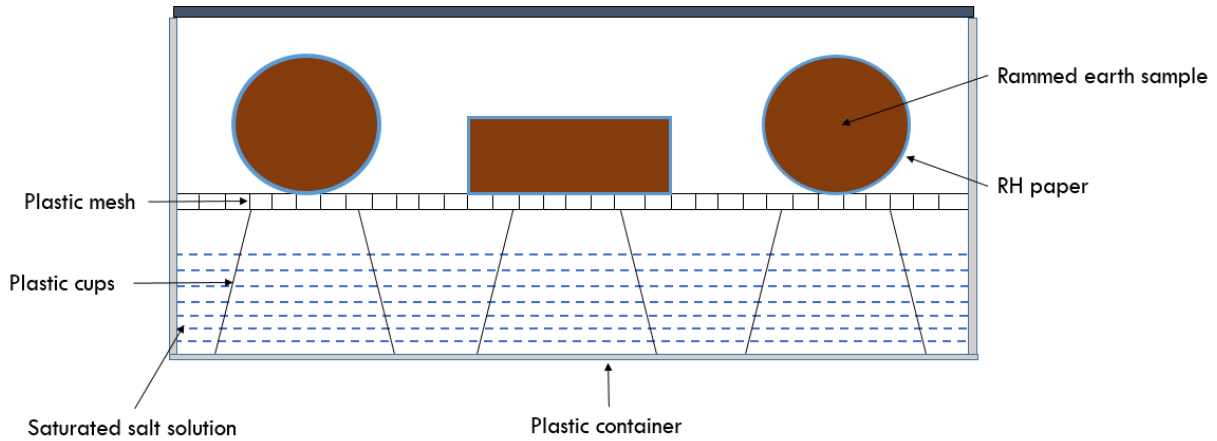


Figure 3.13: A scheme representing the relative humidity boxes which contains the salt solution and rammed earth samples

is based on the assumption that two states are equivalent if they are subjected to the same value of suction even if the individual liquid and gas pressure is different. In this technique, suction is controlled by the application of positive water pressure along with an increase in the ambient air pressure by same amount. Thus, this technique is referred as the axis-translation technique as water pressure has been translated upwards with the air pressure origin and away from the metastable states to eliminate the risk of cavitation.

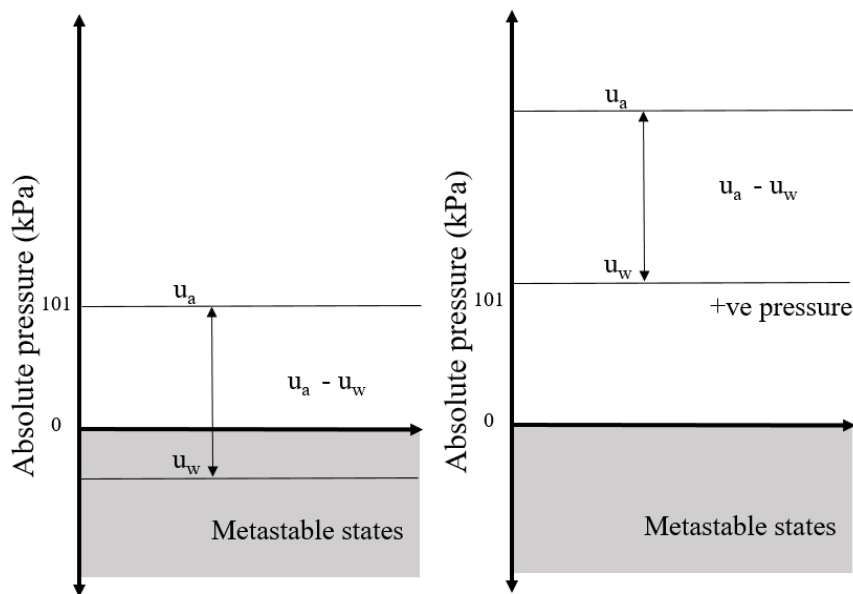


Figure 3.14: Use of axis translation technique to avoid metastable states (left) Atmospheric conditions; (right) axis translation (after Marinho et al. 2009 [23])

In order to avoid cavitation (figure 3.14) in the water system when depression is applied, we keep an atmospheric pressure for the liquid water phase, and we apply an increasing over-pressure in the gas phase. The difference between the two (capillary pressure), is supposed to have the same effect than a capillary pressure obtained with a

depression of the liquid water and an atmospheric pressure of the gas phase.

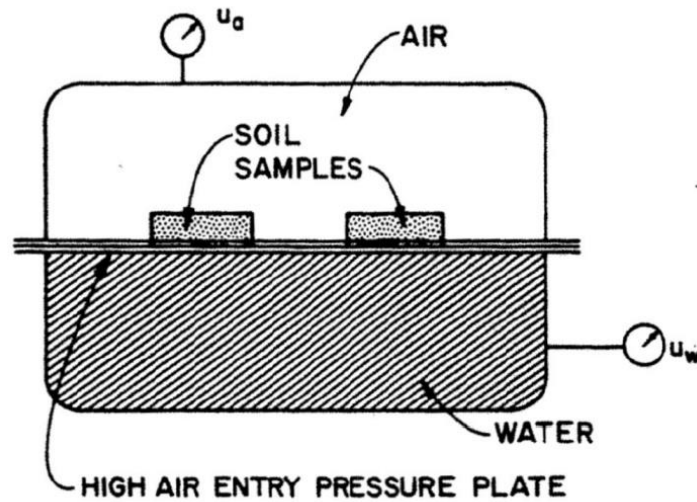


Figure 3.15: Scheme of pressure plate device [21]

Pressure plate tests make use of the axis translation technique. In these tests, a chamber is divided by a high air-entry pressure plate (figure 3.15). Soil samples are placed on the top of the high air entry pressure plate, and the values of air pressure and water pressure are controlled. At the selected values of soil matric suction ($u_a - u_w$), samples are removed and weighed for determination of water content.

3.4.4 Hydric properties of rammed earth

3.4.4.1 Soil water retention curve

The soil water retention curve was obtained using two different methods. Saline solutions were used to have points on the retention curve from suction values ranging for 3.8 MPa to 331.3 MPa, i.e. in the higher range of suction. In order to obtain points in the retention curve for suction less than 3.8 MPa ($RH > 97.3\%$), pressure plate method was adopted.

Liquid vapor equilibrium method

In order to formulate a part of retention curve of the rammed earth in the suction range 3.8 - 331.3 MPa, following procedure was adopted.

1. Firstly, 5 centimetric samples of dry mass ranging from 5-8g were compacted by a similar method of double compaction described before.
2. The samples were air-dried at ambient conditions (temperature = 25 °C and $RH = 62\%$), then placed inside the oven at 70 °C for sufficient duration of time (few days) until the mass was stabilized. It is considered that their water content is zero.

3. The saturation of 7 different saline solutions was checked. It can be determined visually. If there are no crystals at the bottom of the solution, it is unsaturated. In this case, additional salt is added in the solution and mixed with the magnetic agitator to facilitate its dissolution.
4. The five rammed earth samples were then covered with a breathable sheet and tightened with a rubber band.
5. The samples were placed in the KOH saline solution box having the lowest relative humidity (9%). It was made sure that the salt solution is always saturated.
6. When the samples were equilibrated, i.e., mass variation is less than 0.05% in 24 hours, they were transferred to the next higher relative humidity box.
7. In this way, the data points for the sorption curve were obtained.
8. Once equilibrium was reached in the last box with the highest relative humidity (97.3%), the samples were again transferred towards lower relative humidity boxes. In this way, the points for the desorption curve are obtained.

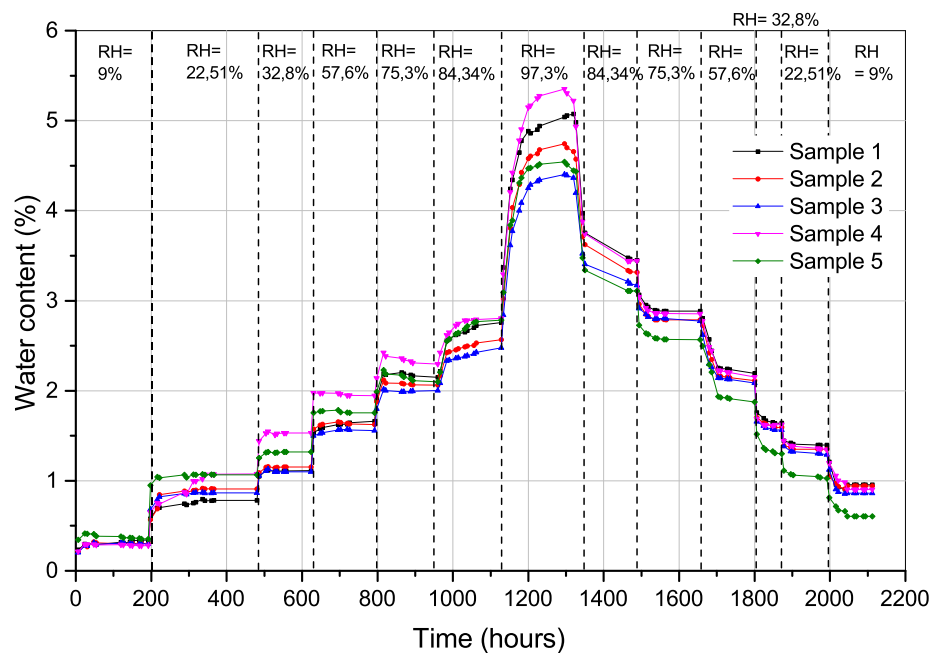


Figure 3.16: Variation of water content with time when the soil samples were move between different relative humidity boxes

Figure 3.16 shows the variation of gravimetric water content with respect to time for the five samples studied. The results of the five samples showed relatively low discrepancy with each other except for the highest relative humidity of 97.3%. The jumps in the water content associated with the change of RH box were clearly visible and were of

greater amplitude in the sorption phase (wetting phase). The highest jump was associated with the change between 84.34% and 97.3% RH boxes for both sorption and desorption phases. The major mass variation (either lost or gained) was recorded within the first hours after changing the RH box, then the change in mass drastically reduces when the difference in RH between the sample and surrounding air is less until reaching equilibrium within 4-5 days. In total, it took about 3 months for the sorption and desorption phase to complete. At relative humidity of 9%, the water content was at 0.31% for the wetting phase, and then it increased up to 4.78% at 97.3% relative humidity. For the same relative humidity of 75.3%, the mean value of water content in wetting phase was 2.13%, whereas it was around 2.78% for the drying phase highlighting the hysteresis effect.

The soil water retention curve, where gravimetric water content and degree of saturation is plotted in function of suction is shown in figure 3.17. This curve covers a range of relative humidity values lying between 97.3% and 9% and respectively an imposed suction from 3.8 and 331.3 MPa given by Kelvin's equation. Thus in order to obtain data points in the higher range of relative humidity and thus lower values of suction, Pressure plate method was adopted. This range of suction can be reached for building in case of humid pathology. The details of this test are presented in the next part.

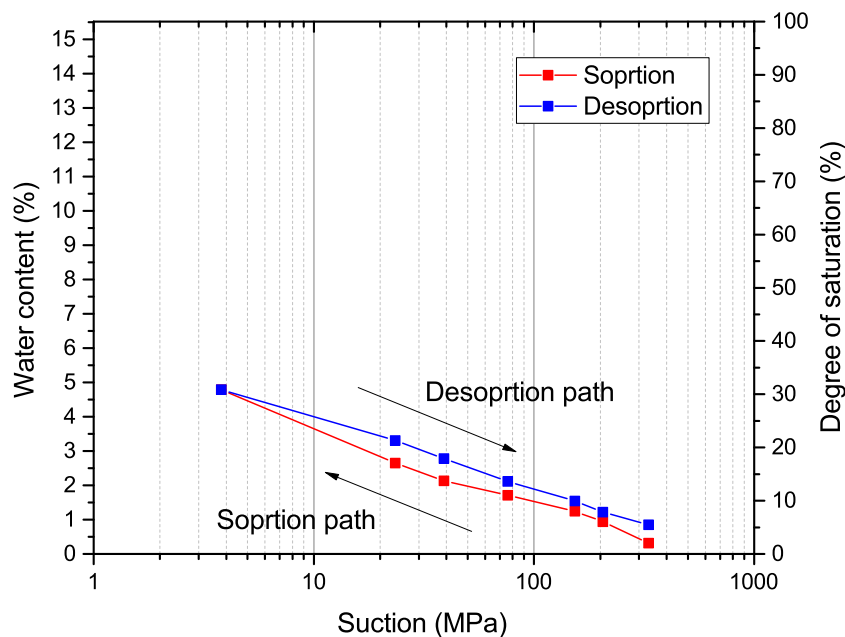


Figure 3.17: Soil water retention curve plotted from Liquid vapor equilibrium method for both sorption and desorption phases

Pressure plate test

Pressure plate test was performed to have data points in the soil water retention curve at lower values of suction (high relative humidity). Following steps were adopted for the sample preparation and performing the test.

1. Sample Preparation: 4 Cylindrical samples of height 1 cm and diameter 5 cm were made in the cylindrical mold used before for sample preparation. Since the thickness of sample is very small, total compaction pressure of 5 MPa was applied from one side instead of performing double compaction keeping the dry density unchanged. The sample was compressed at an optimum water content of 12.5%. After compaction, the samples were placed in a metallic cup and water was sprayed in order to increase the saturation degree of the samples. Then, they were covered with a plastic film and left for homogenization of water content for at least 24 hours. This step was done since; generally, the samples for testing in pressure plate apparatus are immersed in distilled water until constant mass is obtained to saturate the samples. But for the rammed earth samples studied, it was not possible since the samples disintegrated once they were kept in water due to loss of cohesion.
2. Preparation of test: Firstly, the porous ceramic plate was saturated by immersing it in distilled water for a minimum of 8 hours. Kaolin paste was applied to the saturated plate and covered with a layer of acetate cloth in order to ensure good contact without sticking. The water outlet tube was connected to the porous plate, and a container was placed at the water outlet (figure 3.18). The device was then closed and tightened with screws.

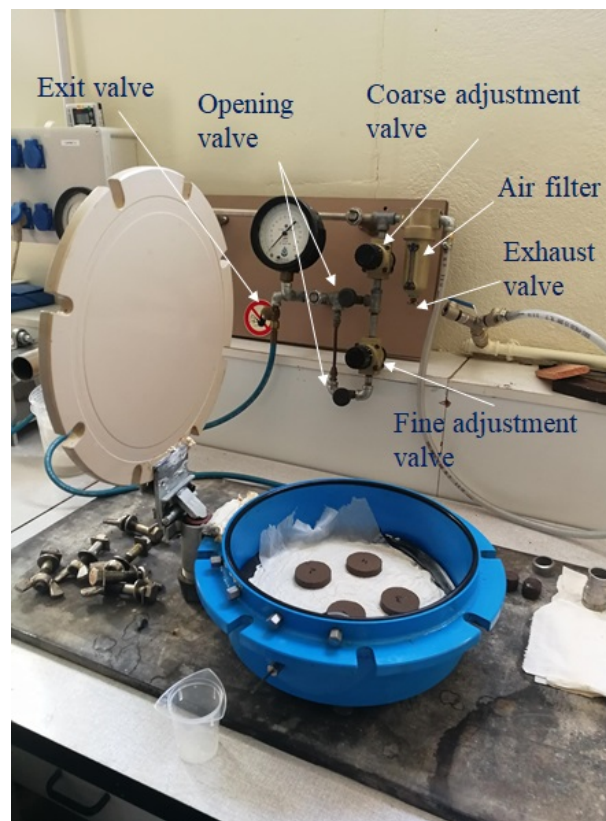


Figure 3.18: Testing of the samples in the pressure plate device and pressure regulation system

3. Procedure of the test: A pressure of 0.19 MPa is applied to the air of the system.

Once the pressure is admitted, it is necessary to wait until the samples are in equilibrium. The equilibrium was supposed to reach when less than 0.05 ml of water flow over a period of 48 hours. When the equilibrium was reached, the device was depressurized, and the cover was opened. The samples were weighed immediately to evaluate the water content/degree of saturation. The pressure was then changed to 0.5 MPa, and the device was pressurized again. The process is repeated to obtain the degree of saturation.

Two additional points on the soil water retention curve at a lower value of suction was obtained through the pressure plate test. The results of this test, combined with the results of desorption phase from saline solution method, is shown in figure 3.19.

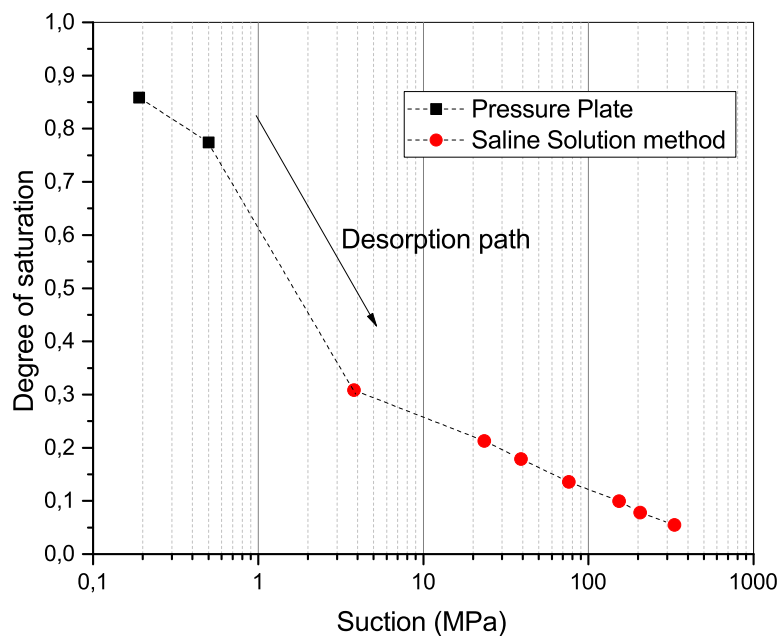


Figure 3.19: Soil water retention curve using the results of pressure plate test and saline solution method (desorption phase)

3.4.4.2 Hydraulic conductivity

The hydraulic conductivity of rammed earth was determined on two static doubly compacted cylindrical samples of diameter 5 cm and a height of 10 cm. The method of sample preparation is mentioned in the previous section. The samples after compaction were saturated in the triaxial device, description of which will be shown in further part (section 3.5.3 and 3.5.4). Once the saturation is reached, a pressure difference of 20 kPa was applied between the top and bottom of the sample. The total volume of water exiting the sample was measured. The results of the test are summarized in table 3.5.

Table 3.5: Hydraulic conductivity test results

Sample no.	Dry density (kg/m^3)	Saturation w (%)	Saturated hydraulic conductivity (m/s)
P1	1938.3	15.1	3.32×10^{-9}
P2	1939.1	15.0	3.23×10^{-9}

The saturated hydraulic conductivity was calculated using the following expression of Darcy's law:

$$k_{sat} = \frac{\rho_l g \Delta l \Delta V}{\Delta u \Delta t A} \quad (3.13)$$

where, ΔV is the change in volume recorded within a certain time Δt , A is the cross-sectional area of the sample, k_{sat} is the saturated hydraulic conductivity, ρ_l is the density of water, Δl is the length of flow path (i.e. length of the sample), and Δu is the pressure difference applied between the top and bottom of the sample (taken as 20 kPa, enough to create a flow path). The values of the computed saturated hydraulic conductivity for the samples were close enough to conclude that the test is repetitive. The saturated hydraulic conductivity of the soil is taken to be the average of the two tests equal to 3.27×10^{-9} m/s. The intrinsic permeability (k_i) can be related to saturated hydraulic conductivity (k_{sat}) by the expression $k_i = (k_{sat} \mu_w) / (\rho_l g)$ where, μ_w is the dynamic viscosity of water. This gives the value of $k_i = 2.97 \times 10^{-16} m^2$.

3.4.5 Conditioning of samples

The rammed earth samples before mechanical testing were placed in relative humidity controlled boxes with saline solutions in order to control the suction state. Figure 3.20 shows the cylindrical and prismatic samples placed in the RH boxes in for suction equilibrium.

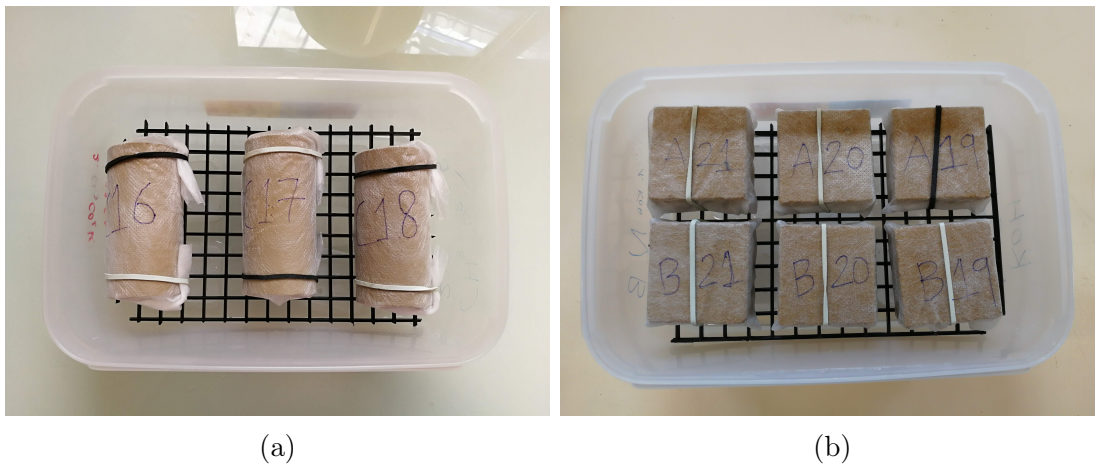


Figure 3.20: Cylindrical specimens (a) and Prismatic specimens (b) placed in RH box for suction equalization

The suction equilibrium of the 21 cylindrical specimens (for UCS test) is shown in figure 3.21. The 21 samples were distributed in 7 different relative humidity boxes equilibrated at the following relative humidities 9%, 22.51%, 32.8%, 57.6%, 75.3%, 84.34% and 97.3% (see table 3.4) in group of 3 samples (similar method was used for unsaturated triaxial samples and direct shear samples). The samples were weighed regularly to follow the variation of water content (average of 3 samples) with time. Every time, the saturation of the saline solutions were checked, in order to ensure that samples equilibrate to the desired suction states. The equilibrium in the samples is supposed to be achieved when the variation of mass becomes less than 0.05% for more than 24 hours.

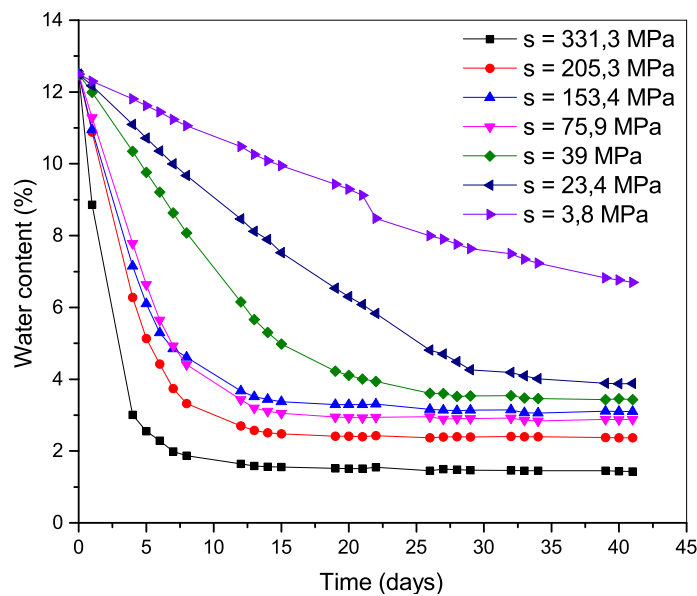


Figure 3.21: Moisture content variation (average of 3 samples) with time during the suction equilibration in humidity controlled boxes for samples of UCS test directly placed in RH boxes after manufacture

The samples which were equilibrated at relative humidity less than 60%, i.e. the ambient relative humidity for our region of France (Savoie), the equilibration time was less than two weeks. For samples at a higher relative humidity (lower suction values), it took them more than a month for moisture balance. From the graph, it was seen that samples equilibrated with $NaBr$ salt (RH = 57.6%) achieve a final water content which is less than the samples with $MgCl_2$ salt (RH = 32.8%), which is inconsistent considering that $NaBr$ imposes higher relative humidity than $MgCl_2$. The saturation of these solutions was checked a posteriori and was found that $MgCl_2$ saline solution was not saturated. Thus, it applies an unknown suction value. In the further sections, the results from this batch are not included. Also, the samples placed in the K_2SO_4 box (RH = 97.3%, $s = 3.8$ MPa) are not fully equilibrated. Thus, before testing, they were kept in the box for a few additional weeks to be sure of the equilibrium.

3.5 Influence of suction on mechanical parameters

In this section, results from unconfined compressive strength (UCS) test (24 samples), direct shear test (DST) (63 samples) and unsaturated triaxial test (21 samples) are presented to study the variation of parameters like UCS, initial tangent modulus, apparent cohesion and friction angle with suction. The analysis in these tests is done in terms of total stresses. In addition, saturated triaxial tests (4 samples) are done to evaluate the intrinsic value of cohesion and friction angle. For the evaluation of the intrinsic parameters, the effective stress concept is used. A scheme of the different test carried out, including the number of tests, and the different hydric states is shown in figure 3.22. The 7 different hydric states correspond to the relative humidity boxes mentioned in table 3.4.

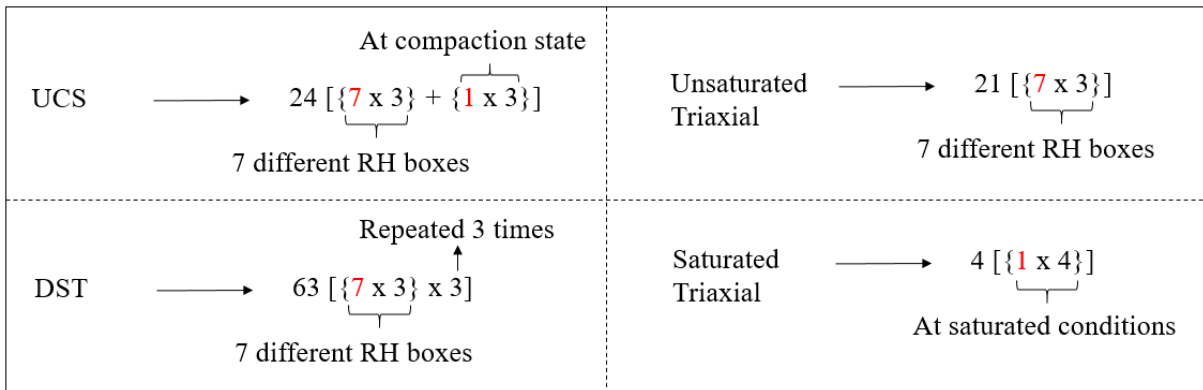


Figure 3.22: Scheme of different tests including the number of tests and hydric states

3.5.1 Unconfined compressive strength test

Unconfined compressive strength (UCS) testing was done on 24 samples, i.e. 3 samples for each 8 suction/RH conditions (3 x 8). These samples after compaction were placed in RH boxes of different relative humidities (except for the samples tested at compaction state) and once equilibrium was achieved, compression test was performed. Firstly, 2 samples from a batch were compressed with monotonic loading to obtain the compressive strength. Then, 1 out of every 3 samples from the batch, was compressed with unload-reload cycles in order to obtain Young's modulus. The unload-reload cycles were done at 30%, 60%, and 90% of the average compressive strength of the previous two samples. During the testing, the strain was determined from a video extensometer surveying two points (marked as crosses on the sample) spaced about 3 cm in the vertical direction in the center of the cylindrical sample. This was done since it was not possible to obtain correct Young's modulus while taking strain from the global strain of the sample because of fretting contact at top and base of the sample.

The samples were compressed with displacement control at a rate of 0.005 mm/s to remain in quasi-static condition. Bui et al. 2014 [5] carried out several tests to observed

the difference between force control or displacement control testing. When the loading is done with force control, the rupture is sudden because the load quickly reaches its maximum value. Whereas in case of displacement control, the speed of advance is constant following the imposed displacement and thus the failure is less sudden, and the post-peak behavior can be observed. However, it was observed that the failure stress was same for both the cases. In addition, Bruno et al. 2015 [79], carried out tests to study the influence of rate of displacement on the rupture of the samples. It was observed that the displacement rate does not affect the peak stress but the shape of stress-stain curve.

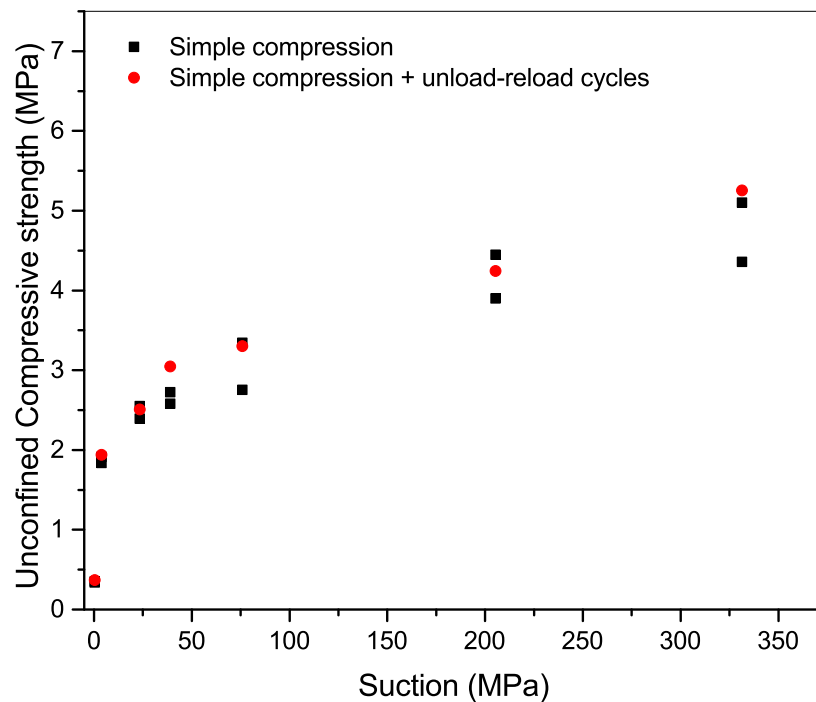


Figure 3.23: Variation of compressive strength with suction, samples compressed with unload-reload cycles shown in circular marking

As a global trend of the variation of UCS with suction, it can be seen on figure 3.23 that, the compressive strength decreases significantly with the decrease of suction. The UCS value varies from 0.35 MPa to 5.25 MPa for suction increasing from 0.328 MPa to 331.3 MPa. It can be related to the gain of resistance of the earth structures in a building from the date of manufacture (corresponding to a water content of around 11-13%) up to a long time state, after several weeks of drying (with a water content of about 2%). Inversely, this can also be related to the loss of mechanical strength for unusual water entry in the material. This helps to analyze the vulnerability of rammed earth structures when subjected to meteorological events such as strong rainfall and inundation, or default in the building (damage of the roof, insulation, base allowing capillarity, etc). The compressive strength observed at the ambient relative humidity of around 60% for European latitude was around 3 MPa. This value is consistent with what was observed in the literature [42].

The stress-strain curve for 3 samples conditioned at 39 MPa suction is shown in figure 3.24. It shows the results of two samples compressed without unload-reload cycles and one sample compressed with unload-reload cycles. The Initial tangent modulus (E_{tan}) was evaluated from the initial slope of the stress-strain curve. The linear elastic region is generally observed up to 30% of the failure load, and the slope of the stress-strain curve in this region is termed as initial tangent modulus. The variation of the initial tangent modulus (expressed as the average of 3 tests at the same suction) with suction is shown in figure 3.25. A significant decrease in the value of initial tangent modulus is observed with a decrease in suction. This behavior is also consistent with the literature [15][9][54]. The trend is similar to the variation of the compressive strength with suction. The initial tangent modulus decreases significantly from 1.37 GPa to 0.015 GPa as the suction reduces from 331.3 MPa to 0.328 MPa. All the stress-strain curves for the UCS test are shown in figure A.1 and A.2 in Appendix A.

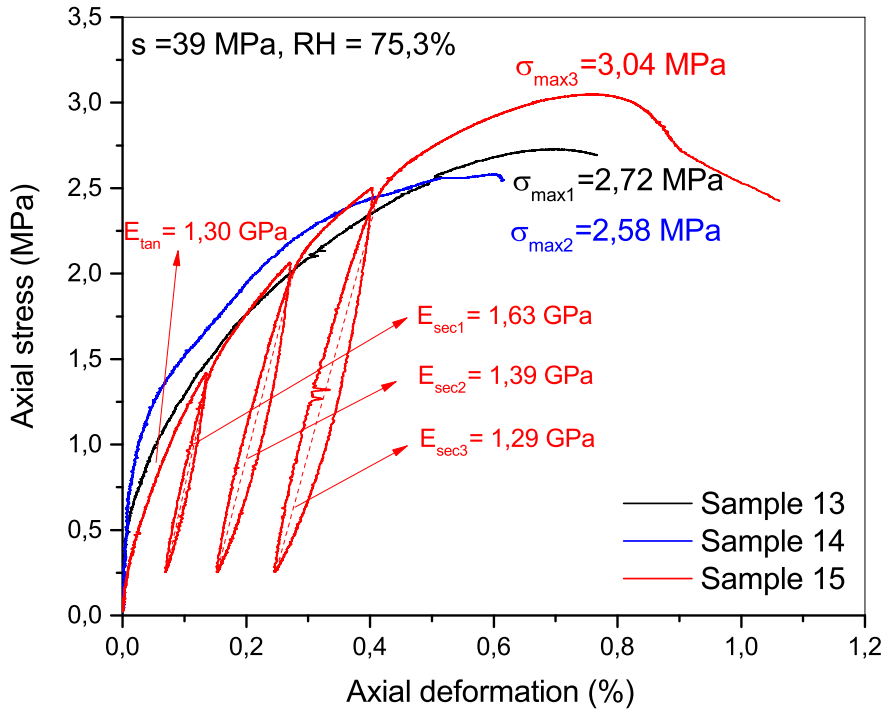


Figure 3.24: Axial stress-deformation curve during unconfined compressive strength test for 3 samples conditioned at 39 MPa suction including testing with unload-reload cycles

The secant modulus was evaluated as the ratio of difference in axial stress to difference in axial strain between the maximum and minimum axial load states of the cycle [9]. The evolution of secant modulus (E_{sec}) with the ratio of maximum axial stress previously experienced to the UCS value is shown in figure 3.26. The ratio of maximum axial stress and UCS represents the progression of the compressive testing and value of 1 represents failure state. A gradual reduction of the secant modulus, i.e. damage, with an increase in axial stress, was observed for most of the samples (except the sample

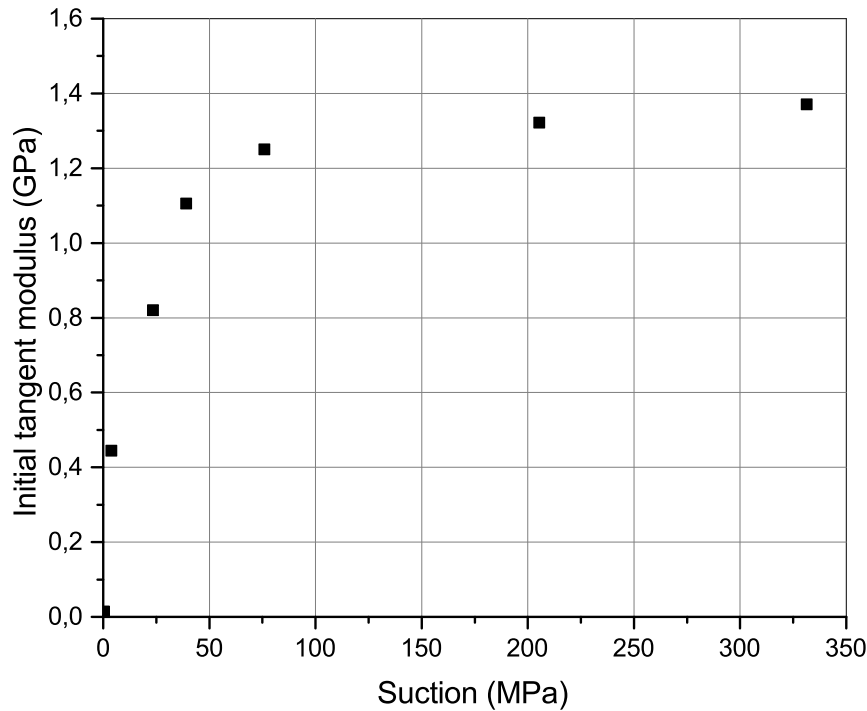


Figure 3.25: Variation of initial tangent modulus E_{tan} with suction conditions

conditioned at 331.3 MPa suction and compaction state). This damage is dependent on the suction state, which is evident from the change in slope and increases with suction. The stiffness degradation varies from 22% at 205.3 MPa suction to 13% at 3.8 MPa suction and almost no variation at the compaction state (0.328 MPa). It means that dryer the earth sample, more sensitive to damage it is and vice-versa.

The evolution of the plastic strain (ϵ_{pres}) (residual strain at the end of the unloading cycles) with the ratio of axial stress and UCS (figure 3.27) shows that residual strain increases with axial stress level. This effect becomes more and more important when the axial load approaches the compression strength. It means that a humid pathology of an earthen structure leads to simultaneous degradation of the material stiffness correlated to an increase of the plastic strain. In addition, the plastic straining is dependent on the suction state of the samples evident by the change in slope. The residual strain was higher for samples at lower suction (wetter samples) and vice-versa.

The damage and plasticity behavior as discussed by Champire et al. [9] suggest that the nature of the clay, notably its activity, is a more determining parameter as compared to the content of clay. More active clays experience strong irreversible strains and less damage and vice versa. The soil investigated in this work is considered to be slightly active and thus shows both plasticity (characterized by residual strains) and damage (characterized by stiffness degradation).

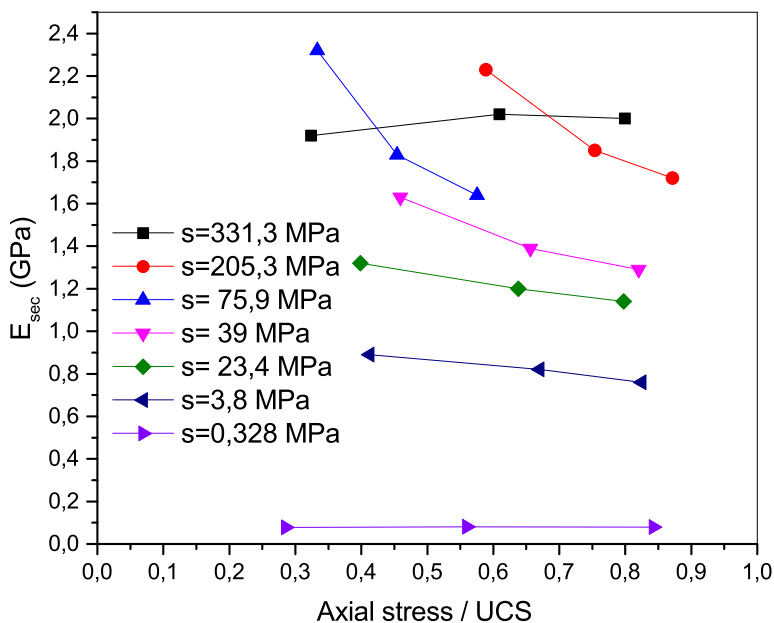


Figure 3.26: Variation of E_{sec} with Axial stress to UCS ratio for different suction conditions

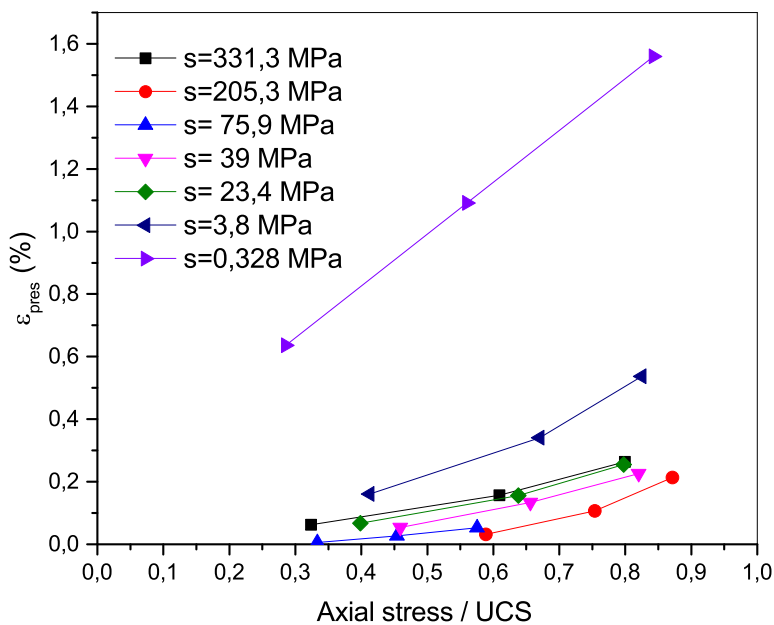


Figure 3.27: Variation of residual strain after unloading with Axial stress to UCS ratio for different suction conditions

3.5.2 Direct shear tests: Influence of suction on shear parameters

In this study, an effort was made to enrich the classical building material approach in which only compressive strength and rigidity of the material are classically determined. It was chosen to investigate mechanical parameters which are more able to describe the strength properties of this unstabilized unsaturated soil: i.e. cohesion (c) and friction angle (ϕ), which are essential parameters in soil mechanics. Very few studies focus on the shear parameters of rammed earth [5][80][81] and none as far as we know, on the influence of hydric conditions on these parameters. So, in the present work, direct shear tests were conducted on different conditioning relative humidities to determine the variation of apparent cohesion (c) and apparent friction angle (ϕ) with suction.

In this regard, 3 series of 21 samples each ($3 \times 21 = 63$ samples) were subjected to direct shear test. The series differ in the normal stress value applied while shearing (table 3.6) varying from 0.139 to 0.556 MPa. These values were chosen as traditional rammed earth wall are loaded by stresses of few hundreds of kPa at the wall base [42]. In each series, there are 21 samples which are tested at 7 different initial suction states from 3.8 MPa to 331.3 MPa as mentioned in table 3.4. For each suction state, 3 samples are tested at different sets of normal stress states, as mentioned in Table 3.6. Direct shear test is a test where only a localized surface is tested mechanically, and the results can thus differ significantly from one test to another. For this reason, it was decided to perform a large number of tests.

Table 3.6: Normal load and stress applied in various series for a particular suction state

Load (kg)	Normal stress (MPa)	Series 1	Series 2	Series 3
5	0.139	o	*	+
10	0.278	o		+
15	0.417	o	*	+
20	0.556		*	

The Direct shear tests were performed on the Casagrande shear box. The rammed earth sample of dimension 60 mm x 60 mm x 30 mm were placed inside a shear box. The shear box contains two independent half boxes, i.e. upper box and lower box, as shown in figure 3.28. The separation between these two boxes is where the shear forces will be applied. The corresponding plane in the sample is called sliding plane. In this test, a constant value of normal force is applied from the top, which remains constant during the test. The sample is further sheared by imposing a constant rate of shear displacement, which applies a horizontal shear force on the sample. The shear force and the corresponding shear stress is noted at failure. The shear stress at failure and normal stress applied is plotted in a graph, and the test is repeated at different values of normal stress.

In order to evaluate the shear parameters of rammed earth, Mohr-Coulomb theory of shear strength was used. According to this theory, the shear strength of a soil

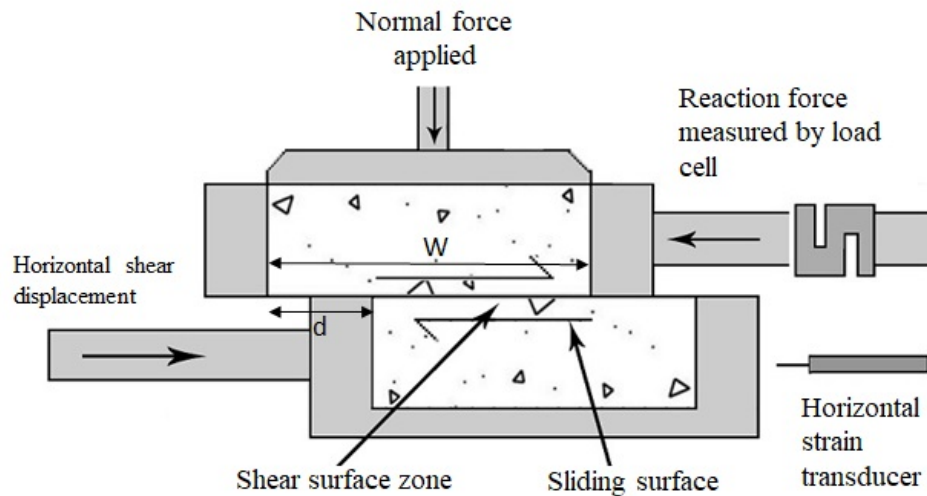


Figure 3.28: Schematic representation of the Casagrande shear box showing the different components (modified from celtest.com)

depends upon:

- Cohesion between particles on the critical plane.
- Angle of internal friction between particles which accounts for interlocking resistance and frictional resistance.
- Normal stress on the critical/Failure plane.

This is to say that:

$$\tau = c + \sigma_n \tan \phi \quad (3.14)$$

where,

ϕ : apparent friction angle of the soil

c: apparent cohesion

σ_n : normal stress on the failure plane

τ : shear strength

This equation is written in total stresses. Upon shearing, the width of the shearing plane changes as the lower box displaces laterally (figure 3.28). Thus, the area of the shearing plane changes and the stress was corrected.

$$\tau = \frac{F}{W(W - d)} \quad (3.15)$$

where, F is the shear force, W is the width of the shear box and d is the displacement measured by the transducer.

Direct shear tests were conducted on the 63 samples at a shear rate of 1 mm/min with the automatic acquisition of both shear force and shear displacement every second. An example of shear stress - shear deformation curve for 4 tests at a conditioning suction state of 153.4 MPa (RH = 32.8%) is shown in figure 3.29. The shear modulus of all 4 samples sheared at different normal stress shows a low discrepancy. This behavior was observed for majority of the direct shear tests. The shear stress - shear deformation curve for all the series is shown in figure B.1, B.2, and B.3 in the Appendix B. Once the shear strength is attained, there was a brittle failure in the samples. In this test, there is no control over the drainage conditions and no mechanism to measure the pore pressure. As it is a quick test, it can be supposed that the condition is undrained. Because the sample are not very saturated, it was assumed that the shear affects the biggest pores (at least at the beginning of the test) and that there is no strong variation of suction.

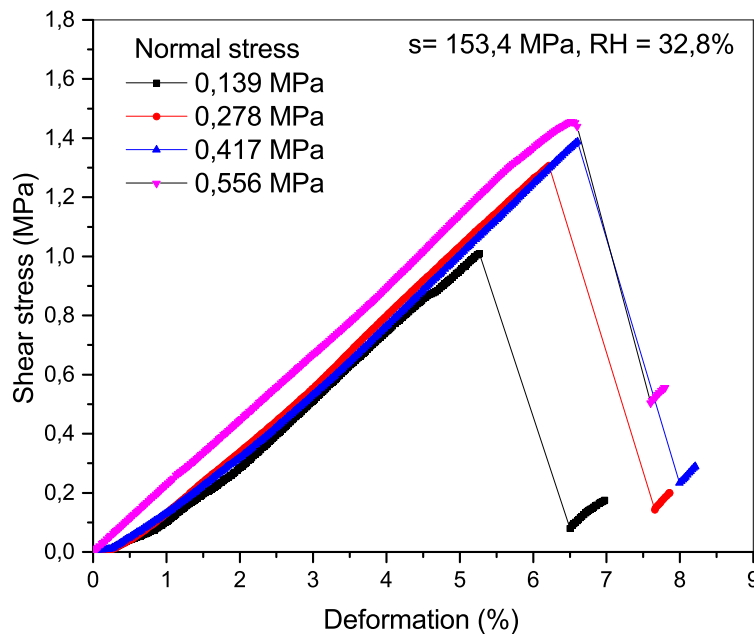


Figure 3.29: Shear stress vs shear deformation curve during the direct shear tests for samples at suction 153.4 MPa, RH = 32.8%

From the values of normal stress imposed on the sample while testing and the corresponding shear strength, linear Mohr-Coulomb envelope was drawn. The Mohr-Coulomb envelope for all the samples of series 1, 2 and 3 are shown in figure 3.30a, b, and c respectively. The values of apparent cohesion and apparent friction angle were evaluated for the different suction conditions from the Mohr-Coulomb theory of shear strength (equation 3.14). The dependency of the shear parameters, i.e. cohesion and friction angle on the conditioning suction conditions, is quite evident. For series 1, the value of apparent cohesion varies from 0.396 MPa to 0.826 MPa as suction increases from 3.8 MPa to 331.3 MPa. The value of apparent friction angle varies significantly from 44.27° to 67.73°. For series 2, the value of cohesion varies from 0.365 MPa to 1.049 MPa

with increase in suction, and apparent friction angle varies between 46.93° to 60.73° . Similarly for series 3, the apparent cohesion varies from 0.341 MPa to 0.835 MPa, and the friction angle varies between 42.77° to 65.71° .

From the results of apparent cohesion and apparent friction angle mentioned before for the 3 series, the average variation of these shear parameters can be plotted. The variation of apparent cohesion and apparent friction angle with suction conditions is shown in figure 3.31a and b respectively, along with error bars expressed as the standard deviation of results of 3 series.

The average value of cohesion of the samples increases from 0.383 MPa to 0.84 MPa with a linear tendency as the suction state changes from 3.8 MPa to 331.3 MPa (figure 3.31a). This behavior is justifiable from the theory of generalized effective stress, as there is an additional capillary cohesion induced by the partial saturation of the earth, which contributes a significant part of the shear strength. In addition, it can be observed that there is a lesser standard deviation in the results for samples conditioned at lower suction states (higher relative humidity). Whereas for the samples conditioned at higher suction states (lower relative humidity), there is a bigger standard deviation in the results. This behavior was also observed in the results of unconfined compressive strength tests (figure 3.23). This can probably be explained by the fact that a dry state of the material induces a fragile behavior. In consequence, the failure is more localized and thus is affected by small defaults in the matter, and its random distribution is responsible for a dispersion of the strength results. On the contrary, wetter samples are ductile, which induces a plastic failure concerning the global mass of the material. In this case, defaults have less influence, and the results present a lower discrepancy.

In addition, there is also a significant variation observed for the average apparent friction angle which varies from 43° to 63° with a non-linear tendency (the effect tends to stabilize from 100 MPa of suction) when suction varies from 3.8 MPa to 331.3 MPa (figure 3.31b). Bigger standard deviation for samples conditioned at higher suction state and vice-versa was also observed in the results of apparent friction angle.

The variation of shear strength with suction at constant value of normal stresses of 0.139 MPa, 0.278 MPa, and 0.417 MPa, and 0.556 MPa are shown in figure 3.32a, b, c, and d respectively. It is clear that the shear strength gradually increases with suction at a constant normal stress. This observation is true except for the variation of shear strength with suction at constant normal stress of 0.278 MPa (figure 3.32b). It can be seen that the shear strength at 153.4 MPa suction state is higher than 205.3 MPa and 331.3 MPa suction state. The shear strength, in this case, is decreasing with increase in suction.

Also, it can be observed that the rate of increase of shear strength with suction is very high at the lower suction values, and this rate tends to decrease as we approach higher suction values. The explanation of this behavior can be found in literature [82][83][84]. Vanapalli et al. 1996 [82] compared the shear strength behavior with the soil water retention curve. There is a linear increase of shear strength up to the air-entry value

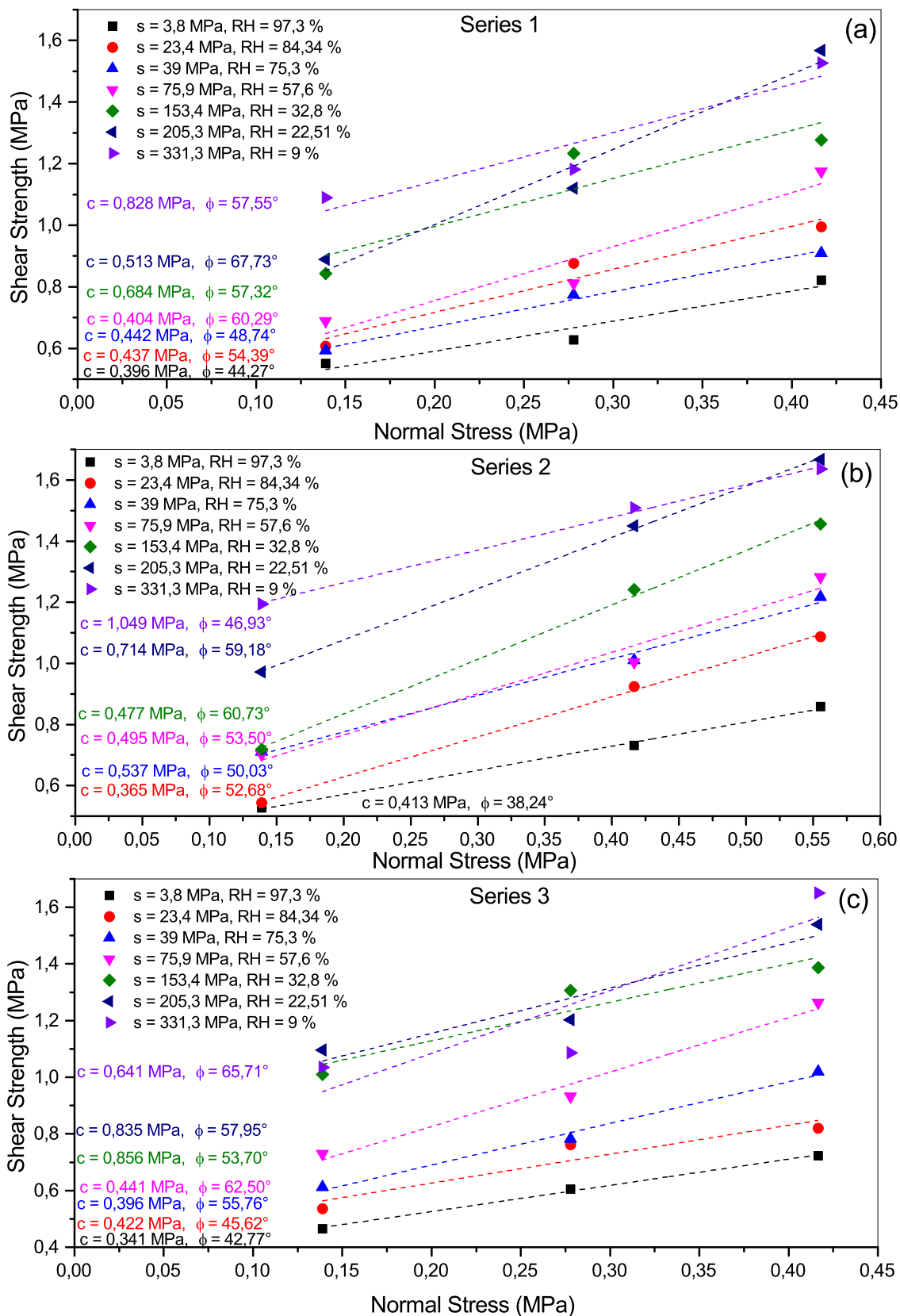
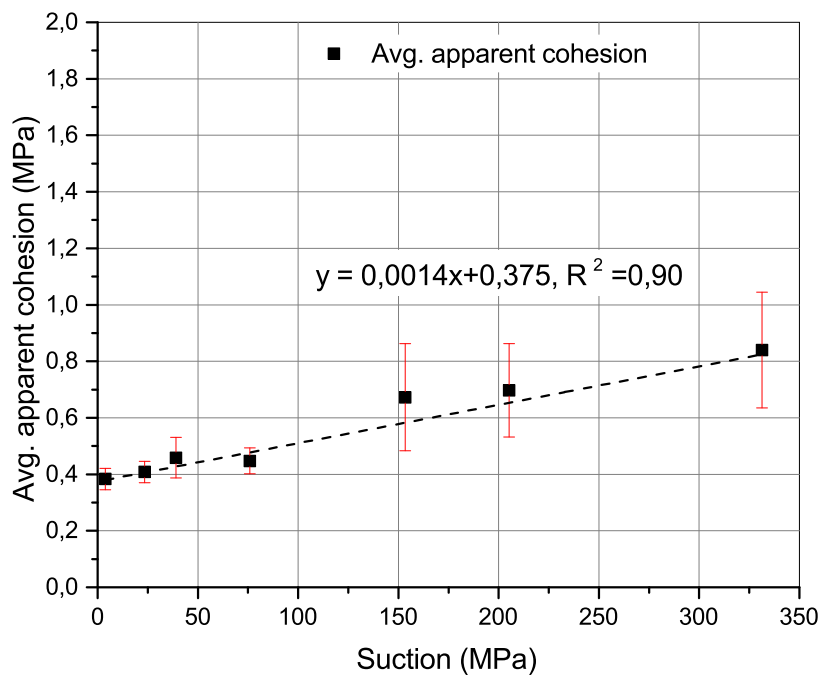
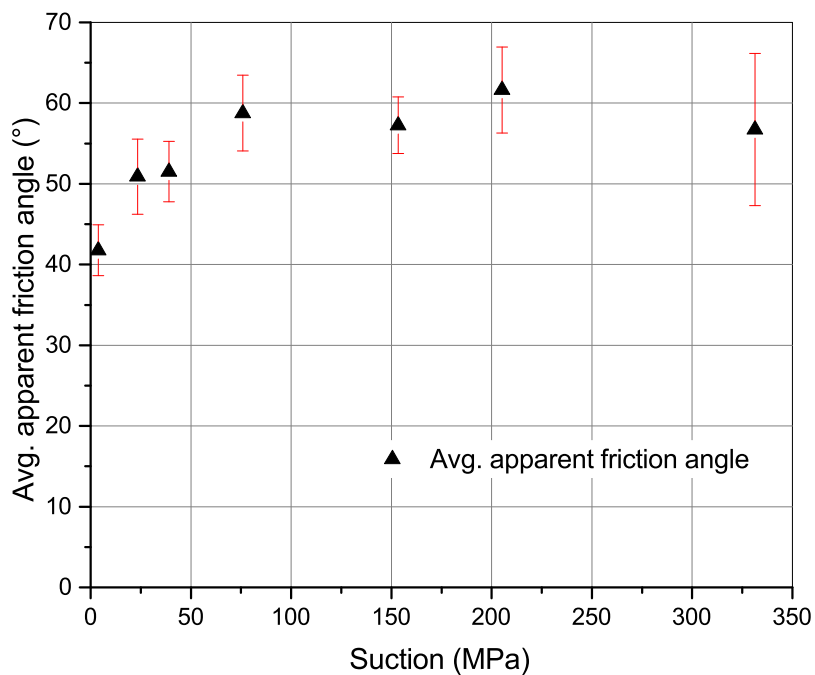


Figure 3.30: Mohr-Coulomb failure envelope for samples conditioned at different suction conditions for series 1,2, and 3



(a)



(b)

Figure 3.31: Variation of apparent cohesion (a) and friction angle (b) from direct shear tests shown with error bars from results of 3 series of tests

of suction. Further, there is a non-linear increase of shear strength up to the residual suction value and then depending on the soil, the strength may increase, decrease, or remain constant upon the increase in suction. On the one hand, for sand and silt water content at residual condition is very low, and it may not transmit suction effectively. Thus, even a substantial increase in suction will not increase shear strength. On the other hand, clay has well defined residual point and even at very high value of suction, there exists considerable water, which helps in effective transmission of suction, which leads to increase in strength. Since the soil in this study is predominantly sand and silt, there is a non-linear increase in shear strength, and at higher values of suction, the shear strength reaches a plateau.

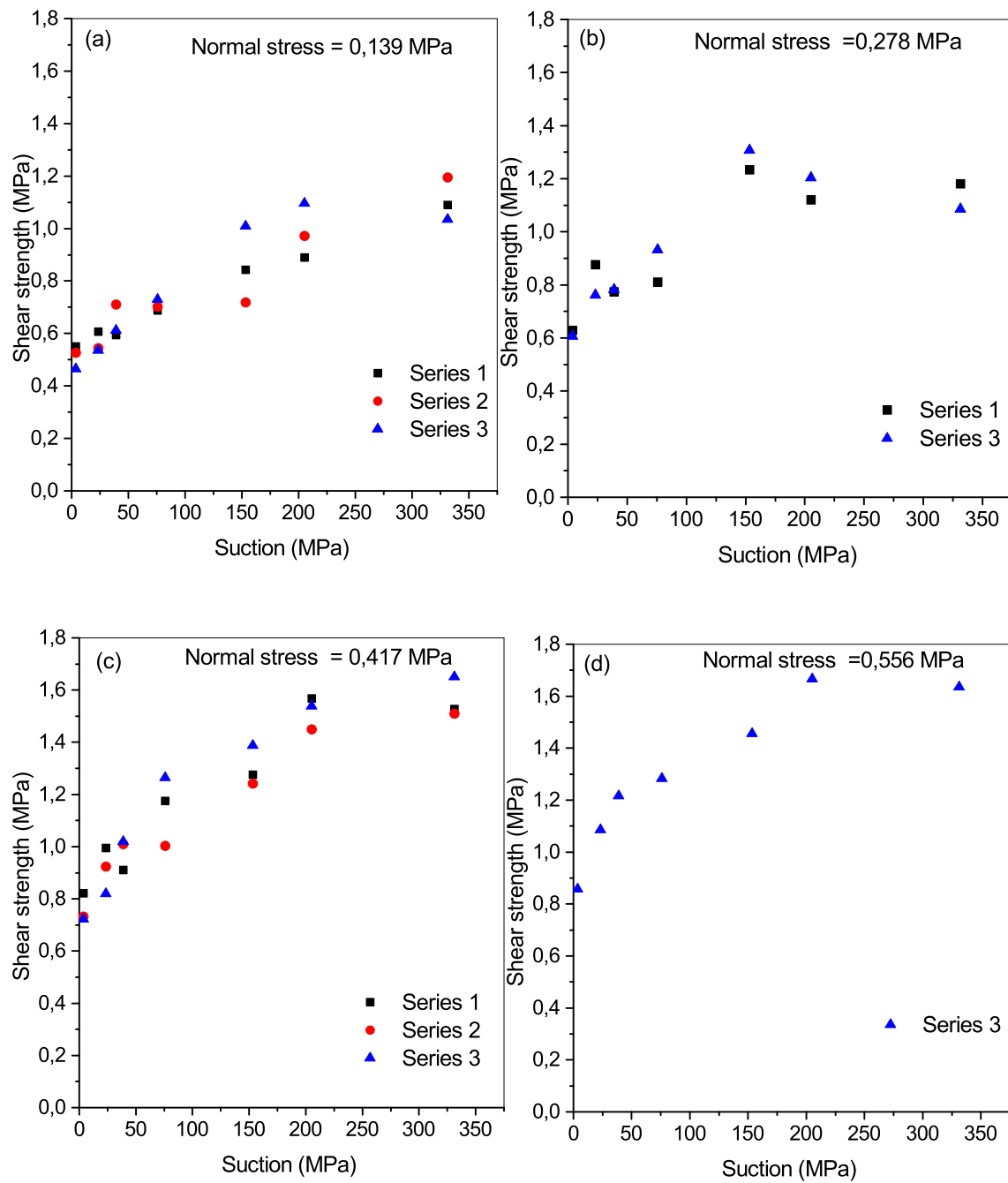


Figure 3.32: Variation of shear strength with suction at a constant normal stress of 0.139 MPa (a), 0.278 MPa (b), and 0.417 MPa (c), and 0.556 MPa (d)

3.5.3 Unsaturated triaxial tests

In order to complete the results of the shear testing of rammed earth, unconsolidated undrained (UU) triaxial tests on unsaturated samples of rammed earth were performed. These tests are further labelled as unsaturated triaxial tests due to the following reasons:

- Firstly, the samples studied here are very dense since the compaction pressure (5 MPa) is higher than the confining stress applied during the triaxial test (0.2-1.5 MPa). Thus the term unconsolidated state is not suitable for the samples; on the contrary, the state of the earth can be described as ‘overconsolidated’.
- Secondly, the maximum degree of saturation at the lowest value of suction studied is around 30%. Thus having drained or undrained conditions might not have a significant effect on the results of the test.

Tests were performed on 21 samples conditioned at 7 different suction states mentioned in table 3.4. For each suction state, 3 samples were tested at 3 different confining pressures (σ_3), i.e. 0.2 MPa, 1 MPa and 1.5 MPa. These values of σ_3 were chosen to plot the Mohr-Coulomb failure envelope at a higher range of normal stress as compared to the direct shear test to obtain the failure envelope at higher normal stresses. The triaxial test has various advantages as compared to direct shear test:

- There is no pre-determined failure surface, which was the case in direct shear tests. The loading thus affects the bulk sample instead of a single surface. The failure plane in the triaxial test is the weakest plane.
- Mohr circles can be drawn at failure conditions.
- Stress distribution on the failure surface is more uniform.
- There is complete control over the drainage conditions, and there is a mechanism to measure the pore pressure during the test. Although during the unsaturated triaxial test, the pore pressure was not measured.

For these reasons, the triaxial test is considered more representative of soil behavior.

Experimental setup

The experimental setup for the triaxial test along with its components is shown in the figure 3.33. The functions of the various triaxial components is described as follows:

- Triaxial Cell: It contains the specimen and cell fluid
- Pedestal and top cap: They guarantee the sample anchorage and drainage ports.

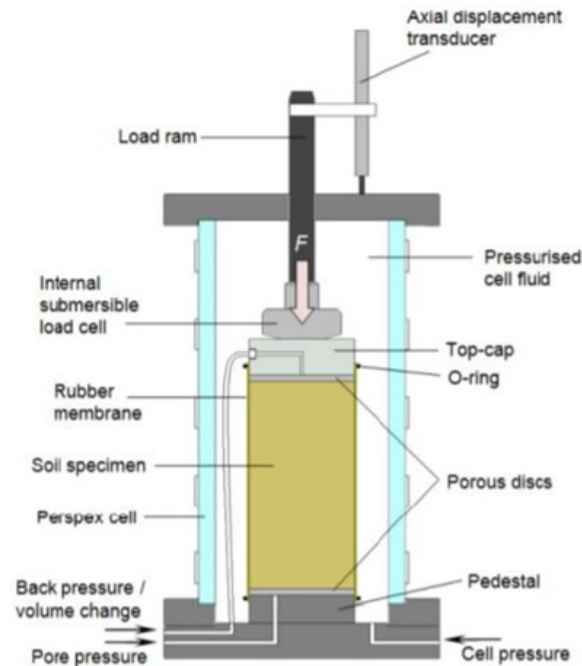


Figure 3.33: The experimental setup and the various components of triaxial test

- Rubber membrane, O-rings: The soil sample is first inserted into the rubber membrane, and O-rings are placed over the membrane to seal the rammed earth sample from the cell fluid which permits the effective stress to be applied.
- Cell fluid inlet / Volume controller: Pressure-meter connected to the cell pressure inlet exerts confining stress to the specimen by pressuring the cell fluid.
- Back Pressure / Volume controller and pore pressure transducer: Pressure-meter is connected to the inlet which exerts the pore/back pressure on the rammed earth sample and measures the variation of volume. Pore pressure transducer can record the pore pressure in the sample during the test. Thus it is possible to either control or measure the pore pressure.
- Velocity controlled loading frame: This helps in shearing the sample by applying axial displacement at a constant rate.
- Internal submersible load cell: It helps in recording the axial force applied to the sample during the shearing process.
- Axial displacement transducer: It records the variation of height of the sample and thus the axial strain.

The unsaturated triaxial test is carried out in two stages:

1. Confining pressure stage: In this stage, an all-around confining pressure (σ_3) was applied using the pressure-meter connected to the cell pressure valve. Three different confining pressures of 0.2 MPa, 1 MPa, and 1.5 MPa were applied to the three

samples tested for each initial suction condition. The test in this stage is unconsolidated, and thus the back pressure drainage valve was closed and the expulsion of pore water is not permitted. However, it can be underlined that the sample is already very dense (compacted at 5 MPa) so that the consolidation phase would have probably not change the state of the earth.

2. Deviatoric stage / Shear stage: The cell pressure was kept constant and additional axial stress is applied which is called deviator stress ($q = \sigma_1 - \sigma_3$). Deviatoric stress was applied by the compression of the sample at a constant rate of axial displacement of 0.1428 mm/min [85]. The deviator stress increases gradually until the soil fails in shear. Since the test is undrained in this stage as well, the drainage valves were closed. However, since the degree of saturation is lower than 30%, the drainage conditions might not impact the results.

Figure 3.34 shows the evolution of deviator stress - axial strain behavior for the three samples conditioned at suction state of 23.4 MPa (84.34% RH). These three samples were tested at different confining stress (σ_3) of 0.2 MPa, 1 MPa, and 1.5 MPa. With the increase of confining stress, the shear strength of the soil consistently increases. From these results, the value of the axial stress at failure (σ_{1f}) can be computed, which was used to plot the Mohr circles at failure (figure 3.35). The apparent value of cohesion and friction angle was computed from the linear envelope of the Mohr Circles (Mohr-Coulomb criterion, see equation 3.14).

Figure 3.36 shows the comparison of the variation of deviator stress and axial strain for samples conditioned at 3.8 MPa (97.3% RH) and 331.3 MPa (9% RH) suction states. At a lower suction state, when the sample is wetter, the behavior is more ductile in nature. The axial strain at failure for samples at 3.8 MPa suction varies from around 3% to 11% at different confining stresses. On the other hand, the axial strain at failure for samples at 331.3 MPa suction varies from around 1.5% to 4%. There is a gradual transition from ductile behavior at lower suction values to a fragile behavior at high suction values. Because of the presence of clay, the material becomes ductile when wetter. This transition of behavior type is more or less significant depending on the clay proportion, and clay nature [19] [9]. Soils having clay with higher activity experiences strong irreversible strains and a ductile failure at high suction values. The transition from ductile to brittle failure can be seen in figure C.1 in Appendix C. In addition, samples tested at a lower value of confining stress behaves more brittle than samples tested at higher confining pressure for the same suction state.

Using the three Mohr circles at each suction state and plotting Mohr-Coulomb envelope, apparent values of cohesion (c) and friction angle (ϕ) were determined at all suction states. The qualitative variation of c with suction, as shown in figure 3.37a is similar to the one observed in the direct shear test (figure 3.31a). The apparent cohesion value increases from 0.5 MPa to 1.8 MPa with suction. The rate of increase of cohesion is higher in the beginning at lower suction values. This rate of increase of cohesion decreases

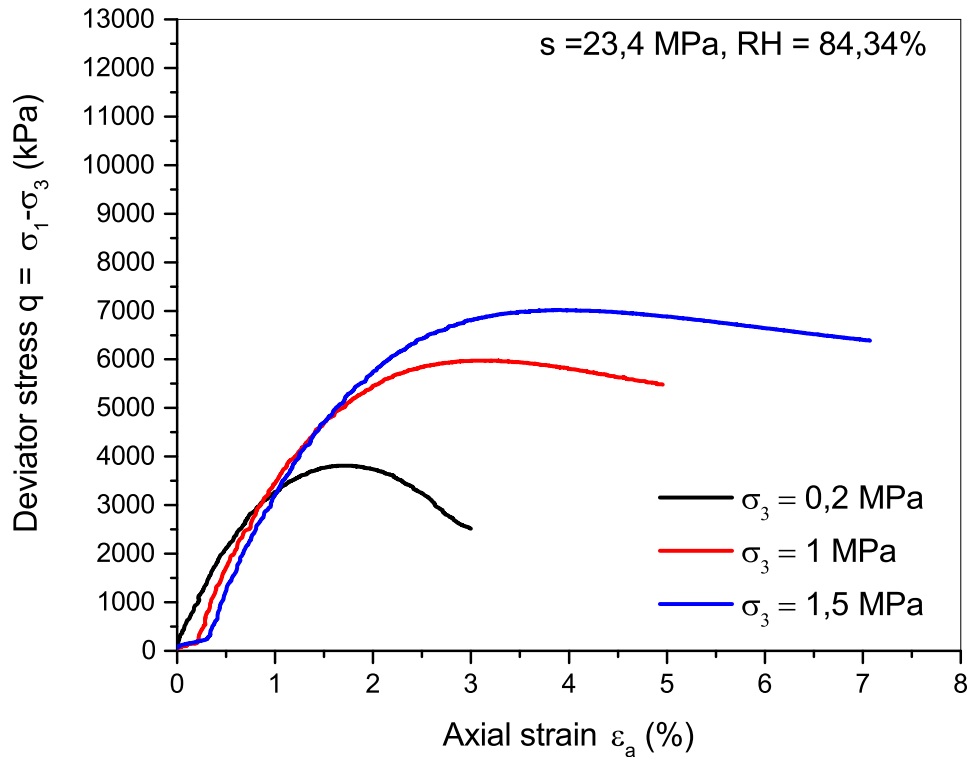


Figure 3.34: Variation of deviator stress versus axial strain during shear stage of triaxial test for samples conditioned at 23.4 MPa suction and 84.34% RH

with suction, and the cohesion increases at a slower rate at higher values of suction. This is due to the fact that the additional suction-induced cohesion increases with suction, but there is a limit to this contribution. At higher values of suction, the saturation degree of sample is lower. So, although the suction increases, it is acting on a lower proportion of water.

On the other hand, there is no significant alteration in the friction angle. The value of friction angle varies between 31° and 37° with a greater variation for low suction and almost no variation from 50 MPa (figure 3.37b). In addition, it appears that values of c and ϕ at a particular suction state are different for direct shear tests (done at lower normal stress) and unsaturated triaxial tests (done at higher normal stress). This behavior indicates that there is non-linearity in the failure envelope ($\tau - \sigma_n$ plane). This non-linearity will be discussed in the further section.

Finally, figure 3.38 shows all the results obtained from UCS, DST, and unsaturated triaxial test for 7 different suction states in $\tau - \sigma_n$ plane. It includes the Mohr circles drawn at failure for the UCS and unsaturated tests and the linear Mohr-Coulomb failure envelope from direct shear tests. It gives a global idea of the various tests performed and makes it possible to plot the failure envelope at a higher range of normal stress. It can be observed that the linear Mohr-Coulomb envelope drawn from the direct shear tests

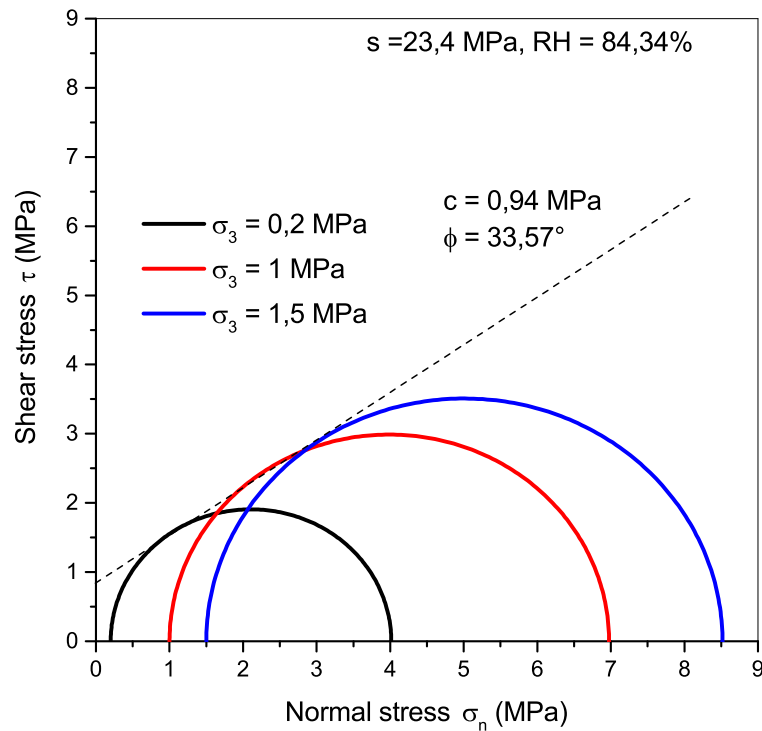
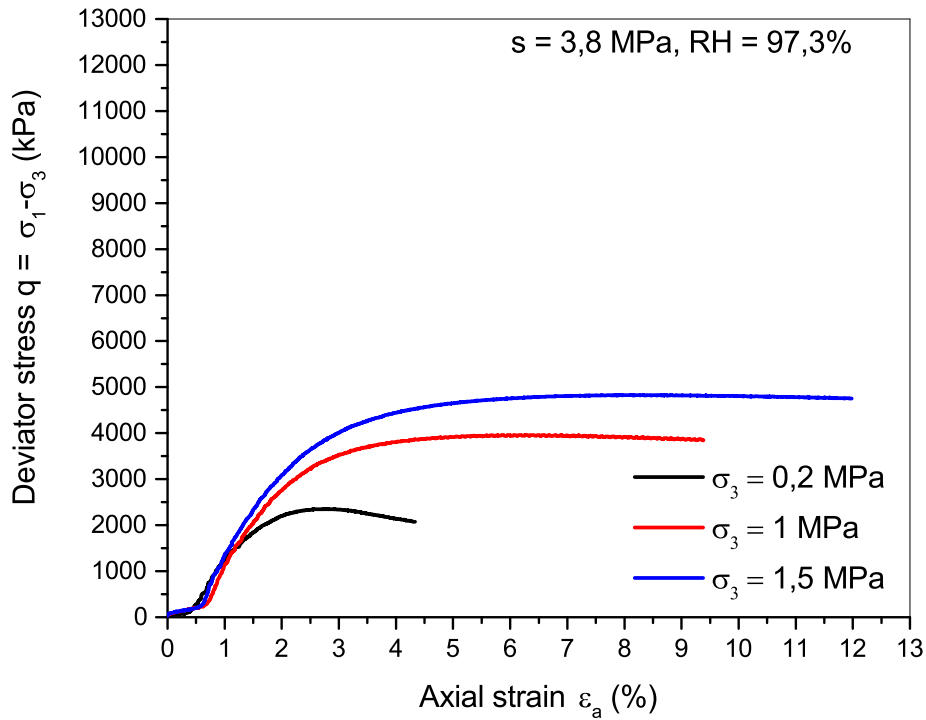
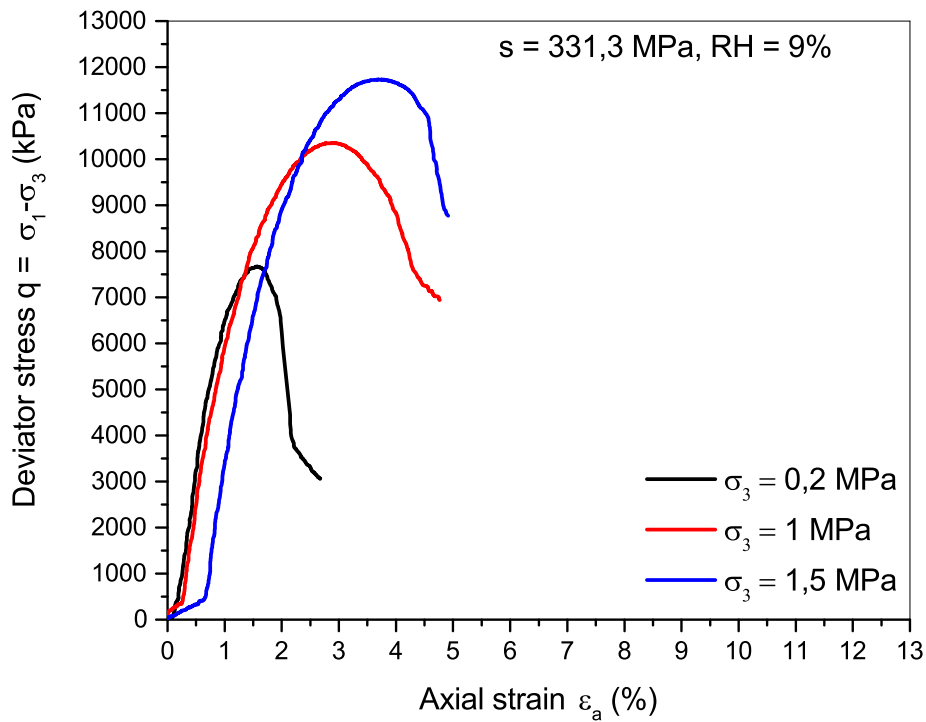


Figure 3.35: Mohr circles at failure for samples conditioned at 23.4 MPa suction and 84.34% RH

fits the results of all the UCS tests and unsaturated triaxial tests carried out at lower confining stress of 0.2 MPa. It is to be noted that the results of UCS tests carried out at suction of 153.4 MPa (32.8% RH) are excluded since the RH box in which they were conditioned was not saturated, as mentioned in the previous section.

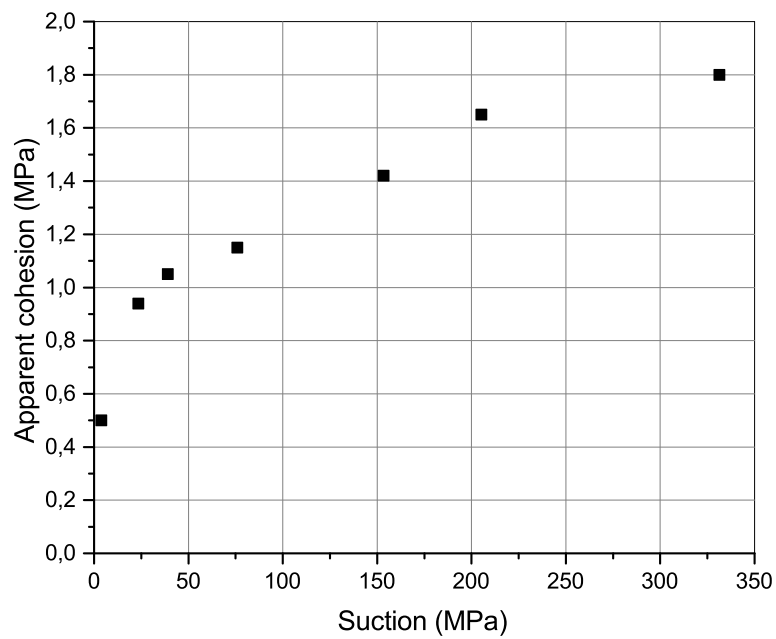


(a)

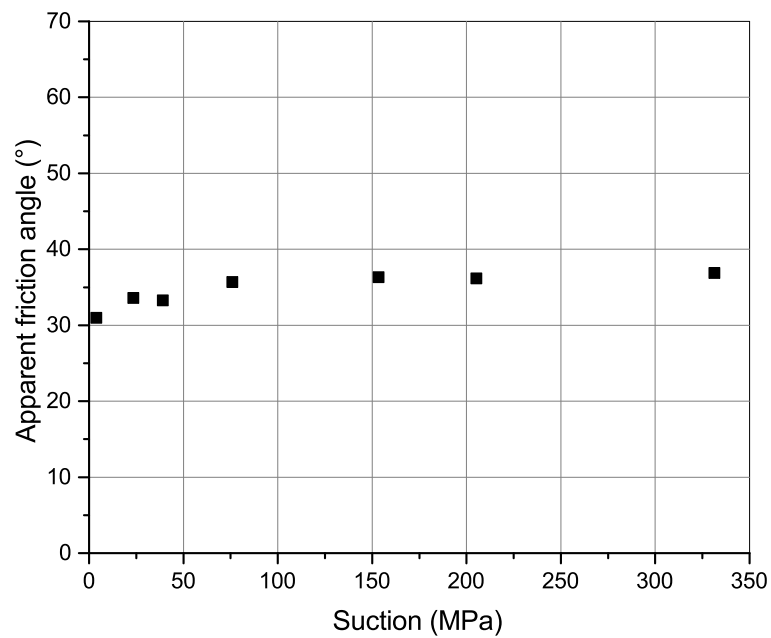


(b)

Figure 3.36: Comparison of the variation of deviator stress with axial strain for samples conditioned at suction values of 3.8 MPa (a) and 331.3 MPa (b)



(a)



(b)

Figure 3.37: Variation of apparent cohesion (a) and apparent friction angle (b) with suction states determined from the unsaturated triaxial tests

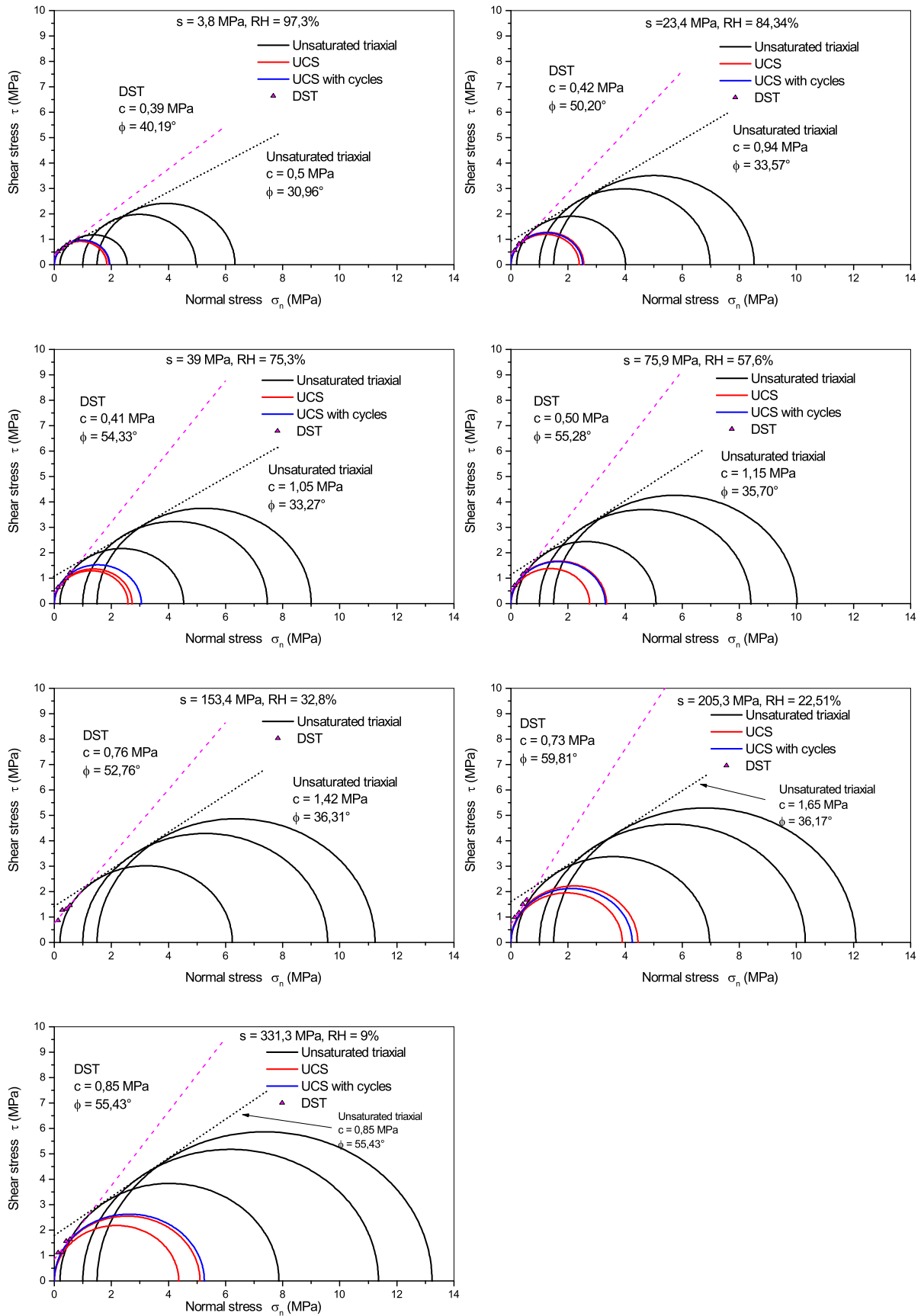


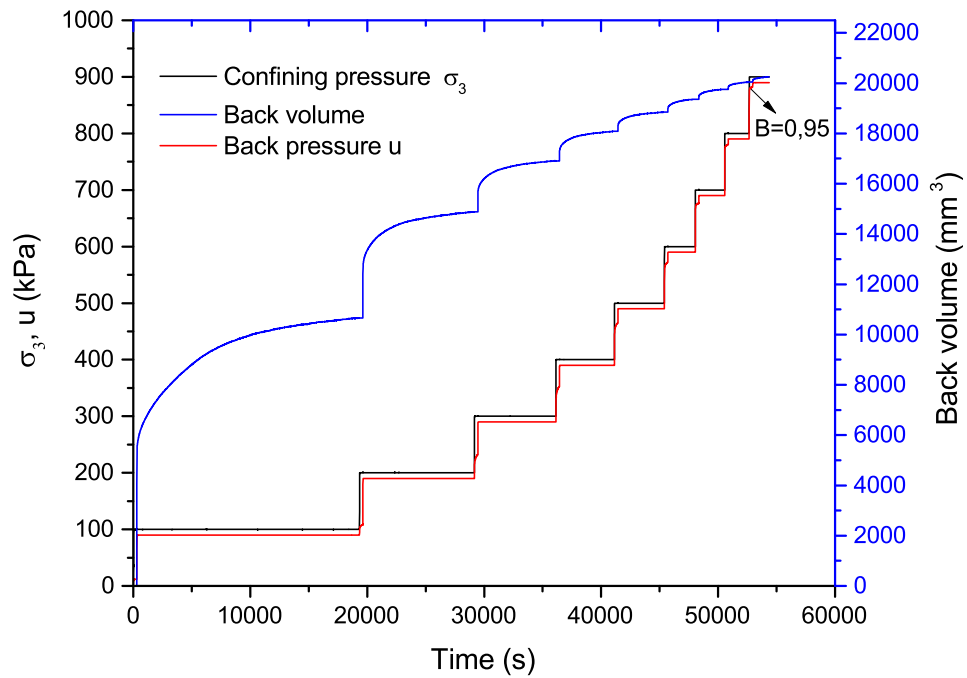
Figure 3.38: Results of UCS, DST, and unsaturated triaxial test in $\tau - \sigma_n$ plane for all suction states

3.5.4 Intrinsic shear parameters

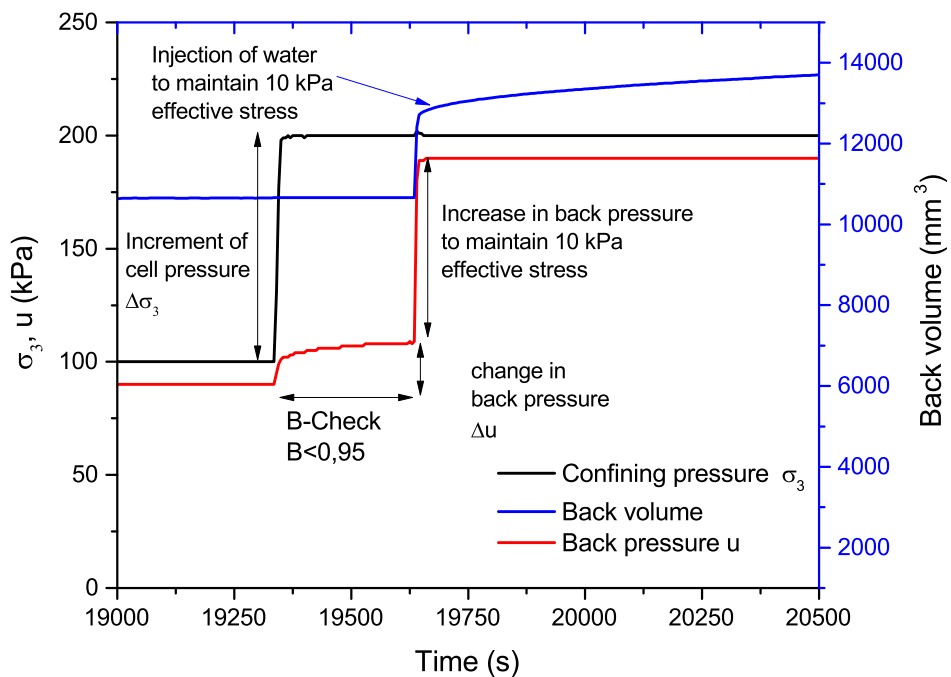
In order to explain the effect of hydric state on the shear parameters, it is necessary to compare apparent parameters and intrinsic parameters i.e. intrinsic cohesion (c') and intrinsic friction angle (ϕ'). The intrinsic parameters are determined for saturated conditions and are independent of suction. In this regard, Consolidated Undrained (CU) saturated triaxial tests were carried out at 4 different effective confining pressures, i.e. $\sigma'_3 = 100$ kPa, 200 kPa, 300 KPa, and 1500 kPa along with measurement of pore water pressure during the test. The tests were conducted in the following stages, and the procedure is outlined as follows:

1. Saturation stage: Since the rammed earth sample is going to be consolidated during the confining pressure stage, it was necessary to saturate the samples before. Rammed earth samples after double compaction can be directly used for performing saturated triaxial tests as the hydric conditions of the samples before the testing was not relevant as saturated conditions are required. Rammed earth sample was inserted into the triaxial cell after the sample is covered with the rubber membrane fixed with O-rings. The triaxial cell is filled with distilled water, and the pressure-meters for cell pressure and back pressure are connected. Before the beginning of saturation stage, it was made sure that air bubbles were removed from all the connecting pipes and the pressure-meters connected for cell pressure and pore water pressure. The method of saturation used here was stepped saturation. In this method, cell pressure increments of 100 kPa were applied, and the evolution of pore water pressure was monitored. During this time, the saturation of the sample was monitored by the value of Skempton's parameter $B = \Delta u / \Delta \sigma_3$. If the value of Skempton's parameter B was less than 0.95, it signifies that the sample is unsaturated. This phase during the test is called B-check. If the sample is unsaturated, the pressure meter for back pressure injects water to increase the pore water pressure (figure 3.39a). This was done to maintain effective stress of 10 kPa. This low value of effective stress was chosen not to affect the soil structure during saturation. The injection of back volume to maintain the effective stress is stopped when the volume change is less than 10 mm^3 for 5 min.

The zoomed-in view of the B-check phase is shown in figure 3.39b. It shows the increment of cell pressure by 100 kPa and the corresponding change in back pressure. The B-value is evaluated, and if it is less than 0.95, the back pressure is increased, and water is injected to maintain 10 kPa of effective stress. Further, the saturation of the sample was rechecked again with the same procedure by increasing the cell pressure by intervals of 100 kPa and monitoring the change in pore water pressure to evaluate the parameter B until reaching saturation (figure 3.39a). Typically, $B \geq 0.95$ confirms full saturation of the sample. B value of 1 represents that for a particular change of cell pressure, the pore pressure changes an equal amount. This means that all the pores are filled with water, and the sample is saturated.



(a)



(b)

Figure 3.39: Variation of confining stress, back pressure, and back volume during the saturation phase for sample (a) and the zoomed-in view of B-check during saturation (b)

2. Cell pressure / Confining pressure stage: After the saturation phase, the confining pressure was 800 or 900 kPa. In this stage, an all around confining pressure (σ'_3) was applied using the pressure-meter connected to the cell pressure valve. An effective value of confining stress $\sigma'_3 = 100$ kPa, 200 kPa, 300 kPa, and 1500 kPa was applied to the samples. Since it is a CU triaxial test, the valve connecting the back pressure was open, and consolidation was allowed to take place due to the effective confining stress. The consolidation phase was supposed to finish when the change in the back volume was less than 10 mm^3 for 5 min. Figure 3.40 shows the variation of back volume with the square root of time for the sample subjected to 300 kPa of effective confining stress.

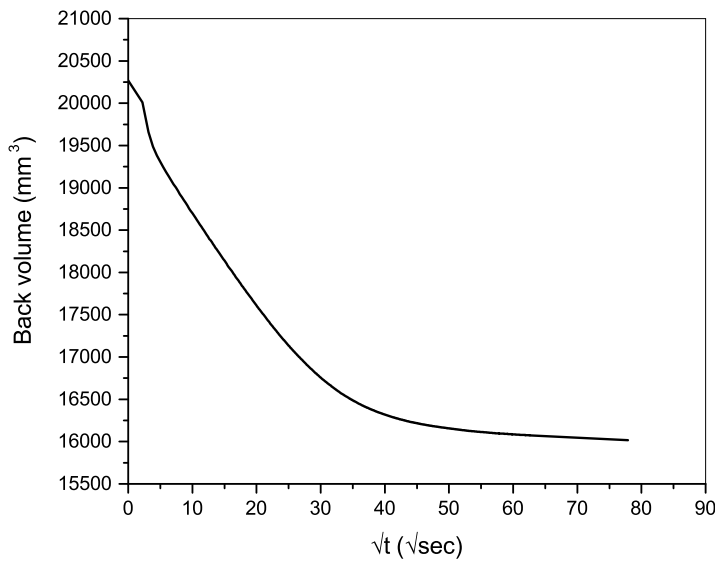


Figure 3.40: Variation of back volume with the square root of time during the consolidation phase of the CU triaxial test

3. Deviator stage / Shear stage: The cell pressure was kept constant and additional axial stress is applied which is called deviator stress ($q = \sigma_1 - \sigma_3$). Deviatoric stress was applied by the compression of the sample at a constant rate determined from the French Norm NF P94-074 [86] for performing Consolidated undrained triaxial test with measurement of pore pressure (CU+u). According to the norm, the rate of axial displacement should not exceed the maximum speed evaluated by the following expression:

$$V_{max} = \frac{H_o \epsilon_f}{at_{100}} \quad (3.16)$$

where,

a: is a coefficient determined based on the drainage conditions during the consolidation phase. For drainage at top and bottom without any lateral drainage $a = 2.1$
 ϵ_f : is the deformation at the presumed rupture. In the absence of this information, it is recommended to use a value of 3% for over-consolidated soils.

t_{100} : is the value of consolidation time. The minimum value recommended is 10 minutes.

H_o : is the initial height of the specimen = 100 mm

The value of rate of axial displacement determined from this expression was 0.1428 mm/s, and the sample was sheared at this rate. The deviator stress increases gradually until the soil fails in shear. Since the test is undrained in this stage, the drainage valves were closed.

In the triaxial conditions, the mean effective stress (p') and deviatoric stress (q) are defined as:

$$p' = \frac{\sigma'_1 + 2\sigma'_3}{3} \quad (3.17)$$

$$q = (\sigma'_1 - \sigma'_3) \quad (3.18)$$

A highly ductile/plastic failure was observed for all samples which can be seen from figure 3.41, where the axial strain during the shear phase was in the range of more than 20%. As the sample is sheared, the deviator stress increases until reaching a plateau and becomes constant even though the axial strain keeps increasing. No cracking or failure plane was observed as the sample kept on dilating, and the radial strain was increasing. The variation of the pore water pressure is shown in figure 3.41b. It was observed that pore water pressure increases in the initial phase of loading and then decreases. This is due to the fact that upon shearing the sample exhibits an initial phase of contraction followed by a dilatant phase. The transition between these two phases occurs nearly around the same axial strain (1%-1.5%) for the samples sheared at different effective confining stress.

According to ASTM D 4767-95 [87], the failure point is defined as the state of maximum effective stress obliquity i.e., maximum value of σ'_1/σ'_3 . The failure points from this criterion has been shown in figure 3.42. Using these failure points, a linear failure envelope was obtained in p' - q plane. The slope and intercept of this failure envelope were determined, and the effective shear parameters c' and ϕ' were evaluated.

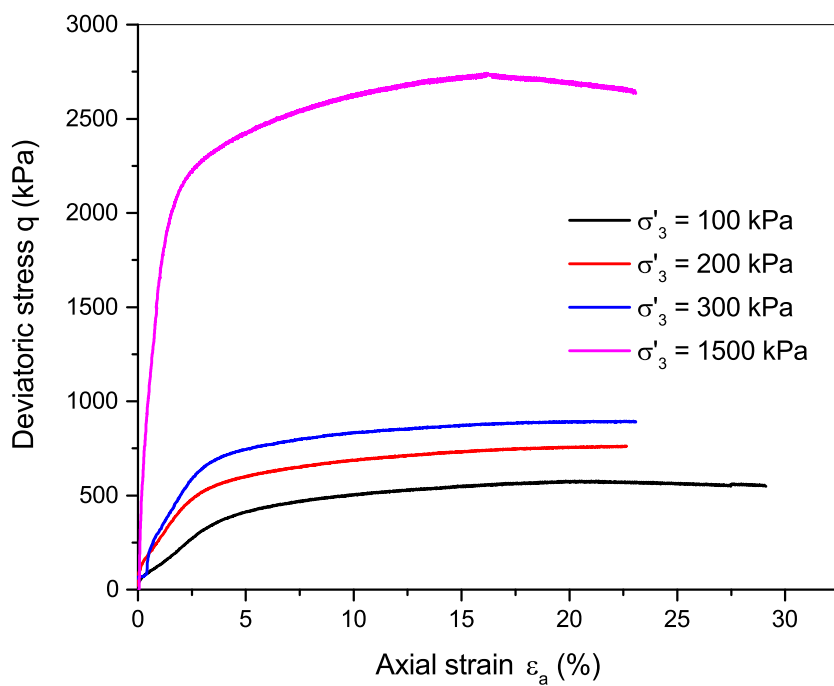
As the failure surface in p' - q and $\tau - \sigma$ plane represent the same failure state, the geometrical relation between these two allow us to compute the intrinsic parameters. The failure criterion in p' - q plane is defined as:

$$q = k + Mp' \quad (3.19)$$

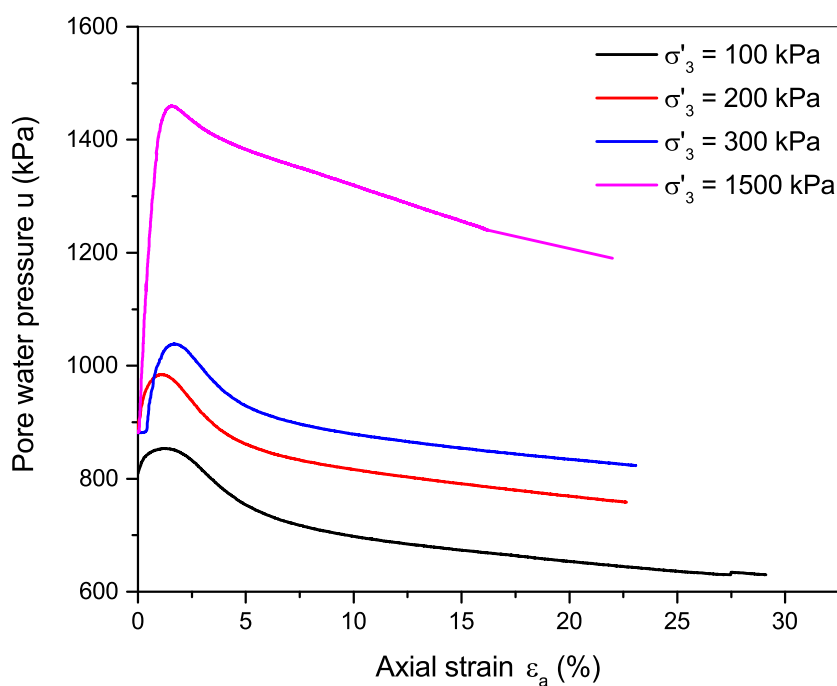
where,

$$M = \frac{6\sin\phi'}{3 - \sin\phi'} \quad (3.20)$$

$$k = \frac{Mc'}{\tan\phi'} \quad (3.21)$$



(a)



(b)

Figure 3.41: Variation of deviatoric stress (a) and pore water pressure (b) for 4 saturated samples at $\sigma'_3 = 100$ kPa, 200 kPa, 300 kPa, and 1500 kPa in the shear phase

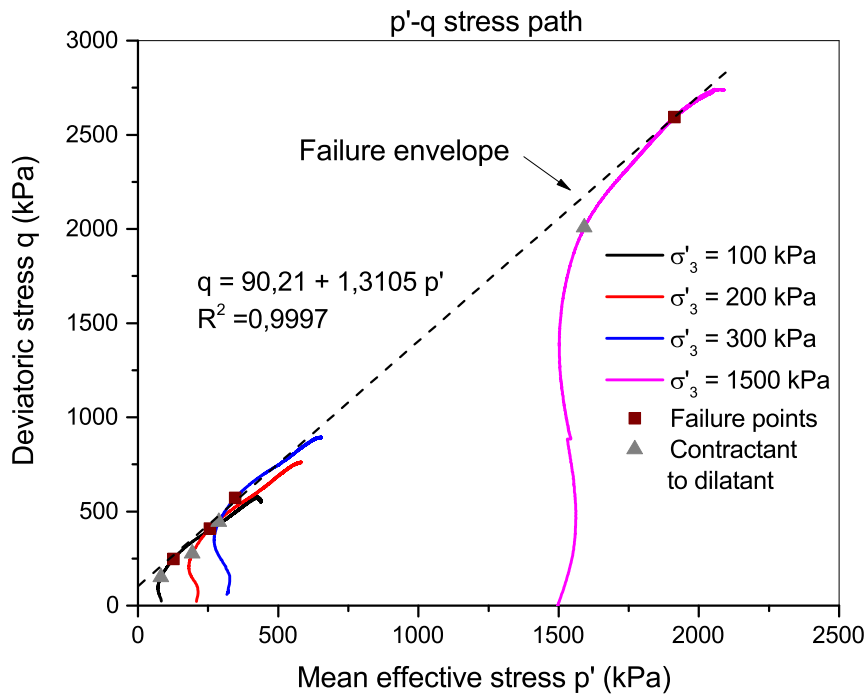


Figure 3.42: Failure envelope from 4 consolidated undrained triaxial test to determine intrinsic shear parameters

From these equations, the effective parameters were evaluated as $c' = 43.91$ kPa and $\phi' = 32.53^\circ$, which are good from a soil mechanics point of view. These value obtained are similar to Gerard et al. 2015 [14], which is justifiable as the particle size distribution of both soil used is similar.

It is interesting to note that, the apparent cohesion at different suction state from unsaturated triaxial is significantly higher than the intrinsic cohesion (figure 3.37). However, the apparent friction angle values are quite similar to the intrinsic friction angle. This supports the fact that, with an increase in suction, the capillary induced cohesion increases and contributes a significant part to the strength. However, the part of shear strength that is due to friction between the particles does not vary so much as it is mostly dependent on the compaction state. Since the compaction state for both these tests was similar, the value of apparent friction angle was comparable.

The comparison between the intrinsic shear parameters from saturated triaxial tests and apparent shear parameters from direct shear test (figure 3.31) shows that apparent cohesion (c) is significantly higher than intrinsic cohesion (c'), which is due to the additional suction induced cohesion. Also, apparent friction angle (ϕ) is also higher than intrinsic friction angle (ϕ'). This was due to the fact that ϕ is evaluated in direct shear test at a normal stress range of 0.139 - 0.556 MPa. Due to the non-linearity in the Mohr-Coulomb failure envelope, the value of ϕ evaluated from the initial part of the curve is significantly higher, which was observed at all the suction states.

3.6 Towards constitutive modeling

Linear Mohr-Coulomb failure criterion is the most common criterion for modeling the behavior of rammed earth when considering plasticity and was used in different research [6][88][89] [54][42]. However, this model has various limitations. For an over-consolidated soil, the failure envelope is not a straight line, but a curved line which is concave towards the normal stress axis [90][91][92]. Also, in the unsaturated samples due to higher confining stresses, the degree of saturation can increase, leading to change in consistency of the sample and affecting the behavior. The linear Mohr-Coulomb failure envelope is not totally suitable in the case of rammed earth within the range of normal stress considered. In addition, it is essential to incorporate the role of suction, for instance, by generalizing the failure criterion as initially proposed by Gerard et al. 2015 [14].

To take into account the non-linearity of the failure envelope, we have used modified Mohr-Coulomb criterion according to Shen et al. [93], in which cohesion c and friction angle ϕ are described as a function of normal stress (σ_n). The expression for the shear strength remains the same, whereas c and ϕ are dependent on normal stress. The following functions were used to describe the shear parameters.

$$\phi = \phi_0 \left(1 - \sqrt{\frac{\sigma_n}{2\sigma_c}}\right) \quad (3.22)$$

$$c = c_0 + (\sigma_c - c_0) \frac{\sigma_n}{2\sigma_c} \quad (3.23)$$

where,

c_0 : apparent cohesion at low confining stress at a particular suction state,

ϕ_0 : apparent friction angle at low confining stress at a particular suction state,

σ_c : the critical confining pressure which is defined as the normal stress after which the shear strength does not increase.

The non-linear Mohr-Coulomb failure envelope was plotted from Mohr circles for UCS and unsaturated triaxial tests. The parameter σ_c was adjusted for each suction state to fit the data and is mentioned in table 3.7. From figure 3.43, the failure envelope is plotted for $s = 205.2$ MPa, $RH = 22.51\%$, parameter $\sigma_c = 6.5$ MPa is chosen to fit the data set. The values of c_0 and ϕ_0 are used from the direct shear tests.

Table 3.7: Values of the parameter σ_c corresponding to each suction state

Suction (MPa)	331.3	205.3	153.4	75.9	39	23.4	3.8
σ_c (MPa)	8.35	6.5	6.4	5.3	4.8	4.7	2.5

In figure 3.44, the failure envelope for all the suction states is plotted. Here, we can observe the evolution of the failure envelopes with both normal stress and suction. The failure envelope from the saturated triaxial test has also been shown to observe the influence of the suction state on the failure envelope compared to the saturated state.

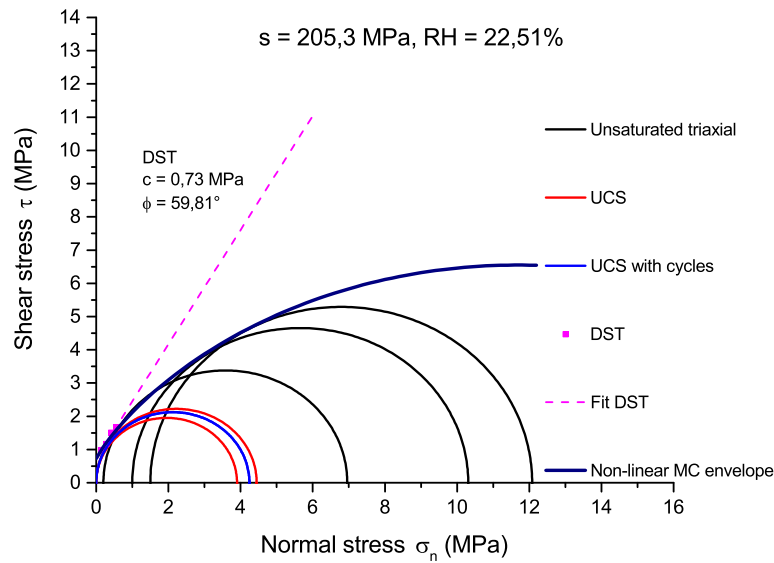


Figure 3.43: Non-linear failure envelope plotted for $s = 205.2 \text{ MPa}$ and $RH = 22.51\%$ using the results of UCS, DST and unsaturated triaxial test

This influence is represented by the vertical shift between the saturated triaxial criterion (in this case suction is null) and unsaturated triaxial ones. Saturated triaxial test give 4 points on the plot that tends to show a linear interpolation, which differs from the unsaturated failure envelope in this range of normal stress.

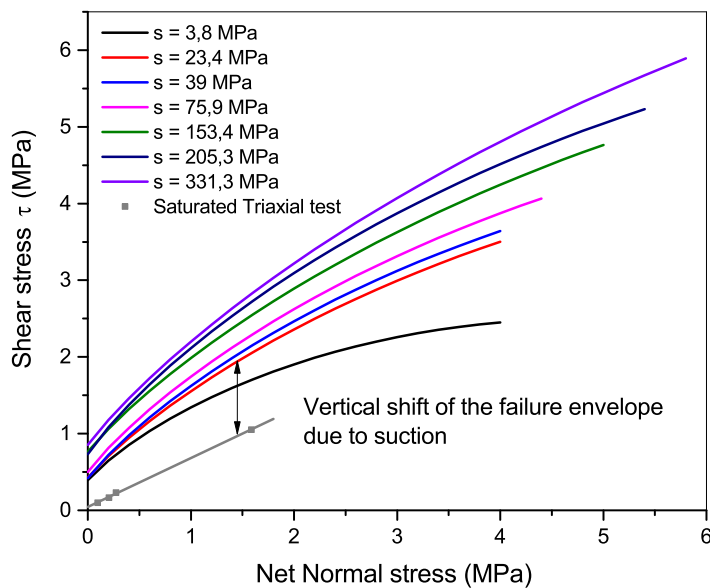


Figure 3.44: Failure envelope plotted for all suction states including the saturated state. For the unsaturated states, net normal stress is defined as $\sigma_n = \sigma - u_a$ and for the saturated state as $\sigma_n = \sigma - u_w$ as $u_a = u_w$

Generalised effective stress

The stress state variables represent the state of equilibrium of the system. For unsaturated soils, there are 2 different approaches to define the system and completely analyze the mechanical response. The first approach uses 2 independent stress state variables out of the 3 state variables for unsaturated soils i.e. net stress ($\sigma - u_a$), effective stress for saturated soils ($\sigma - u_w$) and matric suction ($u_a - u_w$) such as in BBM model [94] and SFG model [93]. Commonly, $\sigma - u_a$ and $u_a - u_w$ are used. This approach allows to model behavior as a collapse for loose soil where only the suction variation can cause failure. The second approach is generalized effective stress approach in which single effective stress defines the stress state of a multi-phase porous medium [95][96][97][98]. Since we have a highly compacted soil, the generalized effective stress approach is more suitable. Here we use Bishop's effective stress [90]:

$$\sigma'_{ij} = \sigma_{ij} + \chi s \delta_{ij} \quad (3.24)$$

where,

σ'_{ij} is the effective stress tensor,

σ_{ij} is the net stress tensor,

s is the suction,

δ_{ij} is the Kronecker delta ($\delta_{ij} = 0$ if $i \neq j$, else $\delta_{ij} = 1$)

χ is the effective stress parameter which is a function of degree of saturation.

To evaluate χ as a function of degree of saturation, first, we need to use the intrinsic shear parameters c' and ϕ' in the approach proposed by Gerard et al. [14]. According to Bishop 1960 [90], in the effective stress state reference, the normal stress shifts by an amount χs . It means that even for UCS test with $\sigma_3 = 0$, in effective stress reference it is internally stressed by an amount χs . To evaluate χ , failure envelope from saturated triaxial is overlapped with Mohr circles from UCS and unsaturated triaxial test in effective stress reference.

Finally, χs is evaluated geometrically from figure 3.45 by using $\sigma'_3 = \chi s$ for UCS and $\sigma'_3 = \sigma_3 + \chi s$ for unsaturated triaxial test. It gives:

$$\chi s = \frac{r - c' \cdot \cos \phi'}{\sin \phi'} - r - \sigma_3 \quad (3.25)$$

where $r = \frac{\sigma_1 - \sigma_3}{2}$ and $\sigma_3 = 0$ for UCS test. The value of χ was evaluated for each test and averaged (3 samples) for each suction state. It is plotted with the corresponding degree of saturation in normal scale and log-log scale in figure 3.46. This gives a relationship that we can model with the following expression :

$$\log \chi = \alpha \log S_i \quad (3.26)$$

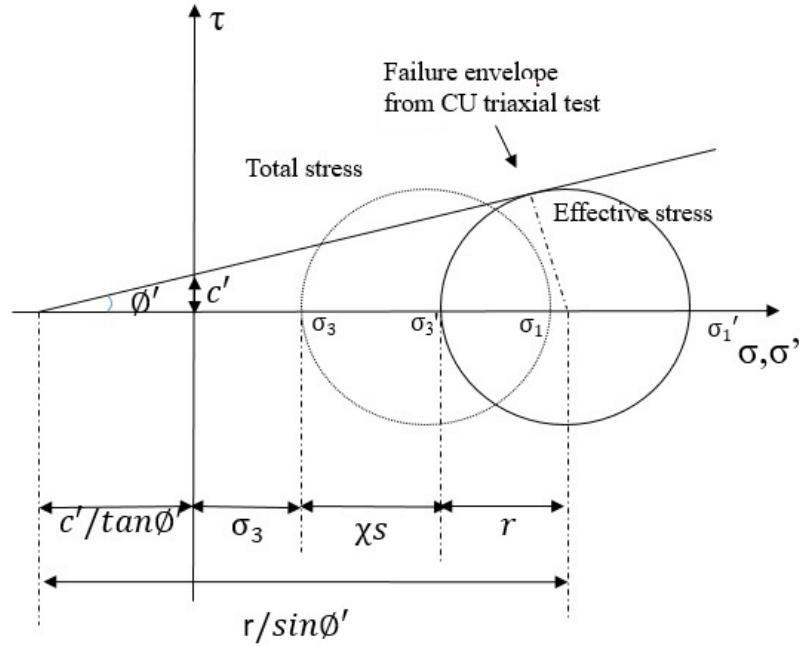


Figure 3.45: Determination of expression for χs using saturated triaxial test and Mohr circles from unsaturated triaxial test and UCS ($\sigma_3 = 0$) using the methodology of Gerard et al .2015 [14]

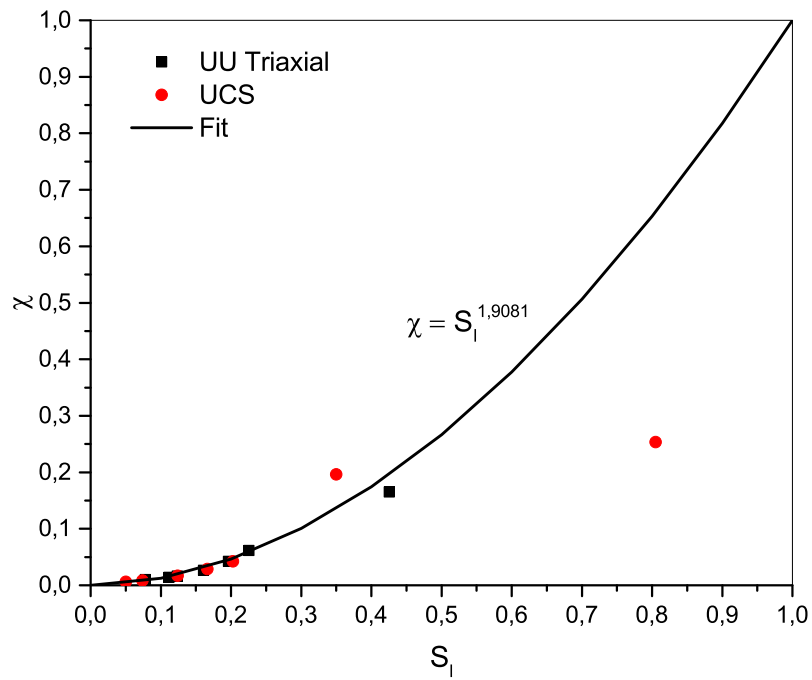
which is equivalent to:

$$\chi = (S_l)^\alpha \quad (3.27)$$

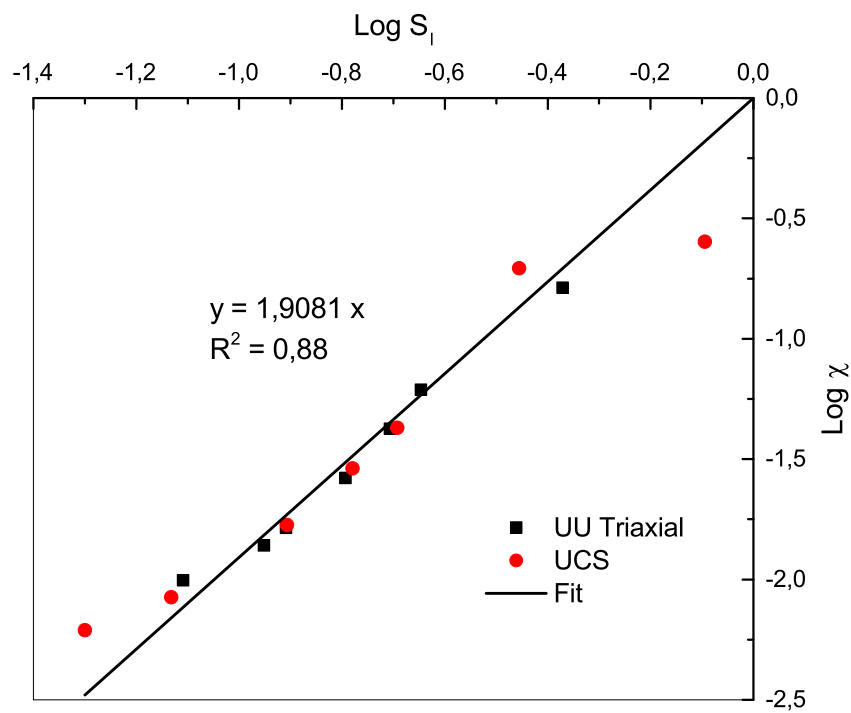
The value of α evaluated from this method is equal to 1.9081. This value is comparable to what was obtained by Gerard et al. 2015 [14]. It can be justified from the fact the particle size distribution in both the studies are close. The expression for Bishop's effective stress is written as:

$$\sigma'_{ij} = \sigma_{ij} + (S_l)^{1.9081} s \delta_{ij} \quad (3.28)$$

In this section, firstly, the results of UCS and direct shear test, which were done at lower level of normal stress and unsaturated triaxial test done at higher normal stress were analyzed. Using the results, a non-linear Mohr-Coulomb envelope was proposed and was plotted for different suction conditions. The influence of suction on the failure envelope was observed from the vertical shift of the envelope compared to the saturated one. Secondly, in order to define the stress state of the medium, the Bishop's effective stress concept was used. This helps to define a constitutive model which takes into account the effect of suction into the stress definition. To determine the Bishop's effective stress for the soil studied, effective stress parameter (χ) needs to be evaluated. For this, failure envelope from saturated triaxial tests was overlapped with Mohr circles from UCS and unsaturated triaxial test in effective stress reference. Finally, χ was determined as a power function of degree of saturation to express the Bishop's effective stress.



(a)



(b)

Figure 3.46: Determination of relation between χ and S_1 in normal scale (a) and log-log scale (b)

In the next chapter, the hydro-mechanical coupled modeling of rammed earth columns will be done. The non-linearity of failure envelope was not taken into account since the normal stresses were low, and a linear failure envelope was considered. The expression of Bishop's effective stress was taken into account to introduce the effect of suction directly in the failure criterion.

3.7 Conclusion

In the present study, a methodology to study the hydric influence on mechanical behavior is presented. The apparent mechanical parameters and intrinsic parameters were studied to provide a synthetic hydro-mechanical model, using some relevant input parameters.

It has been proposed to work with more homogeneously compacted samples by a method of double compaction instead of the traditional method of dynamic compaction. Using this technique, the compaction pressure is better controlled, and samples are repeatable. Although this method differs from the actual method in the field, the dry density obtained is the range for traditional earth construction, and thus, the samples are representative.

Matric suction is a state parameter, and any change in matric suction represents the hydric solicitation inside the material. The samples were conditioned to 7 different suction states using the method of liquid-vapor equilibrium before they were tested.

Unconfined compressive strength test was performed, with and without unload-reload cycles. The compressive strength and initial tangent modulus were found to increase with suction. Direct shear tests were performed with the same technique for sample preparation and control of hydric conditions. A brittle failure was observed upon attaining the shear strength. The shear modulus for samples sheared at different normal stress (but at same suction state) showed very less discrepancy. Apparent values of cohesion and friction angle were determined at different hydric state using the Mohr-coulomb shear strength theory. The cohesion of the sample increased with suction, due to the presence of additional capillary cohesion, which is induced by the partial saturation. The results for lower value of suction were more repeatable, since there was less deviation in the results for samples at lower suction states (wet state), where more ductile failure occurs. On the other hand, for samples at higher suction states (dry state), brittle failure occurred, which is more localized, and small defaults affected the results. A similar observation was found for results of UCS.

The apparent shear parameters were also evaluated with the unsaturated triaxial test at 7 different suction states. The failure envelope, using this test, was plotted at a higher range of normal stress as compared to DST. It indicated that shear strength predicted from the Mohr-Coulomb criterion using DST at higher range of stress is overestimated and in fact, the failure envelope is non-linear. This non-linearity was predominantly due to the unsaturated state of the samples rather than over-consolidation. Non-linearity was introduced in the shear strength equation by varying the cohesion and friction angle with normal stress. Finally, intrinsic shear parameters were determined using saturated triaxial test. By using the intrinsic failure criterion in effective stress state reference and Mohr circles for UCS and unsaturated triaxial test, a log-log relation was observed between χ and S_l . It helped in calculating the effective stress parameter and thus, obtaining the Bishop's effective stress relationship.

By obtaining the global failure envelope and effective stress equation, it is a step-forward for coupled hydro-mechanical constitutive modeling of rammed earth, which can intrinsically introduce the effect of suction in the failure criterion. This will help to reproduce the hydro-mechanical couple behavior of a given earth building and to estimate whether the strains remain admissible and if the resistance of the structure is sufficient or not.

Chapter 4

Experiments and simulation at structural scale on columns

4.1 Introduction

The first objective of the study in this chapter is to investigate the hydro-mechanical behavior of rammed earth columns with enough layers to be a representative element volume (REV) scale during drying. The columns are compacted using the dynamic compaction technique which is used in a real rammed earth wall and the hydraulic boundary conditions are imposed similar to a part of the wall which makes the columns representative of the actual rammed earth wall. The work presented in this chapter includes the drying kinetics and the compression strength evolution during drying of the rammed earth columns. The second objective of this study includes the hydro-mechanical coupled numerical simulation of the drying phase and the compression results using a Finite Element Analysis (FEA) software. The objective is to use the model and parameters obtained from the hydro-mechanical coupled study at material scale which is done in uniform suction conditions and check if it is possible to reproduce the results at a structural scale with non-uniform suction conditions as in a column.

Firstly, this chapter includes the geotechnical characterization of the soil used to prepare the rammed earth columns, including the particle size distribution curve and other basic characterization results.

The experimental plan of this campaign is described, which highlights the duration of drying of columns before compression testing and the boundary conditions to which the samples are subjected. It also describes the type of loading under which the columns are tested, i.e. loading until failure and cyclic loading. The method of sample preparation, hydric instrumentation of them, and the hydro-thermic boundary conditions will be presented.

The results of the drying phase in terms of relative humidity (and thus suction)

obtained from the sensors is presented. The influence of different duration of drying, which imposes non-uniform suction conditions, on the unconfined compressive strength and modulus of elasticity is discussed.

In the last section, the numerical simulations of the drying and the mechanical compression on the experiments carried on columns are performed using CODE_BRIGTH, which is a finite element code. The theoretical aspects of CODE_BRIGTH will be discussed, including the soil-water retention model, hydraulic conductivity model, convection of liquid flow, diffusive flux of water vapor in gas phase and the conductive heat flux. A description of the mechanical model used, i.e. Drucker-Prager model is detailed. The hydraulic boundary condition termed as atmospheric boundary condition mentioned in detail. Finally, the results of the simulations, including the drying behavior and mechanical behavior are compared with the experimental results of the columns testing.

4.2 Experimental study

4.2.1 Material

The material used for this study is the same soil as used previously for carrying out the experimental campaign at material scale with a difference that the soil studied before was sieved at 5 mm, in order to have a representative element volume, considering the chosen size of the samples. In contrast, the present earth is not sieved and has particles of maximum size (d_{max}) equal to 10 mm.

The particle size distribution curve was plotted for this soil using wet sieving and sedimentometry analysis according to French standard NF P 94-057 [99] as described in chapter 3. The PSD curve in figure 4.1 shows that it contains 12% gravel, 30% sand, 51% silt, and 7% clay. The soil used here is not in the limit range specified by Houben et al. 1994 [8] because the soil is taken from a construction site.

The other basic characterization test results have already been mentioned in detail in chapter 3. A small description of the results obtained has been summarized as follows. Its index properties are: liquid limit $w_l = 27.42\%$, plastic limit $w_p = 16.39\%$, and plasticity index $I_p = w_l - w_p = 11.03\%$. It is classified as low plastic silt ($I_p < 12\%$) according to the French classification GTR (Guide de Terrassements Routier) for fine soils. The activity of clay ($A_c = I_p/f$) defined as the ratio of plasticity index (I_p) and percentage of soil passing 2 μm sieve (f) was equal to 1.48. The relatively low value of Specific surface area ($S_{sp} = 14.7 \text{ m}^2/\text{g}$) and Cation exchange capacity (CEC = 2.6 cmol/g) suggests a very low percentage of swelling clays.

The optimum moisture content (OMC) of 12.5% was considered, which is the same value as for the 5 mm sieved soil since the change in granulometry was around 2.4%.

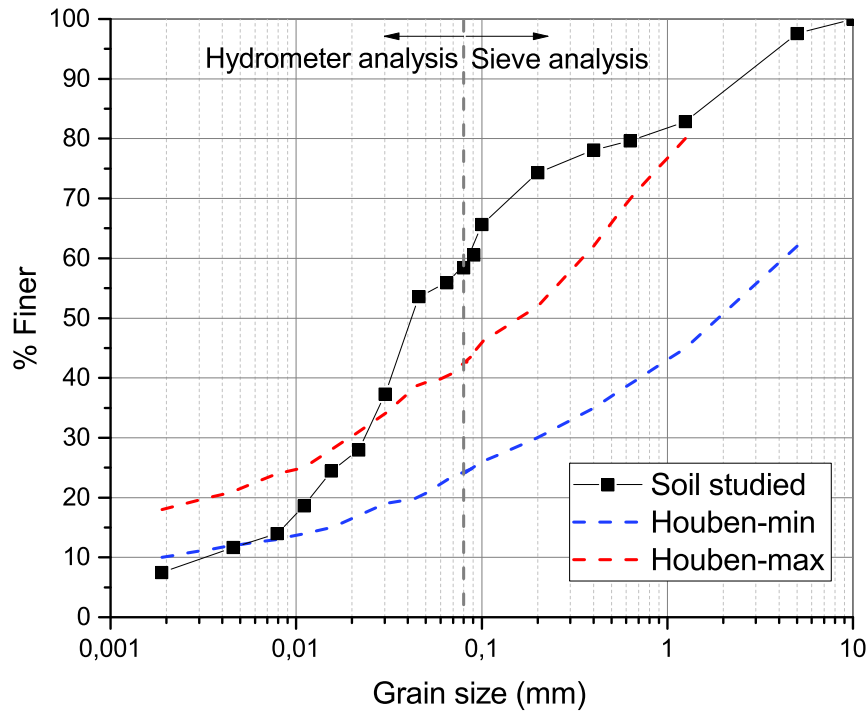


Figure 4.1: Particle size distribution of the soil used for manufacturing columns along with the limit range specified by Houben et al. 1994 [8]

4.2.2 Experimental Protocol

The aim of the following experimental campaign is to characterize the effect of suction conditions on the compressive strength rammed earth columns under realistic conditions of drying, i.e. non-uniform suction conditions. Specifically, the objective is to evaluate the mechanical capacity of rammed earth which is subjected through a drying solicitation that is chosen to replicate a one-dimensional drying occurring in the wall once it is manufactured at optimum compaction conditions. This experimental protocol aims to reproduce both realistic configuration and boundary conditions, with surface drying. The samples are of relatively larger scale, and the dimensions of the samples used for the study are 14 cm x 14 cm x 30 cm. The method of compaction used for the sample preparation used is dynamic compaction in four layers. Thus the sample is prepared in multiple layers similar to the method of compaction of a real rammed earth wall. The sample structure is more realistic than doubly-compacted samples, although it is supposed that the mechanical and hydraulic behavior is similar. The samples after compaction are further subjected to one-dimensional drying, which is similar to the drying occurring in the rammed earth wall. These imposed non-uniform suction conditions are representative of in-situ wall drying conditions. Thus, the samples used in this study is a Representative Elementary Volume (REV) of a rammed earth wall (figure 4.2).

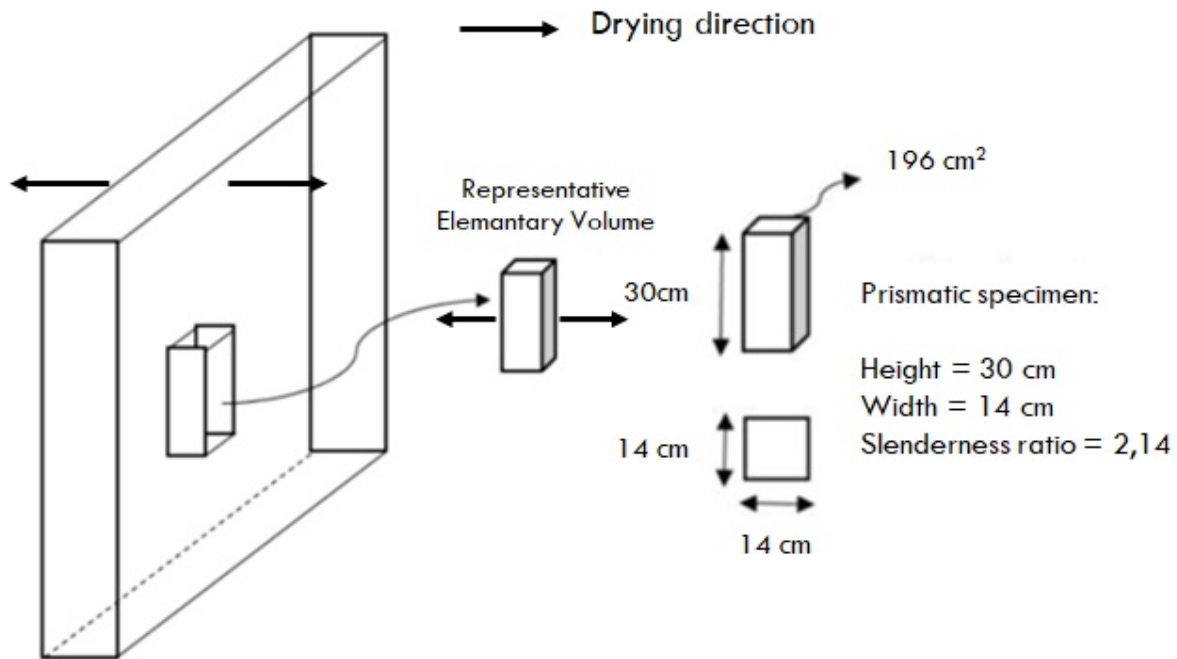


Figure 4.2: Depiction of the samples as a volume representative of the rammed earth wall along with the dimensions and slenderness ratio

The experimental plan (figure 4.3) consists of preparation of 8 prismatic samples of dimensions 14 cm x 14 cm x 30 cm on which Unconfined compressive strength testing was performed. Two samples after compaction at optimum moisture content were compressed directly without any drying phase. These tests were performed to obtain the compressive strength of the column at the uniform suction state at compaction. For the rest of the samples, paraffin was used to cover the top, bottom, and two parallel sides of the samples which induces a 1-D drying process. Out of these 6 samples, samples in a set of two samples were subjected to a drying period of 13 days, 31 days, and 62 days. One out of the two samples at drying duration of 0, 13, 31, and 62 days was loaded directly until failure to obtain the compressive strength. The other samples were compressed with three unload-reload cycles at 25%, 50%, and 75% of the compressive strength obtained in the previous test and were further loaded until failure.

In addition, it is to be noted that the relative humidity within the samples during drying was recorded using SHT capacitive sensors for one of the two samples, as shown in figure 4.3. The relative humidity is related to the suction through Kelvin's law (equation 3.12) and the suction is related to the water content by the soils water retention curve of this material (figure 3.19). For sample 4, the mass variation for 62 days of drying was recorded, which will help to obtain the water content evolution with drying time. R_c and R_c' are respectively, the compressive strength obtained with and without cycles in the mechanical loading.

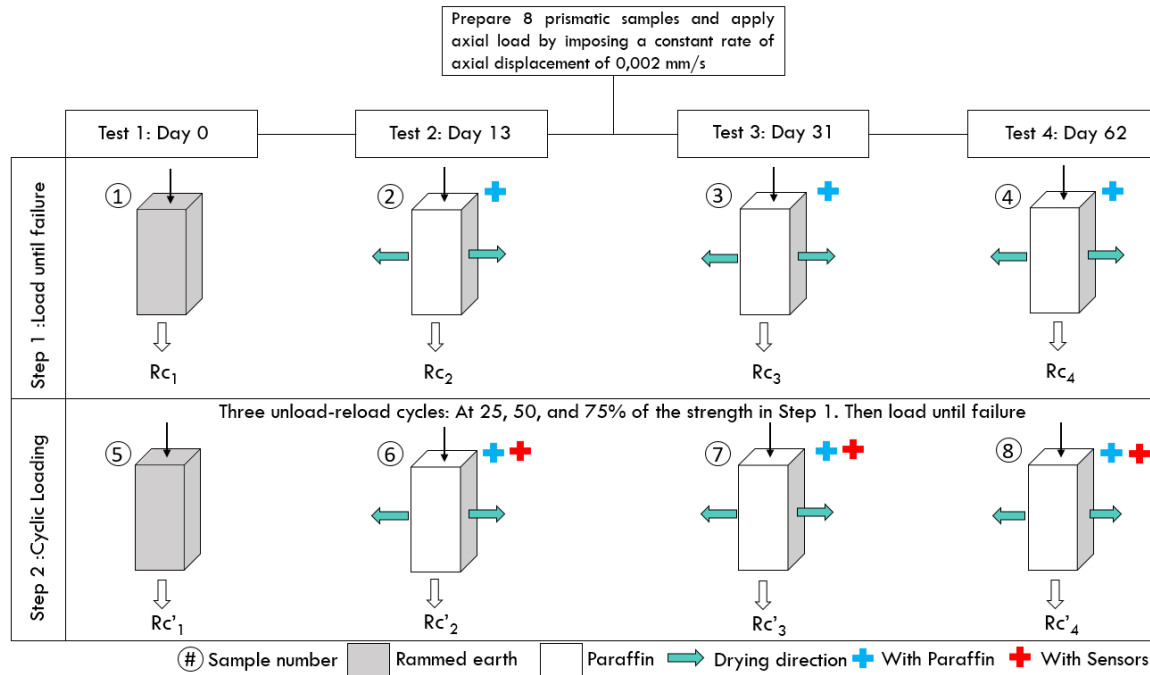


Figure 4.3: Experimental plan depicting the different samples, duration of drying after which they are tested and the loading type

4.2.2.1 Sample Preparation

The following apparatus was used for the preparation of prismatic rammed earth columns:

- Prismatic wooden mold of dimensions 14 cm x 14 cm x 30 cm with removable pieces for removing the samples from the mold.
- Additional wooden attachment at the top to facilitate the compaction of the top layer of soil.
- Pneumatic hammer which is hydraulically operated for the dynamic compaction of the soil.
- Soil mixed at the optimum moisture content.
- Paraffin powder which will be melted and applied using a brush on the faces of rammed earth columns to impose a boundary condition from which the moisture cannot be exchanged.
- SHT sensors which will be placed in the samples to observe the temperature and relative humidity variation during the drying phase.

Following procedure was adopted for the preparation of the rammed earth columns:

- The first step for making the rammed earth columns is preparation of soil. 120 kg of soil, which was enough to make 8 prismatic samples was taken. The mass

of soil needed for 8 samples was estimated using the dry density required and the volume of samples and increasing the mass by at least 10% to take into account any uncertainties.

- Adequate amount of water was added to the soil to reach the optimum moisture content of 12.5%. The soil was mixed thoroughly in a mechanical mixer and covered for at least 24 hours to allow the moisture to homogenize.
- The prismatic mold was mounted (figure 4.4A) and the inner surfaces were lubricated with oil using a brush which will facilitate the demolding of the sample.
- Each layer is poured with a thickness of about 10-15 cm into the framework (figure 4.5).
- The soil layer was rammed using a pneumatic rammer starting from the edges to the center of the sample until reaching a homogeneous and levelled surface (figure 4.4B). After compaction, the thickness of each layer is typically around 6 to 10 cm.
- For the samples that are to be equipped with SHT sensors, three sensors were placed in the middle of the third layer, as shown in figure 4.4C. Then the layer was compacted.
- This compaction procedure was repeated until the 4th layer was compacted and once the required height was achieved, the upper removable part of the framework was removed. The top surface was levelled using a metallic rod, and the whole mold was dismantled to remove the sample (figure 4.4D and E).
- Except for the 2 samples tested directly after the compaction (without drying), the samples were covered with paraffin at the top, bottom, and two parallel faces to impose unidirectional drying. This allows us to reproduce the boundary conditions of a representative elementary volume taken from a bigger rammed earth wall (figure 4.4G).
- These 6 samples after preparation were left to dry in an indoor environment (figure 4.6). The values of ambient relative humidity and temperature were measured at regular intervals until day 62. The mean value of ambient relative humidity and temperature recorded was 65% and 15.5 °C

An additional sample (sample 9) was made which was not covered with paraffin and allowed to dry from all sides in the same ambient conditions. This sample will be tested (without unload-reload cycles) after the drying process is complete to obtain the compressive strength after full drying. The mass variation of this sample will also be recorded to obtain the water content evolution with time.

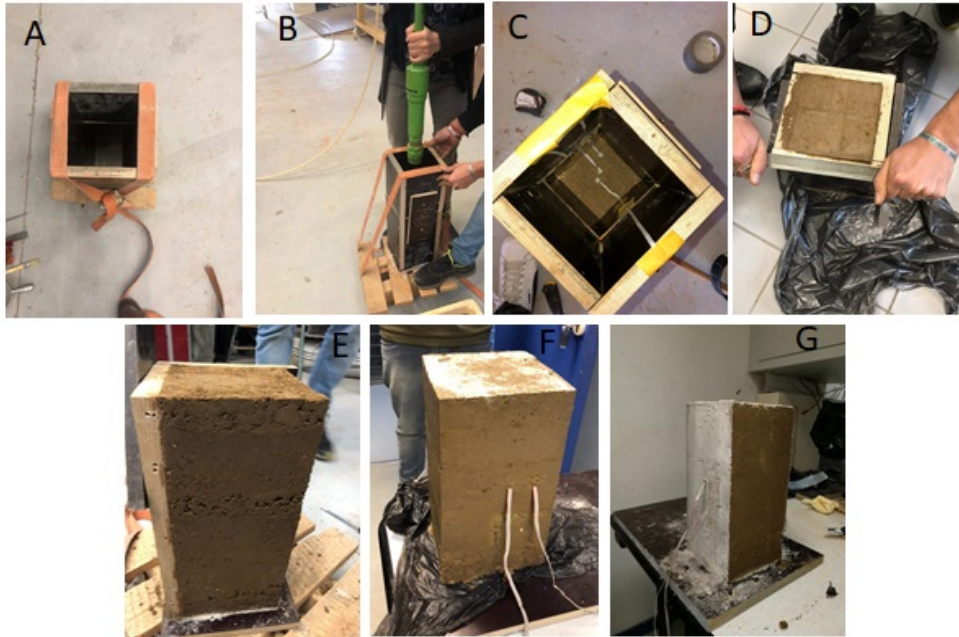


Figure 4.4: Different steps for the preparation of prismatic rammed earth columns

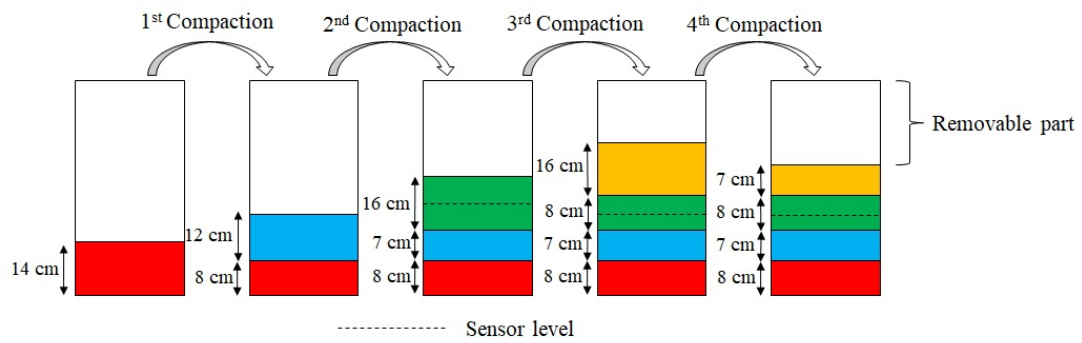


Figure 4.5: Figure depicting the different compaction layers and the placement of SHT sensors



Figure 4.6: Samples left for drying in an indoor environment

4.2.2.2 Sensor calibration and layout

To be able to capture the relative humidity (RH) and temperature (T) inside the sample during the unidirectional drying, a total of 10 SHT75 sensors (figure 4.7) were used in different samples. The SHT75 sensors use a capacitive sensor element for the measurement of relative humidity. For measuring the temperature, it uses a band-gap sensor.

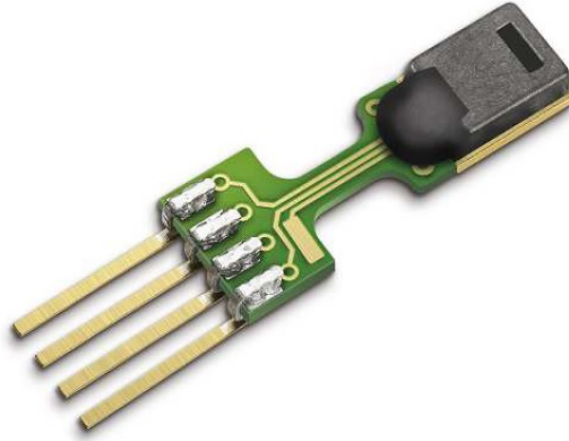
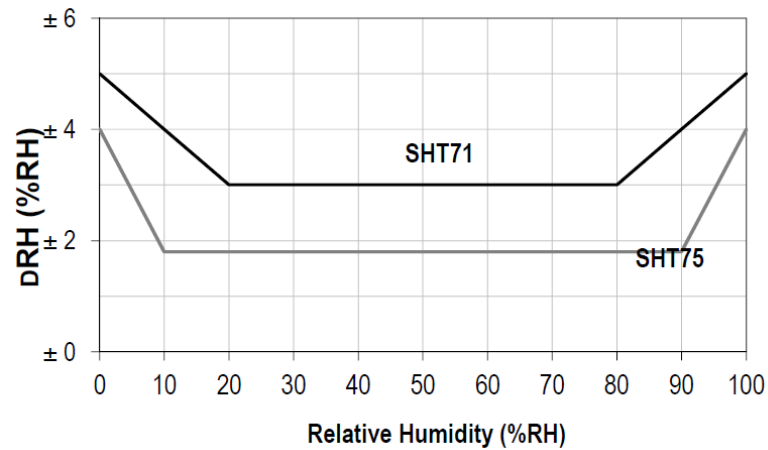


Figure 4.7: The SHT75 sensor used to relative humidity and temperature measurement

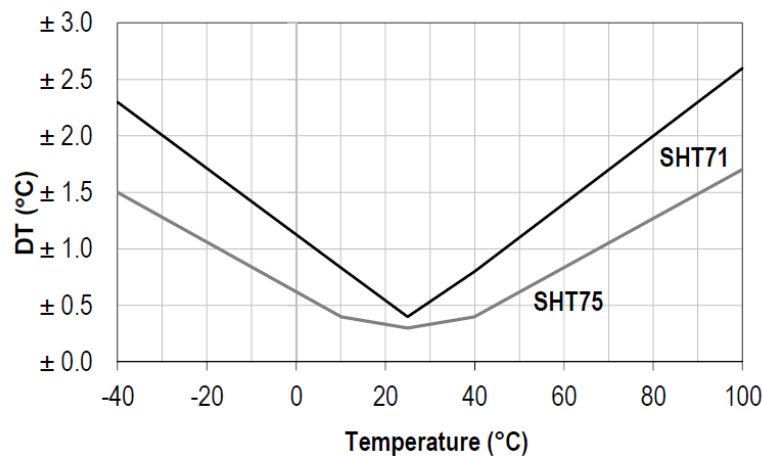
The operating range of this sensor is from 0 to 100% RH. The typical accuracy of SHT75 sensors for the measurement of relative humidity is $\pm 1.8\%$ RH for the range 10-90% RH. The uncertainty in the measurement rises to $\pm 4\%$ RH at either very low RH (less than 10%) or very high RH (greater 90%) as shown in the figure 4.8a. With regards to temperature, the operating range is from -40 to 123.8 °C. The typical accuracy for temperature measurement is ± 0.3 °C, and the accuracy in the whole range is shown in the figure 4.8b. It is to be noted that, long term exposure to conditions outside the normal range, especially at humidity greater than 80% RH, may temporarily offset the RH signal (+3% RH after 60h). After returning to normal range, it slowly returns towards the calibration state by itself.

Before using the sensors for the measurement, all the sensors were formerly calibrated to compute the correction factors. The correction factors needs to be computed individually for both relative humidity and temperature. Following procedure was used for the calibration of sensors:

1. Firstly to calibrate the sensors with regards to relative humidity, the sensors were placed inside an isolated chamber at a constant temperature of 25 °C.
2. The objective was to vary the relative humidity conditions inside the chamber. To do so, the sensors were inserted in sealed boxes containing the saline solutions and thus imposing a certain relative humidity.
3. The saline solutions used for the calibration are the same that were used to condition the smaller samples used in the previous chapter. The details of the saline solutions



(a)



(b)

Figure 4.8: The RH-tolerance at 25 °C (a) and temperature tolerance for the SHT sensor (taken from sensirion.com)

and the relative humidity imposed have been mentioned in table 3.4 in section 3.4.3.1 of the previous chapter.

4. The sensors were first placed in the RH box imposing 9% relative humidity. After a sufficient duration of time, when the readings of the sensors are stable, the sensors were moved to the next higher RH box. This process was continued until the equilibrium was reached in the RH box with highest RH of 97.3%.
5. Then the sensors were moved back again to the lower relative humidity boxes until reaching 9%. The results of the calibration of 10 SHT sensors with regards to relative humidity is shown in figure 4.9. In this way, the calibration factors for relative humidity were computed.
6. In order to calibrate the sensors with regards to temperature, the sensors were placed inside a sealed container including silica gel to impose an almost null relative humidity. The objective was to vary the temperature conditions keeping the relative

humidity as constant.

7. This container was placed inside an isolated chamber and a temperature of 5 °C. After sufficient duration of time, when the readings of the sensors are stable, the temperature in the chamber was changed to 10 °C. The temperature was increased in the interval of 5 °C until reaching 30°C.
8. In the same way as it was done for the calibration with regards to RH, the temperature was decreased back to 5 °C in intervals of 5 °C.
9. In this way, the calibration factors for temperature were computed. The results of the calibration of 10 SHT sensors with regards to temperature is shown in figure 4.9.

The SHT sensors recorded the relative humidity and temperature inside the samples of rammed earth and presented the measurements as raw data. To be able to understand the physical meaning of the acquired measurements, the calibration of the sensors was performed as previously described. Once done, the equations relating the raw data with the actual readings for each sensor was obtained. Having the raw data recorded from the SHT sensors, the real temperature and relative humidity could be computed through the equations obtained from the calibration. The detailed information about both temperature and RH calibration curves and equations for data conversion for each sensor is mentioned in Appendix D.

The sensors were placed inside a plastic protection membrane in order to avoid damage to the sensors during compaction process since the sensors were placed in the middle of a layer which was compacted as shown in the figure 4.10a.

The layout of the sensors for the samples compressed after drying phase of 14, 31, and 61 days is shown in the figure 4.10b. The sensors were placed at a distance of 3 cm, 5 cm, and 7 cm from the drying face. The distance of the sensor from the face on which the paraffin layer will be applied was not important since the drying is unidirectional.

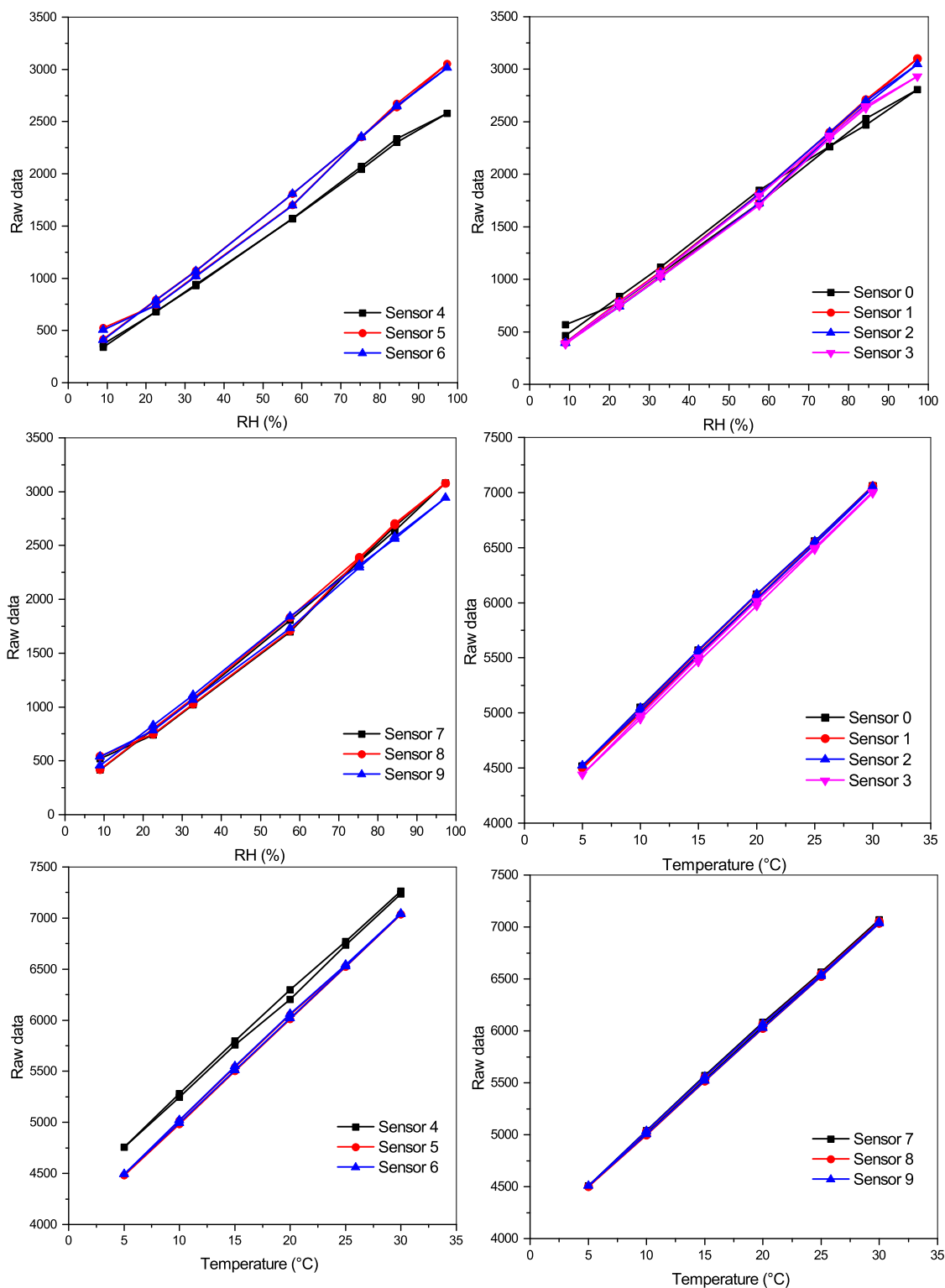


Figure 4.9: Calibration curve with regards to temperature and relative humidity for all the sensors

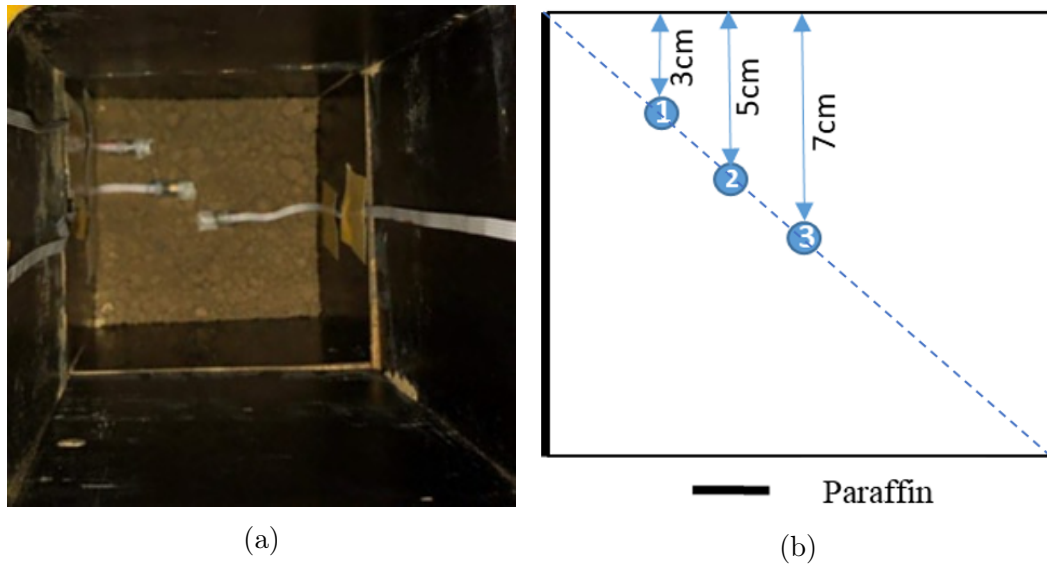


Figure 4.10: Placement of sensors in the middle of rammed earth layer along with the plastic protection membrane (a) and Sensor layout (b)

4.2.3 Results of the drying phase

The ambient relative humidity and temperature were recorded during the drying phase. A mean value of 65% RH and 15.5 ° C. These conditions were considered as the boundary condition. The samples, if allowed to dry for a significant amount of time, will reach this value of relative humidity asymptotically at the end of drying phase.

The measurement of the temperature and relative humidity of the samples was taken once per day. The drying curves, representing the variation of relative humidity with time for the three samples (i.e. sample number 6, 7, and 8 as outlined in figure 4.3) are shown in the figure 4.11. The distance denoted (d) in the figure represents the distance between the sensor and the closest drying face. Some of the sensors did not show any readings after compaction, notably sensor placed at $d = 7$ cm in sample 6, sensor at $d = 5$ cm in sample 7. This problem can be attributed to the compaction process that might have damaged the sensors and their ability to record measurements. Thus, in the future work, it is recommended to change the type of protection membranes used to guarantee the safety of the sensors. Thus, the results of these tests are shown without these measures.

For sample 6, which is to be mechanically compressed after 13 days of drying, the results are shown in figure 4.11a. The results show a little variation of relative humidity within the first 13 days of drying. The sensor placed at $d = 5$ cm did not show any change in the relative humidity in 13 days and remained at the value close to 100% RH. For the sensor placed at $d = 3$ cm, the value of RH remains 100% until 10 days of drying. The RH decreases to about 96% after 13 days of drying. There is a significant drying that has occurred during this time, but without significant variation of relative humidity (due to the liquid-vapour equilibrium with Kelvin law being not linear) or without good precision

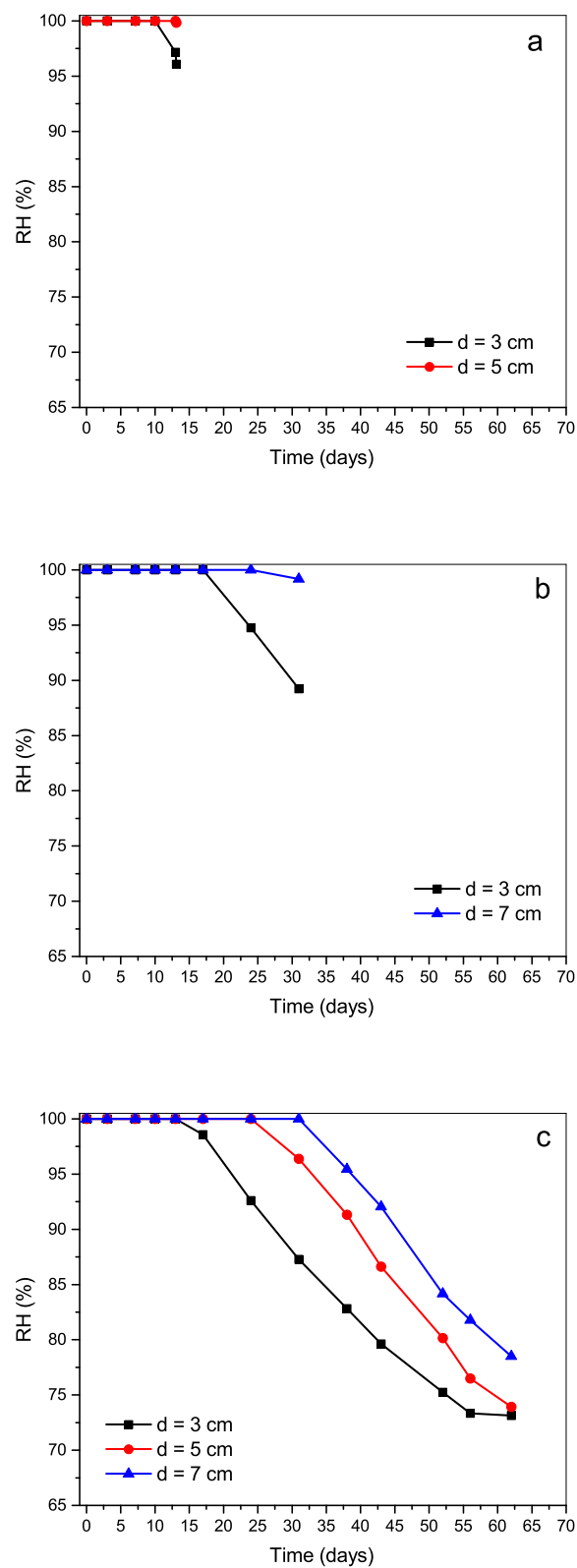


Figure 4.11: Variation of relative humidity vs time for sample 6 (a), 7 (b), and 8 (c), which are to be compressed after 13, 31, and 62 days of drying respectively

of the sensors for this range of RH (as explained later). In addition, there might occur condensation of the water particles within the plastic protection membrane, which might affect the readings of the sensors.

For sample number 7, which is to be mechanically tested after 31 days of drying, the results are shown in figure 4.11b. A similar variation of RH was observed. No change in RH was observed for the sensor placed at $d = 3$ cm for 17 days, and then it decreased to an RH of 89% after 31 days of drying. For the sensor placed at the center of the sample at $d = 7$ cm, it showed very minute variation. It remained at RH of 100% until 24 days of drying and decreased to only 99.18% after 31 days of drying.

For sample number 8, which is to be mechanically tested after 62 days of drying, the results are shown in figure 4.11c. The sensor located at a distance of 3 cm, was affected first. The RH value remained unchanged at 100% for the first 13 days of drying. This value decreased at a significant rate until day 56, reaching an RH of 73.5%. After this time, the rate of decrease of RH becomes less, and the RH reaches a value of 73% at the end of day 62. The sensor placed at $d = 5$ cm, which is higher distance from the drying face, the decrease in the value of RH took more time to be initiated. It took about 24 days for a change to be observed in the RH. After this time, the RH decreases at a significant rate until 56 days, reaching a value of 76.48%. This rate of decrease becomes less, and the RH reaches a final value of 73.93% after 62 days. Finally, for the sensor placed at the centre of the sample at $d = 7$ cm, it took about 31 days for the initiation of change in RH from 100%. The value of RH decreased at a significant rate reaching a final value of 78.5% on day 62. It is interesting to note that during the middle phase of drying from 15 to 50 days, the difference in RH between $d = 3$ cm and $d = 5$ cm is higher as compared to the difference in RH between $d = 5$ cm and $d = 7$ cm. Whereas towards the end phase of drying, the difference in RH between $d = 3$ cm and $d = 5$ cm is lower as compared to the difference in RH between $d = 5$ cm and $d = 7$ cm. In fact the value of RH at $d = 5$ cm is very close to $d = 3$ cm.

Figure 4.12 shows the variation of relative humidity profiles of sample number 8. The curve for day 0 and day 13 coincide at a value of 100% RH, i.e. no decrease of RH was observed. Starting from day 17 and forward, the curves were shifted downwards due to the initiation of drying process. At the beginning of drying phase, the drying curves were concave towards the top, and this curvature seems to flatten after drying duration of 43 days and then at the later stages of drying, the curve becomes convex from the top. This observation was also highlighted in the discussion before, that RH values at $d = 5$ cm are closer to the values at $d = 7$ cm than $d = 3$ cm at the initial stages of drying. Whereas during the later stage, the RH values at $d = 5$ cm are closer to the values at $d = 3$ cm than $d = 7$ cm. This means that during the initial stage of drying, the part of the sample closer to the boundary is significantly affected, while the middle of the sample does not show significant drying. On the other hand, during the later stages, the part of the sample closer to the drying face reached a hydraulic state which tends to be in equilibrium with the boundary conditions, and thus the process of drying becomes slower

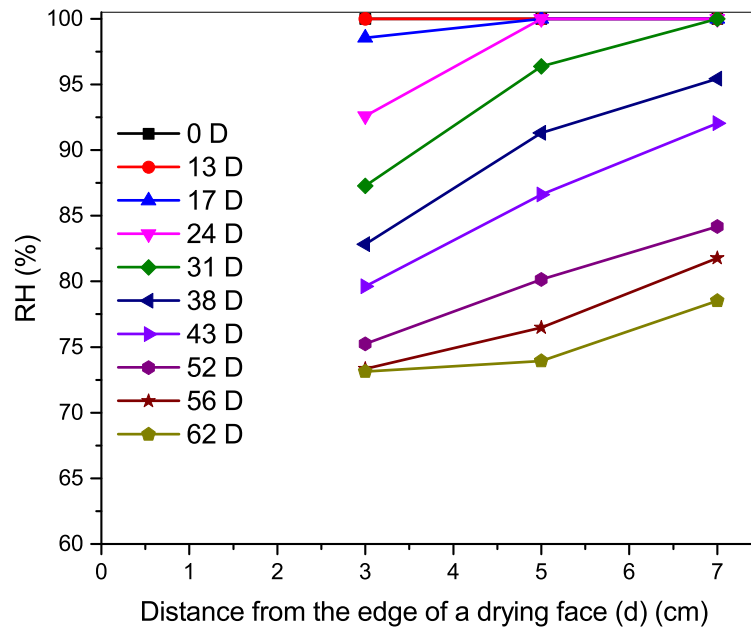


Figure 4.12: Variation of relative humidity with distance from the edge of drying face at different duration of drying for sample 8

while the middle portion of the sample is still undergoing significant drying.

The average water content variation was followed for sample 4, which was covered in paraffin and subjected to 1-D drying (figure 4.13). Within the first 2 weeks, the average water content dropped from 12.5% at compaction state to around 6%. This helps to understand better the drying in the first 2 weeks where no variation in the relative humidity is observed in the SHT sensors. The drying process becomes slower over time, reaching to about 4% in 30 days and finally reaching a value of 2.8% at the end of 62 days. In addition, the average water content evolution is also shown for sample 9, which was not covered with paraffin and allowed to dry from all faces (except the bottom). For sample 9, the water content dropped to about 3% within the first 2 weeks, and the drying is complete in around 30 days, reaching a water content of 2.44%. This final water content can be used to understand the kinetics of drying for the sample under 1-D drying. About 30% of drying occurs in the first 5 days, 50% of drying in 10 days, and around 96% drying in 62 days.

In addition, it is to be noted that, for these sensors, i.e. SHT75, the uncertainty in the measurement of relative humidity increases from $\pm 1.8\%$ to $\pm 4\%$ linearly when the RH values increase from 90% to 100%. Also, long term exposure at RH values higher than 95% leads to a temporary offset of +3% RH. These could be the possible reasons for the minimal change of RH during the initial phase of drying. Thus, the values of RH needs to be corrected. Except for the readings at day 0 where the RH is around 100 %, all the other readings with RH = 100% are discarded. All the readings are shown with

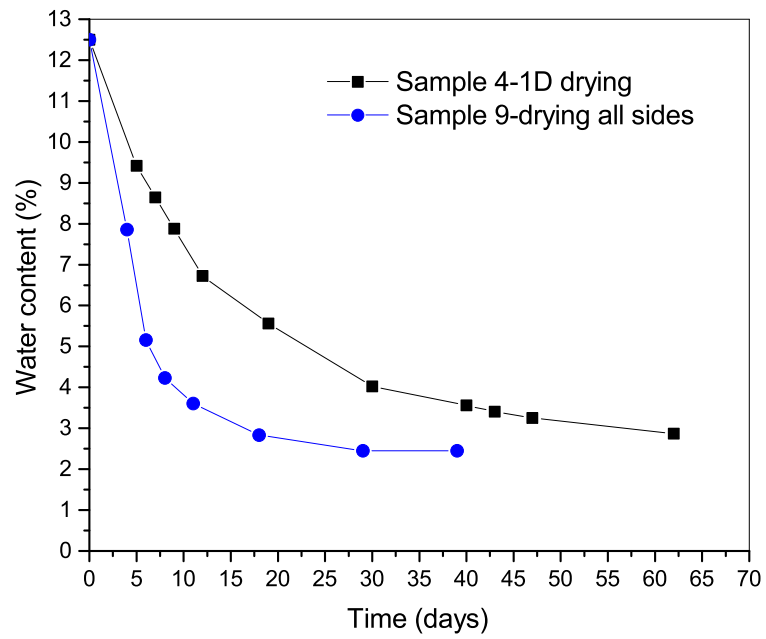


Figure 4.13: Variation of average water content with time for sample 4: 1D drying and sample 9: drying from all sides

corrections due to the offset and error bars based on the uncertainty in measurement in figure 4.14.

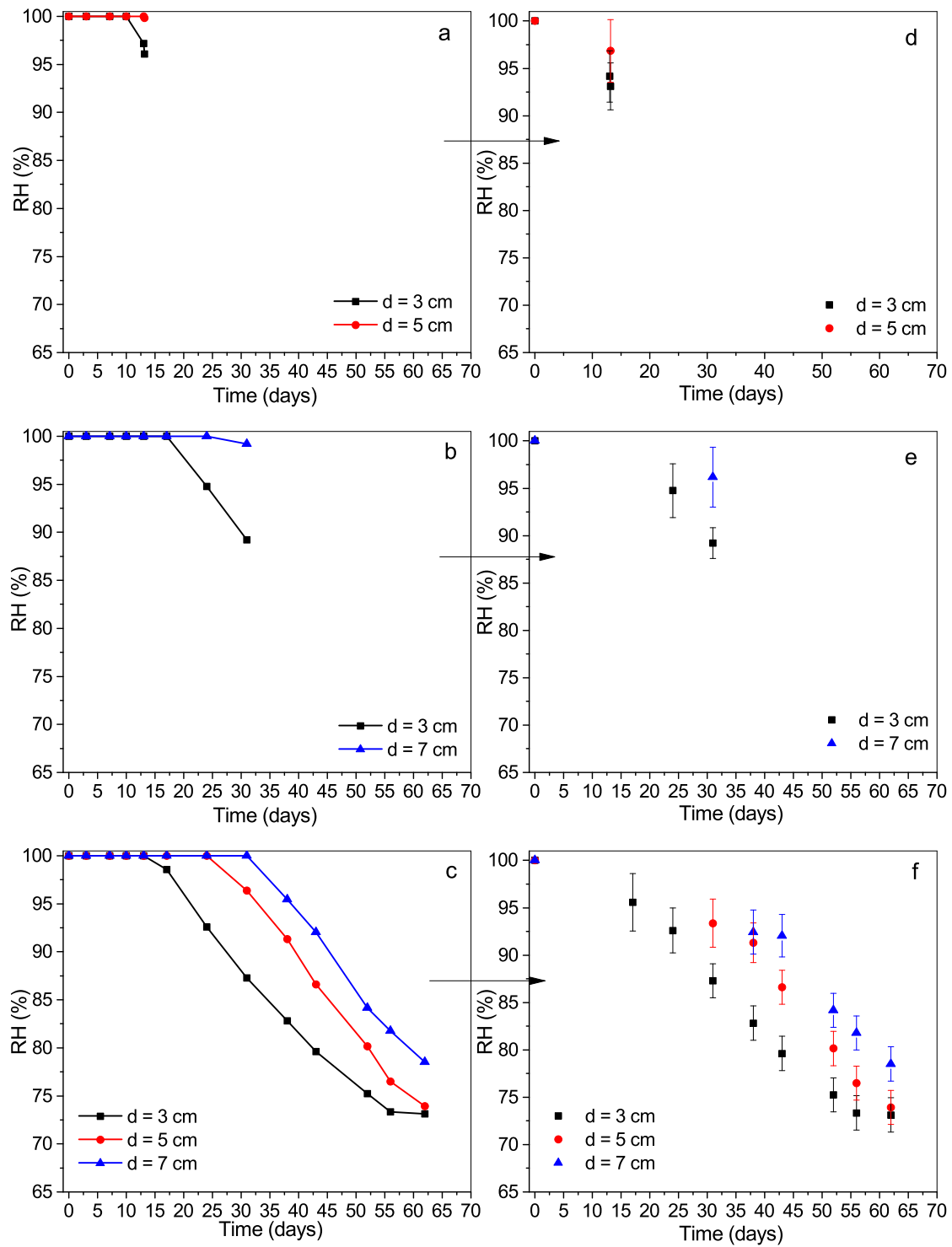


Figure 4.14: Variation of RH with time showing the raw measured data (a), (b), and (c) along with the corrected data (d), (e), and (f) for samples 6, 7, and 8 respectively

4.2.4 Unconfined compression test on columns

The main purpose of the following experiment is to study the mechanical behavior of rammed earth columns at non-uniform hydric conditions. Thus, the purpose is to extend the understanding of suction influence on the mechanical properties of the sample.

The compression test is typically used to compute the mechanical properties of the soil samples, i.e. compressive strength and Young's modulus of elasticity (initial tangent modulus and secant modulus for testing with unload-reload cycles). In these tests, different hydric states were considered, varying from high to low relative humidity with an interval of around two weeks between different tests. Two tests were done at uniform hydric state which was the condition just after compaction of the sample ($w = 12.5\%$ and $s = 0.328$ MPa), whereas the other samples were tested at non-uniform suction state due to the drying of the samples. In this way, the effect on the mechanical behavior of rammed earth can be studied with the variation of suction conditions.

The following apparatus was used for performing the compression test:

- 8 prismatic rammed earth columns.
- Electro-mechanical press of capacity of 100 kN.
- Data acquisition unit: converts the analog readings from the load cell to digital data.
- Metal plates which are placed at the top and bottom to ensure an uniform distribution of the load.
- Sensors and the acquisition system for measuring the relative humidity and temperature inside the samples and of ambient air.

4.2.4.1 Experimental procedure

The rammed earth columns were compressed in the mechanical press using the following procedure:

1. The samples which were to be tested at 0 days of drying just after compaction, i.e. Sample 1 and 5, were placed directly into the press with a metal plate at top and bottom (figure 4.15).
2. These samples were axially compressed at a constant rate of axial displacement of 0.002 mm/s until failure.
3. The load and the displacement variation was recorded to obtain the stress-strain curves.

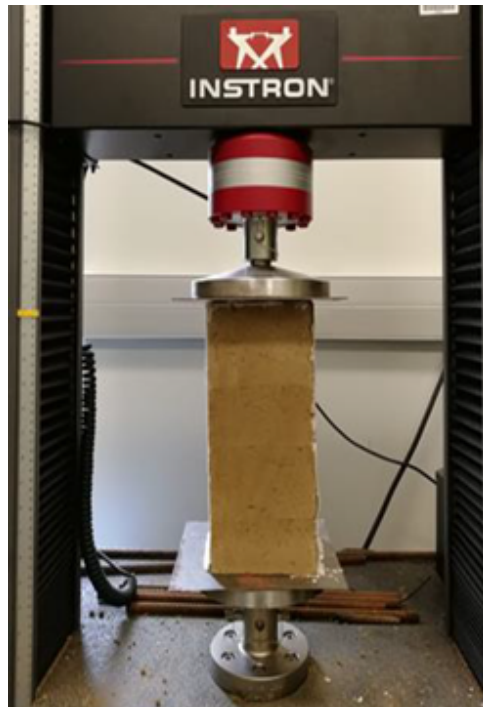


Figure 4.15: Experimental setup for unconfined compression test

4. The samples with paraffin covering which were dried for 13, 31, and 62 days (i.e. sample 2,3, and 4) without any sensors were also compressed in the similar method mentioned in step 2-4.
5. The compressive strength obtained from the previous test will be further used to determine the stress at which the unload-reload cycles will be performed.
6. The samples with paraffin covering and equipped with sensors which were dried for 13, 31, and 62 days (i.e. sample 6, 7, and 8) were compressed at a constant rate of axial displacement of 0.002 mm/s along with three unload-reload cycles at 25%, 50%, and 75% of the corresponding compressive strength previously obtained. It is to be noted here that the unload-reload cycles might not correspond exactly to the same percentage in these samples since the compressive strength can vary.
7. Finally, sample 9 was compressed without unload-reload cycles after the drying process was complete.

4.2.4.2 Results of the compression test

The results of the compression test in terms of axial stress and axial strain with and without unload-reload cycles are shown in figure 4.16 and 4.17. It is to be noted that, the result of the test on sample 7 have not been shown in figure 4.17a since the mechanical press did not function properly and the stress values were incorrect. Thus, the results of this test will be disregarded in the further investigation. The results of all the tests,

including compressive strength, tangent modulus of elasticity, axial strain at failure have been collected in table 4.1.

Figure 4.16a shows the mechanical response of sample 1 and 5 which were tested just after compaction at their ‘at compaction’ uniform hydric state ($w = 12.5\%$ and $s = 0.328$ MPa). The compressive strength of both the samples was similar. Sample 1 and 5 reached a compressive strength of (Rc_1) 144.1 kPa and (Rc'_1) 146.6 kPa respectively. The tangent modulus of elasticity was higher for sample 5, which was compressed with unload-reload cycles.

The results of the compression test for sample 2 and 6, which were tested after 13 days of drying period has been shown in figure 4.16b. The compressive strength of sample 2 which was compressed by directly loading until failure ($Rc_2 = 1550.4$ kPa) was significantly higher than the compressive strength of sample 6 ($Rc'_2 = 1185.4$ kPa) which was tested with unload-reload cycles.

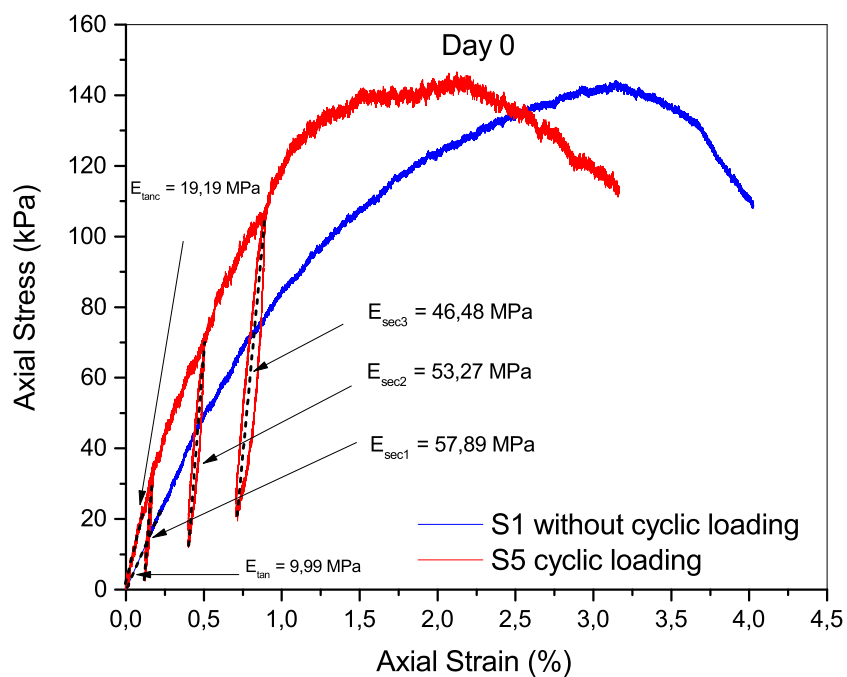
Since the compressive strength of sample 6 was lower, the 3rd unload-reload cycle was very close to the failure stress. Sample 2 was also stiffer than sample 6. The tangent modulus of elasticity of sample 2 and 6 are mentioned in table 4.1.

The result of compression test after 31 days of drying is shown in figure 4.17a. Due to the reason mentioned before the result of sample 7 have not been shown. Thus, it was not possible to compare samples 3 and 7. The compressive strength of sample 3 was $Rc_3 = 1837.5$ kPa, and the tangent modulus was equal to 166.1 MPa.

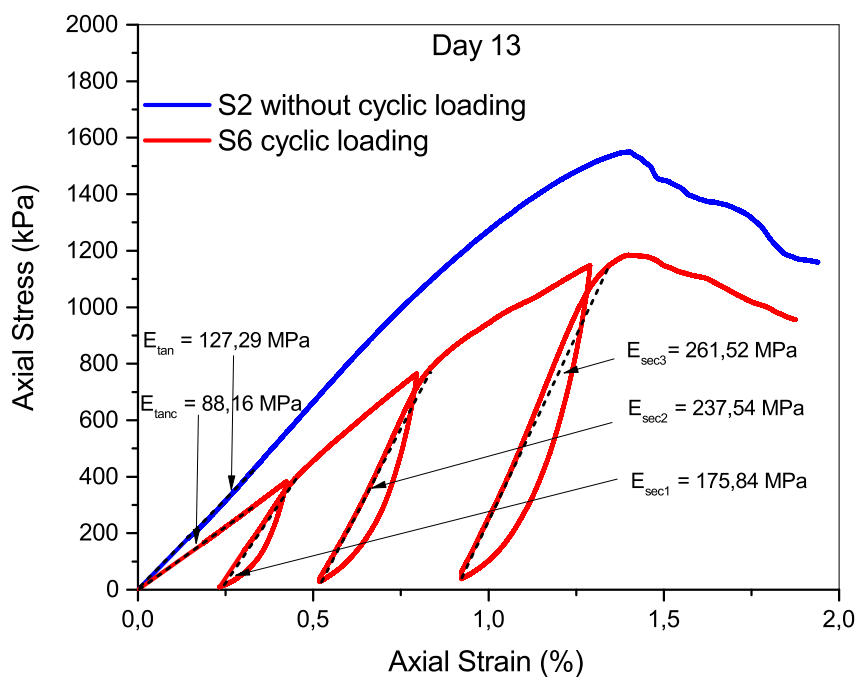
Figure 4.17b shows the compression results of sample 4 and 8, which were tested after 62 days of drying. Both of the samples exhibited a greater compressive strength compared to the previous samples. The compressive strength of sample 4 which was compressed by directly loading until failure ($Rc_4 = 2025.2$ kPa) was higher than compressive strength of sample 8 ($Rc'_2 = 1755.5$ kPa) which was tested with unload-reload cycles. A similar trend was also observed for the values of initial tangent modulus, which was higher for sample 4 as compared to sample 8.

Table 4.1: Compressive strength, tangent modulus, axial strain at failure for all samples

Sample no.	Tangent modulus (E_{tan}) MPa	Compressive strength (Rc) kPa	Axial strain at failure (ϵ_f) %
1	9.9	144.1	3.14
2	127.3	1550.4	1.4
3	166.1	1837.5	1.22
4	201.2	2025.2	1.13
5	19.2	146.6	2.12
6	88.2	1185.4	1.4
8	137.4	1755.5	1.38
9	235.1	2452.5	1.25

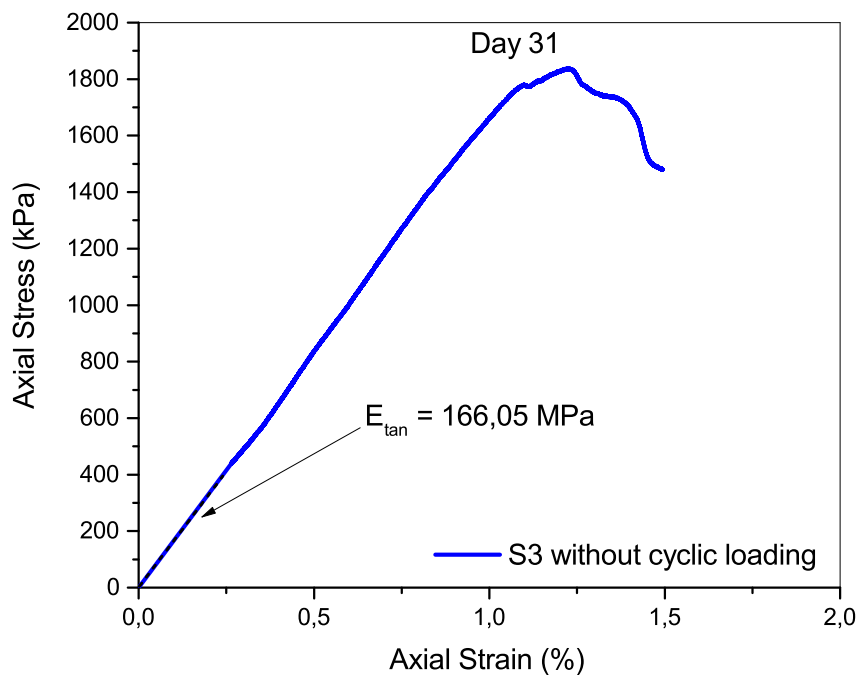


(a)

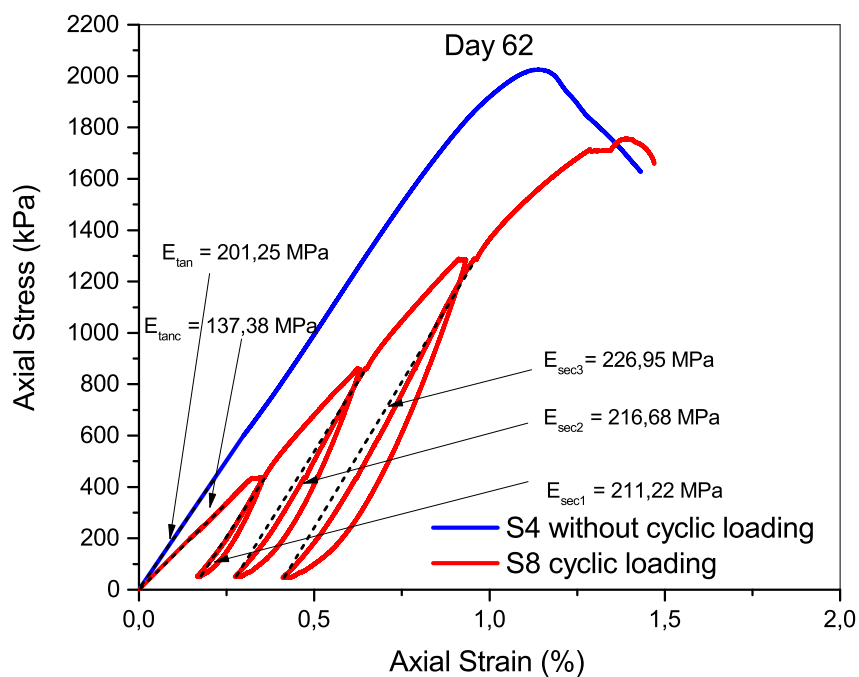


(b)

Figure 4.16: Axial stress-strain curve for samples after 0 (a), 13 (b) days of drying with and without unload-reload cycles

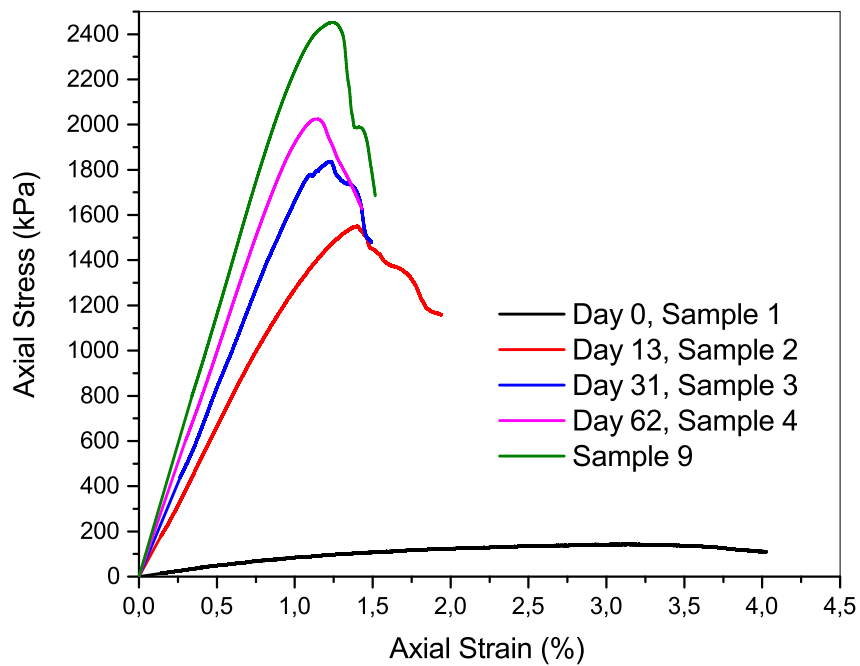


(a)

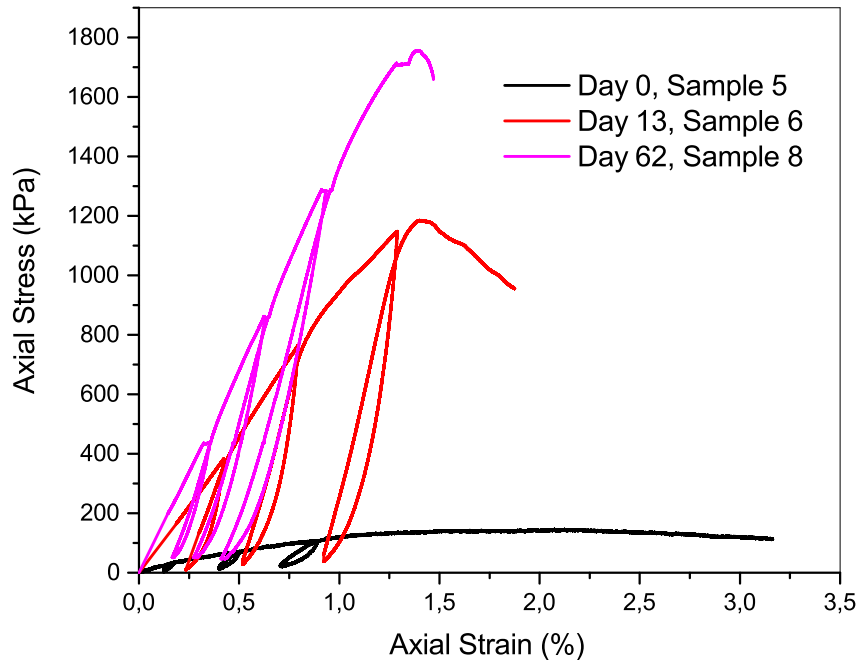


(b)

Figure 4.17: Axial stress-strain curve for samples after 31(a) and 62 (b) days of drying with and without unload-reload cycles



(a)



(b)

Figure 4.18: Axial stress-strain curves for samples loaded until failure (a) and with unload-reload cycles (b) at different drying duration

The results of the compression test for sample 9, which is fully dried within 30 days is shown in figure 4.19. The compressive strength of sample 9 was $R_{c9}=2452.5$ kPa, and the tangent modulus was higher than all the other samples tested. This shows that samples are still capable of gaining strength and stiffness upon further drying after 62 days.

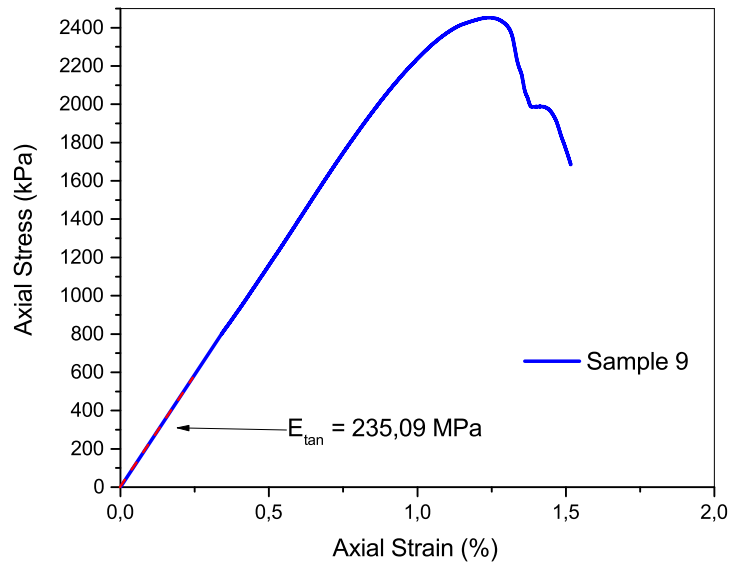


Figure 4.19: Axial stress-strain curve for sample 9 which is fully dried after 30 days without unload-reload cycles

The stress-strain curves for all the samples tested are shown in figure 4.18. It can be observed from these curves that the mechanical behavior of a rammed earth columns changes from more plastic at conditions of higher relative humidity (lower suction) to more brittle failure at lower relative humidity (higher suction conditions). Samples 1 and 5, which were tested without any drying, failed at an axial strain of about 2.1% and 3.1% respectively. In contrast, the other samples which were dried for significant duration failed at about 1.1-1.4% axial strain (table 4.1). This transition was also observed for the smaller cylindrical samples tested in the previous chapter. In addition, during the transition of the qualitative behavior of rammed earth samples, the modulus of elasticity and the compressive strength also increases.

The variation of compressive strength for the different rammed earth columns with drying duration has been shown in figure 4.20. A substantial increase in the compressive strength from around 144.1 kPa at day 0 to 1550.4 kPa at day 13 was observed. After day 13, the increase in strength was at a slower rate reaching a value of 1837.5 kPa at day 31 and 2025.2 kPa at day 62. Thus, the major part of strength is gained within the first two weeks of drying. As the sample is drying, the RH is decreasing, and the suction is increasing. The suction contributes to additional part of strength by giving the soil an additional suction induced cohesion as put in evidence in the material scale

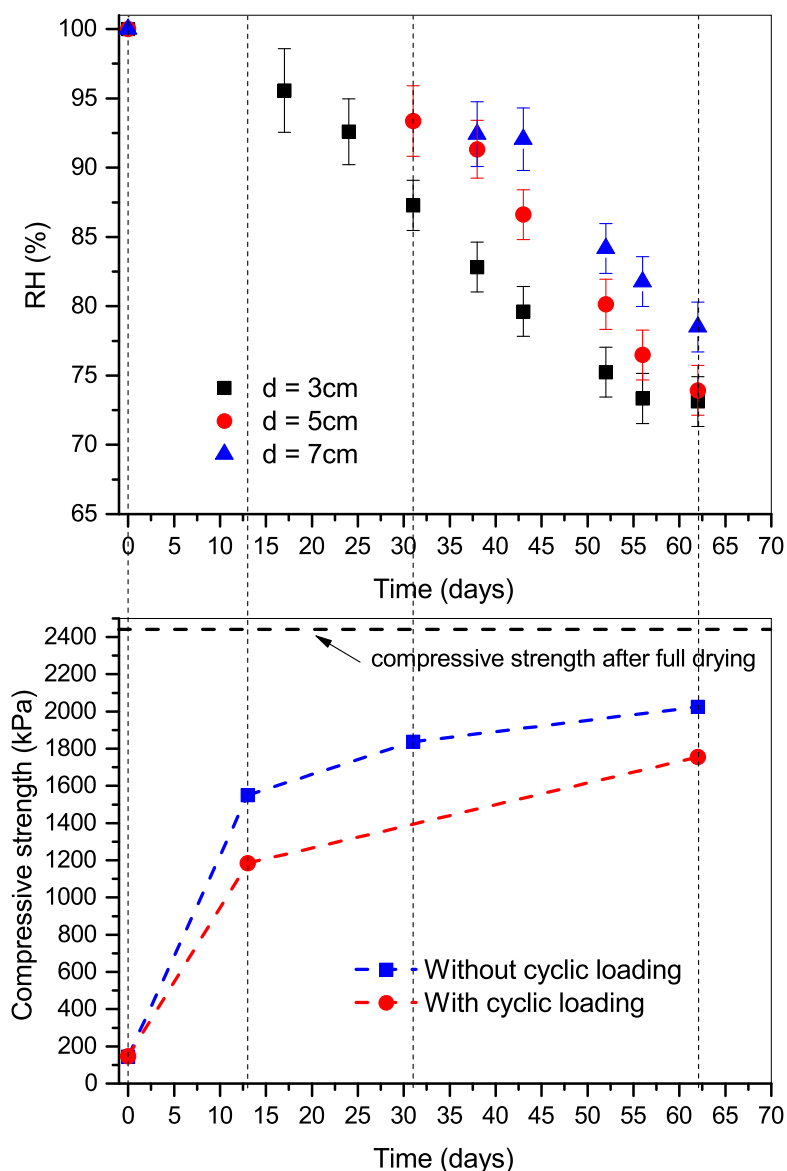


Figure 4.20: Variation of compressive strength and RH (sample 8) with duration of drying for samples with (sample 5-8) and without (sample 1-4) unload-reload cycles

hydro-mechanical experiments of chapter 3. This gain in strength is limited as water inside the sample quantified by degree of saturation is decreasing [69]. The additional suction induced cohesion is acting on a drier sample with less water. The rate of increase of strength gain is higher in the beginning phase of drying, then it decreases consequently, and the strength reaches an asymptotic value. Actually, around 13 days were enough for the rammed earth to attain 63% of its strength attained after complete drying. The compressive strength of samples tested with unload-reload cycles also followed a similar strength gaining significant strength in the beginning. The complete trend of strength cannot be discussed since the strength value is missing at 31 days. Also, the compressive strength without the unload-reload cycles is generally higher or similar to strength with

the cycles.

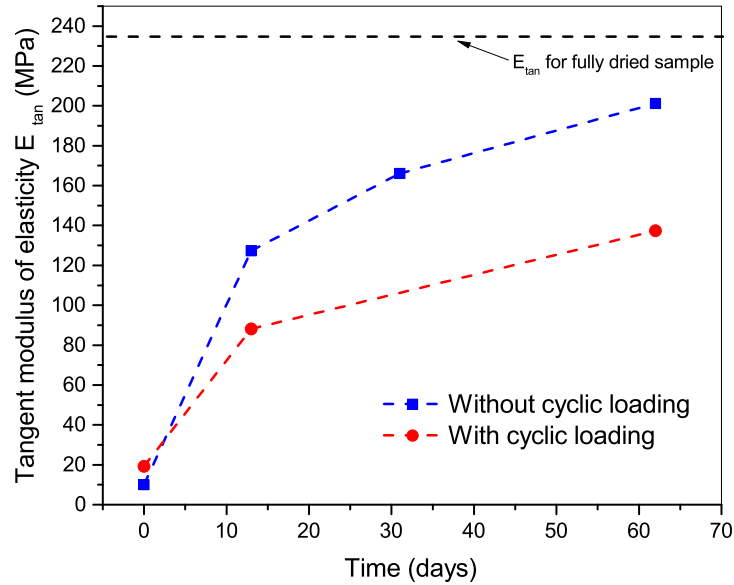


Figure 4.21: Variation of tangent modulus of elasticity with duration of drying for samples with and without unload-reload cycles

The initial tangent modulus (E_{tan}) was calculated from the initial part of the stress-strain curve from the global strain of all the samples, and not the local strain of the central part. Therefore, they are not fully representative of the one of the material but more of the structural stiffness. However, it gives an idea of the evolution of this stiffness with time, considering the same geometry and boundary conditions for all samples. The variation of initial tangent modulus with the duration of drying is shown in figure 4.21. The trend is very similar to the compressive strength variation. E_{tan} increases significantly from around 10 MPa at day 0 to 127.3 MPa at day 13. Further, the rate of increase of tangent modulus reduced and it reached a value of 166.1 MPa at day 31 and 201.2 MPa at day 62. The tangent modulus for samples with cyclic loading was slightly higher at day 0, while lower at other days of testing compared to without cyclic loading. The tangent modulus for the sample, which was fully dried is also shown and is higher than other samples tested.

4.3 Numerical analysis

Rammed earth after preparation at optimum moisture content is subjected to drying, and it leads to a gain in strength. This gain in strength is attributed to the additional suction-induced cohesion in the unsaturated state of the material. Conversely, when it is subjected to wetting (e.g., rainfall or inundation), a reduction in strength is observed. During the lifetime, rammed earth structure is subjected to changing humidity conditions (affecting the matric suction), which induces moisture transfers through the wall. Thus in order to predict the mechanical response, it is very important to estimate the hydraulic conditions of the material properly.

Thus the objective of this section is to perform the numerical simulations of the drying phase, and the compression tests performed previously on the rammed earth columns using a finite element code, i.e. CODE_BRIGTH (Olivella et al. 1996 [100]). It is a Finite Element Method (FEM) program capable of performing thermo-hydro-mechanical (THM) analysis in geological media. The first part aims to simulate the progressive drying of rammed earth column representative of a rammed earth wall which subjected to drying condition, from its initial compaction water content. The results from the simulations will be compared with the results obtained from the experiments, i.e. from SHT sensors which were used to record the drying behavior. Once a satisfactory matching with the experimental results is achieved based on the correct values of parameters used, mechanical simulations will be performed. In this second part, the rammed earth columns after being subjected to different duration of drying were compressed axially in order to simulate the failure stress. Finally, the failure stress obtained from the simulation will be compared to the experimental results.

4.3.1 Theoretical aspects of CODE_BRIGTH

For the basic formulations in CODE_BRIGTH, a porous medium which is composed of grains, water, and gas is considered. The different aspects which are taken into account are thermal, hydraulic, and mechanical resolution, and the coupling between them. It uses a multi-phases and multi-species approach. The different phases that we consider here include solid phase (s): soil particles, liquid phase (l): water and dissolved air, and gas phase (g): dry air and water vapor. The different species include solid (s): same as solid phase, water (w): liquid water and evaporated in gas phase, and air: dry air and dissolved in liquid phase. Some of the aspects and assumptions which are considered are mentioned below:

- The three phases are considered to be at the same temperature, i.e. a thermal equilibrium between phases.
- The various state variables (also called as unknowns) considered are solid displacements in 3 directions (\mathbf{u}), liquid pressure (P_l), gas pressure (P_g), and temperature

(T).

- Balance of momentum for the medium as a whole is reduced to the equation of stress equilibrium together with a mechanical constitutive model to relate stresses with strains. Strains are defined in terms of displacements.
- Small strains and small strain rates are assumed for solid deformation. Advective terms due to solid displacement are neglected after the formulation is transformed in terms of material derivatives.
- Balance of momentum for dissolved species and for fluid phases are reduced to constitutive equations (Fick's law and Darcy's law).
- Physical parameters in constitutive laws are function of pressure and temperature e.g. dynamic viscosity in Darcy's law depends on temperature.

The equations governing the problem is divided into 4 main groups. These are balance equations, constitutive equations, equilibrium relationships and definition constraints. For writing the balance equations following notations were used:

ϕ_p : porosity (-)	\mathbf{b} : body forces (MN)
ρ : density (kg/m^3)	ω : mass fraction (kg/kg)
\mathbf{j} : total mass flux (*)	e : specific internal energy (J)
\mathbf{i} : non-advective mass flux (*)	\mathbf{i}_c : conductive heat flux (*)
\mathbf{q} : advective flux (*)	\mathbf{j}_e : energy flux for mass motion (*)
\mathbf{u} : solid displacements (m)	S_l : liquid degree of saturation (-)
$\boldsymbol{\sigma}$: stress tensor (MPa)	S_g : gas degree of saturation (-)

Superscripts w and a refer to water and air, respectively. Subscripts s , l and g refer to solid, liquid and gas phase, respectively. (*) represents that the units of these flux terms depend on the type of flux such as point, line, surface, and volume flux.

4.3.1.1 Balance equations

The balance equations for mass considers an compositional approach which means that mass balance is performed for water, air, and solid species instead of phases. The total mass flux of a species in a phase (e.g. flux of water in gas phase \mathbf{j}_g^w) is defined as the sum of 3 terms:

- Non-advective flux: \mathbf{i}_g^w , i.e. diffusive/dispersive,
- Advective flux due to fluid motion: $\omega_g^w \rho_g \mathbf{q}_g$, where \mathbf{q}_g is the Darcy's flux,

- Advective flux due to solid motion: $\omega_g^w \rho_g S_g \phi_p \frac{d\mathbf{u}}{dt}$, where $\frac{d\mathbf{u}}{dt}$ is the vector of solid velocities

Mass balance of Solid

Mass balance of solid present in the medium is presented as:

$$\frac{\partial(\rho_s(1 - \phi_p))}{\partial t} + \nabla \cdot \mathbf{j}_s = 0 \quad (4.1)$$

where, ρ_s is mass of solid per unit volume of solid and \mathbf{j}_s is the flux of solid. The expression of porosity variation derived from equation 4.1 is as following:

$$\frac{D_s \phi_p}{Dt} = \frac{(1 - \phi_p)}{\rho_s} \frac{D_s}{Dt} + (1 - \phi_p) \nabla \cdot \frac{d\mathbf{u}}{dt} \quad (4.2)$$

where, D_s/Dt is the material derivative in Lagrangian framework. Thus the porosity variation expressed in equation 4.2 is due to the volumetric deformation and solid density variation.

Mass balance of water

The water exists in both liquid and gaseous phase, thus the total mass balance of water is written as:

$$\frac{\partial((\omega_g^w \rho_g S_g + \omega_l^w \rho_l S_l) \phi_p)}{\partial t} + \nabla \cdot (\mathbf{j}_g^w + \mathbf{j}_l^w) = f^w \quad (4.3)$$

where, $\omega_g^w \rho_g$ is mass of water in gas phase, $\omega_l^w \rho_l$ is mass of water in liquid phase, and f^w is the external supply of water. Using the material derivative following equation is obtained:

$$\begin{aligned} & \phi_p \frac{D_s(\omega_g^w \rho_g S_g + \omega_l^w \rho_l S_l)}{Dt} + (\omega_g^w \rho_g S_g + \omega_l^w \rho_l S_l) \frac{D_s \phi_p}{Dt} \\ & + (\omega_g^w \rho_g S_g + \omega_l^w \rho_l S_l) \phi_p \nabla \cdot \frac{d\mathbf{u}}{dt} + \nabla \cdot (\mathbf{j}_l^w + \mathbf{j}_g^w) = f^w \end{aligned} \quad (4.4)$$

where, \mathbf{j}' represents the sum of the non-advective and fluid motion advective terms i.e. excluding the solid motion advective terms from the total flux.

In order to evaluate the unknowns from the balance equations, the dependent variables are related to the unknowns. In equation 4.4, porosity occurs not only as a coefficient but also in the term involving its variation caused by different processes. In addition, there are variables that depend on porosity (e.g. intrinsic permeability). Thus, the derivative of porosity as a function of state variable is expressed via the mass balance of solids (4.2). In order to obtain the coupled flow-deformation equations, the material derivative in equation 4.4 can be approximated as Eulerian if the assumption of small strain rate is performed while the volumetric change (porosity derivative and volumetric

strain) is not neglected.

Mass balance of air

After obtaining the mass balance equation for water, the mass balance equation for air is expressed in the same manner taking into account the dry air as the main component of gas phase and air dissolved in liquid phase. The mass balance of air is written as:

$$\begin{aligned} \phi_p \frac{D_s(\omega_g^a \rho_g S_g + \omega_l^a \rho_l S_l)}{Dt} + (\omega_g^a \rho_g S_g + \omega_l^a \rho_l S_l) \frac{D_s \phi_p}{Dt} \\ + (\omega_g^a \rho_g S_g + \omega_l^a \rho_l S_l) \phi_p \nabla \cdot \frac{d\mathbf{u}}{dt} + \nabla \cdot (\mathbf{j}_l^a + \mathbf{j}_g^a) = f^a \end{aligned} \quad (4.5)$$

Momentum balance of the medium

Momentum balance of the porous medium is reduced to stress equilibrium if the internal terms of stresses are neglected:

$$\nabla \cdot \boldsymbol{\sigma} + \mathbf{b} = \mathbf{0} \quad (4.6)$$

where, $\boldsymbol{\sigma}$ is the stress tensor and \mathbf{b} represents the vector for body forces.

Internal energy balance of the porous medium

By taking into account the internal energy of each phase (e_s, e_l , and e_g), the internal energy balance equation for the porous medium can be expressed as:

$$\begin{aligned} \frac{\partial(e_g \rho_s (1 - \phi_p) + e_g \rho_g S_g \phi_p + e_l \rho_l S_l \phi_p)}{\partial t} - \frac{\phi_p S_g p_g}{\rho_g} \frac{\partial \rho_g}{\partial t} \\ + \nabla \cdot (\mathbf{i}_c + \mathbf{j}_{es} + \mathbf{j}_{eg} + \mathbf{j}_{el}) = f^Q \end{aligned} \quad (4.7)$$

where, \mathbf{i}_c is the energy flux due to conduction through the porous medium, \mathbf{j}_{es} , \mathbf{j}_{eg} , and \mathbf{j}_{el} are the advective fluxes of energy by mass motion of every species in the medium, and f^Q is an internal/external energy supply.

These governing equations have been established by Olivella et al. 1996 [100]. This theoretical work has been implemented for the development of finite element method computer program CODE_BRIGTH which was used in this work. The various equilibrium equations and independent variables (unknowns) are summarized in table 4.2.

4.3.1.2 Constitutive equations and equilibrium restrictions

In table 4.3, a summary of the constitutive laws and equilibrium restrictions that are incorporated in the formulation of the problem. The dependent variable computed for each constitutive laws is also mentioned.

Table 4.2: Independent variables (unknowns) summary

VARIABLE NAME	Notation	Equilibrium equation of resolution
displacements	\mathbf{u}	Balance of momentum
liquid pressure	P_l	Mass balance of water
gas pressure	P_g	Mass balance of air
temperature	T	Internal energy balance

Table 4.3: Constitutive equations and equilibrium restrictions

EQUATION	VARIABLE NAME	Notation
Constitutive equations		
Darcy's law	liquid and gas advective flux	$\mathbf{q}_l, \mathbf{q}_g$
Fick's law	vapour and air non-advective fluxes	$\mathbf{i}_g^w, \mathbf{i}_l^a$
Fourier's law	conductive heat flux	\mathbf{i}_c
Retention curve	Liquid phase degree of saturation	S_l, S_g
Mechanical constitutive model	Stress tensor	$\boldsymbol{\sigma}$
Equilibrium restrictions		
Henry's law	Air dissolved mass fraction	ω_l^a
Psychrometric law	Vapour mass fraction	ω_g^w

The constitutive equations relate the independent variables (unknowns) with the dependent variables. The governing equations are finally expressed in the form of unknowns by substituting the constitutive equations in the balance equations. In addition to the constitutive equations, another form of equations that links the independent and dependent variables are the equilibrium restrictions. They are developed by considering chemical equilibrium for dissolution of the different species (air and vapour) in phases (liquid, gas).

Darcy's law

The equation used for the liquid advective flux (\mathbf{q}_l) was the Darcy's law defined as:

$$\mathbf{q}_l = -\frac{k_i k_{rl}}{\mu_l} (\nabla P_l - \rho_l g) \quad (4.8)$$

where, μ_l (MPa.s) is the liquid dynamic viscosity, P_l is liquid pressure (MPa), k_i is the intrinsic permeability, and k_{rl} is the relative liquid hydraulic conductivity.

Retention curve

The retention behavior of rammed earth was defined by using the Van Genuchten 1980 [101] (VG) model. The Van Genuchten expression for effective degree of liquid saturation (S_{el}) is defined as:

$$S_{el} = \frac{S_l - S_{rl}}{S_{ml} - S_{rl}} = \left[\frac{1}{1 + (\alpha_w s)^{n_w}} \right]^{m_w} \quad (4.9)$$

where, S_l is the actual degree of liquid saturation, α_w (MPa)⁻¹, n_w , and m_w are model parameters, s is matric suction (MPa). Here, the maximum (S_{ml}) and residual (S_{rl}) degree of saturation were considered as 1 and 0 respectively, so $S_{el} = S_l$. m_w is related to n_w as $m_w = (n_w - 1)/n_w$.

The unsaturated hydraulic conductivity function was defined as $k_l = k_{rl}k_{sat}$, where k_r is the relative hydraulic conductivity and k_{sat} is the saturated hydraulic conductivity. Mualem hydraulic conductivity model (1976) [24] using the Van Genuchten retention curve parameters was used to express k_r as a function of S_l coupled with Van Genuchten retention model, which gives:

$$k_{rl} = \sqrt{S_l} \left[1 - \left(1 - S_l^{1/m_w} \right)^{m_w} \right]^2 \quad (4.10)$$

The intrinsic permeability (k_i) can be related to the saturated hydraulic conductivity (k_{sat}) by the expression:

$$k_i = \frac{k_{sat} \cdot \mu_w}{\rho_l g} \quad (4.11)$$

where, ρ_l is the density of water and μ_w is the dynamic viscosity of water.

Fick's law

The diffusive flux of water vapor in gas phase (\mathbf{i}_g^w) was evaluated using Fick's law of vapor diffusion:

$$\mathbf{i}_g^w = - (t_s \phi_p \rho_g S_g D_g^w \mathbf{I}) \nabla \omega_g^w \quad (4.12)$$

where, t_s = tortuosity, ϕ_p = porosity, ρ_g = gas density, $S_g = 1 - S_l$ is the gas degree of saturation, D_g^w (m^2/s) is diffusion coefficient of water vapor in gas phase, ω_g^w (kg/kg) is the mass fraction of water vapor in gas phase.

The molecular diffusion of vapor in gas phase is determined from the following equation:

$$D_g^w = D \left[\frac{(273.15 + T)^d}{P_g} \right] \quad (4.13)$$

where, P_g is the gas pressure in Pa, D ($m^2 s^{-1} K^{-2.3} Pa$), d are the vapor diffusion parameters.

Fourier's law

In order to determine the conductive flux of heat, Fourier's law was used. Thermal conductivity was used in the Fourier's law to compute the conductive heat flux \mathbf{i}_c :

$$\mathbf{i}_c = \lambda \nabla T \quad (4.14)$$

where, λ ($W m^{-1} K^{-1}$) is the thermal conductivity of the porous medium, which is further

defined as:

$$\lambda = \lambda_{sat} \sqrt{S_l} + \lambda_{dry} (1 - \sqrt{S_l}) \quad (4.15)$$

where, λ_{dry} and λ_{sat} are the thermal conductivity of the medium in dry phase and saturated phase respectively. These parameters are further evaluated from the thermal conductivity of each phase taking into account the porosity of the medium as follows:

$$\lambda_{dry} = \lambda_{solid}^{1-\phi_p} \lambda_{gas}^{\phi_p} \quad (4.16)$$

$$\lambda_{sat} = \lambda_{solid}^{1-\phi_p} \lambda_{liq}^{\phi_p} \quad (4.17)$$

where, ϕ_p is the porosity, λ_{solid} , λ_{gas} , and λ_{liq} ($Wm^{-1}K^{-1}$) are the thermal conductivity of solid, gas and liquid phases respectively.

Mechanical constitutive model

The most suitable model that was found in CODE_BRIGHT was viscoplasticity model for unsaturated soils and rocks. This model, when combined with linear elasticity model and adjusting the parameters used for viscosity in order to remove the viscous effects, a linear elastic-perfectly plastic model can be obtained.

A linear elastic model is based on Hook's law which is a linear stress-strain relationship. This law relates the total or effective stress to strains. It can be expressed using two soil parameters, modulus of elasticity (E) and Poisson's ratio (ν). This model can be written in an incremental form as follows:

$$d\boldsymbol{\sigma} = \mathbf{D}^e . d\boldsymbol{\epsilon}^e \quad (4.18)$$

where, $\boldsymbol{\sigma}$ is the incremental stress tensor, $d\boldsymbol{\epsilon}^e$ is the incremental elastic strain tensor, and \mathbf{D}^e is the elastic stiffness matrix. In CODE_BRIGHT, the modulus of elasticity is defined as follows:

$$E = E_0 + (\phi_p - \phi_{p0}) \frac{dE}{d\phi_p} \geq E_{min} \quad (4.19)$$

where, E is Young's modulus of elasticity, E_0 is the reference Young's modulus of elasticity, $\frac{dE}{d\phi_p}$ represents the change in Young's modulus with porosity (ϕ_p), ϕ_{p0} is the reference porosity. In this study, ϕ_p is taken as equal to ϕ_{p0} , thus the Young's modulus is independent of porosity ($E = E_0$).

The elastic stresses are limited by plasticity. The yield function (F) and the associated plastic potential (G) are defined using the Drucker-Prager model (figure 4.22) which is

based on Mohr-Coulomb parameters:

$$G = F = q - Mp - Mc/\tan\phi' \quad (4.20)$$

with

$$M = \frac{6\sin\phi'}{3 - \sin\phi'} \quad (4.21)$$

where, p is the mean stress, q is the deviatoric stress, c is the apparent cohesion (defined in terms of effective cohesion and suction), and ϕ' is the effective friction angle respectively.

Invariants used in the models are defined as:

$$p = \frac{1}{3}I_1 = \frac{1}{3}(\sigma_{xx} + \sigma_{yy} + \sigma_{zz}) \quad (4.22)$$

$$q = \frac{1}{\sqrt{2}}\sqrt{(\sigma_{xx} - \sigma_{yy})^2 + (\sigma_{yy} - \sigma_{zz})^2 + (\sigma_{zz} - \sigma_{xx})^2 + 6(\tau_{xy}^2 + \tau_{yz}^2 + \tau_{zx}^2)} \quad (4.23)$$

In the constitutive framework of unsaturated soils, there are two different approaches to define the system and completely analyze the mechanical response. The first approach uses 2 independent stress state variables out of the 3 state variables for unsaturated soils i.e. net stress ($\sigma - u_a$), effective stress for saturated soils ($\sigma - u_w$) and matric suction ($u_a - u_w$). Commonly, $\sigma - u_a$ and $u_a - u_w$ are used. The second approach is generalized effective stress approach in which single effective stress such as Bishop's effective stress which defines the stress state of a multi-phase porous medium. In the constitutive framework used in the original model, 2 independent stress state variables i.e. $\sigma - u_a$ and $u_a - u_w$ are used. The coupled problem and the failure criterion is written in terms of total stress, notably with the expression of cohesion term, which is only apparent and not intrinsic. Thus, in order to use this particular model in our study, the expression of Bishop's effective stress [90] have been included in the shear strength expression.

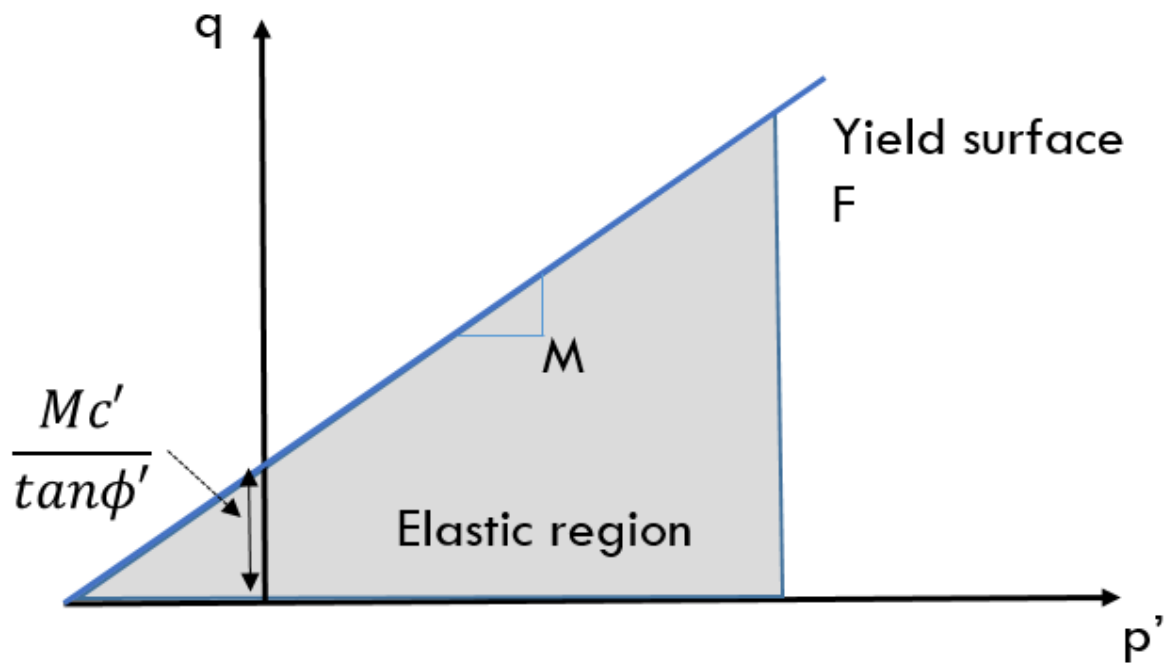
In the original code, the shear strength (τ) was modelled in the form given by Fredlund and Morgenstern [102]:

$$\tau = c + (\sigma - u_a)\tan\phi' \quad (4.24)$$

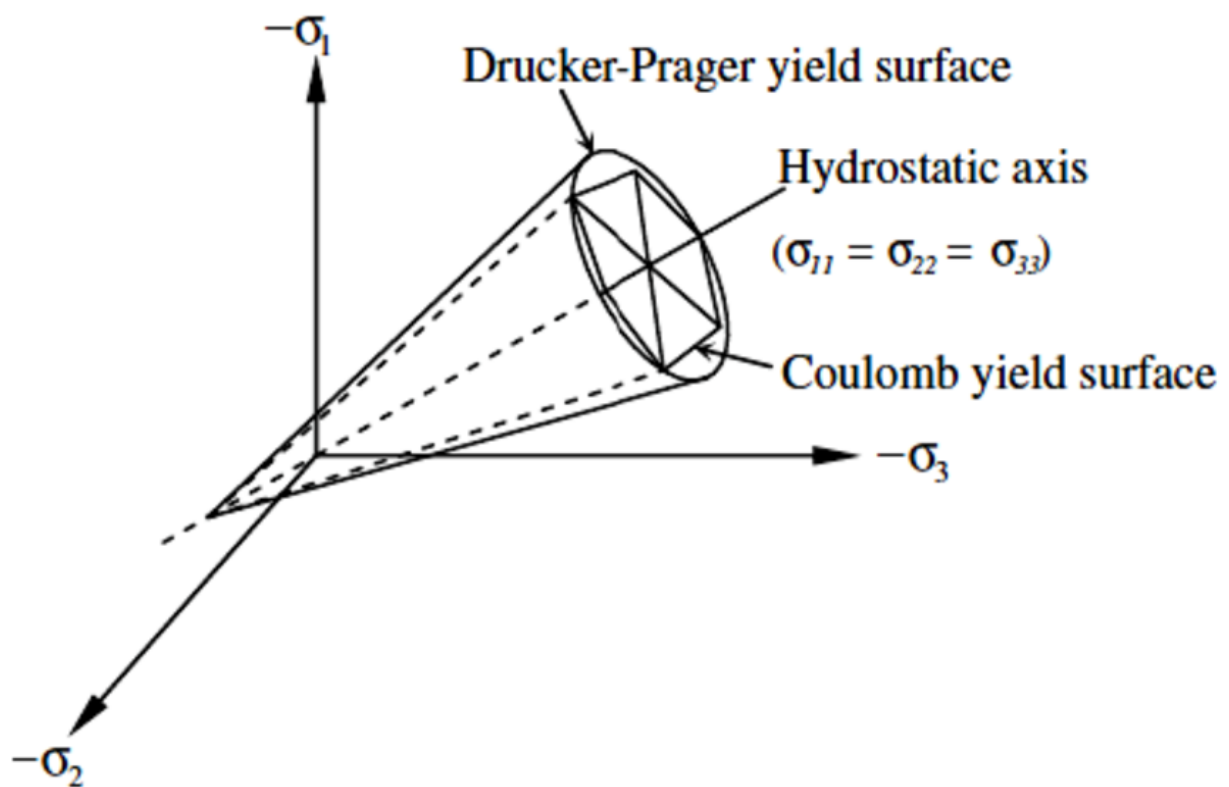
where, σ is the total stress, u_a is the pore-air pressure, ϕ' is the effective friction angle, and c , which is the apparent cohesion is expressed as:

$$c = c' + b.s \quad (4.25)$$

where, $s = u_a - u_w$ is the suction, c' is the effective cohesion, and b is the parameter of the model which determines the rate of change of cohesion with suction. Also, equation 4.25 shows that the apparent cohesion is increasing linearly with suction. In the experimental study done before, it was evident that apparent cohesion and thus, shear strength does



(a)



(b)

Figure 4.22: Yield surface for Drucker-Prager plasticity model in p' - q space (a) and in principal stress space (b)

not increase linearly with suction. The rate of increase of shear strength is higher at low suction values, and this rate decreases with increase of suction to finally reach a plateau. The variation in shear strength is not only dependent on suction but also on the degree of saturation which highlights the proportion of water on which the given suction is acting. Thus, in order to solve this issue, changes were made in the code to include the effect of degree of saturation on the apparent cohesion.

The shear strength expression using the effective stress (σ') can be written as:

$$\tau = c' + \sigma' \tan \phi' \quad (4.26)$$

The expression for effective stress given by Bishop [90] is as follows:

$$\boldsymbol{\sigma}' = \boldsymbol{\sigma} - u_a \mathbf{I} + S_l^\alpha s \mathbf{I} \quad (4.27)$$

Using this expression of effective stress in equation 4.26, gives the following equation for shear strength:

$$\tau = c' + s S_l^\alpha \tan \phi' + (\sigma - u_a) \tan \phi' \quad (4.28)$$

Thus, the modified version of code uses the following expression for c :

$$c = c' + s S_l^\alpha \tan \phi' \quad (4.29)$$

Finally, the parameter b used in the original code was changed to α in the modified version of the code. It is to be noted that friction angle does not change with suction in the model. This is acceptable since in the triaxial tests, the friction angle does not vary significantly and is close to the intrinsic value. This approach has a limitation since the Young's modulus of elasticity is a constant value and does not change with suction. In addition, the non-linearity of the failure envelope in $\tau - \sigma$ plane has not been taken into account since the compression testing of columns is without any confining stress. In lower range of normal stress the failure envelope is considered linear.

The coupling between the thermal, hydric and mechanical analysis is shown in figure 4.23. The hydric effect on the thermal behavior is taken into account by using Fourier's law as the thermal conductivity of the soil is dependent on the degree of saturation. The mechanical effect on the thermal behavior is considered in a similar manner since the change in porosity of the soil leads to change in degree of saturation.

The thermal effect on the hydric behavior is taken into account through Fick's law where the diffusion coefficient is dependent on the temperature. The mechanical effect on the hydric behavior is considered as the change in porosity leads to change in degree of saturation and the liquid flow linked using Darcy's law.

It is considered that there are no direct thermal effects on the mechanical behavior. Still, the thermal effects on hydric behavior can affect the mechanical behavior through liquid pressure/suction. The most important coupling for this study is the hydro-

mechanical coupling. The effect of hydric state on mechanical behavior is considered using suction and the introduction of effective stresses in the failure criterion.

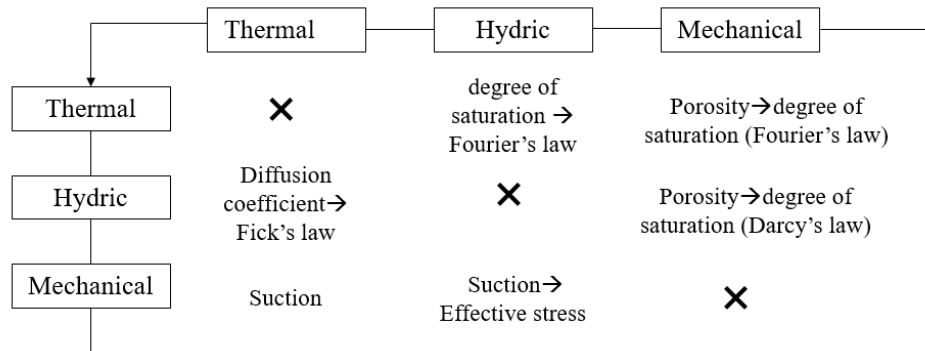


Figure 4.23: The coupling between the thermal, hydric and mechanical analysis shown as the effect of T/H/M (shown in horizontal) on the T/H/M (shown in vertical)

The various parameters required to perform the couple thermo-hydro-mechanical analysis are shown in table 4.5. The hydraulic parameters includes the retention curve parameters (α_w and n_w), intrinsic permeability (k_i), and the vapor diffusion parameters (D, d , and t_s). The thermal conductivity of solid (λ_{solid}), liquid (λ_{liq}), and gas phase (λ_{gas}) respectively are the required thermal parameters. Finally, the mechanical parameters required are elastic parameters (E and ν), plasticity parameters (c' , ϕ' , and α), and porosity (ϕ_p). The values used for these parameters is described in the next section.

Table 4.4: Synthesis of hydraulic, thermal, and mechanical parameters required for the THM coupled modelling

Hydraulic parameters	Thermal parameters	Mechanical parameters
α_w	λ_{solid}	E
n_w	λ_{liq}	ν
k_i	λ_{gas}	c'
D		ϕ'
d		ϕ_p
t_s		α

4.3.2 Material parameters

4.3.2.1 Hydro-thermal parameters

The Van-Genuchten (VG) model [101] for soil-water retention curve previously described in equation 4.9 was used for the retention behavior (figure 4.24). The VG model parameters were evaluated as $\alpha_w = 3.479$, $n_w = 1.379$, and $m_w = 0.2748$.

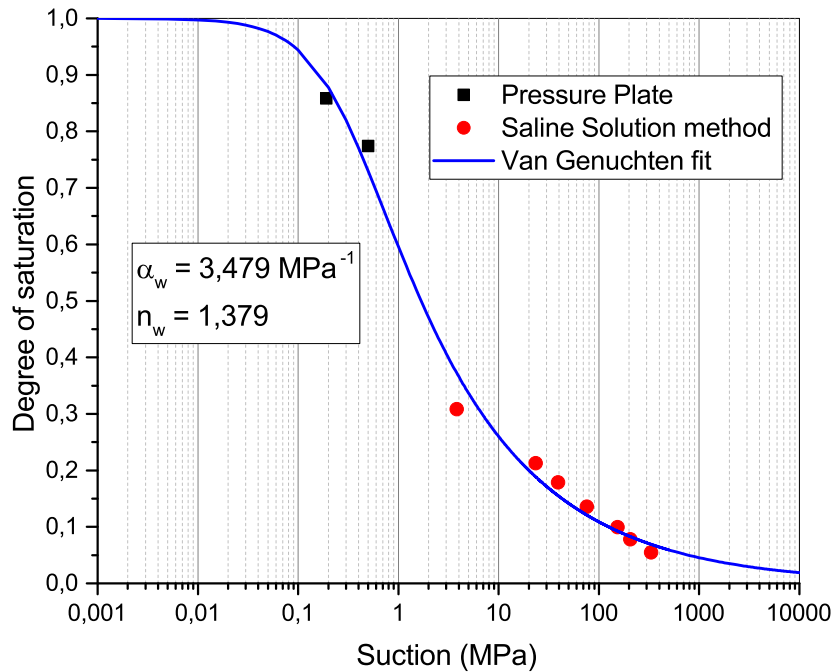


Figure 4.24: Soil water retention curve obtained from pressure plate and saline solution method using Van-Genuchten fitting parameters

The unsaturated hydraulic conductivity (k) which was defined previously as the product of saturated hydraulic conductivity (k_{sat}) and relative hydraulic conductivity (k_r) was modeled using Mualem hydraulic conductivity model which uses the parameter m_w of Van-Genuchten retention curve model. The variation of relative hydraulic conductivity (k_r) evaluated using equation 4.10 as a function of liquid degree of saturation is shown in figure 4.25.

The saturated hydraulic conductivity was evaluated from the rammed earth columns by drilling the columns in the direction of drying, i.e. horizontally. These samples were tested in a triaxial device as mentioned in the previous section. The average saturated hydraulic conductivity was determined equal to 6.3×10^{-9} m/s, and the intrinsic permeability was evaluated using equation 4.11 as 5.7×10^{-16} m^2 .

To study the diffusive flux of water vapor in gas phase, Fick's law of diffusion was used. The parameters used to evaluate the molecular diffusion of vapor in gas phase

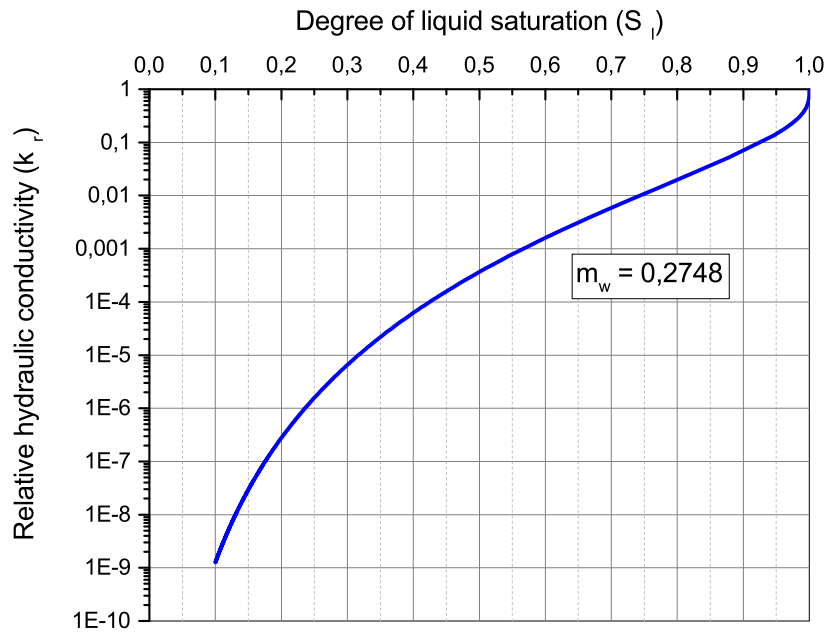


Figure 4.25: Relative hydraulic conductivity as a function of liquid degree of saturation using Mualem model [24]

in equation 4.13 are $D (m^2 s^{-1} K^{-2.3} Pa) = 5.9 \times 10^{-6}$ and $d = 2.3$. Tortuosity (τ) was taken as constant equal to 1.

The range of thermal conductivity (λ) of rammed earth in its dry state recommended according to "Guide de Bonnes Pratiques (GBP) Pisé, 2018" [25] is from 0.46 - 0.81 ($W m^{-1} K^{-1}$). In the model used here, the values of thermal conductivity for each phase, i.e. solid, liquid, and gas phase are used, and the thermal conductivity of the porous medium is evaluated based on the degree of saturation. The thermal conductivity of liquid (λ_{liq}) and gas (λ_{gas}) phase taken as thermal conductivity of water and air is 0.6 and 0.025 ($W m^{-1} K^{-1}$) respectively. The thermal conductivity of solid phase (λ_{solid}) based on the range specified before was taken as 1.5 ($W m^{-1} K^{-1}$). All the hydro-thermal parameters used are summarized in table 4.5.

4.3.2.2 Mechanical parameters

For the elastic part, only a linear elastic model with a constant value of modulus of elasticity was used. It was observed before that the elastic modulus varies with suction, and this model is not able to take the evolution of elastic modulus with suction into account. Thus, the elastic modulus used in the model is corresponding to the experimental values tested at different duration of drying in order to fit the results of the simulations with the experimental results. The value of Poisson's ratio (ν) was taken as constant equal to 0.25 from the literature [5][20]. This value was taken since there was no accurate

data for this parameter.

The mechanical response was considered fully elastic up to the yield limit, which corresponds to the failure limit. Thus the mechanical behavior is elastic-perfectly plastic. As the elastic behaviour is not reproducible, we only have efficient modelling of the sustainable limit stress. Indeed our approach is close to a limit analysis approach, and we are predicting the failure stress and not the stress-strain curve.

For the plasticity part, the Drucker-Prager failure surface, which is based on Mohr-Coulomb parameters, was adopted (equation 4.20). The values of effective cohesion (c') and effective friction angle (ϕ') were taken from the consolidated undrained (CU) triaxial tests carried out on saturated small cylindrical samples in chapter 3. The value of c' and ϕ' was taken as 43.91 kPa and 32.53°.

The expression of Bishop's stress was taken into account in the expression of shear strength (equation 4.28). To define this, the effective stress parameter χ , which is a function of liquid degree of saturation ($\chi = S_l^\alpha$) needs to be determined. Based on the experimental study done before on the same material shown in section 3.6 in chapter 3, the value of exponent was taken as $\alpha = 1.9081$. The value of all the mechanical parameters is summarized in table 4.5.

Table 4.5: Various material parameters used for THM coupled problem and the method of determination of these parameters, where 'Exp' represents determined experimentally, 'C' represents that the classical or default value is chosen, and 'L' represents taken from literature

Parameters	Symbols	Units	Values	Determination
Hydric parameters				
VG Retention curve parameter	α_w	$(MPa)^{-1}$	3.479	Exp
VG Retention curve parameter	n_w	-	1.379	Exp
Intrinsic permeability	k_i	m^2	5.7×10^{-16}	Exp
Vapor diffusion parameter	D	$m^2 s^{-1} K^{-2.3} Pa$	5.9×10^{-6}	C
Vapor diffusion parameter	d	-	2.3	C
Tortuosity	t_s	-	1	C
Thermal parameters				
Thermal conductivity of solid	λ_{solid}	$(W m^{-1} K^{-1})$	1.5	C
Thermal conductivity of liquid	λ_{liq}	$(W m^{-1} K^{-1})$	0.6	C
Thermal conductivity of gas	λ_{gas}	$(W m^{-1} K^{-1})$	0.025	L (GBP Pisé, 2018 [25])
Mechanical parameters				
Poisson's ratio	ν	-	0.25	L [5][20]
Effective cohesion	c'	kPa	43.91	Exp
Effective friction angle	ϕ'	°	32.53	Exp
Exponent of effective stress parameter	α	-	1.9081	Exp
Porosity	ϕ_p	-	0.291	Exp

4.3.3 Numerical simulations of drying phase

Numerical simulations of the drying process of rammed earth were performed using CODE_BRIGHT. Here, THM coupled analysis was performed considering an immobile gas phase. Thus the gas pressure (P_g) was assumed to be atmospheric ($P_g = 0.1$ MPa). The geometrical model considered was a 3D column representing the experimental column of height 0.3 m, and length and width of 0.14 m (figure 4.26). The mesh was refined along the direction of drying (x) since the drying problem is a 1D problem. Although for the drying phase of the problem, a 3D model is not required, but it is used since the same model will be used for the compression problem as well. A mesh of 50 x 10 x 5 (2500) linear hexahedral (C3D8) elements were used (figure 4.26). The mesh generated had a '0.1' concentration of mesh close to the edges in the x-direction since the drying problem begins at the boundary of the column. Whereas in the z-direction, no exchange of water is taking place, and thus only 5 elements were used without any mesh concentration. The total number of nodes was 3366. It is to be noted that the layers of the columns were not taken into account, and homogeneous density was taken in the model.

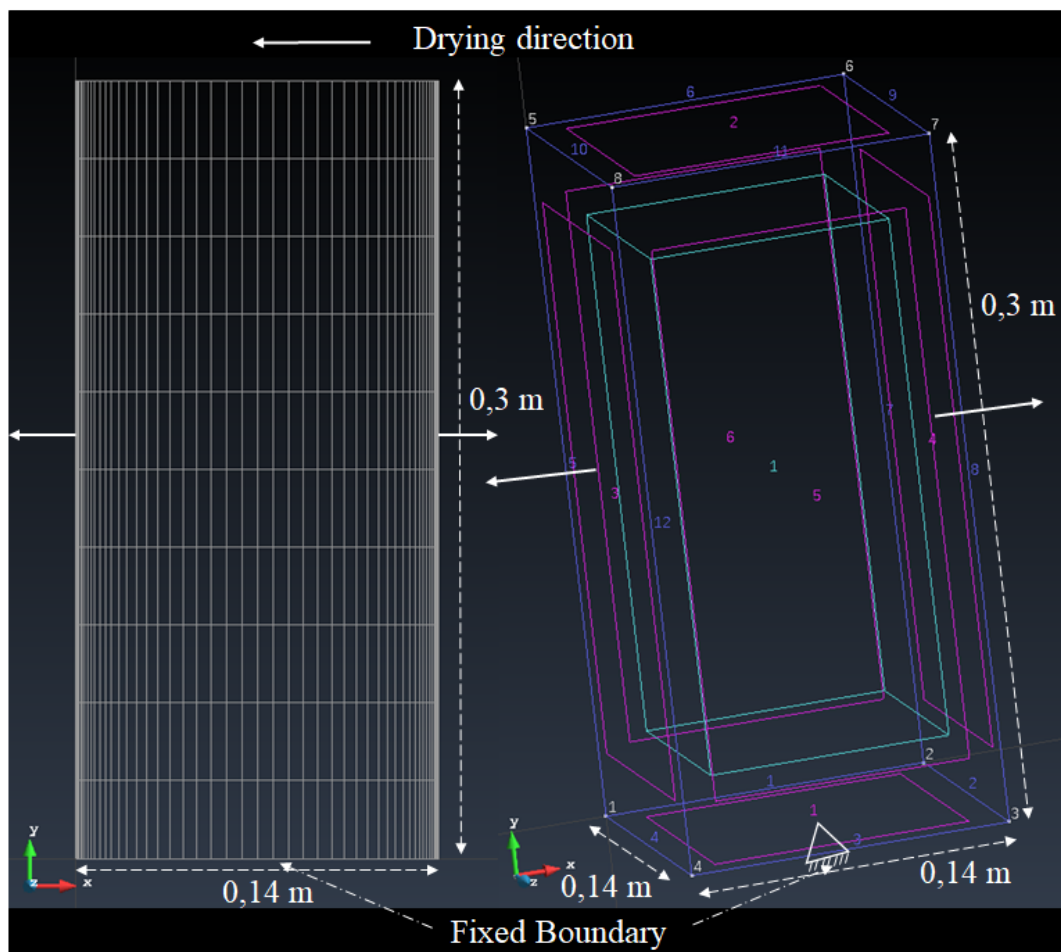


Figure 4.26: The geometrical 3D model of the problem (right) and the 2D mesh composition (left)

4.3.3.1 Initial conditions and boundary conditions

From the experimental campaign at REV scale, the initial degree of liquid saturation after compaction at optimum moisture content was 0.805. The initial condition of liquid pressure (P_l) of the numerical model was chosen from the retention curve. From the Van Genuchten retention model, the initial suction corresponding to degree of liquid saturation (S_l) was equal to 0.328 MPa. As the gas pressure (P_g) in the problem is constant equal to 0.1 MPa, the initial liquid pressure used in the simulation was equal to -0.228 MPa (negative values means depression in code convention). The initial temperature was measured from the SHT sensors and was taken as $T=15.5$ °C.

When an imposed liquid pressure (and hence suction) is applied as the boundary condition, the boundary immediately reaches the final suction state and is supposed to be in equilibrium with the atmosphere. This condition is not realistic since the equilibrium at the surface is reached over time, and the boundary reaches the final suction state asymptotically. Thus, in this study, a more realistic atmospheric boundary condition was used. CODE_BRIGHT allows imposing a boundary condition that includes mass and heat conditions to be applied in terms of atmospheric data.

Atmospheric boundary condition allows the application of boundary conditions in terms of evaporation, rainfall, radiation, and heat exchanges. In this way, it is able to simulate the complex soil-atmosphere interactions. Flux boundary condition was used to express these phenomena for the three different components, i.e. water, air, and energy in terms of their respective state variables, i.e. liquid pressure, gas pressure, and temperature or dependent variables (such as liquid saturation degree, fraction of water in gas phase as water vapor). In addition, it uses various ambient conditions such as relative humidity, atmospheric gas pressure, ambient temperature, and air velocity. These conditions can further vary with time or remain constant. Here the data related to solar radiation and rainfall have not been used since this boundary condition was used for an indoor environment. The water flux was computed as follows:

Flux of water

In order to simulate natural convection, the flux due to evaporation has been modified since this atmospheric boundary condition is generally used for an outdoor environment. In CODE_BRIGHT, the evaporation flux E_v ($kg s^{-1} m^{-2}$) is defined by an aerodynamic diffusion relation:

$$E_v = \frac{kv_a s_f}{\left(\ln \frac{z_a}{z_o}\right)^2} (\rho_{va} - \rho_v) \quad (4.30)$$

The evaporation flux can also be defined as [103]

$$E_v = h_m (\rho_{va} - \rho_v) \quad (4.31)$$

where, ρ_{va} and ρ_v are the absolute humidity of the atmosphere and at the boundary

respectively, k is the von Karman's constant, s_f is a stability factor, v_a the wind velocity, z_o is the roughness length, z_a is the screen height at which v_a and ρ_{va} are measured, h_m (m/s) is the surface mass transfer coefficient. Thus, by equating equations 4.30 and 4.31 we have:

$$h_m = \frac{kv_a s_f}{\left(\ln \frac{z_a}{z_o}\right)^2} \quad (4.32)$$

Arbitrary values the parameters on right side of equation 4.32 were chosen to implement the value of surface mass transfer coefficient (h_m) and thus it is the key parameter instead of air velocity (v_a). The surface mass transfer coefficient (h_m) can be evaluated from the heat transfer coefficient h_c ($Wm^{-2}K^{-1}$) using Lewis relation:

$$h_m = \frac{h_c}{\rho_a C_p} \quad (4.33)$$

where, ρ_a is the air density = 1.223 kg/m^3 and C_p is the air specific heat = $1.006 \text{ kJkg}^{-1}K^{-1}$ at $T = 15.5 \text{ }^\circ\text{C}$.

According to Kusuda et al. 1983 [104], a heat transfer coefficient of $h_c = 0.85Wm^{-2}K^{-1}$ can be used to evaluate the mass transfer coefficient (h_m) for indoor conditions where natural convection takes place. Also, Howell et al. 2005 [105], suggests the value of heat transfer coefficient h_c to be in the range $2\text{-}25 \text{ }Wm^{-2}K^{-1}$ for natural convection for gases. Thus, the bibliography study gives values of heat transfer coefficient (h_c) between 0.85 and $25 \text{ }Wm^{-2}K^{-1}$. From this data, the value of surface mass transfer coefficient (h_m) is in the range $0.0007\text{-}0.02 \text{ m/s}$. Since the experimental determination of either mass transfer or heat transfer coefficient was difficult, this parameter will be adjusted to fit the experimental results while taking into account the limits given in the bibliography.

Other parameters for the atmospheric boundary conditions were $P_g = 0.1\text{MPa}$ and $T = 15.5 \text{ }^\circ\text{C}$. Relative humidity of 65% was chosen as the ambient RH, and this value was recorded from the SHT sensors. This corresponds to a suction value of 55.85 MPa using Kelvin's law at the given temperature.

Regarding the mechanical initial conditions, the initial stresses in all directions were taken as 0. The initial values of unknowns i.e. displacements in x,y, and z direction, was also taken as 0. The mechanical boundary conditions during the drying phase was only the bottom surface being fixed ($u_x = u_y = u_z = 0$) while all the other surfaces were stress-free with displacements being allowed.

4.3.3.2 Drying phase simulation results

In this section, the results of the simulations for the drying phase is presented. The value of the heat transfer coefficient was adjusted in order to fit the experimental results sufficiently. In addition, it was made sure that the value is coherent with the guidelines given in the literature by Howell et al. 2005 [105]. The value of heat transfer coefficient

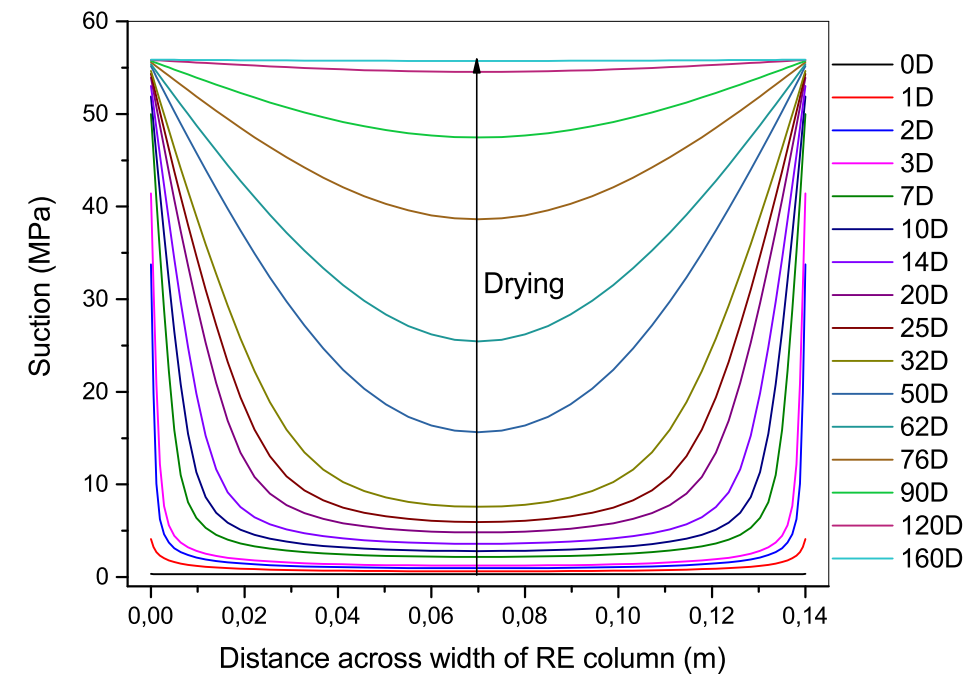
(h_c) was taken as $25 \text{ Wm}^{-2}\text{K}^{-1}$ which corresponds to a value of mass transfer coefficient (h_m) of 0.02 m/s using the Lewis relationship.

Figure 4.27 shows the isochrones of suction and degree of liquid saturation across the width of rammed earth column. From the suction profiles, it can be seen that suction at the boundary does not reach the final equilibrium suction state immediately and is gradually increasing over time and approaches the final equilibrium suction of 55.85 MPa which is the equilibrated value for an ambient relative humidity of 65%. Thus, there are lower gradients of suction between the boundary and inside of the sample than would occur if the boundary reached the final suction state at time $t = 0$. At the beginning of drying phase, the change in suction is predominantly close to the boundary and increases at a high rate. The suction at the boundary reaches to about 51.88 MPa after 10 days of drying. This rate of suction increase decreases once the boundary reaches close to the equilibrium state. The suction increased from 51.88 MPa after 10 days to 55.37 after 62 days and finally close to final suction of 55.85 MPa after 160 days of drying. Whereas at the middle of the sample, the suction increases slowly to about 2.8 MPa after 10 days of drying from 0.228 MPa at the beginning of drying. This rate of increase in suction increases in the middle stage of drying. The suction increases from 2.8 MPa after 10 days to 25.43 MPa after 62 days. Once the middle of the sample reached close the final equilibrium suction state, the process of drying slows down, and the rate of increase of suction decreases. The suction increases at a slower rate gradually from 54.54 MPa after 120 days to 55.72 MPa after 160 days of drying, still not reaching the final suction state.

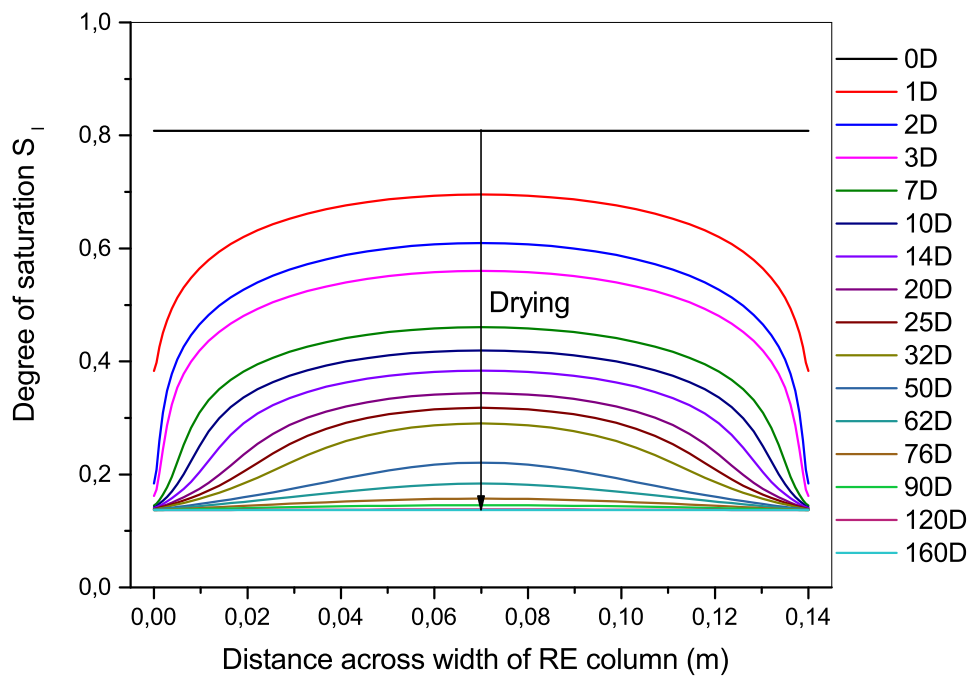
A similar observation can be made for the variation of liquid degree of saturation. The degree of saturation decreases significantly at the boundary reaching to about 0.14 after 10 days of drying. This rate of decrease in degree of saturation reduces once the boundary reaches close to the final state. The degree of saturation reduces from 0.14 after 10 days to 0.137 after 62 days and finally to 0.136 after 160 days of drying period. At the middle of the sample, the rate of decrease of degree of saturation is lower as compared to the boundary at the beginning of drying phase. The change in degree of saturation at the middle is greater once the boundary reaches close to the final state. It changes from 0.419 after 10 days to 0.183 after 62 days and finally after 160 days it reaches to 0.136.

From figure 4.27a, it appears that after 3 days of drying period the suction in the middle third of the sample is hardly affected, but from the degree of saturation profiles, it is clear that a significant amount of water has been taken out. The degree of saturation at the boundary decreased from 0.805 to 0.16, whereas at the center of the sample, it decreased to 0.56. This behavior is due to the nature of the retention curve (figure 4.24), as a significant amount of water needs to dry in order to have larger values of suction.

Figure 4.28 shows the comparison of the experimental and simulation results for relative humidity. The experimental results are shown with error bars due to the uncertainty in the measurement of relative humidity by the sensors. The results of the simulation after during drying were fairly close to the experimental results. The relative humidity across the whole width reached close to the final value of 65% in around 160



(a)



(b)

Figure 4.27: Isochrones of suction (a) and liquid degree of saturation (b) across the width of rammed earth column

days. Although the drying process takes a longer time, the pattern of drying is similar. The difference in relative humidity between 5 cm and 7 cm is lower compared to 3 cm and 5 cm. This gradient across the width first increases and then decreases as the drying process approaches its final stage.

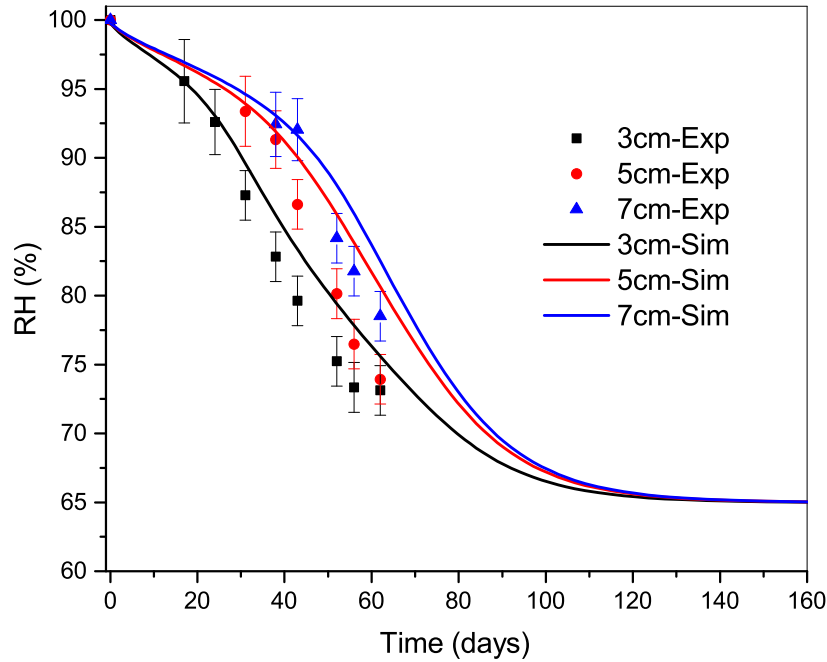


Figure 4.28: Comparison of experimental and simulation results for relative humidity

The following discussion includes the comparison of relative humidity at three different duration of drying at which the mechanical tests were carried out, i.e. 13, 31, and 62 days. After 13 days of drying experimental results shows no variation of RH from 100% at 3 cm, 5cm, and 7 cm. Whereas for the numerical simulation, the relative humidity was 96.51%, 97.31%, and 97.47% at 3 cm, 5cm, and 7 cm respectively. As discussed before, it is possible that the sensors show no change on account of being at a very high relative humidity. After 31 days of drying, the relative humidity for the experiments were 87.27%, 93.37%, and 100% at 3 cm, 5cm, and 7 cm respectively. Whereas for the relative humidity for the simulations were 89.73%, 93.99%, and 94.67% at 3 cm, 5cm, and 7 cm respectively. A maximum difference of 5.3% between the results is obtained at 7 cm, which is acceptable. Finally, after 62 days of drying, the experimental results show relative humidity of 73.13%, 73.93%, and 78.51% at 3 cm, 5cm, and 7 cm respectively. Whereas for the relative humidity for the simulations were 75.13%, 80.52%, and 82.39% at 3 cm, 5cm, and 7 cm respectively. The maximum percentage difference at 3 cm distance from the drying phase was 3.26%, and a maximum difference of 8.91% was obtained at 5 cm. These difference in the results can be justified due to the reasons mentioned above, and a decent fit between the results was obtained.

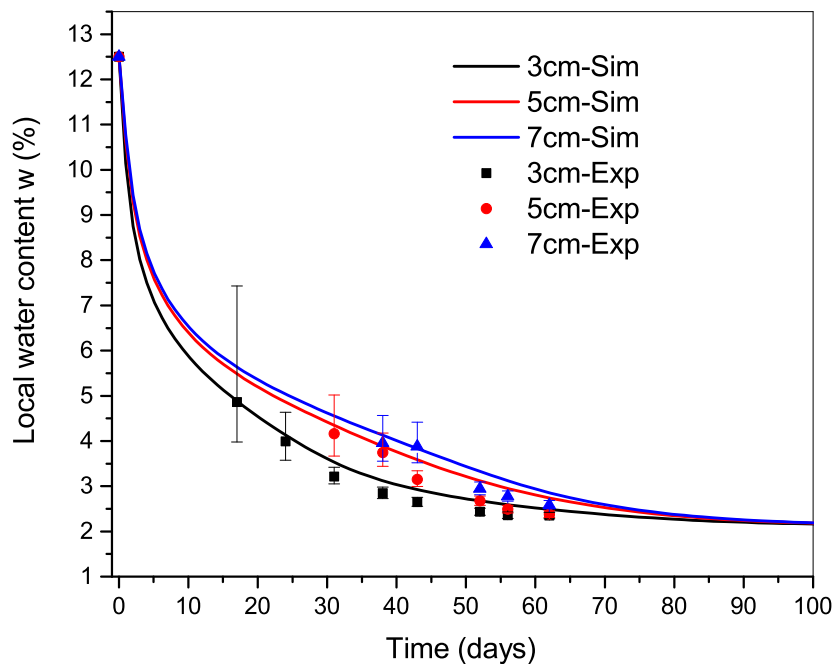


Figure 4.29: Comparison of experimental and simulation results for water content

Figure 4.29 shows the comparison of experimental and simulation results for local water content across the width of the sample at 3 cm, 5 cm, and 7 cm. For the experimental results, the water content at the initial stage after compaction is equal to the optimum water content of 12.5%. The relative humidity values were linked with the suction using Kelvin's equation. The suction was finally linked with degree of saturation and thus the water content. For the readings where the relative humidity remained at 100%, the water content value has not been shown. It is because, for a relative humidity value of 100%, the theoretical value of suction is zero, which is not the case for the experimental columns. The water content for all the other cases is shown in the figure at different duration of drying and at different distance from the drying face. The experimental water content at 3 cm distance after 24 days of drying decreases significantly from 12.5% at the beginning to around 3.98%. Whereas at 5 cm distance the water content reached around 4.16% after 31 days, and at 7 cm distance it reached around 3.95% after 38 days.

The results of the simulation show the variation of the water content with the duration of drying. A significant decrease in water content at a very high rate is observed at the beginning of the simulation. The water content decreases from 12.5% to around 6% after 5-10 days of drying at 3 cm, 5 cm, and 7 cm distance from the boundary. The rate of decrease of water content decreases over time, and the water content across the sample after 100 days of drying was around 2.11%. The gradient of water content across the width first increases and then decreases as the drying process approaches towards completion. The water content at 3 cm distance from surface fits well with the experimental results

except at 14 days of drying. After 31 days of drying, the experimental water content at 3 cm and 5 cm was 3.21% and 4.16% respectively, whereas for the simulation it was 3.55% and 4.36 %. After 62 days of drying the water content from experiment and simulations were fairly close to each other. Finally, from this curve, it appears that both the results are tending towards a similar value of final water content.

The comparison of average water content from the experiment and simulations is shown in figure 4.30. The average water content after 62 days of drying was closer to the experimental results, whereas the initial behavior of drying was not reproduced accurately.

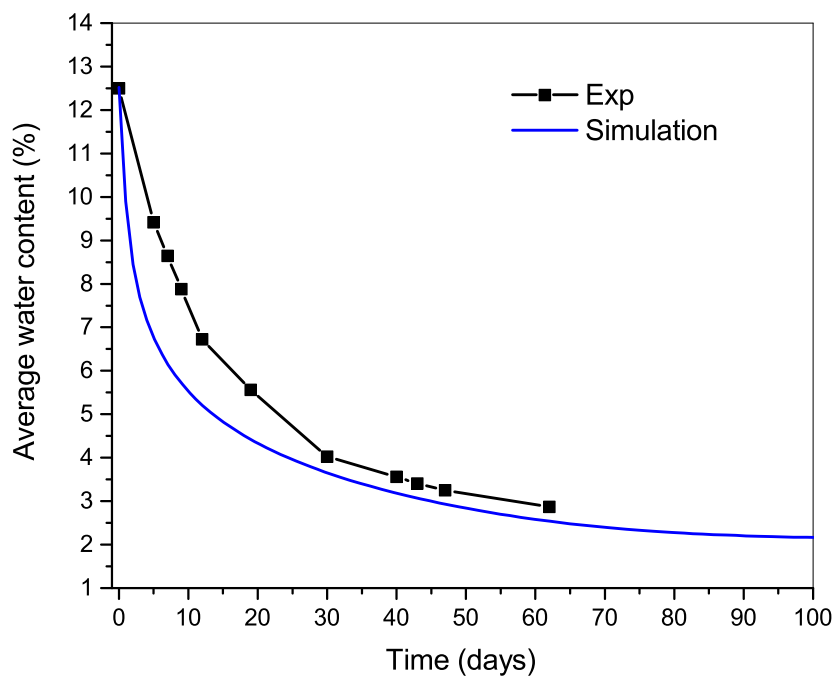


Figure 4.30: Comparison of experimental and simulation results for global average water content

4.3.4 Numerical simulations of compression phase

In order to perform the THM coupled analysis for the compression of columns, the same model used previously for the drying simulations was used. During these simulations, an additional modeling phase of axial compression was added, and only the boundary conditions are changing. In the previous phase, the drying was performed for different duration corresponding to the experiments i.e. 0 day (no drying), 13 days, 31 days, and 62 days. Then in the second phase, after a particular duration of drying, the column was axially compressed at a constant rate of axial displacement in order to determine the failure stress of the columns. It is to be noted that, the same mesh refinement was not used while performing both drying and mechanical simulations together, since the time of computation was very long. A coarser mesh was used to save computational time while making sure that the drying and failure stress is not affected.

4.3.4.1 Initial state and boundary conditions

For this modeling phase, which is the mechanical compression, the initial hydric state is corresponding to the results of the drying phase. Figure 4.31 shows an example of the initial suction state after 62 days of drying. The hydric state will be based on the duration of drying. For the sample tested without any drying, i.e. day 0, a constant suction of 0.328 MPa is fixed.

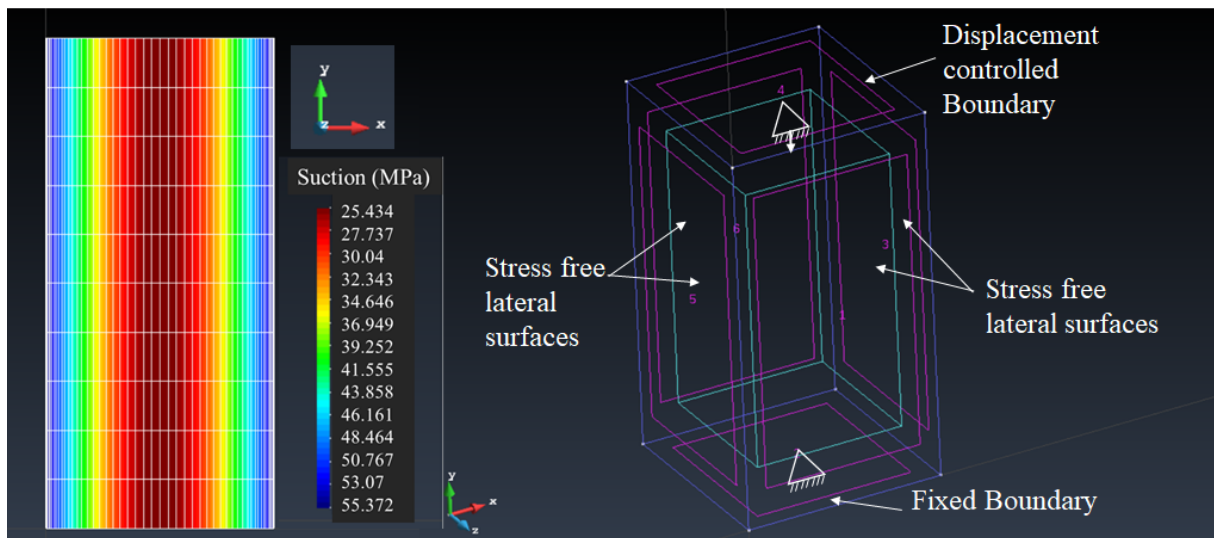


Figure 4.31: Initial hydric state (for 62 days of drying) for the compression phase (left) and mechanical boundary conditions for the compression of rammed earth columns (right)

The boundary condition for the second interval is also shown in figure 4.31. The four lateral surfaces were free as no stresses are applied ($\sigma_{ii} = 0$ and $\tau_{ij} = 0$) and displacements are allowed perpendicular to the sample surface. The bottom boundary is considered fixed, i.e. the displacements are not allowed in any direction ($u_x = u_y = u_z = 0$), which will generate moment induced stresses. The top boundary is fixed in the lateral directions i.e.

displacements are not allowed in x and z direction ($u_x = u_z = 0$). In the y-direction, a constant rate of axial displacement (\dot{u}_y) of 10^{-6} m/s is imposed, which will lead to the compression of the column.

For the hydraulic boundary condition in this phase, it was assumed that the duration of compression phase is not significant compared to the drying phase. Any changes due to the atmospheric drying were not taken into account. Thus all the boundaries were considered impermeable, and no exchange of water is taking place through the boundaries.

4.3.4.2 Compression phase simulation results

In this section, the results from the mechanical simulations after different duration of drying is compared with the experimental results of the compression testing of columns. The main result which will be compared between the two is the compressive strength, i.e. the failure stress. The sample which did not undergo any drying, i.e. tested just after compaction has a uniform suction state, whereas all the other samples have a non-uniform suction state. Thus the suction distribution before the compression testing is shown. The stress-strain response of the material upon compression testing at uniform and non-uniform suction states is also shown.

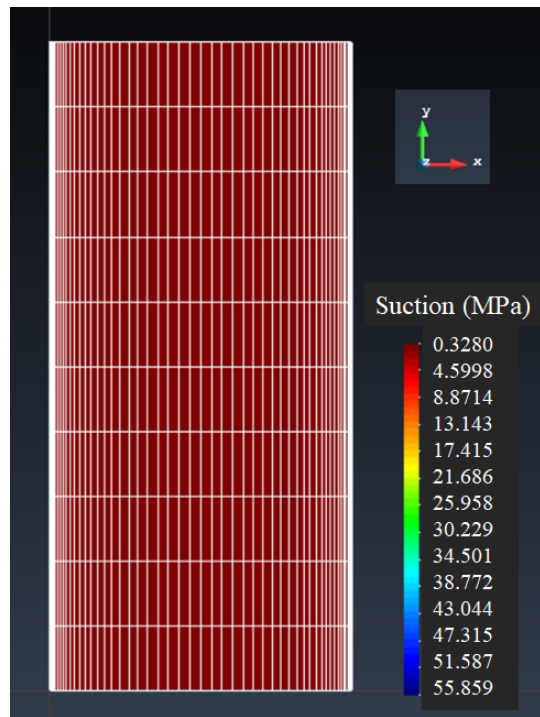
Compression at day 0:

For the compression test to be simulated without any drying period, the suction distribution is shown in figure 4.32a. It can be seen that the model has uniform liquid pressure of -0.228 MPa and thus uniform suction condition ($s = 0.328$ MPa). This suction condition is corresponding to the compaction state determined from the retention curve.

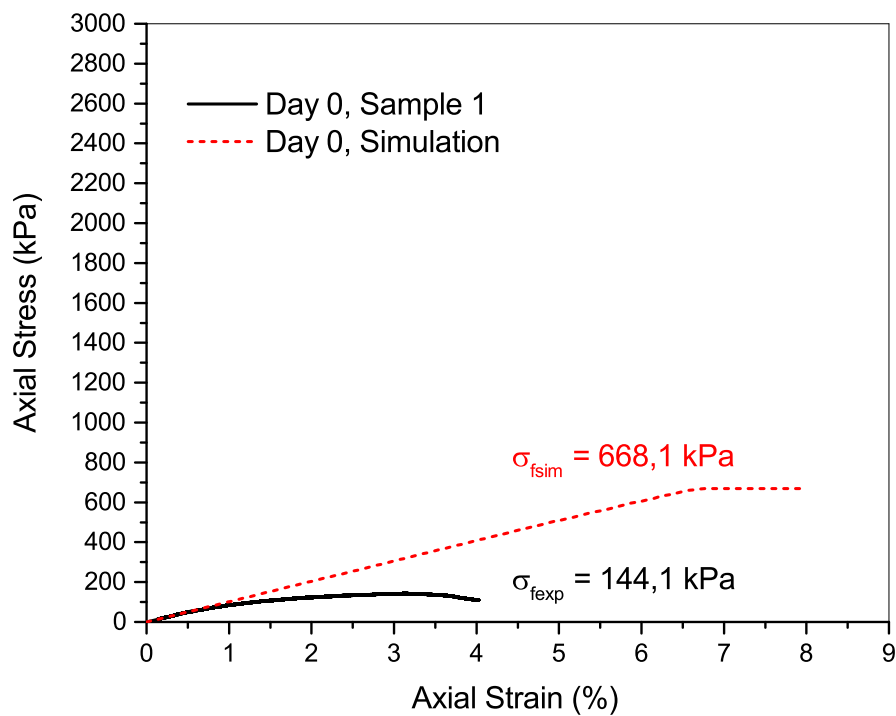
The mechanical response in terms of axial stress and axial strain from the simulation is shown along with the experimental test done without any unload-reload cycles (4.32b). The tangent modulus of elasticity of 9.99 MPa was used in the simulations. As we are not reproducing the stress-strain behaviour, the only result on which we will focus on is the strength comparison between the model and the experiment. The axial stress and axial strain shown here for the simulations are the average values over the whole volume. It can be seen that the strength of the sample from the simulation ($\sigma_{f\text{sim}}$) is 668.1 kPa which is higher compared to the experimental strength ($\sigma_{f\text{exp}}$) of 144.1 kPa.

Compression at day 13:

The suction distribution after 13 days of drying is shown in figure 4.33a. The non-uniform distribution of suction shows that at the middle of the model, the suction value is around 3.3 MPa, while the suction near the boundary is around 52.8 MPa. Thus the apparent strength of the material in the middle is lower compared to the apparent strength near the boundary. This is due to the fact that apparent cohesion increases due to the additional component of cohesion induced by suction. This means that elements in the central region will reach plasticity first, and upon further compression, the elements near the boundary will plasticize.



(a)

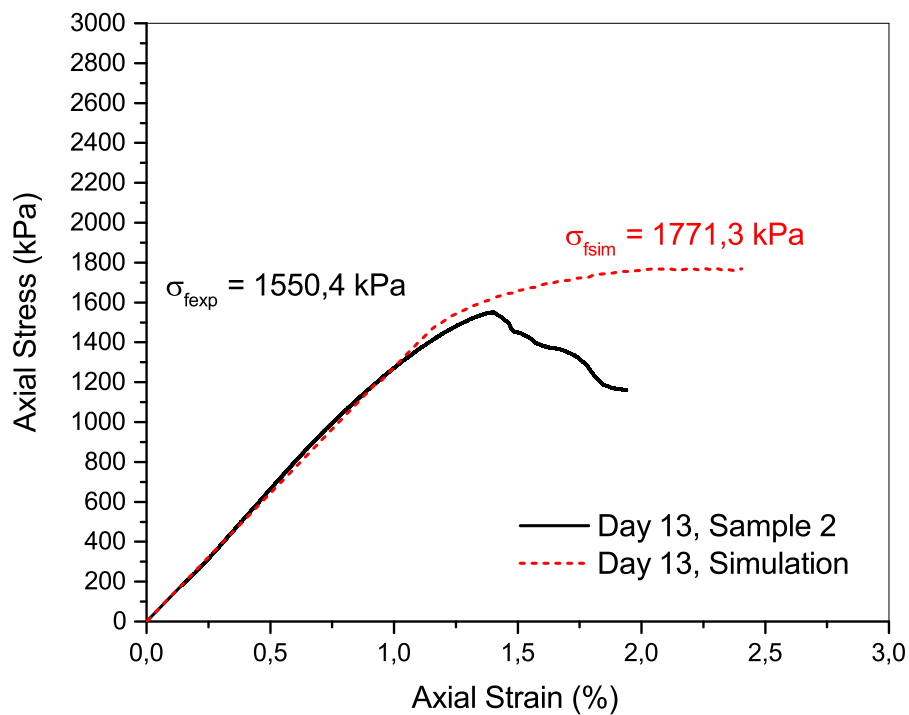


(b)

Figure 4.32: Suction distribution (a) and comparison of the compression test conducted without any drying phase i.e. 0 days with the simulation results (b)

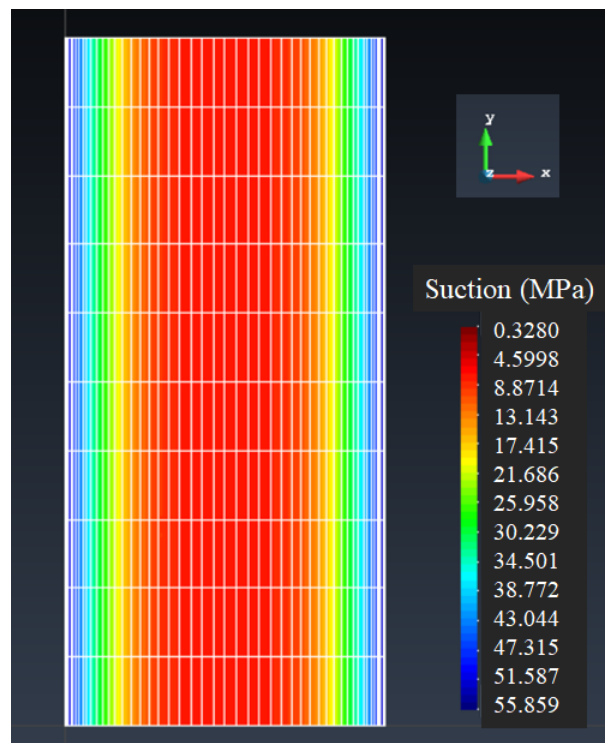


(a)

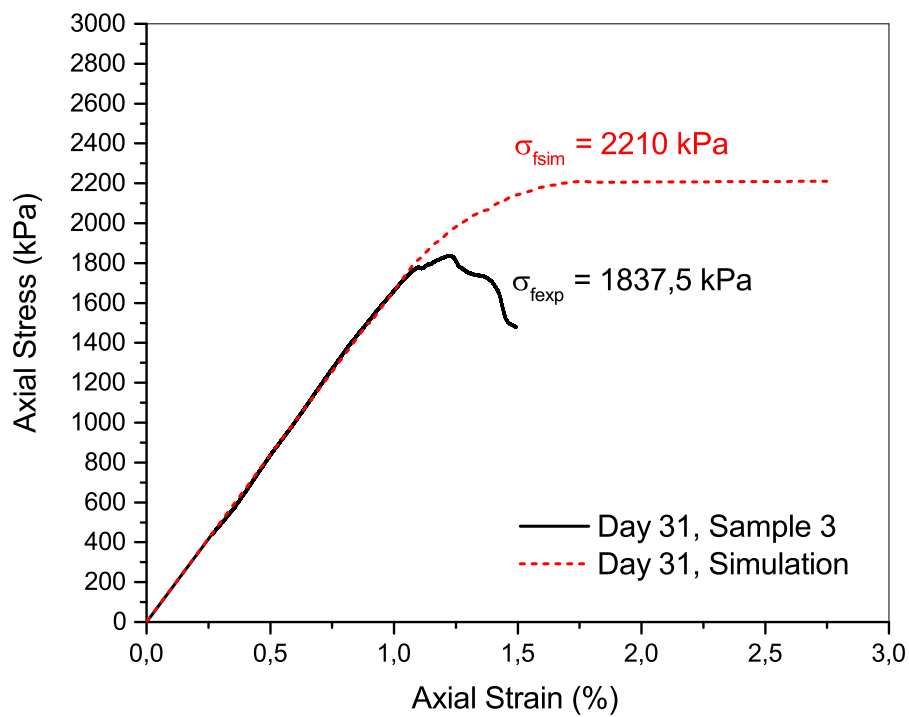


(b)

Figure 4.33: Suction distribution (a) and comparison of the compression test conducted after 13 days of drying period with the simulation results (b)

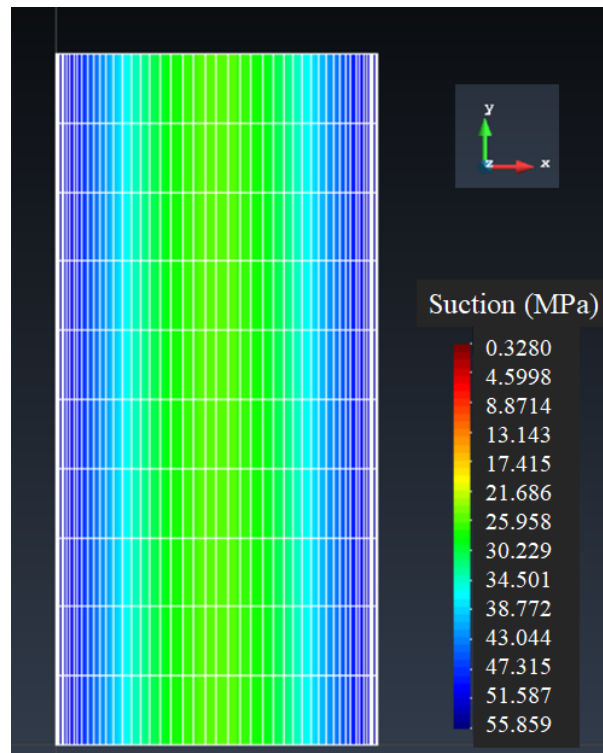


(a)

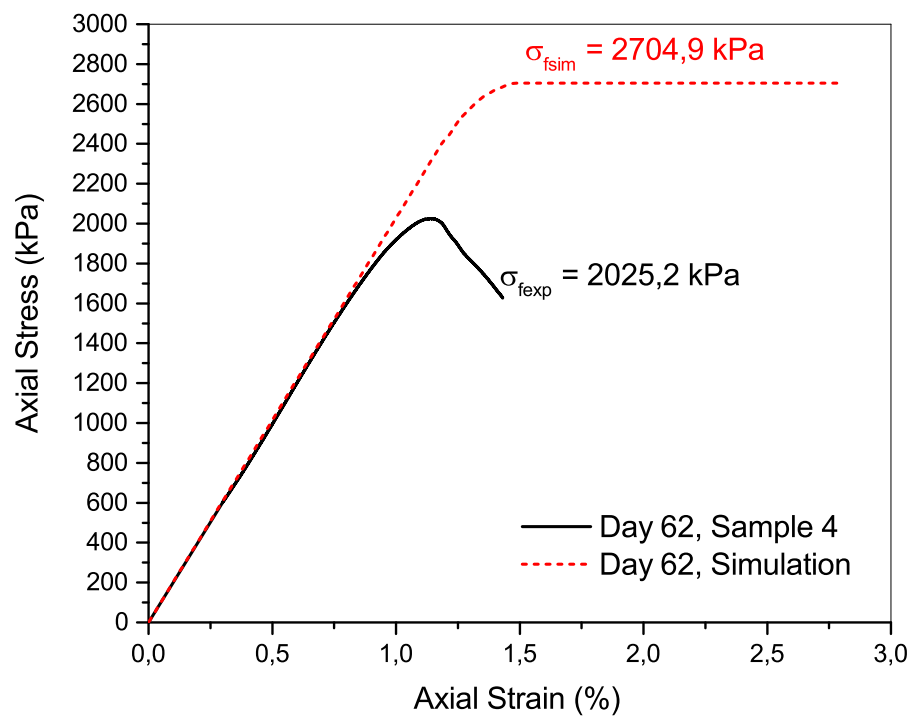


(b)

Figure 4.34: Suction distribution (a) and comparison of the compression test conducted after 31 days of drying period with the simulation results (b)



(a)



(b)

Figure 4.35: Suction distribution (a) and comparison of the compression test conducted after 62 days of drying period with the simulation results (b)

The axial stress-axial strain variation of the sample tested at day 13 without unload-reload cycle is shown along with the simulation results in figure 4.33b. The modulus of elasticity in this simulation was taken as 127.29 MPa from the experimental results. It can be seen that the first plasticity appears around 1500 kPa. This observation could be due to the central part of the model reaching plasticity first, and upon further compression when all the elements reach plasticity, it reaches the maximum stress state of $\sigma_{f_{sim}} = 1771.3$ kPa. The strength obtained from the model was 12.2 % higher compared to the experimental strength ($\sigma_{f_{exp}}$) of 1550.4 kPa. It can be observed that the change in the slope of stress-strain curve from the simulations takes place close to the maximal experimental axial stress.

Compression at day 31:

For the simulation that was carried out for 31 days of drying, the suction distribution is shown in the figure 4.34a. The suction distribution was non-uniform, ranging from 7.2 MPa at the center to 54.6 MPa at the boundary.

The modulus of elasticity for this simulation was taken as 166.05 MPa. The axial stress-axial strain curve (figure 4.34b) shows that the slope of the curve changes around 1800 kPa of axial stress. This is due to the huge difference in the values of suction in the central region and close to the boundary. Thus the central region reaches plasticity before the region close to the boundary. Also, the change in slope from the results of the simulation occurs around the maximal axial stress. This behavior was also observed for simulation after 13 days of drying. The compressive strength from the simulation ($\sigma_{f_{sim}}$) was 2210 kPa which was higher than the experimental strength ($\sigma_{f_{exp}}$) of 1837.5 kPa.

Compression at day 62:

Finally for the simulation carried out after 62 days of drying, the suction distribution is shown in figure 4.35a. The suction is non-uniform ranging from 25.4 MPa at the center to 55.3 MPa at the boundary. A lower gradient of suction across the width was observed compared to the previous simulations.

The modulus of elasticity for this simulation was taken as 201.25 MPa. The slope of the stress-strain curve changed slightly around 2500 kPa. This observation could be due to the fact that although there is suction variation across the width, the suction difference is lower compared to the previous simulations. Thus the strength of the central part is higher and comparable with the part close to the boundary. The compressive strength obtained from the simulation ($\sigma_{f_{sim}}$) was 2704.9 kPa. This value was significantly higher than compressive strength from the experimental strength ($\sigma_{f_{exp}}$) of 2025.2 kPa.

The variation of compressive strength with time from the simulations is shown in figure 4.36. During the initial period of drying the compressive strength from the simulation increases at a very high rate from 668.1 kPa to 1685.1 kPa within 10 days. This rate of increase in strength reduces upon further drying, reaching to a value of 2704.9 kPa after 62 days. After this, the rate of increase of strength becomes slower and the

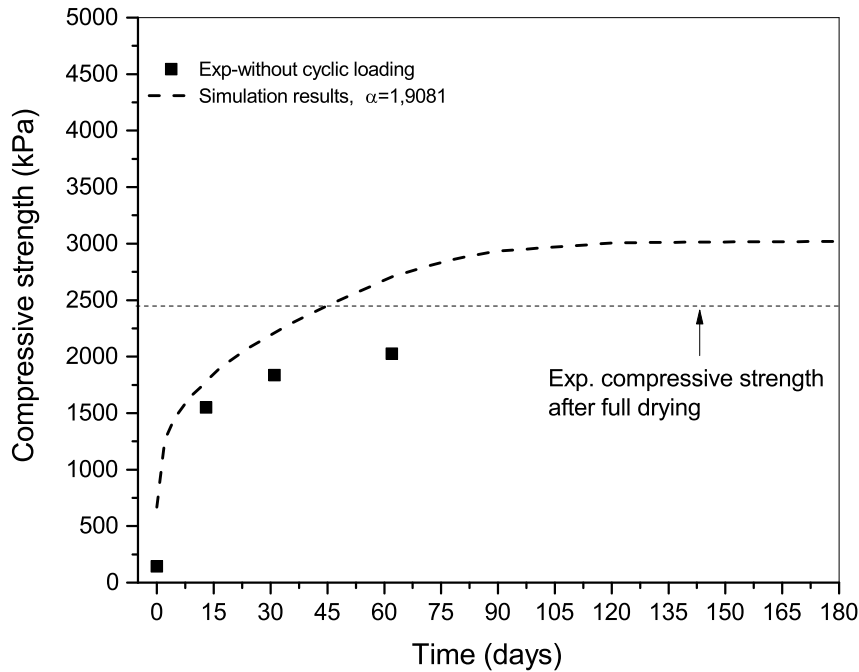


Figure 4.36: Comparison of the compressive strength for samples tested without unload-reload cycles and the simulation results at different duration of drying

compressive strength reaches a value of 3020.5 kPa after full drying. This observation is attributed to the fact that the additional suction induced cohesion varies in the same manner. It increases at a higher rate at the beginning with an increase in suction and then at higher suction values this rate reduces and tends towards a final value asymptotically.

The comparison of the compressive strength obtained from the simulations and the experimental results without unload-reload cycles at different duration of drying is also shown in figure 4.36. There is a significant difference in the compressive strength for the sample tested at 0 day and the simulation result. In general, the simulations predict a higher compressive strength at all duration of drying.

The compressive strength from experiments with cyclic loading is not compared in figure 4.36. Indeed, we suppose that the values with cycles are somehow slightly degraded and thus less representative.

Additional experimental campaign

In order to understand the reasons for the differences between the experimental and the simulation results, a short experimental campaign was done. Since the mechanical parameters were taken from the experimental study carried out at material scale on static doubly compacted cylindrical samples ($\phi_d = 5$ cm, $H=10$ cm) which was sieved at 5 mm. On the other hand, the experimental study here was done on columns which were dynamically compacted in layers on a prismatic sample ($L=W=14$ cm, $H=30$ cm) which

had particles of maximum size of 10 mm. There are be 4 factors which could have contributed to the difference such as granulometry, compaction method, scale effect, shape effect. In order to study these effects, tests were conducted on samples with similar slenderness ratio and at the compaction hydric state. Unconfined compressive strength was done on the samples shown in table 4.6. It is to be noted that, samples T4 and T5 have already been tested in the experimental study before.

Table 4.6: The details of the samples studied including the shape, size, method of compaction and granulometry

Sample no.	Dimensions (cm)	Type of compaction	Layers	d_{max} (mm)
T1	Cylindrical ($\phi_d = 16$, H=32)	Dynamic	4	5
T2	Cylindrical ($\phi_d = 16$, H=32)	Dynamic	4	10
T3	Prismatic (L=W=14, H=30)	Dynamic	4	5
T4	Cylindrical ($\phi_d = 5$, H=10)	Static doubly compacted	1	5
T5	Prismatic (L=W=14, H=30)	Dynamic	4	10

As all the configurations are tested only once, it has to be underlined that this is only a preliminary attempt which aims to identify if there is any parameter (in the four parameters studied) which has more impact on the compressive strength than the others.

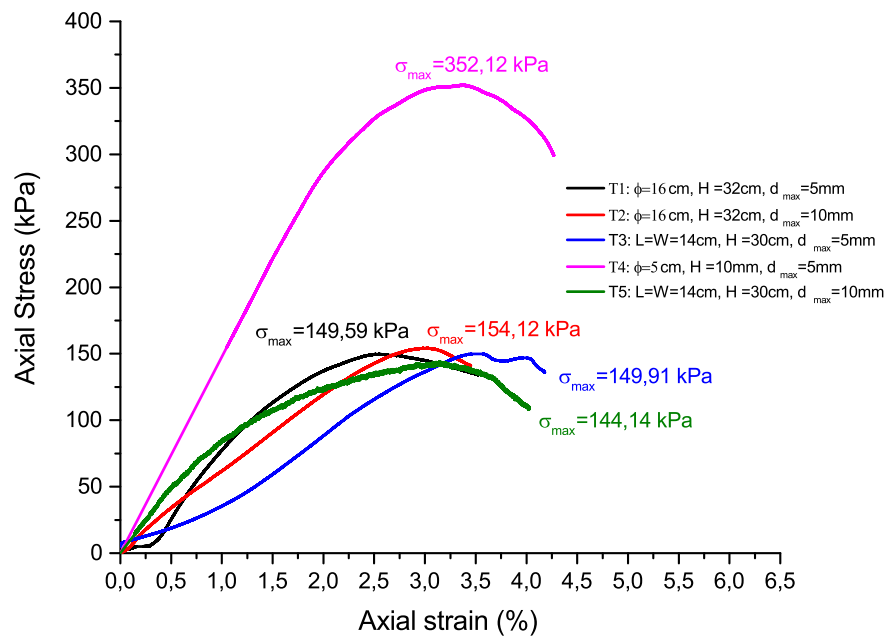


Figure 4.37: Comparison of the compressive strength for samples tested at the same hydric state but at different geometry, granulometry, scale, compaction method

Figure 4.37 shows the axial stress-strain curves with the compressive strength for the samples discussed before. Following interpretations can be made based on the results:

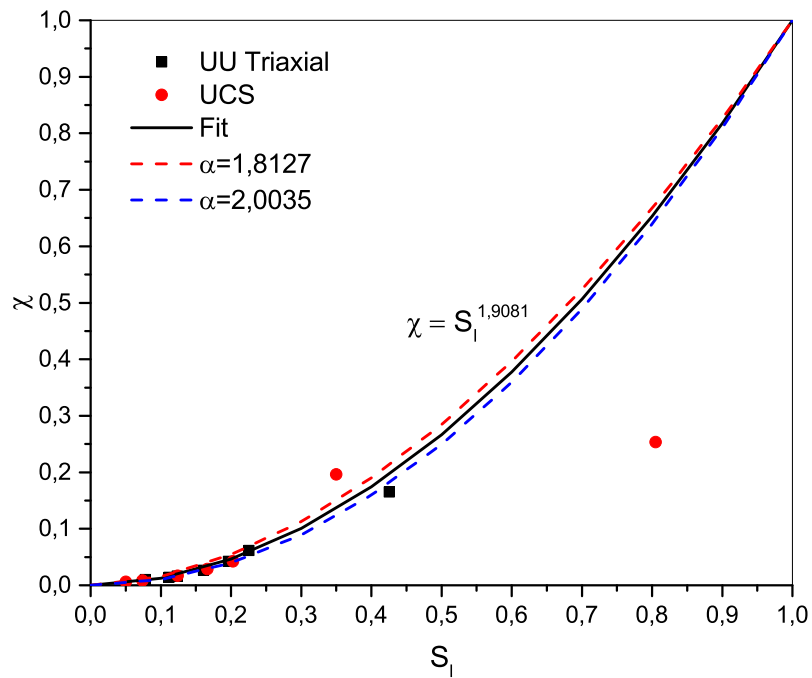
- Granulometry: Sample T1 and T2 are both cylindrical samples with same size but with different granulometry. The results show that sample T1 and T2 have a compressive strength of 149.59 kPa and 154.12 kPa respectively, which is comparable. Similarly, sample T3 and T5 are both prismatic samples with the same dimension but different granulometry. Compressive strength of sample T3 and T5 are 149.91 kPa and 144.14 kPa respectively, which is comparable. This highlights that granulometry does not a great influence on the compressive strength in our configuration.
- Shape effect: Sample T1 and T3 are both dynamically compacted samples using the same granulometry ($d_{max} = 5\text{mm}$) but with different shapes. Compressive strength of the cylindrical sample ($\sigma_{max} = 149.59\text{ kPa}$) was similar to the prismatic sample ($\sigma_{max} = 149.91\text{ kPa}$). Sample T2 and T5 are both dynamically compacted samples using same granulometry ($d_{max} = 10\text{ mm}$) but with different shapes. The compressive strength of cylindrical sample ($\sigma_{max} = 154.12\text{ kPa}$) was comparable to prismatic sample ($\sigma_{max} = 144.14\text{ kPa}$). This highlights that the shape of the sample did not have significant effect on the compressive strength. It is to be noted that slenderness ratio of both samples was around 2.
- Compaction method and scale effect: Sample T4 was doubly compacted to obtain small cylindrical samples ($\phi_d = 5\text{ cm}$, $H=10\text{ cm}$). The compressive strength of sample T4 ($\sigma_{max} = 352.12\text{ kPa}$) was significantly higher than the other samples. Since granulometry and shape do not have significant effect on compressive strength, the difference in results was due to the combined effect of compaction method and scale. The doubly compacted samples are more uniformly compacted and without layers. Bigger samples have a greater possibility of a defect arising during compaction. In addition, the columns had higher gravel content which can also lead to reduction of strength.

The different reasons for the higher strength obtained from simulations as compared to the experiment results were discussed in this section. It is to be noted that all the samples were tested at the same hydric state, i.e. at “as compacted hydric state”. In order to confirm the results, the tests can also be carried out at uniform hydric state different from compaction state.

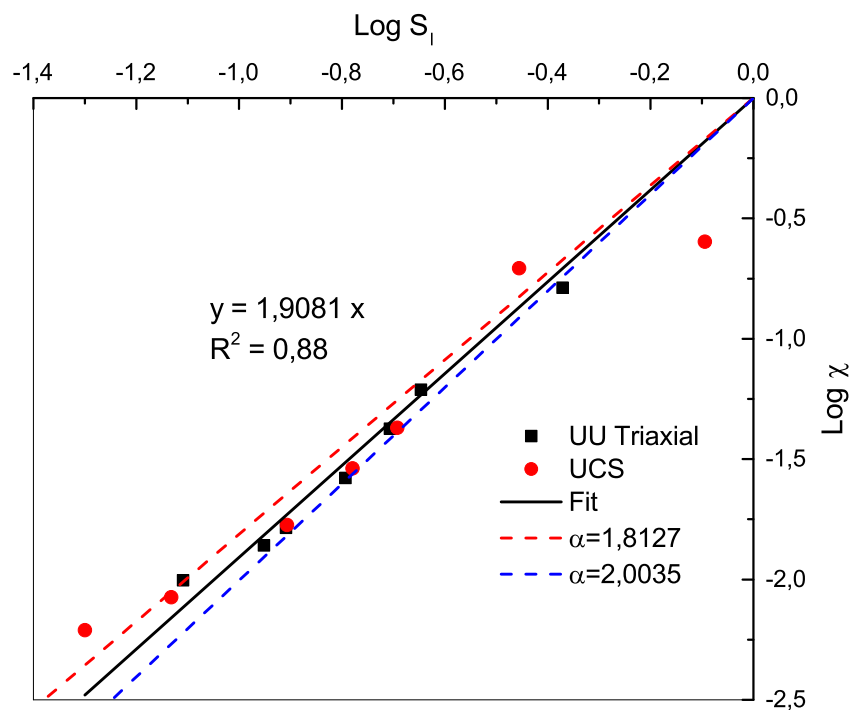
Sensitivity analysis

In addition to the reasons mentioned above, a sensitivity analysis on the effective stress parameter ($\chi = S_t^\alpha$) was performed. The value of α for fitting with the experimental data was 1.9081, and the R-squared value for the fit was 0.88 (figure 4.38). Thus, an interval of 10% was chosen and the sensitivity analysis for the effective stress parameter χ was done for $\alpha \pm 5\%\alpha$ i.e. $\alpha = 1.8127$ and $\alpha = 2.0035$.

Figure 4.39 shows the variation of compressive strength of columns obtained for the different values of effective stress parameter. It can be seen that, for a small change in the value of χ (figure 4.38), there is a very significant change in the value of compressive



(a)



(b)

Figure 4.38: The variation of χ - S_l (a) and $\text{Log } \chi$ - $\text{Log } S_l$ (b) for $\alpha = 1.8127$ and $\alpha = 2.0035$

strength. Thus the compressive phase simulations are very sensitive to the effective stress

parameter χ . The compressive strength from the simulations at $\chi = S_l^{2.0035}$ are very close to the experimental results except at the initial phase of drying.

In addition, it can be seen in figure 4.38 that the expression of χ chosen for the study does not fit well with the experimental results at the compaction degree of saturation. For this reason, the compressive strength simulation results at the compaction conditions are significantly overestimated. Thus in order to more accurately predict the compressive strength of columns, a different expression for χ should be used which fits the experimental results better at higher range of degree of saturation. Also, more tests should be done near the compaction degree of saturation to determine χ accurately.

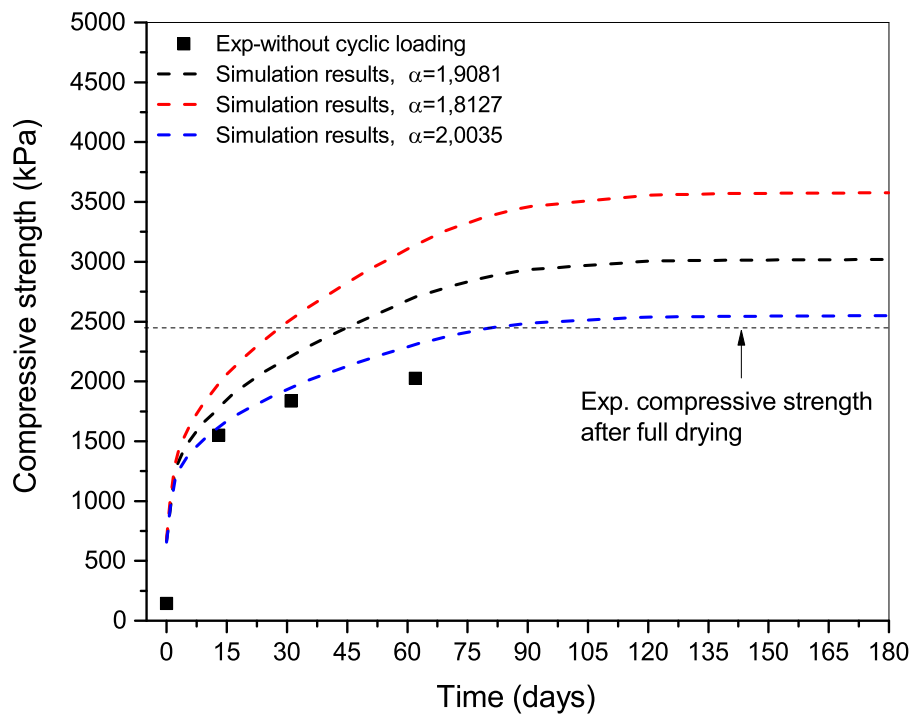


Figure 4.39: The variation of compressive strength for the sensitivity analysis performed on the effective stress parameter χ

4.4 Conclusions and Perspective

In the present study, the hydro-mechanical behavior of rammed earth columns at a representative element volume (REV) scale was investigated. The columns were compacted using dynamic compaction, and the boundary conditions for drying were implemented similar to a part of the wall, which makes the columns representative of a real wall.

Rammed earth columns were subjected to 1D drying in an indoor environment for different duration of drying along with measurement of relative humidity and temperature using SHT sensors. It was observed that during the initial phase of drying, there were minimal changes in the RH, and after two weeks, the variation in RH could be observed. Whereas, the water content of the samples reduced to about half of the initial water content. This was attributed to the fact that uncertainty in the measurement of RH at higher values was greater. Thus the sensor readings were corrected by using error bars in measurements. These sensors are less relevant at the beginning of drying from the manufactured state because the signal is always saturated. However, during the serviceability lifetime of the building, they are relevant. Regarding the kinetics of drying phase, 50% of drying occurred within the first 10 days and at the end of 62 days drying was around 96% done reaching asymptotically towards completion.

The compressive strength of rammed earth columns was studied after natural convection drying. It was observed that the compressive strength increases substantially after two weeks of drying. The rate of increase of strength gain was higher in the beginning phase of drying, then it decreases consequently, and the strength tends towards a final asymptotic value. Two weeks of drying were enough to attain 63 % of strength attained after full drying. The variation of compressive strength of samples tested with unload-reload cycles was similar, although the strength of these samples was either similar or lower to samples tested without cycles. The tangent modulus showed a similar variation as compressive strength. It increased at a higher rate at the beginning of drying and then consequently tending towards an asymptotic value.

Coupled THM simulations of the drying phase and the compression tested were performed using CODE_ BRIGHT. For this, 7 parameters were required to be determined experimentally, while the others were taken from literature or a classical value was used. For the drying phase, atmospheric boundary conditions were used due to which the suction at the boundary reached its final stage gradually, which is more realistic than an imposed suction condition at the boundary. The value of heat/mass transfer coefficient was adjusted to fit the experimental results while being coherent with the guidelines in the literature for natural convection in an indoor environment. A satisfactory fitting with the experimental results was obtained for drying after taking into account the uncertainties in the sensor measurements. It took around 160 days for the columns to dry completely for the 1D drying boundary conditions. In addition, using this numerical approach, it is possible to reproduce the drying of any rammed earth configuration.

Coupled THM simulations were also performed for the compression of the columns after different duration of drying. A linear elastic-perfectly plastic mechanical constitutive model was used. The parameters of the viscoplastic model were adjusted to obtain the plasticity model. A Drucker-Prager yield surface based on Mohr-Coulomb parameters was used. The shear strength expression was modified to take into account the non-linear increase of apparent cohesion with suction and incorporate the expression of Bishop's effective stress. The model was not able to incorporate the variation of elastic modulus with suction, and thus only the failure stress was predicted and not the stress-strain curve. The mechanical parameters used were taken from the extensive experimental campaign performed on cylindrical samples at a material scale. The compressive strength obtained from the simulation were higher than the experimental strength results of the tests with and without unload-reload cycles. Still, the trend of variation of compressive strength with drying duration was reproduced fairly. The possible reasons for the higher strength in the simulations were due to the compaction method and scale factor. In addition, the mechanical simulations were very sensitive to the effective stress parameter.

The failure criterion and the parameters used in these simulations will be further used in the next chapter where the drying and mechanical behavior of rammed earth walls will be studied.

The different perspectives for the future improvement of this work are discussed in the following points:

1. Some of the sensors did not show any readings during the test due to possibly being damaged during the compaction process. Thus it is recommended to change the protection membrane used to guarantee safety during compaction. The other possible solution is to insert the sensors once the compaction procedure is done by drilling small holes in the desired locations. This method will be suitable if only the hydric behavior is to be studied since it is possible that the mechanical strength of the columns might be affected.
2. A different type of sensor can be used, which is more suitable for the range of relative humidity that is being studied, such as TDR sensors (measures water content). This can help in eliminating the uncertainties in the hydric measurements.
3. The value of surface mass transfer coefficient was used from the literature. An experimental methodology can be developed to measure this parameter for the ambient conditions and the rammed earth studied.
4. Additional experimental tests at material scale should be done in the higher range of degree of saturation to have an expression of effective stress parameter that fits well in the whole range of degree of saturation. In addition, since the mechanical simulations are very sensitive to the effective stress parameter, its determination should be done accurately.

5. A mechanical model in which the effective stress can be directly expressed as Bishop's effective stress can be used. In this way, the generalized effective stress approach can be used, which is more suitable for highly compacted soil as rammed earth. It would allow taking into account the variation of elastic modulus with suction.

Chapter 5

Case study: THM coupled simulations of rammed earth walls

5.1 Introduction

The objective of this chapter is to study the early age drying and consequences on the mechanical behavior of rammed earth walls. In rammed earth construction, the drying time required for the walls to gain sufficient strength in order to build a subsequent floor is a major practical issue. In this regards, a numerical case study is performed on the walls, which takes into account the thermo-hydro-mechanical coupled modeling in order to answer this question.

Firstly, a description of the failure envelope used for this study is presented. Then, two different environmental conditions will be detailed, which are corresponding to Le Bouget-du-Lac in the Savoie region of France. A methodology will be proposed based on the work carried out in this thesis in order to determine the drying time required for subsequent floor construction.

The mechanical behavior of the wall at compaction hydric state will be studied. Further, the walls will be subjected to drying, and the mechanical response will be analyzed at each drying state. The drying time required will be determined once the walls are safe corresponding to the failure criterion proposed. This methodology will be used in two environmental conditions for two wall configurations.

Finally, a synthesis of the results and proposition for the future improvement of this methodology will be presented.

5.2 General considerations for the simulations

5.2.1 Failure envelope

The Drucker-Prager failure envelope described in section 4.3.1.2 is shown in figure 5.1 and is labelled as ultimate failure surface. The equation for this failure surface is as follows:

$$q = k + Mp' \quad (5.1)$$

where, $k = 0.09021$ MPa, and $M = 1.3105$ as already determined in the previous chapter (section 3.5.4), q is the deviatoric stress, and p' is the mean effective stress defined as:

$$p' = p - u_a + \chi s \quad (5.2)$$

where, p is the mean stress, u_a is the air pressure taken as 0.1 MPa, $\chi = S_l^{1.9081}$ (see section 3.6) is the effective stress parameter, and s is the suction. The analysis in this chapter will be led in terms of effective stresses.

In the practical guide used for construction using rammed earth in France called "Guide de Bonnes Pratiques (GBP) Pisé, 2018" [25], it is mentioned that the stresses in the wall should not exceed 0,2 MPa or the one-third of the failure stress of the rammed earth. In a similar approach, a safety factor was proposed in order not to reach the ultimate failure surface. This safety failure envelope is chosen such that the angle of the failure envelope (α_f) is taken as one-third of the ultimate failure surface, i.e. $\alpha_f = \beta_f/3$ (figure 5.1). This failure envelope is the central third cone of the original Drucker-Prager failure surface in the 3D principal stress plane. The equation for this failure surface is as follows:

$$q = k_s + M_s p' \quad (5.3)$$

where, $k_s = 0.0217$ MPa and $M_s = 0.3163$, which were determined from the geometrical relation between the failure envelopes.

These hypotheses could lead to an estimation of the drying time for safety. It has to be noticed that the relevance of this safety failure envelope choice could be enhanced by further studies. The safety failure envelope will be further used to study the mechanical behavior of rammed earth walls and to determine the appropriate time of drying required for subsequent floor construction.

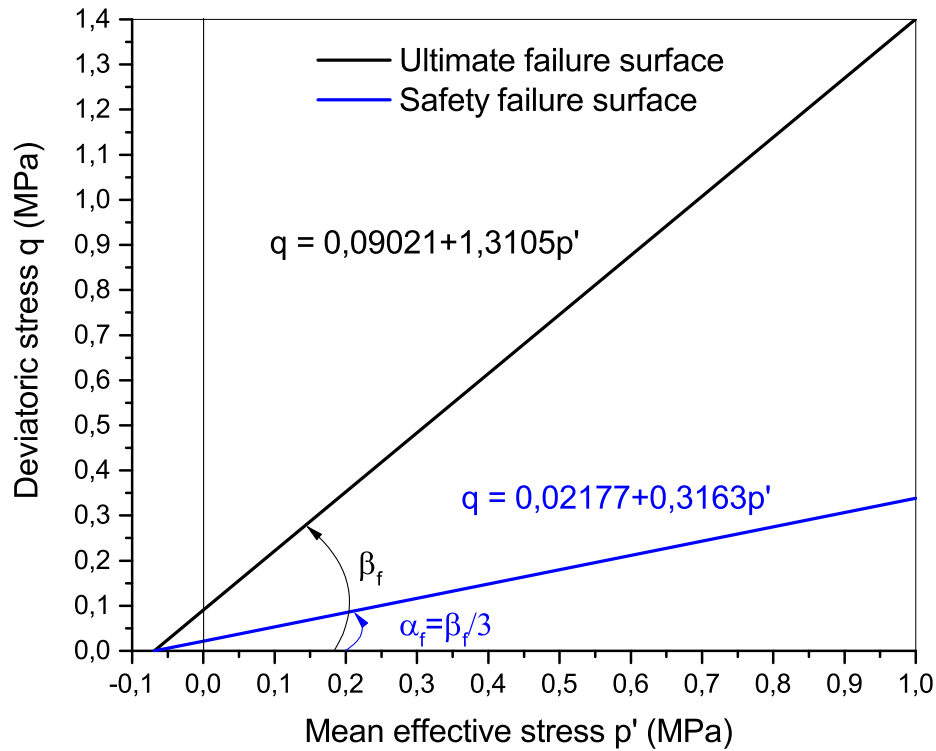


Figure 5.1: The ultimate failure envelope and safety failure envelope in p' - q plane

5.2.2 Environmental conditions

Two different environmental conditions are considered for performing the drying simulations, i.e. a warm and cold conditions. These conditions are considered based on the temperature and relative humidity values at Le Bouget-du-Lac region in France (figure 5.2).

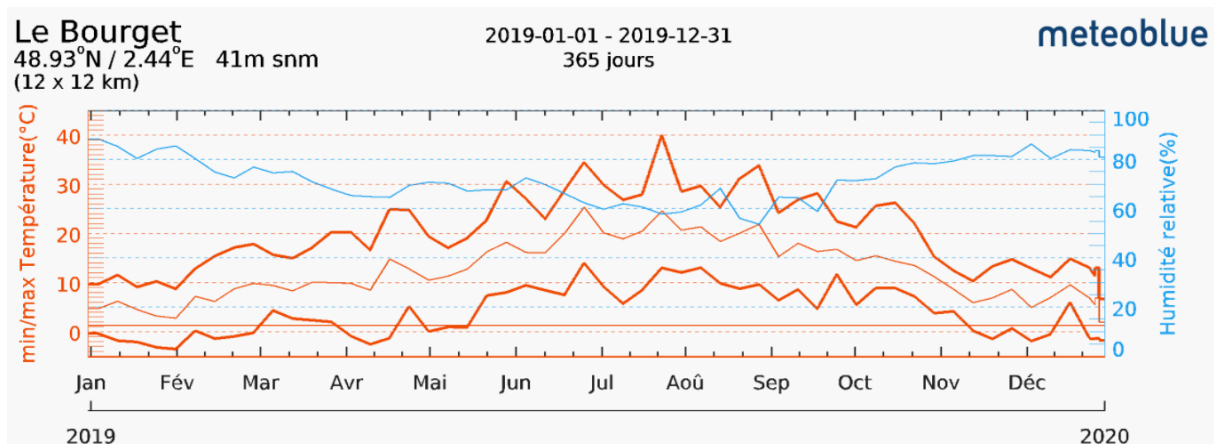


Figure 5.2: The weather data related to temperature and relative humidity for Le Bouget-du-Lac (year 2019) taken from meteoblue.com

In warm conditions, the temperature and RH are taken as 20°C and 60% respectively. These are the average values during the summer months (June-Aug). Whereas in cold conditions, the temperature and RH are taken as 5°C and 85% respectively. These are the average values during the winter months (Nov-Jan). These values are only an estimation since it is not possible to take a single value for different months. The suction values corresponding to these conditions are also mentioned in table 5.1.

In addition, regarding the atmospheric boundary conditions for drying simulations, the value of surface heat transfer coefficient (h_c) is taken as $25 \text{ Wm}^{-2}\text{K}^{-1}$, which is corresponding to a value of surface mass transfer coefficient (h_m) of 0.02 m/s. This value is suggested by Réglementation Thermique 2012 [106] for drying in an external environment in France. This recommended value is slightly low with respect to wind condition. All the different values used for the atmospheric boundary conditions used are mentioned in table 5.1.

Table 5.1: Synthesis of parameters in two different environmental conditions

Env. condition	T (°C)	Relative humidity (%)	Suction (MPa)	h_m (m/s)
Warm	20	60	69.13	0.02
Cold	5	85	20.86	0.02

In the next part, hydro-mechanical coupled behavior of two different wall configurations, i.e. single wall and two walls joined at right angle will be studied in these environmental conditions. All the material parameters used in these simulations are the same as the previous chapter and the method to obtain them are mentioned in table 4.5 in section 4.3.2.

5.3 Single Wall

THM coupled numerical simulations of rammed earth wall were performed using CODE_BRIGHT. The gas phase in the model was considered immobile, and atmospheric gas pressure was considered ($P_g = 0.1$ MPa). The 3D geometrical model of the wall considered has a length and height of 3m, and a width of 0.45m which are classical values for rammed earth walls in France (figure 5.3). A mesh of 12Y x 10X x 10Z (1200) linear hexahedral (C3D8) elements was used.

Regarding the mechanical boundary conditions considered for these simulations, the bottom surface was fixed ($u_x = u_y = u_z = 0$). On the two lateral surfaces (perpendicular to x-direction), displacement in the perpendicular directions was not allowed ($u_x = 0$). While the other two lateral surfaces (perpendicular to z-direction) were stress-free ($\sigma_{ii} = 0$ and $\tau_{ij} = 0$) with displacements being allowed. Vertical stress will be applied on the top surface.

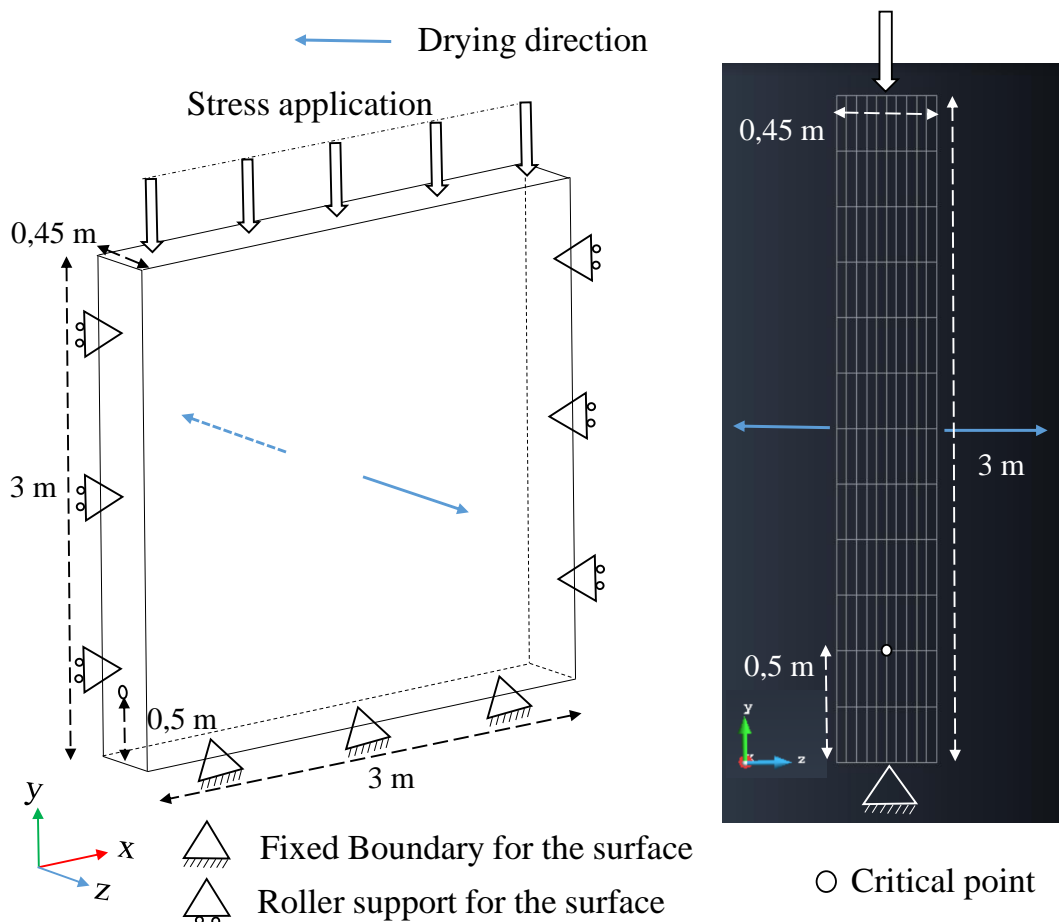


Figure 5.3: The geometrical model (3D) of the problem (left) and the 2D mesh composition (right) showing the drying direction and loading

5.3.1 Compression of wall at compaction hydric state

In this part, a mechanical only simulation was carried out by applying vertical stress gradually at the top surface in order to determine the load sustained by the wall before any part of the wall reaches plasticity. Both the ultimate and safety failure surface was considered. The initial hydric state of the wall was corresponding to the ‘as compacted state’ of the material, i.e. $s = 0.328$ MPa and water content of 12.5%. Since it is a mechanical only simulation, no hydric boundary conditions were required.

Figure 5.4 shows the stress path of the most critical point during the gradual loading of the wall, which is at 0.5 m from the bottom and at the middle of the wall. The stress path for this point begins at the initial suction state where even though the wall is free of stress at its boundary, the internal stress is not zero but depends on the water retention conditions through the product between the suction and effective stress parameter χ (equation 5.2). In other words, suction provides internal confining stress to the wall.

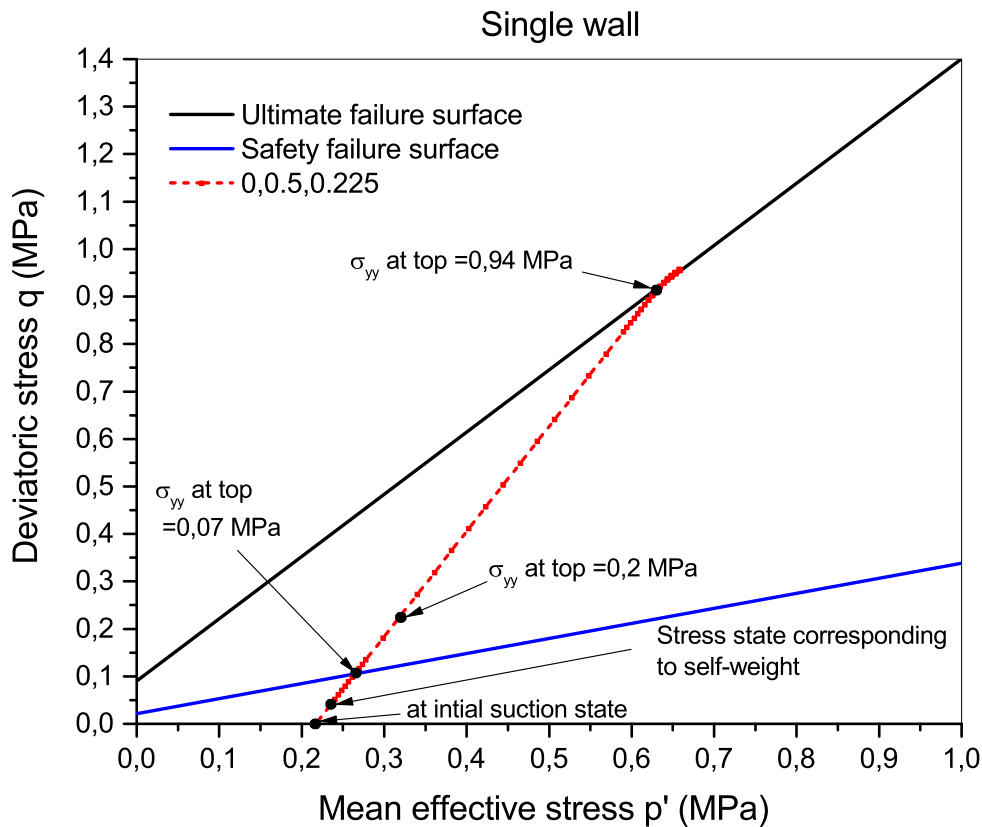


Figure 5.4: Stress path for single wall at the critical point due to vertical stress at top starting from optimum compaction hydric state

The stress state due to self-weight of the wall at the critical point, is shown in figure 5.4. Once the stress is applied on the top surface gradually, the stress path evolves

linearly, and the critical point reaches the safety failure surface at 0.07 MPa vertical stress and ultimate failure envelope at 0.94 MPa vertical stress.

According to GBP, Pisé[25], the vertical stress to be considered for subsequent floor construction can be taken as 0.2 MPa taking into account the self-weight of the walls in the subsequent floor, floor loading, and other live loads. The detailed calculation of this value of stress is shown in Appendix E. It can be seen from the stress path that at 0.2 MPa stress, the wall is very safe with regards to the ultimate failure surface. On the other hand, the stress state is outside the safety failure surface. Thus it can be inferred that the safety criterion suggested by the practical guide is very conservative.

In the further simulations, the walls will be subjected to drying for different duration, and after the drying period, vertical stress of 0.2 MPa will be applied from the top. The drying period will be determined when the critical point is safe with regards to the safety failure envelope.

5.3.2 Drying in warm conditions

These simulations will be carried out in two phases. In the first phase, drying will be imposed on the two lateral surfaces as shown in figure 5.3 using the atmospheric boundary conditions for the warm environment (table 5.1) at different duration. In the second phase, the wall is compressed by gradually increasing the vertical stress from the self-weight stress state up to an increment of 0.2 MPa at the top boundary. The safety of the same critical point mentioned previously with regards to the safety failure envelope will be analyzed.

Figure 5.5 shows the stress path of the critical point at 0, 30, 60, 90, and 120 days of drying. Firstly from the initial compaction suction state, the self-weight is applied on the wall. Due to drying the stress path translates to the right by an amount χs in the p'-q plane, which depends on the suction and degree of saturation. After the first 30 days of drying, the stress path is significantly shifted to the right. The suction value at the critical point increase while the degree of saturation decreases but the product of $S_l^{1.9081}s$ increases. Still, upon the stress application of 0.2 MPa, the stress path is above the safety failure surface. This drying process is continued for another duration until the stress state lies below the safety failure surface. The effect of drying on the stress path is non-linear since the increase in χs decreases at the drying intervals of 30 days.

The isochrones of suction and degree of saturation across the width of the rammed earth wall have been shown in figure 5.6. From the suction profiles, it can be seen that suction at the boundary increases gradually over time and approaches the final equilibrium value of 69.13 MPa (table 5.1). At day 0 of drying, the wall is at a uniform suction state of 0.328 MPa ($S_l = 0.805$), while at other days, the wall has non-uniform suction state. At 30 days of drying, the suction at the center of the wall reaches to suction of 1.4 MPa and degree of saturation of 0.53. Thus, a significant amount of drying has taken place within the first 30 days. Finally, at 120 days of drying, the suction at the

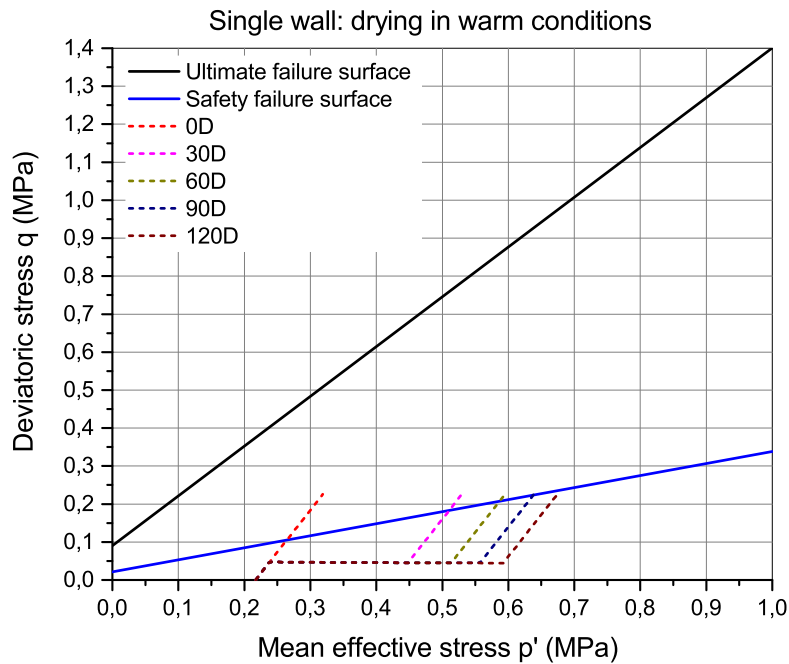
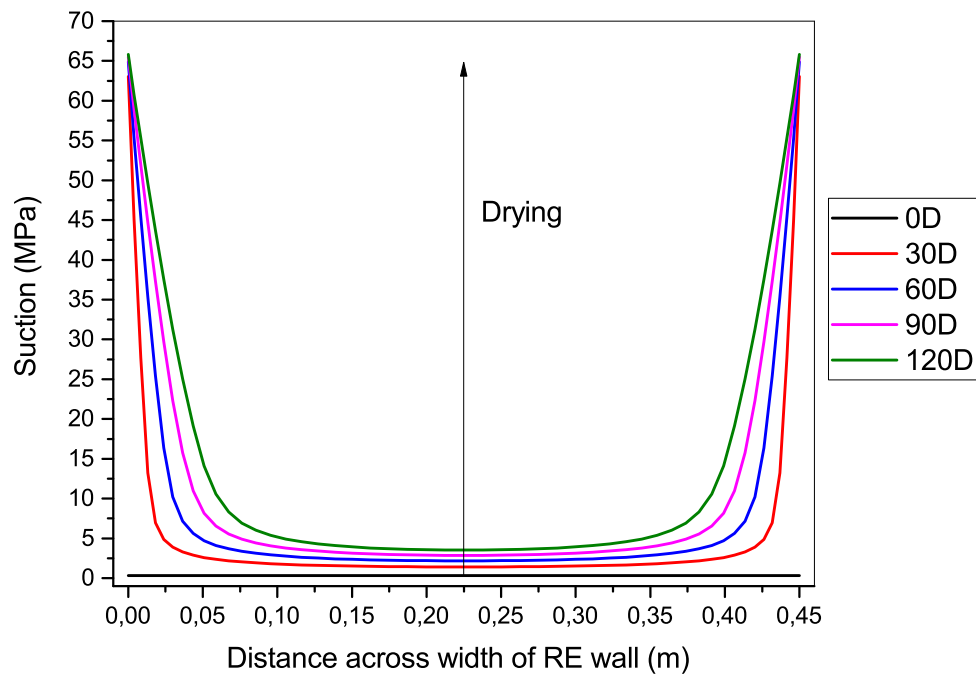


Figure 5.5: The stress path in p' - q plane for the critical point in the wall at different duration of drying in warm environmental conditions

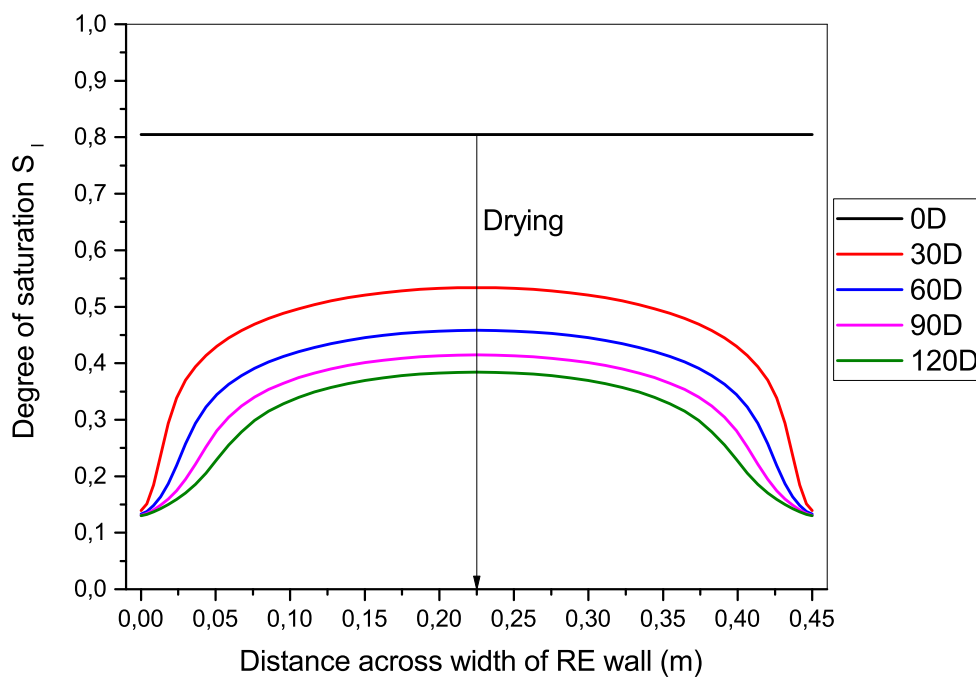
center of the wall reaches 3.53 MPa with degree of saturation of 0.38. The stress path after 120 days of drying is safe with regards to the safety failure surface.

Finally, it takes between 3-4 months of drying for the critical point in the wall to be safe. Also, this period of drying is also recommended in the practical guide [25]. This drying period at the same value of relative humidity and temperature is reasonably possible between the months of June and September, based on the actual weather data shown in figure 5.2. Thus, it takes a significant amount of time for the single wall to dry sufficiently in warm conditions in order to construct another floor above it by taking into account the safety criterion suggested in the practical guide. It is to be noted that there can be different reasons for this estimated long drying period:

- In these simulations, the solar radiation is not taken into account, which can affect the drying duration.
- The surface mass/heat transfer coefficient value needs to be evaluated for the actual conditions taking into account the air velocity profile.
- The choice of failure surface recommended by the practical guide might be very conservative. This choice is arbitrary and could be more adapted in later simulations, according to a comparison between the field guidelines and the simulations.



(a)



(b)

Figure 5.6: Suction (a) and degree of saturation (b) variation across the width of rammed earth wall at 0, 30, 60, 90, and 120 days of drying period in warm environmental conditions

5.3.3 Drying in cold conditions

In these simulations, the drying was carried out in cold environmental conditions, as mentioned in table 5.1. The stress path for the drying and stress application is shown in figure 5.7. Due to the higher relative humidity and lower temperature, the drying process is slower compared to warm conditions and the increase in mean effective stress due to drying is significantly reduced. The effect of drying on the stress path can be seen in figure 5.7, where the stress path is evolving non-linearly at 30 days drying intervals. The drying time required for the critical point to be safe is around 180 days.

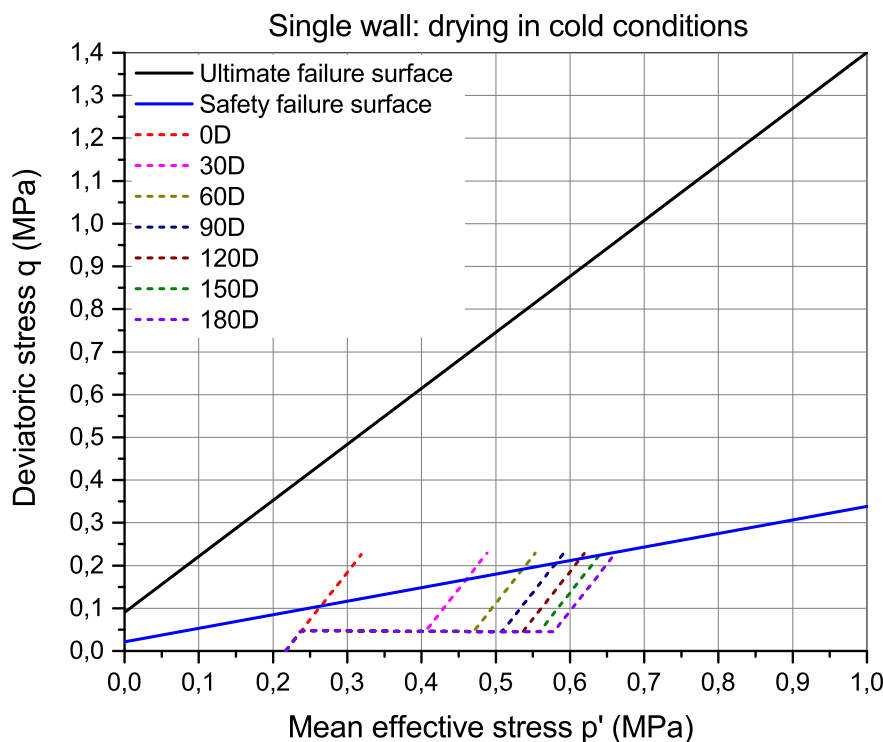
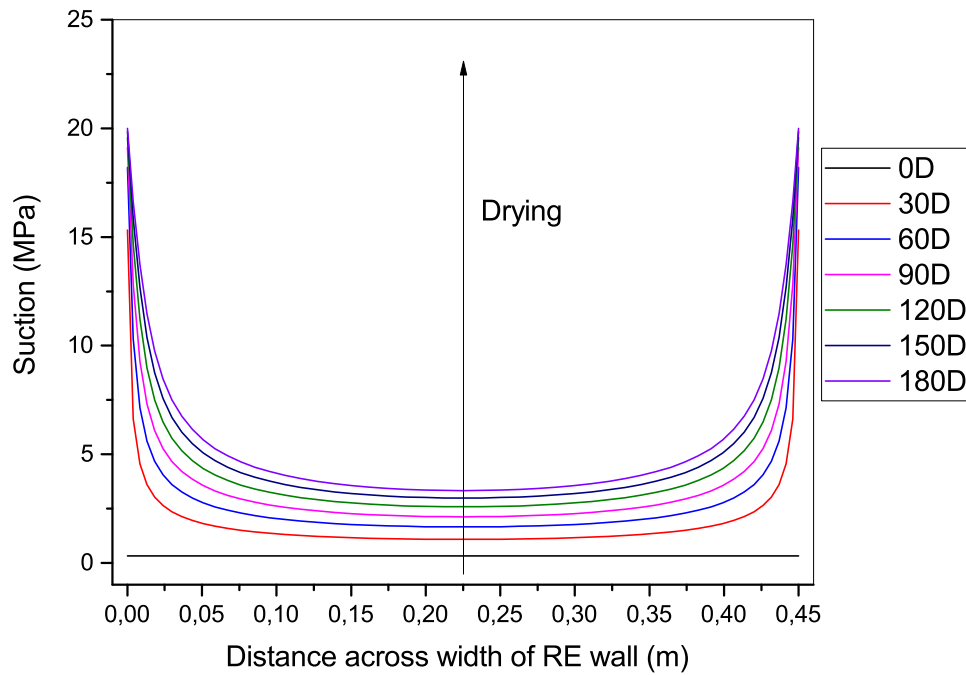


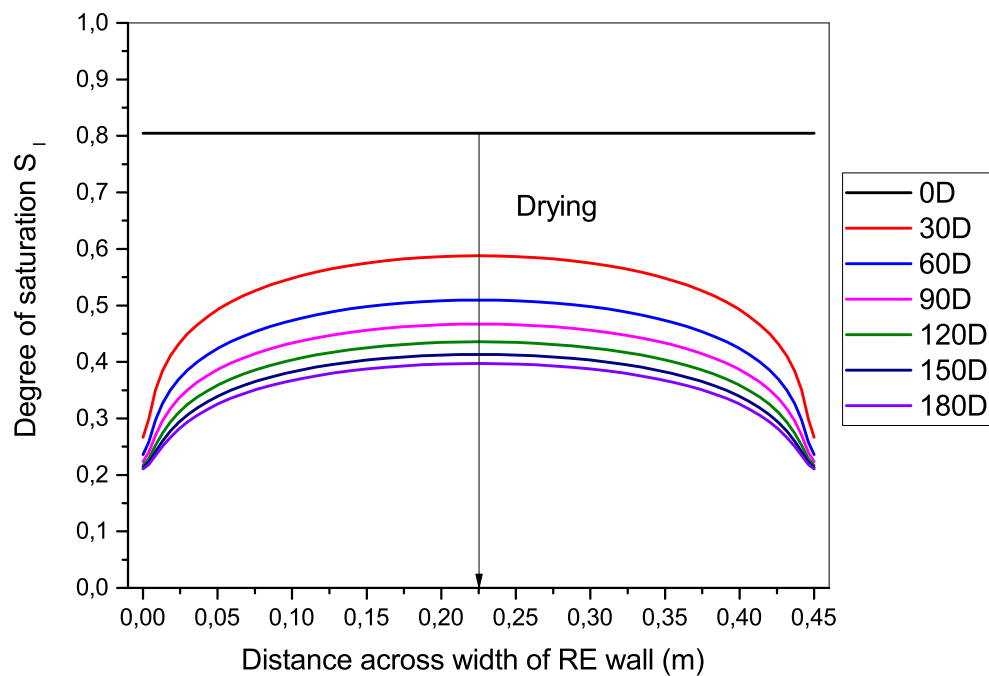
Figure 5.7: The stress path in p' - q plane for the critical point in the wall at different duration of drying in cold environmental conditions

The suction and degree of saturation isochrones along the width of rammed earth wall are shown in figure 5.8. The suction profiles show that the suction at the boundary increases gradually over time and approaches the final equilibrium value of 20.86 MPa (table 5.1). After 30 days of drying, the center of the wall reaches the suction of 1.08 MPa and degree of saturation of 0.58. Finally, at 180 days of drying, the center of wall reaches suction of 3.32 MPa and degree of saturation of 0.39. A comparison between the degree of saturation profiles with warm conditions can be made (figure 5.6). The isochrones in the warm conditions start to flatten close to the boundary at around 30 days, whereas in cold conditions, the whole curve is mostly concave downwards at 180 days of drying.

The time for the drying simulations based on the cold environmental conditions



(a)



(b)

Figure 5.8: Suction (a) and degree of saturation (b) variation across the width of rammed earth wall at 0, 30, 60, 90, 120, 150, and 180 days of drying period in cold environmental conditions

considered is longer than the actual cold weather conditions shown in figure 5.2. Thus it is not possible to dry the wall in these conditions. In the practical guide, it is mentioned that it is not reasonable to build in winter conditions. Hence another point of improvement would be to take the real-time weather data instead of a constant value of relative humidity and temperature. In addition, all the points discussed for the drying in warm conditions (section 5.3.2) such as the solar radiation, surface heat/mass transfer coefficient, and the choice of failure criterion can be improved to get more accurate value of drying period.

The suction evolution at the center of the wall is also compared in figure 5.9. The time lag between the warm and cold conditions is around 10 days for 1 MPa suction, 26 days for 2 MPa suction, and 56 days for 3 MPa suction. This time lag is gradually increasing for the duration of drying studied.

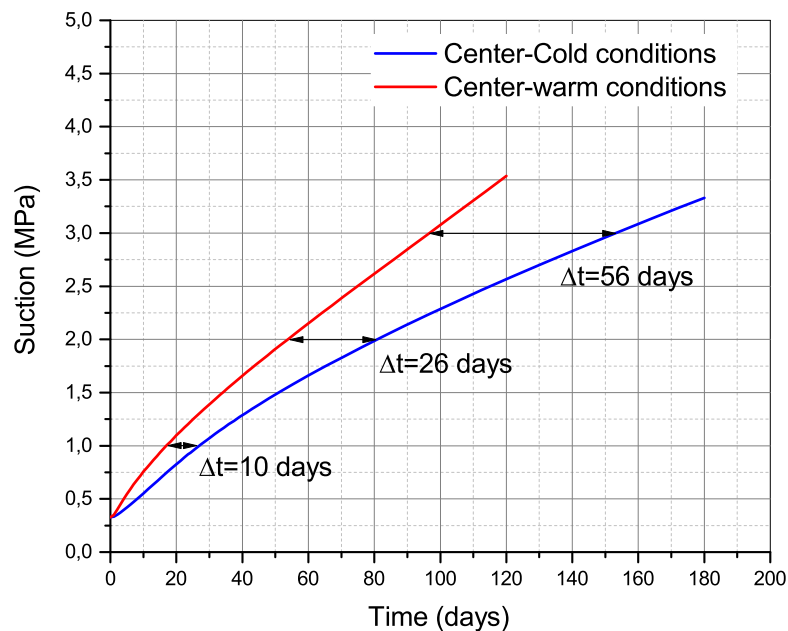


Figure 5.9: Comparison of suction evolution at the critical point (at the center) for warm and cold environmental conditions

5.4 Two walls joined at right angle

The 3D geometrical model considered was 2 walls perpendicular to each other, as shown in figure 5.10. The length and the height of the walls were 3m, and the width was 0.45m. The mechanical boundary conditions are also shown. The bottom surfaces were fixed ($u_x = u_y = u_z = 0$). For the left wall, one lateral surface (perpendicular to z -direction), displacement in the perpendicular direction was not allowed ($u_z=0$). Whereas, for the right wall, one lateral surface (perpendicular to x -direction), displacement in perpendicular direction was also not allowed ($u_x=0$). While the other surfaces were stress-free ($\sigma_{ii} = 0$ and $\tau_{ij} = 0$) with displacements being allowed. The vertical stress was applied on the top boundary, and the direction of drying has also been shown. Regarding the mesh composition (figure 5.11), 10 elements along the width, 12 elements along the height, and 5 elements along the length were taken to have 2400 linear hexahedral (C3D8) elements. The number of nodes was 3003.

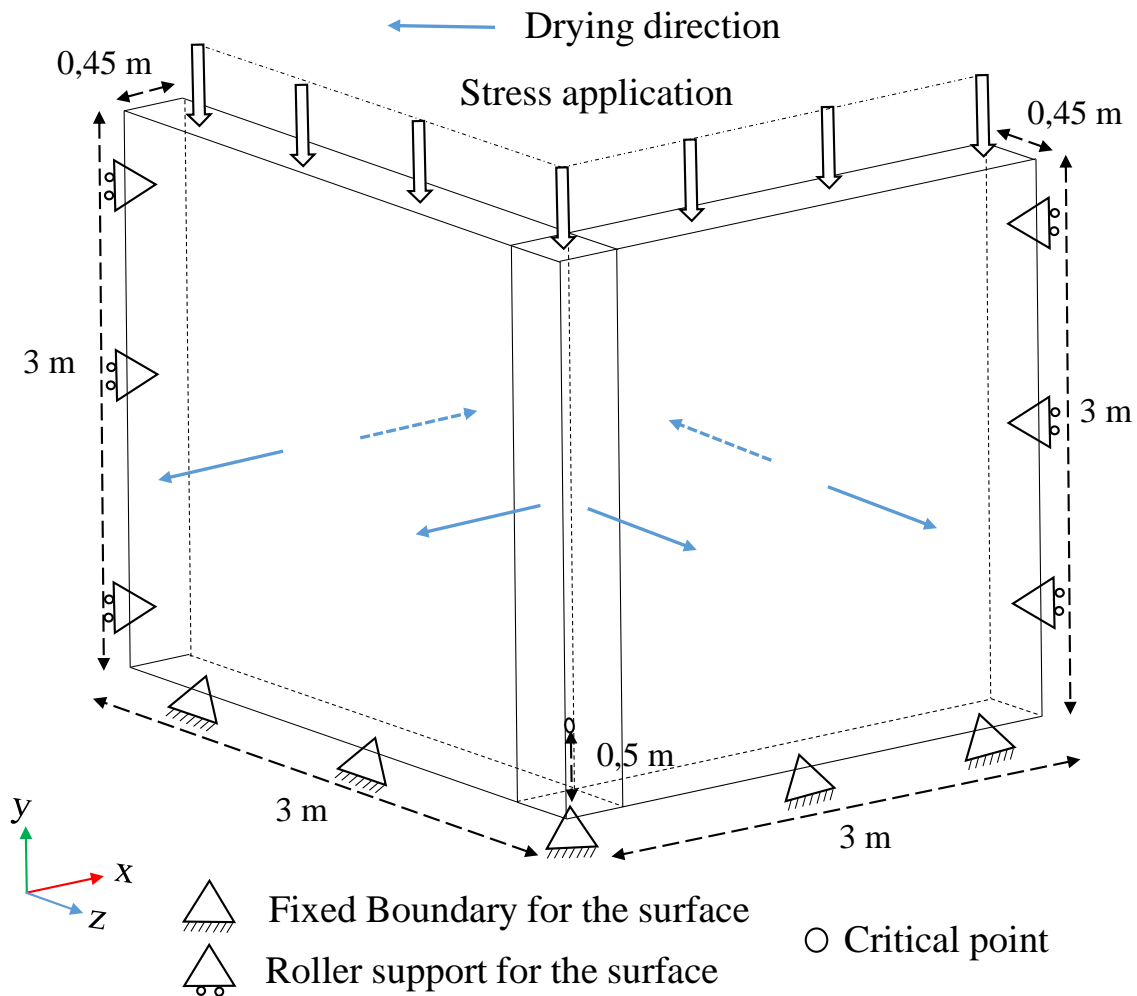


Figure 5.10: 3D model of the 2 walls showing the boundary conditions and direction of drying

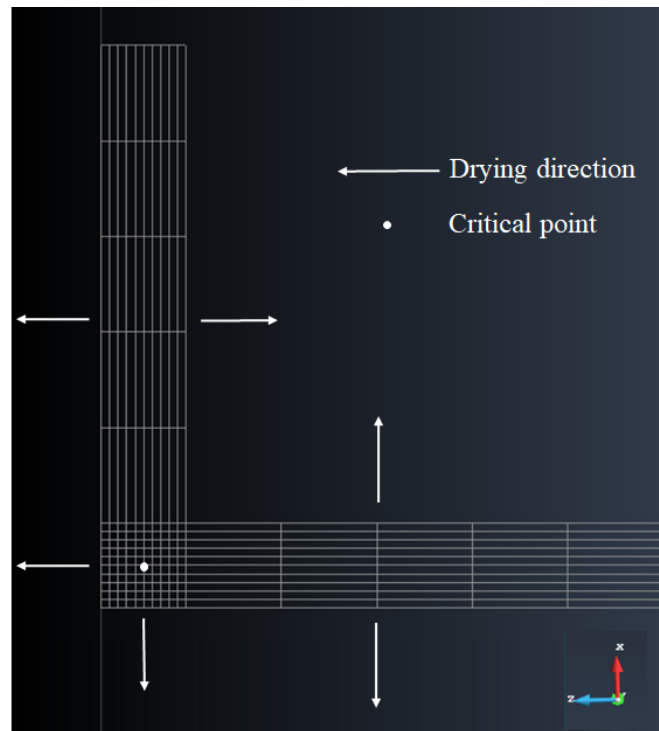


Figure 5.11: The 2D mesh composition of the model in XZ plane (top view)

Drying in warm conditions

In these simulations, the critical point is at the center of column formed at the junction of the 2 walls at a distance of 0.5 m from the bottom. Thus, the stress path of this point will be shown in figure 5.12. The simulations were carried out in two phases. In the first phase, the wall was subjected to drying in warm conditions from 0-240 days in the interval of 30 days. In the second phase, vertical stress of 0.2 MPa was applied gradually, similar to the single wall case.

For no drying, i.e. at compaction hydric state, the stress state evolves linearly (figure 5.12). The stress path, in this case, is steeper than a single wall and reaches higher deviatoric stress. This is due to stress concentration close to the bottom of the column since out of plane displacements are allowed in the column in both x and z-direction.

The stress path is translated to the right in the p' - q plane, depending on the suction and degree of saturation values at the critical point. A drying period of more than 240 days is required for the critical point to be safe with regards to the safety failure surface. This long drying period at the same value of relative humidity and temperature is not reasonable based on the actual weather data (figure 5.2).

Figure 5.13 shows the suction distribution across the width of the walls at the end of 240 days of drying. The drying front due to the atmospheric boundary conditions applied for this configuration can be followed along the longer distance across the wall, which is the diagonal line materialized in figure 5.13. Thus, the isochrones of suction and degree of saturation are shown in figure 5.14 along the diagonal of the column and the

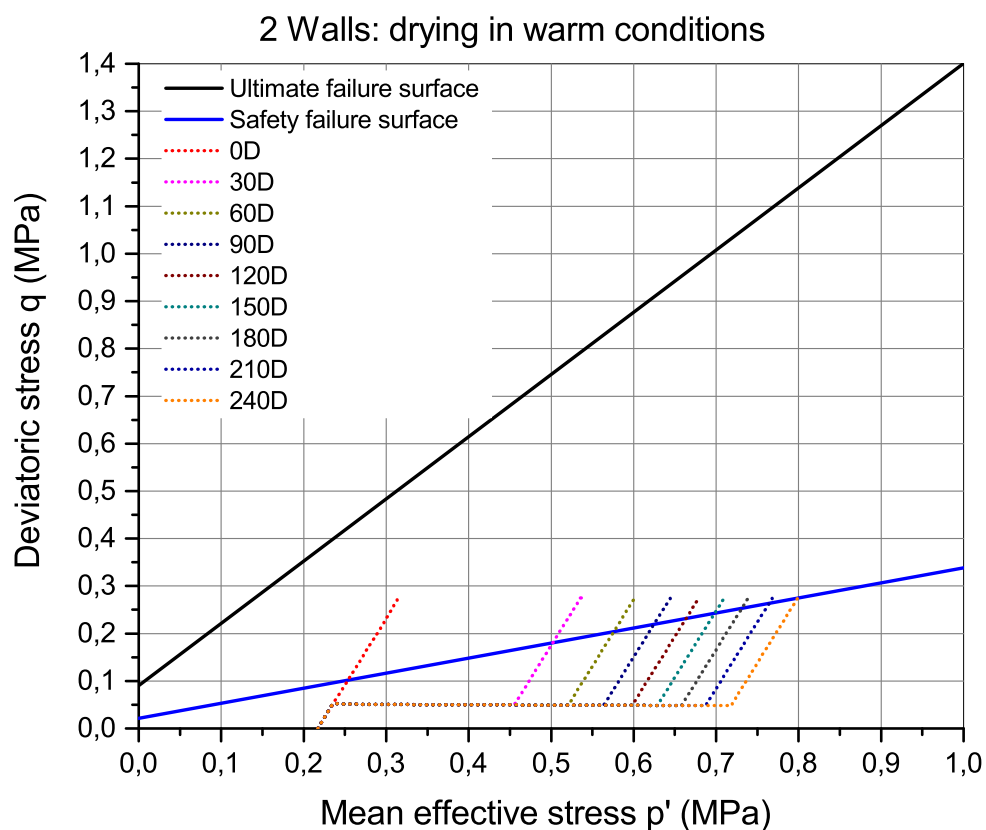


Figure 5.12: The stress path in p' - q plane for the critical point in the wall at different duration of drying in warm environmental conditions

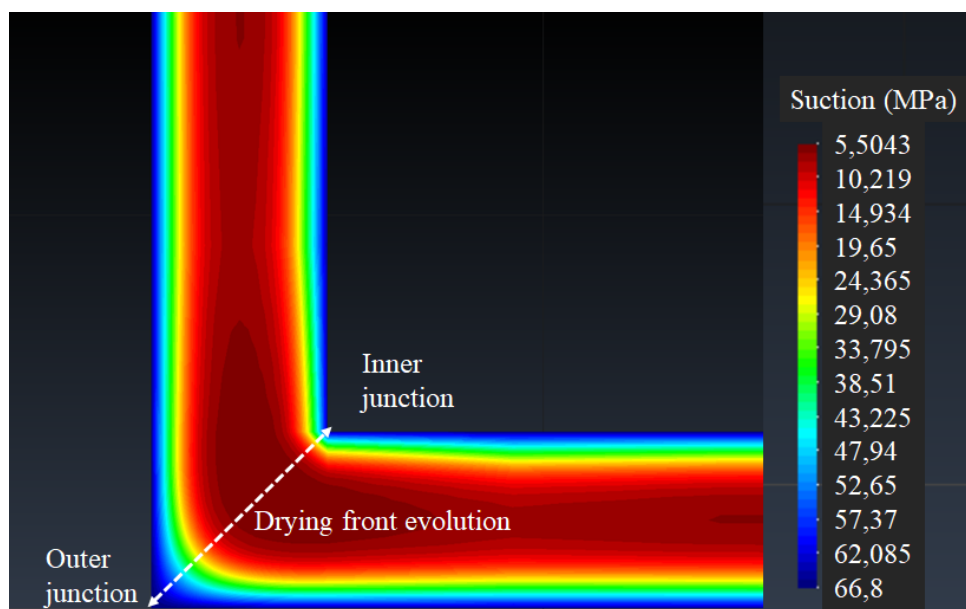
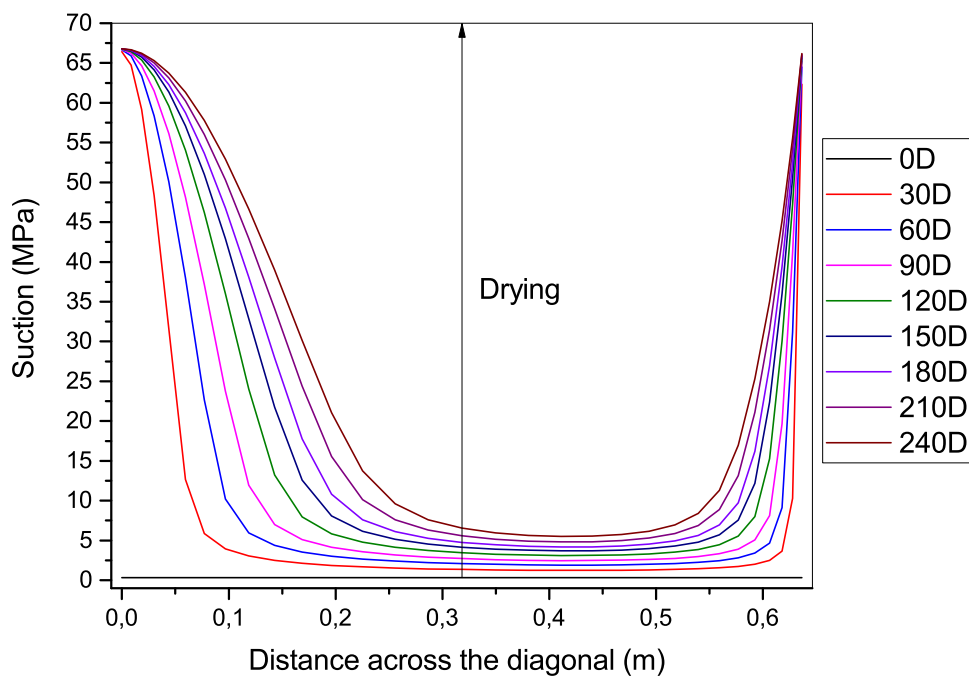
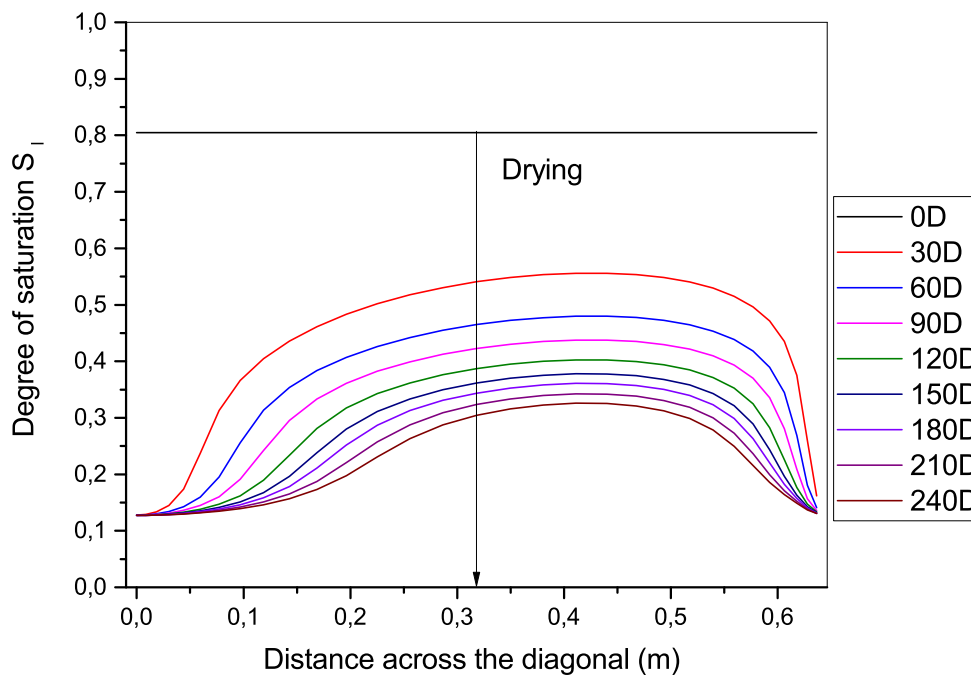


Figure 5.13: Suction distribution across the width of rammed wall after 240 days of drying period



(a)



(b)

Figure 5.14: Suction (a) and degree of saturation (b) variation across the diagonal of rammed column formed at the junction of 2 walls at different drying period in warm environmental conditions

distance is represented from the outer junction towards the inner junction.

In figure 5.14, the vertical line labelled as drying is intersecting the isochrones at the critical point which is at the center of the column. The suction and degree of saturation evolve more towards the outer junction since there are two perpendicular faces on which drying is taking place. The suction values at the center, increase from 0.328 MPa at initial state to 6.56 MPa at 240 days of drying. Corresponding to these suction values, the degree of saturation evolves from 0.805 at initial state to 0.3 at 240 days of drying.

Although the points towards the inner junction are wetter and have slightly lower suction values, the stress path for these points was checked, and they were safer compared to the critical point. Since it took more than 8 months of drying for this wall configuration to be safe, it again highlights the conservative nature of the hypothesis chosen for drying conditions and safety criterion. Regarding the drying in cold conditions, it will take more than 8 months and thus is not feasible for that climatic conditions. Hence, the results for that case have not been studied here.

To conclude, it takes a significant amount of drying time for this wall configuration in both warm and cold conditions. Drying at the same value of relative humidity and temperature is not reasonable for 8 months based on the actual weather data shown in figure 5.2. Hence the simulations should be carried out with the actual weather data. In addition, all the points of improvement mentioned for the single wall (section 5.3) are also valid for this case.

5.5 Conclusion and Perspective

In this chapter, a methodology was developed in order to determine the drying period required for the walls to gain enough strength in order to build the subsequent floor, which is a major practical issue in rammed earth construction. In this regards, THM coupled simulations of two different configurations of walls were carried out at warm and cold environmental conditions while taking into account a safety criterion using a similar approach from Guide des Bonnes Pratiques.

For a single wall subjected to drying in warm conditions, a drying period between 3-4 months was needed according to our results. This period is also recommended in the guide of good practices [25]. Whereas, in the cold conditions, a drying period of around 6 months was needed according to our results and our weather conditions. This seems not to be reasonable cause winter period in Le Bourget-du-Lac is not so long. Nevertheless, the guide of good practices indicates that it is not reasonable to build in winter [25].

For two walls joined at right angle, a drying period upwards of 8 months was determined in warm conditions. Whereas in the cold conditions, the duration obtained would be higher. Thus, it was inferred that it takes a significant amount of time for the walls to dry sufficiently in order to construct an additional floor by taking into account the safety criterion proposed. It doesn't seem reasonable under today's construction conditions. Hence this safety criterion is too conservative and very far from the ultimate failure criterion for the material. Nevertheless, our approach makes it possible to objectify the conditions for drying a rammed earth wall, which is very important for future work which is mentioned as follows:

- In these simulations, solar radiation and rainfall were not considered, which can be taken into account to improve the analysis.
- The surface heat/mass transfer coefficient value was taken from the literature, which was slightly conservative in nature. Thus, it can be determined for the actual conditions by taking into account the wind velocity.
- Since it was observed that the drying period was higher than 4 months of the actual warm/cold conditions, which is not practical, it is recommended to use actual time-varying weather conditions.
- A less conservative safety criterion can be proposed without significantly compromising the safety factor. In this way, the drying duration required will be significantly reduced while still being far from the ultimate failure state.

Chapter 6

Conclusions and perspectives

The thesis work presented an experimental and numerical study in order to understand the coupled hydro-mechanical behavior of unstabilized rammed earth. The experimental study was done at both material and structural scale.

At the material scale, compression and shear testing were performed at different suction states. The samples used were compacted using a technique of static double compaction. It was observed that various mechanical parameters such as compressive strength, Young's modulus, apparent cohesion, apparent friction angle increased with the suction state of the material. It showed that suction has an effect on the internal stress state of the material, which, in turn, affects its mechanical behavior. It was demonstrated that a framework based on the concepts of unsaturated soil mechanics using generalized effective stress helps to study the mechanical response by taking into account the effect of suction inside the stress state. Suction multiplied with effective stress parameter, which is a function of degree of saturation plays the same role as confining pressure, thus providing additional strength.

Hydro-mechanical coupled behavior was also studied for rammed earth columns under non-uniform suction conditions. The columns were subjected to 1D drying, which is representative of real rammed earth walls. The local and global evolution of the hydric state of the material was studied. Also, the drying phase kinetics were determined. In addition, the compressive strength testing of the columns was done after natural convection drying. It was observed that the columns gain a significant amount of strength and stiffness within the first two weeks of drying from the initial hydric state. This is due to the additional suction induced cohesion in the material. In addition to the effect on the strength and stiffness, drying also affected the consistency of the material. The material behavior changes from more plastic at lower suction states to more brittle at higher suction states.

Coupled THM simulations of drying and compression of columns were performed on the rammed earth columns using finite element analysis. The drying phase simulations were carried out using atmospheric boundary conditions, which are more realistic than

imposed suction at the boundary. The mechanical behavior was coupled with the hydric state by using the generalized effective stress for unsaturated soils. The coupled model was calibrated based on conventional soil mechanics tests. Both the drying and compression behavior was reproduced reasonably accurately. Accurate determination of the effective stress parameter is important since the mechanical simulation are very sensitive to this parameter.

Finally, the numerical case study was done to determine the drying period required for subsequent floor construction. It was observed that a significant amount of drying time was required based on the recommendation from the practical guide used in France for rammed earth construction. It showed that the safety criterion suggested was very conservative. This study helped to present a methodology to answer a practical issue faced in rammed earth construction. This modeling was done in order to prove the suitability and the potential that this PhD work provides for the earth construction sector.

In order to perform this numerical analysis, 7 parameters need to be determined experimentally. A synthesis of the tests required is described as follows:

- Determination of the soil water retention curve for the whole range of suction. Pressure plate (2 tests) and saline solution method (7 tests) were both necessary in order to determine points for low and high values of suction, respectively.
- Determination of intrinsic permeability of the material (3 tests). Triaxial apparatus was used in order to saturate the rammed earth sample and to impose differential pressure across the boundaries.
- Unconfined compressive strength tests (3x8) and unsaturated triaxial tests (3x7) on samples at different suction states. Using these tests, the expression for effective stress parameter as a function of degree of saturation is determined.
- Saturated triaxial tests (4) in order to determine the intrinsic value of cohesion and friction angle.

Perspectives

There are different limitations in the study carried out which can be improved in the future study and are presented here as perspectives:

- Additional experimental tests at material scale should be done in the higher range of degree of saturation to have a better expression of the effective stress parameter that fits well in the whole range of degree of saturation. This will help to better study the early age drying behavior of rammed earth.
- For the drying of the rammed earth columns, SHT sensors were used which are suitable for the serviceability lifetime of rammed earth building but are less relevant

at the beginning phase of drying. A different type of sensor such as TDR sensors which measures water content should be used when the earth is closer to saturation.

- The value of surface mass/heat transfer coefficient was used from the literature. An experimental methodology should be developed in order to measure this parameter for the ambient conditions in which the drying is taking place and for the rammed earth material being studied.
- In the mechanical model used, the effective stress expression was introduced in the shear strength expression to perform the coupled analysis. Using this, only the failure compressive strength of the columns was predicted. A mechanical model which can be directly expressed in terms of effective stress should be used. This will allow to take into account the variation of elastic modulus with suction state and predict the accurate stress-strain behavior. This could be possible in another FEM code, integrating this effective stress definition.
- In the wall case study, the effect of solar radiation and rainfall can be taken into account to improve the analysis. Moreover, real-time weather data for relative humidity, temperature, and air velocity should be used. A less conservative safety criterion without compromising the safety factor should be used, which will help to obtain a more accurate drying period required during construction.

Chapter 7

Synthèse

Dans le contexte mondial, le secteur du bâtiment est responsable de plus de 40% des émissions totales de gaz à effet de serre, ce qui contribue à des niveaux élevés de pollution. Selon l'ADEME 2015 [107], la quantité de déchets issus du secteur du bâtiment représente environ 44% du total des déchets en France. Ces déchets ne sont généralement pas facilement recyclables et sont éliminés dans des décharges, ce qui entraîne une perte importante de terres. Ainsi, il existe un besoin d'un matériau de construction alternatif ayant des caractéristiques plus écologiques par rapport aux matériaux de construction conventionnels tels que l'acier et le béton. La terre crue est une solution possible à ce problème.

La terre est l'un des matériaux de construction les plus anciens. Même aujourd'hui, la construction en terre existe dans le monde entier et c'est le principal processus de construction pour certains pays. Environ 30% de la population mondiale vit encore dans des bâtiments en terre. L'utilisation mondiale de la construction en terre et de divers sites du patrimoine mondial de l'UNESCO a été illustrée dans la figure 1.1.

L'une des techniques importantes de construction en terre est le pisé. C'est une technique de construction ancienne par laquelle des murs porteurs denses peuvent être réalisés par compactage dynamique de sol humide entre les coffrages amovibles. La terre crue (c'est-à-dire sans aucun liant supplémentaire) présente divers avantages en tant que matériau de construction durable. Cela conduit à une réduction de l'énergie intrinsèque. L'énergie intrinsèque requise pour un matériau en terre est d'environ 1% de l'énergie nécessaire pour la construction avec des matériaux à base de ciment [32]. Cela conduit également à une réduction de l'énergie opérationnelle due aux effets hygro et thermorégulateurs [32]. De plus, la terre est entièrement recyclable lors de la démolition des bâtiments et ne nécessite aucune décharge pour son stockage. Enfin, il offre une résistance suffisante pour la construction d'un bâtiment de 1 à 2 étages.

Malgré les nombreux avantages de la terre en ce qui concerne la durabilité, diverses limitations entravent l'utilisation généralisée de matériaux de terre tels que la terre battue pour la construction. L'une des plus grandes limites de l'utilisation d'un

matériau en terre est sa sensibilité à l'eau, ce qui rend son utilisation difficile à généraliser. En effet, la pénétration d'humidité induit des changements dans la consistance de la terre du solide au plastique. Cela conduit à une modification de la résistance mécanique et de la rigidité. Pendant la durée de vie du bâtiment, les conditions ambiantes sont en constante évolution, ce qui affecte les performances mécaniques. Ainsi le manque de caractérisation de cette influence hydrique est un inconvénient majeur pour son application pratique directe. Un autre inconvénient auquel la construction en terre fait face est le manque de directives techniques et de dispositions codales. Bien que certains pays aient leur propre ensemble de directives et de normes, il existe des incertitudes dans les méthodologies de conception. En outre, il existe un manque de cohérence entre les lignes directrices des différents pays.

L'objectif principal de cette étude est de mettre l'accent sur l'utilisation de la terre battue pour la construction économe en énergie et d'avoir une meilleure compréhension du comportement hydromécanique de pisé. Ce couplage hydromécanique est essentiel pour être compris et quantifier tant pour la construction neuve que pour la préservation des bâtiments et monuments historiques, qui sont aujourd'hui très pertinents. Les différents objectifs de la thèse sont présentés dans la figure 7.1 et mentionnés comme suit :

- Étudier l'effet hydrique sur les paramètres mécaniques à l'échelle du matériau.
- Étudier l'évolution de la résistance et de la rigidité à l'état hydrique sur un élément structurel représentatif, c'est-à-dire une colonne de pisé structurée en couche.
- Reproduire numériquement l'effet de l'eau sur le comportement mécanique à l'échelle de la structure sur des colonnes en pisé.
- Développer une méthodologie pour déterminer la période de séchage requise avant la construction ultérieure du plancher en réalisant une étude de cas numérique sur des murs en pisé.

7.1 Etude expérimentale à l'échelle du matériau

Le plan expérimental de cette étude comprend les tests suivants:

1. Essai de résistance à la compression non confiné : 24 échantillons (3 chacun à 8 états hydriques différents) afin de déterminer la variation de la résistance à la compression et de la rigidité avec l'état hydrique.
2. Essai de cisaillement direct : 63 échantillons (9 chacun à 7 états hydriques différents) ont été testés pour déterminer la variation des paramètres de cisaillement apparent avec l'état hydrique.

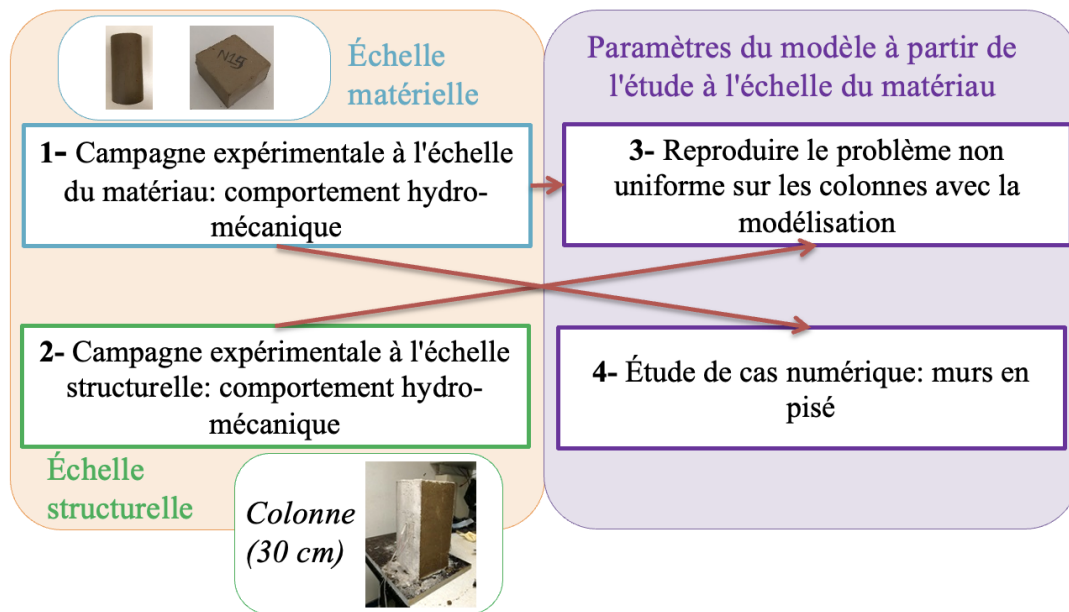


Figure 7.1: Méthodologie du travail de thèse

3. Essai triaxial :

- Triaxial non saturé : 21 échantillons (3 chacun à 7 états hydriques différents) pour déterminer la variation des paramètres de cisaillement apparent avec l'état hydrique.
- Triaxial saturé : 4 échantillons pour déterminer les paramètres intrinsèques de cisaillement.

Le sol pour cette étude a été prélevé sur un chantier de construction existant en Auvergne Rhône Alpes en France. La courbe de distribution granulométrique montre qu'elle contient environ 12% de gravier, 30% de sable, 51% de limon et 7% d'argile. Afin de caractériser finement l'argile, l'activité (rapport de l'indice de plasticité et du pourcentage plus fin que 2 micromètres) a été déterminée à 1,44 et est de nature légèrement active. De faibles valeurs de capacité d'échange cationique et de surface spécifique indiquaient une absence ou de faibles quantités d'argiles gonflantes. Afin de classer le sol, les limites d'Atterberg ont été évaluées et selon la classification française (Guide de terrassement routier [25]), le sol est qualifié de limon plastique faible.

Afin de déterminer la quantité d'eau à ajouter pour un compactage optimal, un test Normal Proctor a été effectué. Une teneur en eau optimale de 12,5% a été obtenue correspondant à une densité sèche maximale d'environ 1900 kg/m^3 . Pour la préparation des échantillons, une méthode de double compactage a été utilisée où la compression est appliquée des deux côtés pour obtenir une densité plus uniforme dans les échantillons. Une pression de compactage de 5 MPa a été choisie, pression classique pour les blocs de terre comprimée. Dans la première étape, 80% de la pression totale, c'est-à-dire 4 MPa est appliquée d'un côté et dans la deuxième étape, 100% de la pression totale est appliquée

des deux côtés. Des échantillons cylindriques de diamètre 5 cm, hauteur 10 cm et des échantillons prismatiques de 6 cm x 6 cm x 3 cm ont été préparés. Cette méthode de préparation des échantillons présente les avantages suivants:

- Plus d'uniformité de densité dans l'échantillon contrairement au compactage dynamique.
- Les échantillons ont été préparés avec une très bonne répétabilité (l'écart type maximum sur la densité est de 1,74% a été observé entre les échantillons) alors qu'en compactage dynamique l'écart type pouvait atteindre 11% [76].
- Un meilleur contrôle de la pression de compactage.
- Les échantillons ont une masse volumique sèche ($\rho_m=1908 \text{ kg}/m^3$) représentative d'un mur de pisé réel ($\rho_{wall}= 1700\text{-}2200 \text{ kg}/m^3$) [36].

Afin de représenter l'état hydrique, le paramètre succion totale a été utilisé. Succion totale est définie comme le potentiel thermodynamique de l'eau libre par rapport au potentiel de référence de l'eau libre. Il est composé de deux parties:

1. Succion matricielle : due aux effets combinés de la capillarité et des effets d'adsorption à courte portée. Les effets d'adsorption à courte portée sont négligés car ils sont pertinents à de très faibles valeurs de teneur en eau lorsque l'eau interstitielle adsorbée est principalement sous la forme de films minces recouvrant la surface des particules. Ainsi, la succion matricielle est définie comme la pression capillaire, c'est-à-dire la différence de pression d'air et d'eau interstitielle.
2. Succion osmotique : due aux solutés dissous dans l'eau interstitielle et à l'activité chimique du sol entraînant des forces sur les molécules d'eau. En général, de l'eau distillée est utilisée ainsi et le composant osmotique est considéré comme nul.

Afin de contrôler la succion, une méthode d'équilibre liquide-vapeur a été utilisée. Dans cette méthode, l'humidité relative de l'atmosphère est contrôlée et imposée autour de l'échantillon. Cette méthode est réalisée en utilisant des solutions salines. La solution aqueuse saturée de différents sels (tableau 3.4) permet de contrôler l'humidité relative de l'air autour des échantillons de 9% à 97,3%. La relation entre l'équilibre de l'humidité relative de l'air interstitiel et la succion imposée à l'éprouvette est basée sur l'équilibre thermodynamique de Kelvin (équation 3.12).

Les résultats des différents tests afin de déterminer la variation des paramètres apparents avec la succion sont discutés ici.

7.1.1 Test de résistance à la compression non confiné (UCS)

En tant que tendance globale de la variation de la résistance à la compression non confinée avec succion, on peut voir sur la figure 3.23 que la résistance à la compression diminue de manière significative avec la diminution de la succion. La valeur UCS varie de 0,35 MPa à 5,25 MPa pour une succion passant de 0,328 MPa à 331,3 MPa. Elle peut être liée au gain de résistance des structures en terre dans un bâtiment à partir de la date de fabrication (correspondant à une teneur en eau d'environ 11-13%) jusqu'à un état de longue durée, après plusieurs semaines de séchage (avec un teneur en eau d'environ 2%). Inversement, cela peut également être lié à la perte de résistance mécanique pour une entrée d'eau inhabituelle dans le matériau. De même, le module tangent initial augmente de manière non linéaire de 0,015 GPa à 1,37 GPa lorsque la succion augmente de 0,328 MPa à 331,3 MPa (figure 3.25). Cela indique que la terre battue gagne en force et en rigidité avec la succion.

7.1.2 Essai de cisaillement direct (DST)

Un test de cisaillement direct a été réalisé sur 63 échantillons à 7 états de succion différents. Dans cet essai, l'échantillon est cisailé tandis qu'une valeur constante de contrainte normale est appliquée et la résistance au cisaillement est déterminée. En utilisant la théorie de la résistance au cisaillement de Mohr-Coulomb, où une partie de la résistance au cisaillement dépend de la cohésion entre les particules et une autre partie est due au frottement entre les particules qui dépend de la contrainte normale (équation 3.14). En utilisant cela, la cohésion et l'angle de frottement ont été déterminés.

La valeur moyenne de cohésion des échantillons augmente de 0,383 MPa à 0,84 MPa avec une tendance linéaire lorsque l'état de succion passe de 3,8 MPa à 331,3 MPa (figure 3.31a). Ce comportement est justifiable à partir de la théorie de la contrainte effective généralisée, car il existe une cohésion capillaire supplémentaire induite par la saturation partielle de la terre, qui contribue pour une part importante à la résistance au cisaillement. De plus, on peut observer qu'il y a un moindre écart type dans les résultats pour les échantillons conditionnés à des états de succion inférieurs (humidité relative plus élevée). Alors que pour les échantillons conditionnés à des états de succion plus élevés (humidité relative plus faible), il y a un plus grand écart type dans les résultats. Ce comportement a également été observé dans les résultats d'essais de résistance à la compression non confinés (figure 3.23). Ceci peut probablement s'expliquer par le fait qu'un état sec du matériau induit un comportement fragile. En conséquence, la défaillance est plus localisée et donc affectée par de petits défauts dans la matière, et sa distribution aléatoire est responsable d'une dispersion des résultats de résistance. Au contraire, les échantillons plus humides sont ductiles, ce qui induit une rupture plastique concernant la masse globale du matériau. Dans ce cas, les valeurs par défaut ont moins d'influence et les résultats présentent un moindre écart. De plus, on observe également une variation

significative de l'angle de frottement apparent moyen qui varie de 43° à 63° avec une tendance non-linéaire (l'effet a tendance à se stabiliser à partir de 100 MPa de succion) lorsque la succion varie de 3,8 MPa à 331,3 MPa (figure 3.31b). Un écart type plus grand pour les échantillons conditionnés à un état de succion plus élevé et vice-versa a également été observé dans les résultats de l'angle de frottement apparent.

7.1.3 Test triaxial non saturé

Les tests triaxiaux ont été réalisés sur 21 échantillons à 7 états de succion. Ce test présente divers avantages par rapport aux tests de cisaillement direct car il n'y a pas de surface de rupture prédéfinie et un meilleur contrôle des conditions de drainage. Ce test a été réalisé en deux étapes. Dans la première étape, trois pressions de confinement différentes (σ_3) de 0,2 MPa, 1 MPa et 1,5 MPa ont été appliquées aux trois échantillons testés pour chaque condition de succion initiale. Dans la 2ème étape, le déviateur de contrainte a été appliqué ($q = \sigma_1 - \sigma_3$), avec une vitesse de déplacement axial de 0,1428 mm/min.

En utilisant la valeur de σ_1 et σ_3 , les cercles de Mohr ont été tracés et la valeur apparente de la cohésion et l'angle de frottement ont été déterminés. La valeur de cohésion apparente augmente de 0,5 MPa à 1,8 MPa avec succion (figure 3.37a). Le taux d'augmentation de la cohésion est plus élevé au début à des valeurs de succion inférieures. Ce taux d'augmentation de la cohésion diminue avec la succion, et la cohésion augmente à un taux plus lent à des valeurs de succion plus élevées. Cela est dû au fait que la cohésion supplémentaire induite par la succion augmente avec la succion, mais il y a une limite à cette contribution. À des valeurs de succion plus élevées, le degré de saturation de l'échantillon est plus faible. Ainsi, bien que la succion augmente, elle agit sur une plus faible proportion d'eau.

En revanche, il n'y a pas de modification significative de l'angle de frottement. La valeur de l'angle de frottement varie entre 31° et 37° avec une plus grande variation pour une faible succion et presque aucune variation à partir de 50 MPa (figure 3.37b). De plus, il apparaît que les valeurs de c et ϕ à un état de succion particulier sont différentes pour les tests de cisaillement direct (effectués à une contrainte normale inférieure) et les tests triaxiaux non saturés (réalisés à une contrainte normale plus élevée). Ce comportement indique qu'il y a non-linéarité dans l'enveloppe de rupture (plan $\tau - \sigma_n$).

7.1.4 Test triaxial saturé

Les paramètres de cisaillement intrinsèque ont été déterminés à l'aide d'essais triaxiaux saturés. C'est un test indirect pour appliquer une contrainte efficace au squelette granulaire. Ce test a été réalisé en 3 étapes. Dans la première étape, la saturation de l'échantillon a été effectuée. Dans la 2ème étape, différentes valeurs de pressions de confinement effectives ($\sigma'_3 = 100, 200, 300$ et 1500 kPa) sont appliquées. Dans la troisième

étape, la pression de confinement est maintenue constante et une contrainte déviatorique est appliquée à une vitesse constante de déplacement axial de 0,1428 mm/min.

Les paramètres efficaces ont été évalués comme $c' = 43,91$ kPa et $\phi' = 32,53^\circ$, qui sont bons du point de vue de la mécanique des sols. Ces valeurs obtenues sont similaires à celles de Gerard et al. 2015 [14], ce qui se justifie car la distribution granulométrique des deux sols utilisés est similaire.

7.1.5 Vers une modélisation constitutive

Afin d'utiliser les résultats décrits précédemment pour la modélisation constitutive, le premier point de discussion est la non-linéarité de l'enveloppe de défaillance. Le Mohr-Coulomb linéaire a été modifié, où la cohésion et l'angle de frottement ne sont pas des valeurs constantes mais dépendent de la contrainte normale (équation 3.22 et 3.23). σ_c est un paramètre d'ajustement défini comme la contrainte normale après laquelle la résistance au cisaillement n'augmente pas. En utilisant cela, l'enveloppe de défaillance non linéaire est tracée pour tous les états de succion avec l'enveloppe saturée (figure 3.44). L'influence de la succion est représentée sur la base du décalage de l'enveloppe de défaillance par rapport à l'enveloppe de défaillance saturée.

Pour la modélisation constitutive, l'approche utilisée pour analyser la réponse mécanique est l'approche des contraintes effectives généralisées. Dans cette approche, une seule contrainte effective définit l'état de contrainte d'un milieu poreux multiphase tel que la contrainte effective de Bishop (équation 3.24). Dans cette équation, χ est le paramètre de contrainte effective dépendant du degré de saturation. En utilisant l'enveloppe de rupture du test triaxial saturé et les cercles de Mohr dans la référence d'état de contrainte effective du test triaxial non saturé, la valeur de χ peut être déterminée à partir de la relation géométrique. Une relation de puissance a été observée et ainsi la valeur de $\chi = S_l^{1.9081}$ a été déterminée. Enfin, l'expression du stress effectif de Bishop s'écrit comme suit:

$$\sigma'_{ij} = \sigma_{ij} + (S_l)^{1.9081} s \delta_{ij} \quad (7.1)$$

7.2 Etude expérimentale à l'échelle structurelle sur colonnes

Le comportement hydromécanique des colonnes de pisé à une échelle de volume d'élément représentatif (REV) a été étudié. L'objectif est d'évaluer la capacité mécanique d'une colonne de pisé soumis à une sollicitation de séchage reproduisant un processus de séchage 1-D comme dans un véritable mur de pisé de terre.

Le plan expérimental comprend le test de 9 colonnes de pisé. Il comprend l'échantillon testé sans aucun séchage (jour 0) et séchage à différentes durées, c'est-à-dire jour 13, jour 31 et jour 62. À chaque durée, les échantillons ont été comprimés avec des cycles de déchargement-rechargement. Les échantillons soumis au séchage ont été recouverts de paraffine sur 4 faces afin d'imposer un séchage 1D. Un échantillon supplémentaire a été préparé que l'on a laissé sécher de tous les côtés jusqu'à séchage complet pour déterminer la résistance à la compression et la teneur finale en eau après séchage complet. Les échantillons ont été compactés avec la méthode de compactage dynamique à l'aide d'un marteau pneumatique en 4 couches à l'intérieur d'un moule en bois fait maison. Les échantillons soumis au séchage étaient également équipés de capteurs capacitifs SHT au milieu de la 3ème couche à une distance de 3,5, et à 7 cm de la face de séchage. Les échantillons ont été laissés à sécher dans un environnement fermé à une humidité relative ambiante (HR) de 65% et à une température de 15,5°C.

7.2.1 Comportement au séchage

Il a été observé que pendant la phase initiale de séchage, il y avait des changements minimes dans l'HR, et après deux semaines, la variation de l'HR pouvait être observée. Alors que la teneur en eau des échantillons a été réduite à environ la moitié de la teneur initiale en eau. Cela a été attribué au fait que l'incertitude dans la mesure de l'HR à des valeurs plus élevées était plus grande. Ainsi, les lectures du capteur ont été corrigées en utilisant des barres d'erreur dans les mesures. Ces capteurs sont moins pertinents au début du séchage à partir de l'état de fabrication car le signal est toujours saturé. Cependant, pendant la durée de vie utile du bâtiment, ils sont pertinents. En ce qui concerne la cinétique de la phase de séchage, 50% du séchage a eu lieu dans les 10 premiers jours et au bout de 62 jours, le séchage était d'environ 96% atteint asymptotiquement vers la fin.

7.2.2 Comportement de compression

La résistance à la compression des colonnes de pisé a été étudiée après séchage par convection naturelle. Il a été observé que la résistance à la compression augmente sensiblement après deux semaines de séchage. Le taux d'augmentation du gain de résistance était plus élevé au début de la phase de séchage, puis il diminue en conséquence, et la résis-

tance tend vers une valeur asymptotique finale. Ceci est dû à la cohésion induite par succion supplémentaire en raison de la saturation partielle du sol. Deux semaines de séchage ont suffi pour atteindre 63% de la résistance obtenue après un séchage complet. La variation de la résistance à la compression des échantillons testés avec des cycles de déchargement-rechargement était similaire, bien que la résistance de ces échantillons était soit similaire, soit inférieure à celle des échantillons testés sans cycles. Cela pourrait être dû à l'introduction de capteurs dans ceux-ci qui auraient pu interférer avec les essais mécaniques et conduire à une détérioration des paramètres mécaniques. Le module tangent a montré une variation similaire à la résistance à la compression. Il a augmenté à une vitesse plus élevée au début du séchage et tendant par conséquent vers une valeur asymptotique. Outre le comportement quantitatif, le comportement qualitatif des colonnes a également été affecté. Il est passé de plus de plastique à plus fragile avec le séchage, ce qui a également été observé dans l'étude à l'échelle du matériau.

7.3 Simulation du comportement de séchage et de compression des colonnes de pisé

L'objectif de cette partie est de simuler le comportement de séchage et de compression des colonnes de pisé en utilisant CODE_BRIGTH qui est un code FEM pour les problèmes couplés thermo-hydro-mécaniques dans les milieux géologiques.

En ce qui concerne les aspects théoriques du modèle, les différentes équations d'équilibre utilisées étaient la quantité de mouvement de masse et la conservation de l'énergie. Les différentes équations constitutives utilisées sont résumées ici. Pour le flux advectif liquide, la loi de Darcy (équation 4.8) a été utilisée. Pour le flux diffusif de vapeur d'eau en phase gazeuse, la loi de diffusion de Fick (équation 4.12) a été utilisée. Pour le flux de chaleur conductrice, la loi de Fourier (équation 4.14) a été utilisée, où la conductivité thermique dépend du degré de saturation et de porosité. Le comportement de rétention a été modélisé en utilisant le modèle de Van Genuchten (équation 4.9) et la conductivité hydraulique insaturée en utilisant le modèle de Mualem (équation 4.10) qui a utilisé la perméabilité intrinsèque et les paramètres du modèle de Van Genuchten.

Concernant le modèle mécanique, un modèle constitutif mécanique linéaire élastique parfaitement plastique a été utilisé. Les paramètres du modèle viscoplastique ont été ajustés pour obtenir le modèle de plasticité. Une surface de rendement Drucker-Prager basée sur les paramètres de Mohr-Coulomb a été utilisée. L'expression de la résistance au cisaillement a été modifiée pour tenir compte de l'augmentation non linéaire de la cohésion apparente avec succion et incorporer l'expression de la contrainte effective de Bishop [90].

Pour ces simulations, 7 paramètres devaient être déterminés expérimentalement tandis que les autres étaient tirés de la littérature ou une valeur classique a été utilisée.

Tous les paramètres et la méthode de détermination sont mentionnés dans le tableau 4.5.

7.3.1 Simulation de phase de séchage

Pour la phase de séchage, des conditions aux limites atmosphériques ont été utilisées en raison desquelles la succion à la limite a atteint son stade final progressivement, ce qui est plus réaliste qu'une condition de succion imposée à la limite. La valeur du coefficient de transfert de chaleur / masse a été ajustée pour s'adapter aux résultats expérimentaux tout en étant cohérente avec les lignes directrices de la littérature pour la convection naturelle dans un environnement intérieur. Un ajustement satisfaisant avec les résultats expérimentaux a été obtenu pour le séchage après prise en compte des incertitudes dans les mesures des capteurs. Il a fallu environ 160 jours pour que les colonnes sèchent complètement pour les conditions limites de séchage 1D. De plus, en utilisant cette approche numérique, il est possible de reproduire le séchage de n'importe quelle configuration de pisé.

7.3.2 Simulation de phase de compression

Pour les simulations de phase de compression, les paramètres mécaniques utilisés sont issus de la vaste campagne expérimentale réalisée sur des échantillons cylindriques à l'échelle du matériau. Le modèle n'a pas été en mesure d'incorporer la variation du module élastique avec la succion, et donc seule la contrainte de rupture a été prédite et non la courbe contrainte-déformation. La résistance à la compression obtenue à partir de la simulation était supérieure aux résultats de résistance expérimentale des essais avec et sans cycles de déchargement-rechargement. Pourtant, la tendance à la variation de la résistance à la compression avec la durée du séchage a été reproduite assez bien. Les paramètres de simulation ont été déterminés sur de petits échantillons compactés statiquement, alors que la colonne est compactée dynamiquement en couches. Ainsi, les différentes raisons de la surestimation de la résistance à la compression pourraient être la différence de méthode de compactage, d'effet d'échelle, de couches et d'hétérogénéité.

En ce qui concerne l'expression de χ , la valeur R-carré de l'ajustement était de 0,88, ce qui est faible. Ainsi, un intervalle de 10% a été choisi et l'analyse de sensibilité pour le paramètre de contrainte effective χ a été effectuée pour $\alpha \pm 5\% \alpha$ soit $\alpha = 1,8127$ et $\alpha = 2,0035$. Pour un petit changement de la valeur de χ , il y a un changement très significatif de la valeur de la résistance à la compression. Ainsi, les simulations de phase de compression sont très sensibles au paramètre de contrainte effective χ . Les résistances à la compression issues des simulations à $\chi = S_l^{2,0035}$ sont très proches des résultats expérimentaux sauf en phase initiale de séchage.

De plus, l'expression de χ choisie pour l'étude ne correspond pas bien aux résultats expérimentaux au degré de saturation de compactage. Pour cette raison, les résultats de la simulation de la résistance à la compression aux conditions de compactage

sont considérablement surestimés. Ainsi, afin de prédire plus précisément la résistance à la compression des colonnes, une expression différente pour χ doit être utilisée, qui correspond mieux aux résultats expérimentaux à une plage plus élevée de degré de saturation. De plus, d'autres tests doivent être effectués à proximité du degré de saturation de compactage pour déterminer χ avec précision.

7.4 Étude de cas: simulations couplées THM de murs en pisé

Une méthodologie a été développée afin de déterminer la période de séchage nécessaire pour que les murs acquièrent suffisamment de résistance pour construire le plancher suivant, ce qui est un problème pratique important dans la construction en pisé. À cet égard, des simulations couplées THM de deux configurations de murs différentes ont été réalisées dans des conditions environnementales 'chaudes' ($T_{moyenne} = 20^{\circ}\text{C}$, HR = 60%) et 'froides' ($T_{moyenne} = 5^{\circ}\text{C}$, HR = 85%) en tenant compte d'un critère de sécurité selon une approche similaire du Guide des Bonnes Pratiques [25].

Pour un seul mur soumis à un séchage 'chaud', une période de séchage de 3 à 4 mois était nécessaire selon nos résultats. Cette période est également recommandée dans le guide de bonnes pratiques [25]. Alors que, par temps 'froid', une période de séchage d'environ 6 mois était nécessaire selon nos résultats et nos conditions météorologiques. Ce n'est pas raisonnable car la période hivernale au Bourget-du-Lac n'est pas si longue. Néanmoins, le guide de bonnes pratiques indique qu'il n'est pas raisonnable de construire en hiver [25].

Pour deux murs assemblés à angle droit, une période de séchage de plus de 8 mois a été déterminée dans des conditions 'chaudes'. Alors que dans les conditions 'froides', la durée obtenue serait plus élevée. Ainsi, il a été déduit qu'il faut un temps important pour que les murs sèchent suffisamment pour construire un plancher supplémentaire en tenant compte du critère de sécurité proposé. Cela ne semble pas raisonnable dans les conditions de construction d'aujourd'hui. Par conséquent, ce critère de sécurité est trop prudent et très éloigné du critère de rupture ultime du matériau. Néanmoins, notre approche permet d'objectiver les conditions de séchage d'un mur en pisé, ce qui est très important pour les travaux futurs qui sont évoqués comme suit:

- Dans ces simulations, le rayonnement solaire et les précipitations n'ont pas été pris en compte, ce qui peut être pris en compte pour améliorer l'analyse.
- La valeur du coefficient de transfert de chaleur / masse de surface a été tirée de la littérature, qui était de nature légèrement conservatrice. Ainsi, il peut être déterminé pour les conditions réelles en tenant compte de la vitesse du vent.

- Utilisation des conditions météorologiques réelles variant dans le temps au lieu d'une valeur constante de l'humidité relative et de la température.
- Un critère de sécurité moins prudent peut être proposé sans compromettre significativement le facteur de sécurité. De cette manière, la durée de séchage requise sera considérablement réduite tout en étant encore loin de l'état de rupture ultime.

Enfin, afin de réaliser cette analyse numérique, 7 paramètres doivent être déterminés expérimentalement. Une synthèse des tests requis est décrite comme suit :

- Détermination de la courbe de rétention d'eau du sol pour toute la plage de succion. La plaque de pression (2 tests) et la méthode de la solution saline (7 tests) étaient toutes deux nécessaires pour déterminer les points de valeurs de succion faibles et élevées, respectivement.
- Détermination de la perméabilité intrinsèque du matériau (3 tests). Un appareil triaxial a été utilisé afin de saturer l'échantillon de pisé et d'imposer une pression différentielle à travers les limites.
- Essais de résistance à la compression non confinée (3x8) et essais triaxiaux insaturés (3x7) sur des échantillons à différents états de succion. À l'aide de ces tests, l'expression du paramètre de contrainte effective en fonction du degré de saturation est déterminée.
- Essais triaxiaux saturés (4) pour déterminer la valeur intrinsèque de la cohésion et de l'angle de frottement.

Appendix A: Stress-strain curve for UCS test

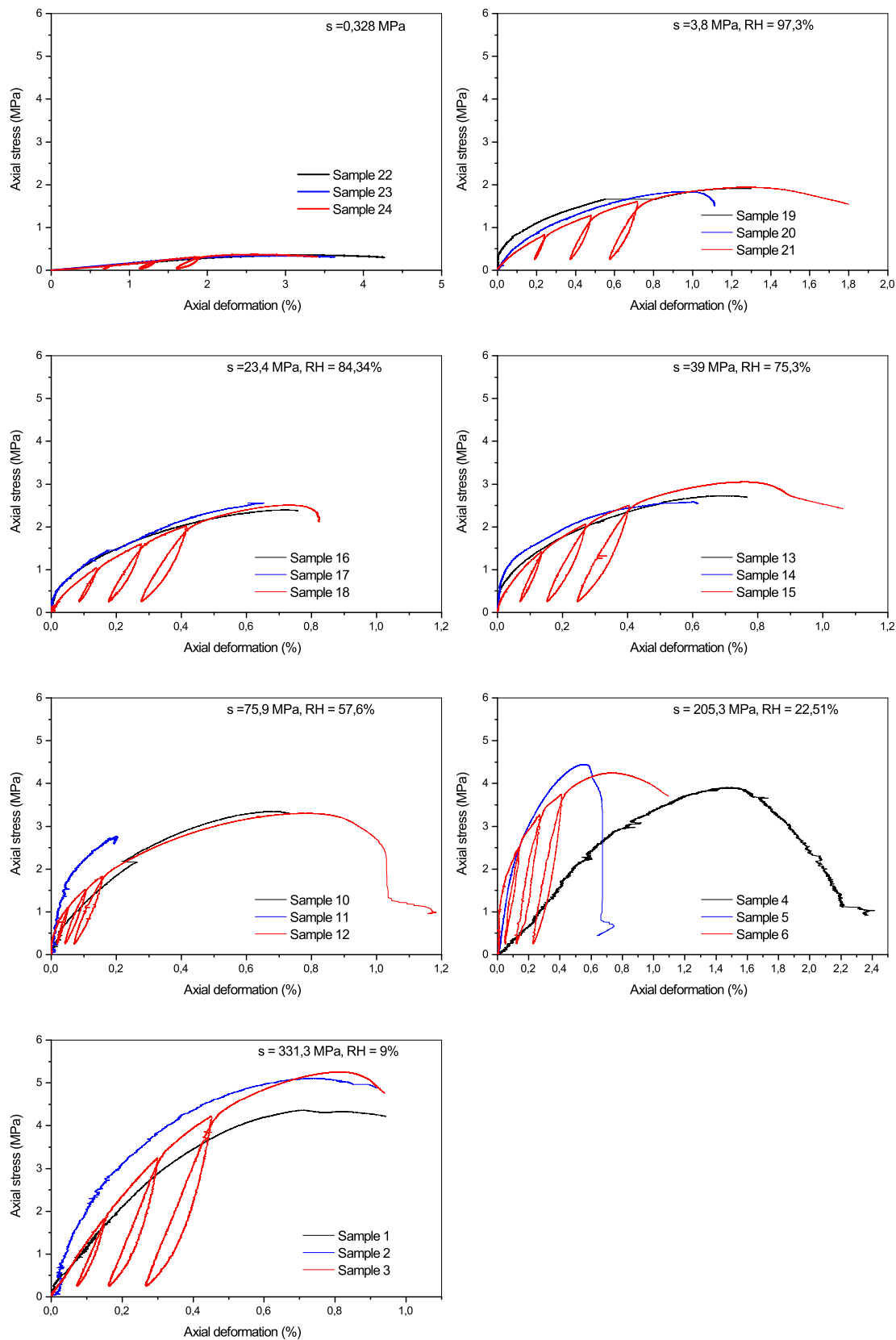


Figure A.1: Axial stress vs deformation curve for the unconfined compressive strength test conducted at different initial suction states

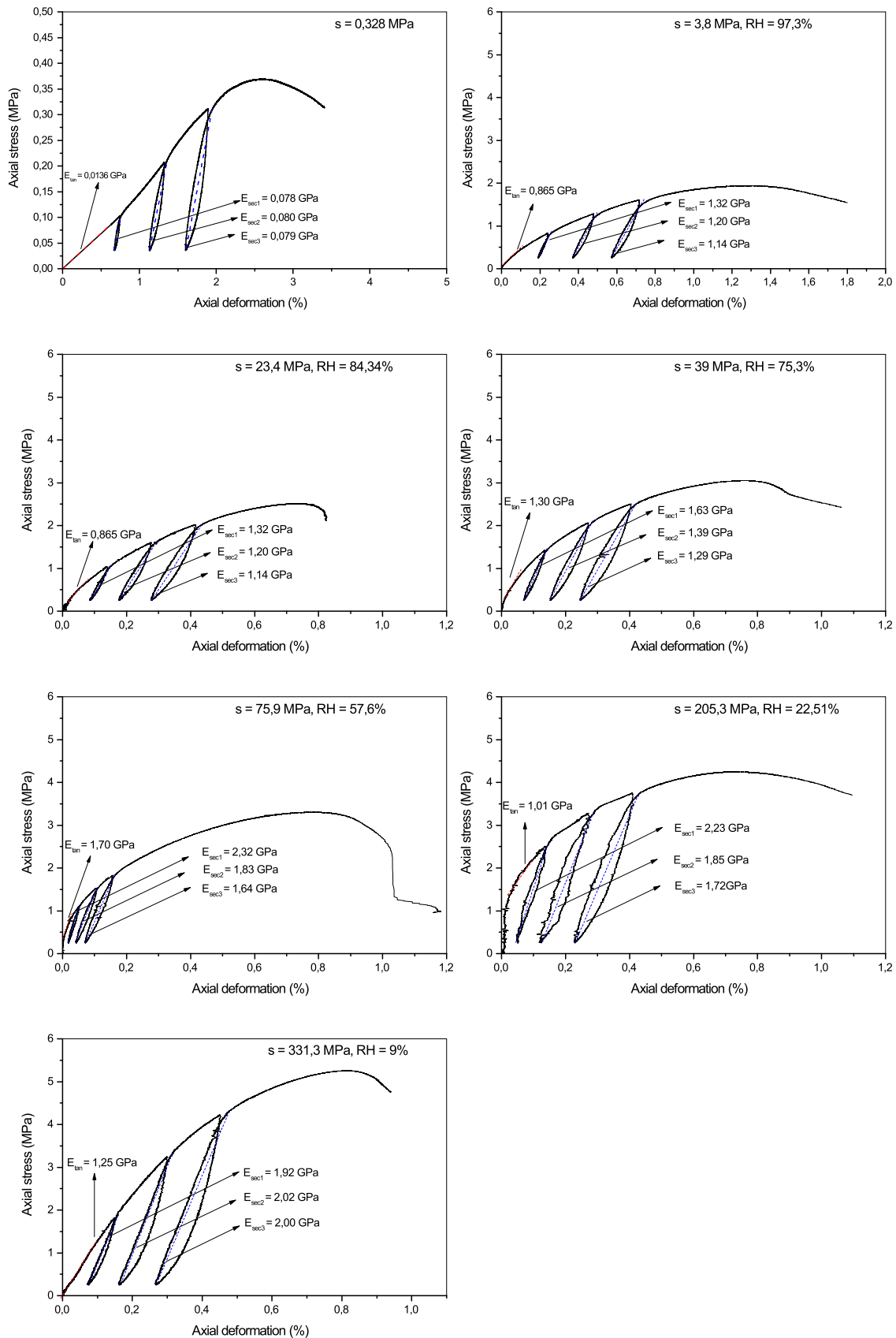


Figure A.2: Determination of initial Young's modulus and secant modulus for the unconfined compressive strength test conducted at different initial suction states

Appendix B: Results of DST test

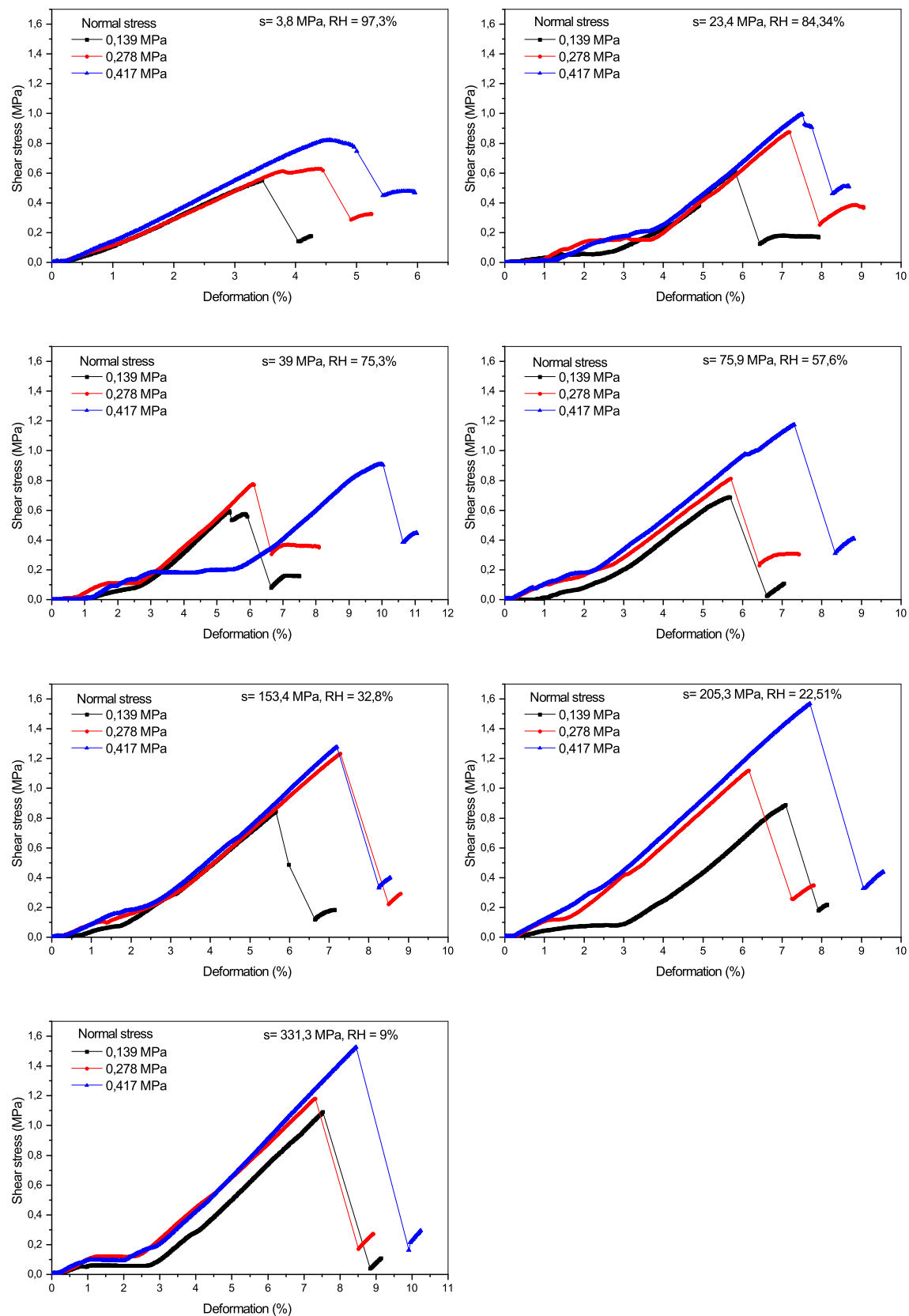


Figure B.1: Shear stress vs shear deformation curve during the direct shear tests for all samples of series 1

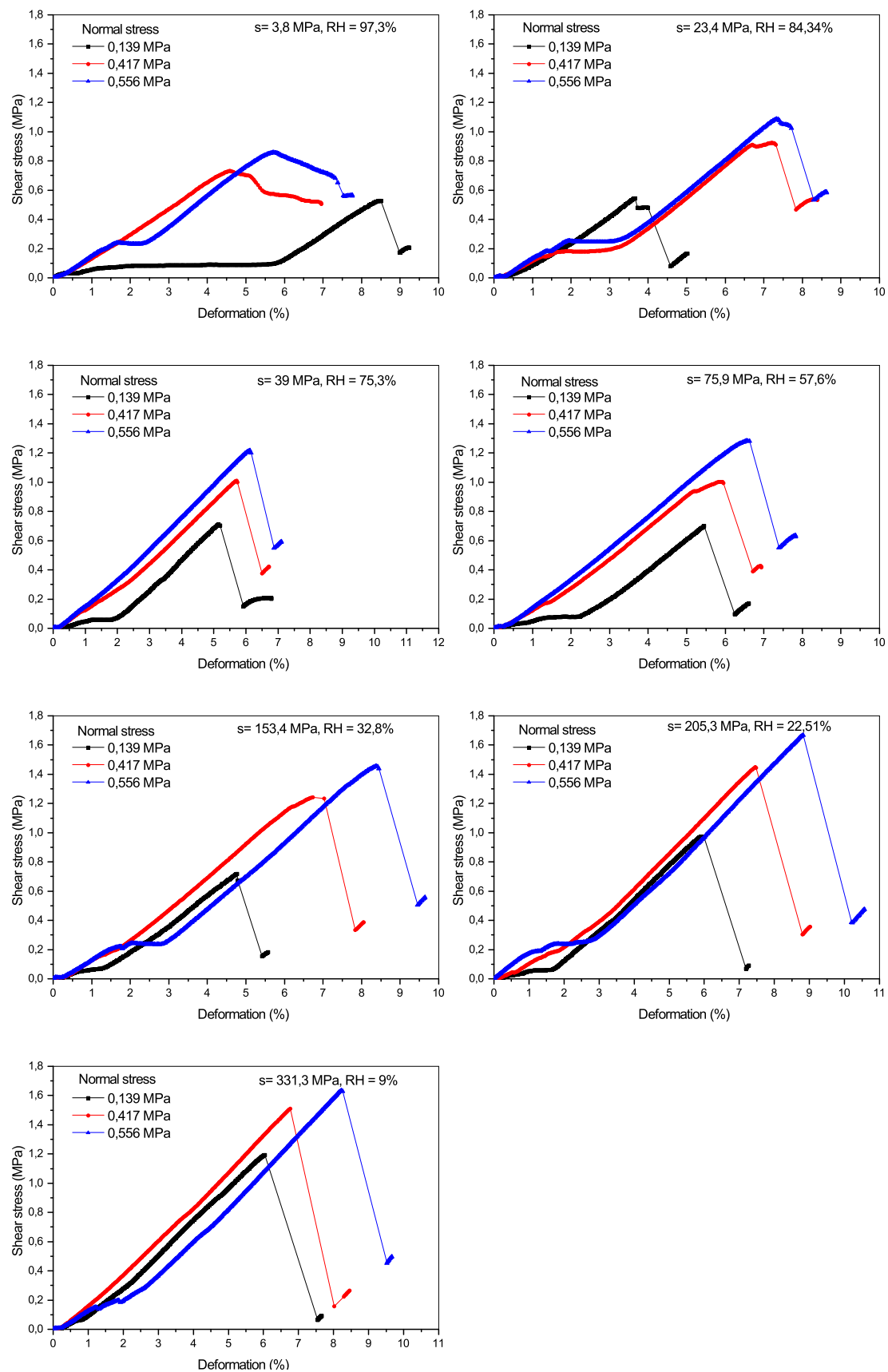


Figure B.2: Shear stress vs shear deformation curve during the direct shear tests for all samples of series 2

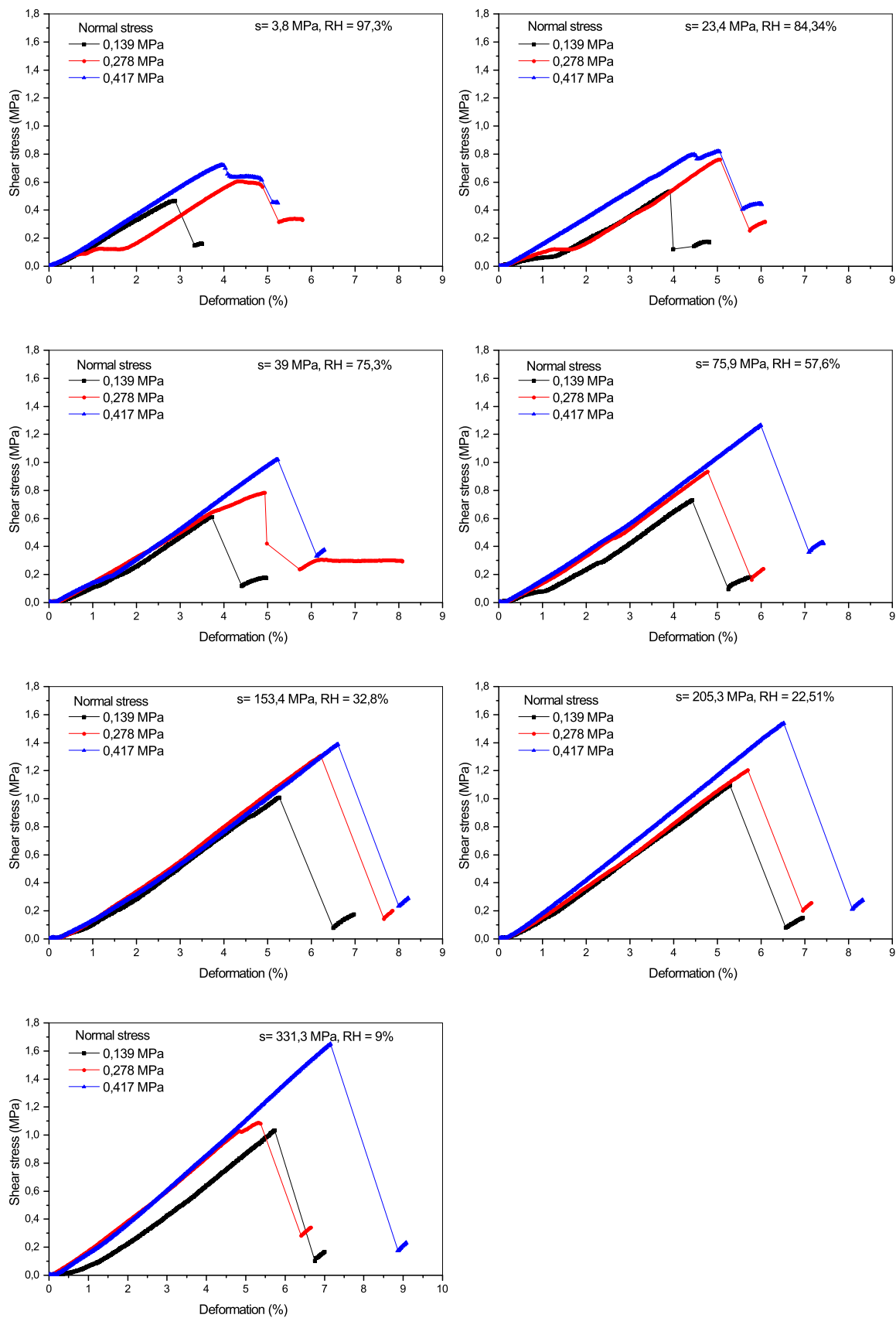


Figure B.3: Shear stress vs shear deformation curve during the direct shear tests for all samples of series 3

Appendix C: Results of unsaturated triaxial test

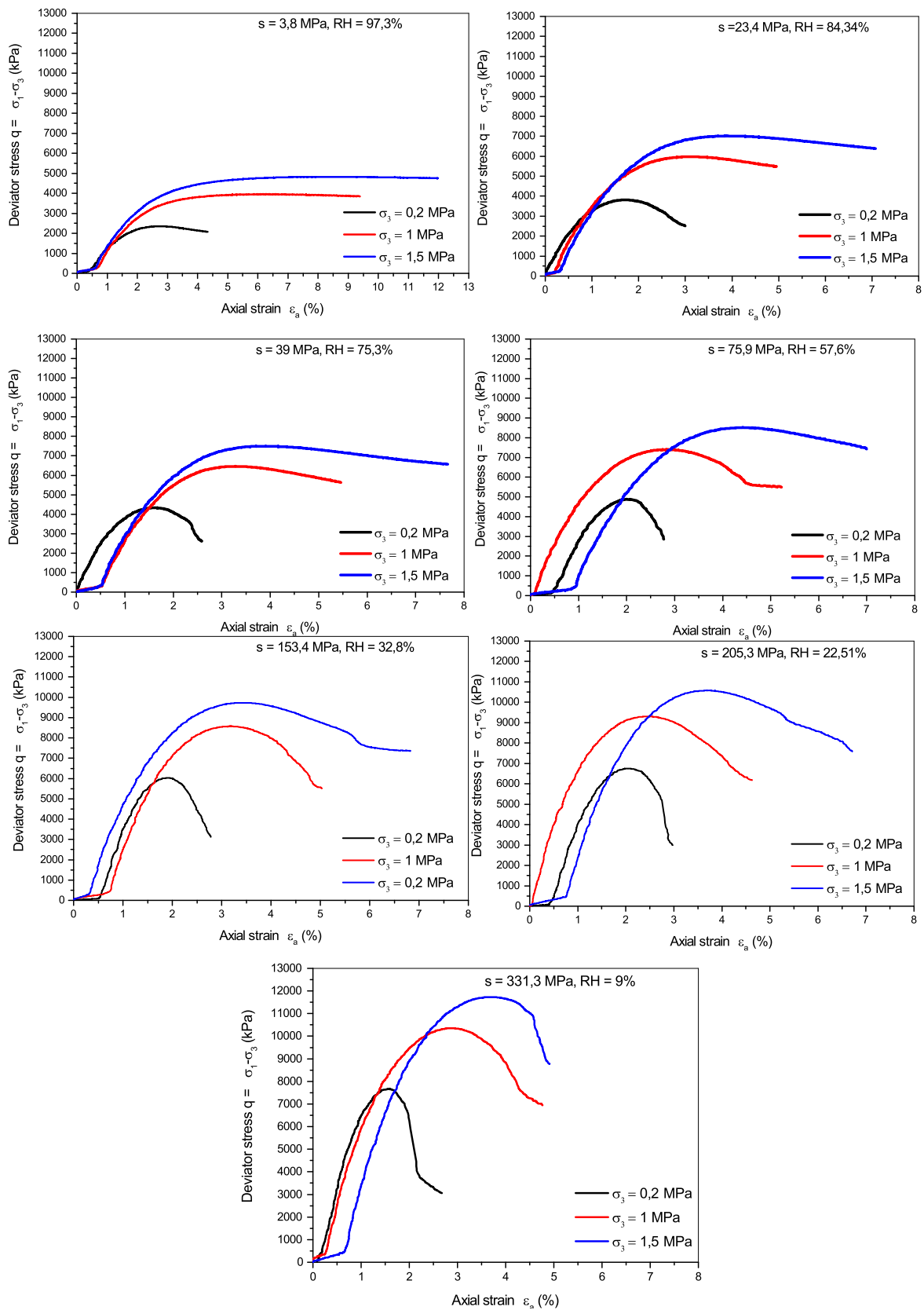


Figure C.1: Deviator stress vs axial strain curve for all samples tested in the unsaturated triaxial tests (Unconsolidated undrained) at 7 different initial suction states

Appendix D: SHT sensors calibration

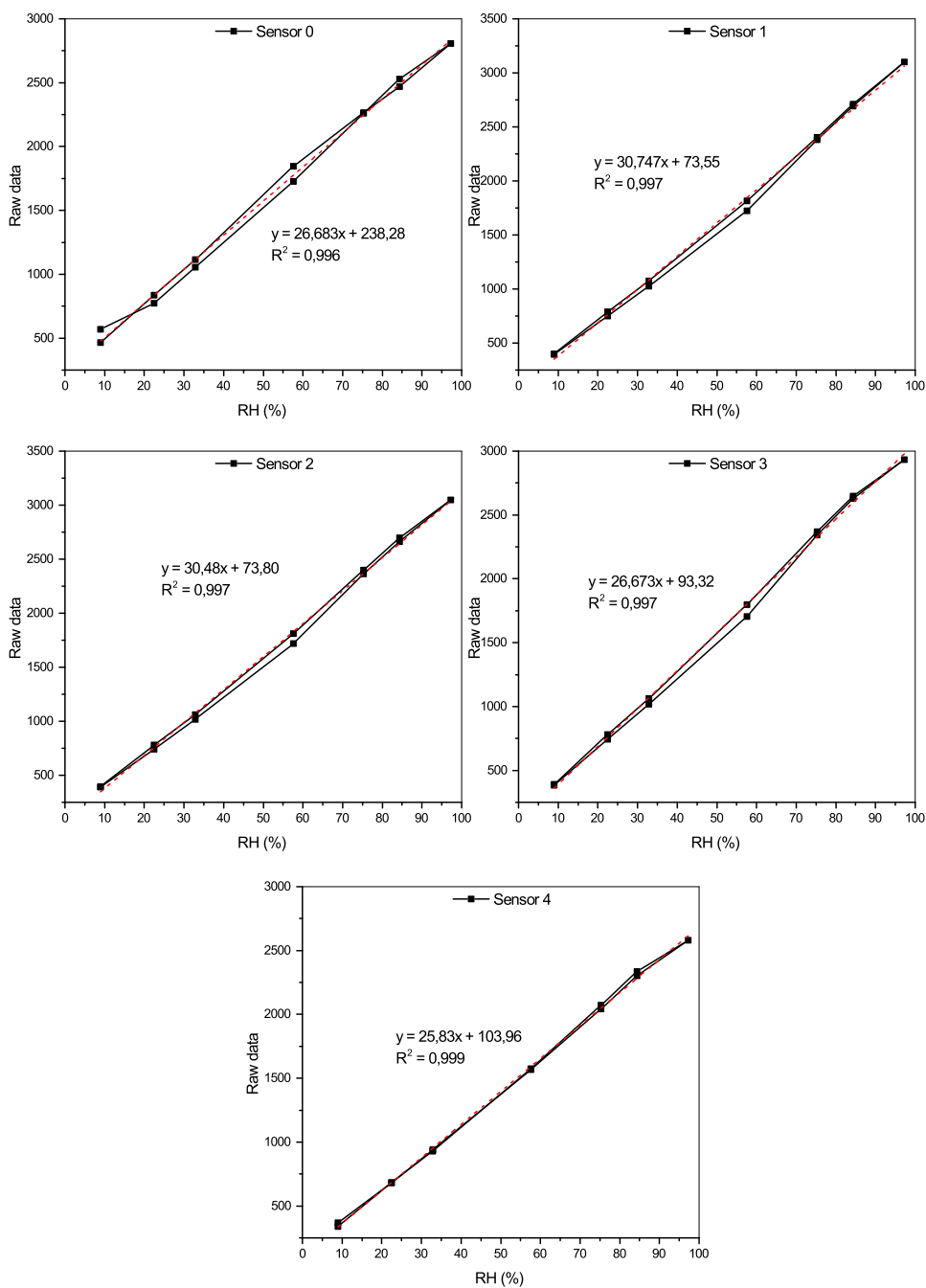


Figure D.1: Relative humidity calibration factors for SHT sensors 0-4

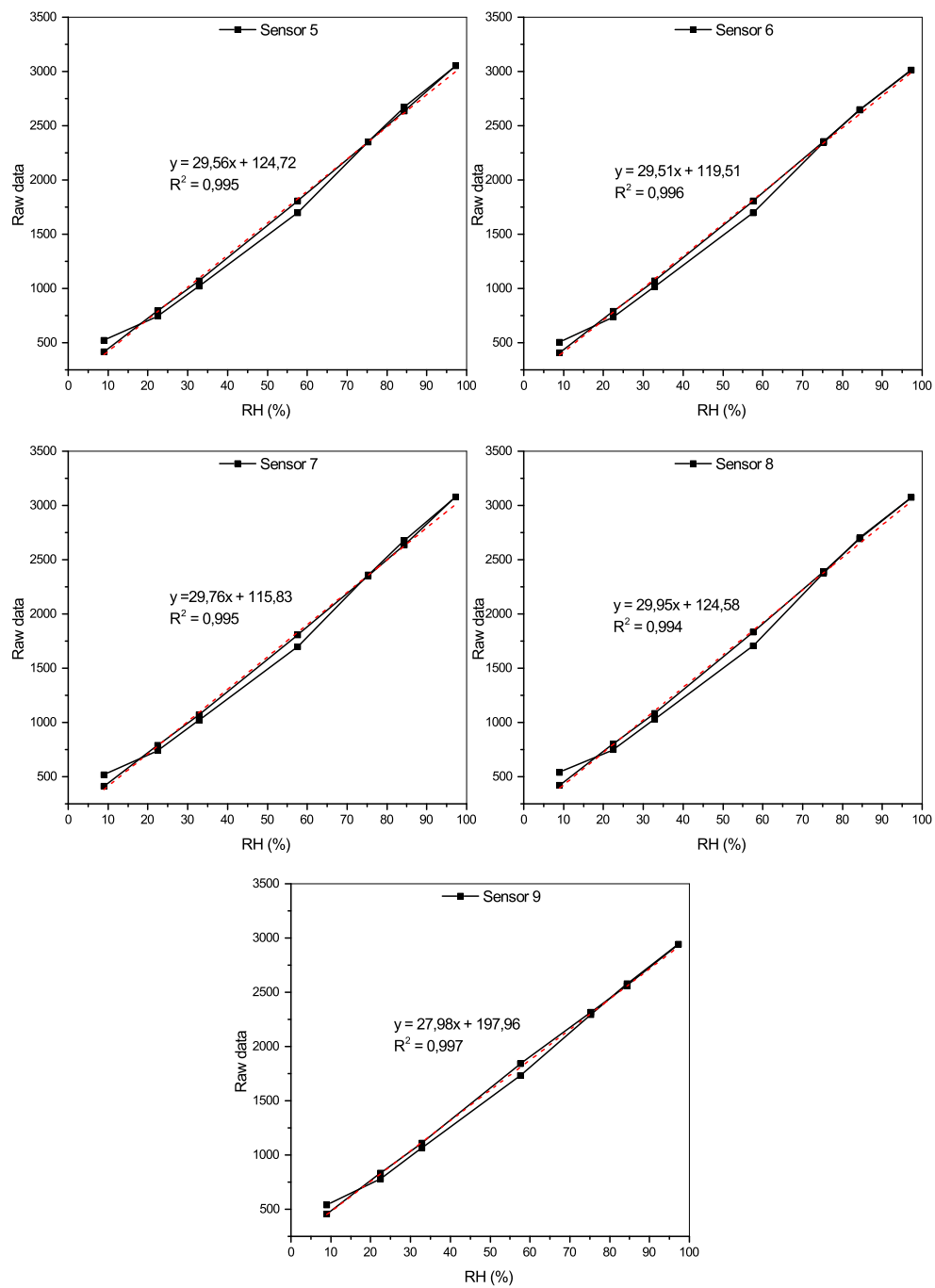


Figure D.2: Relative humidity calibration factors for SHT sensors 5-9

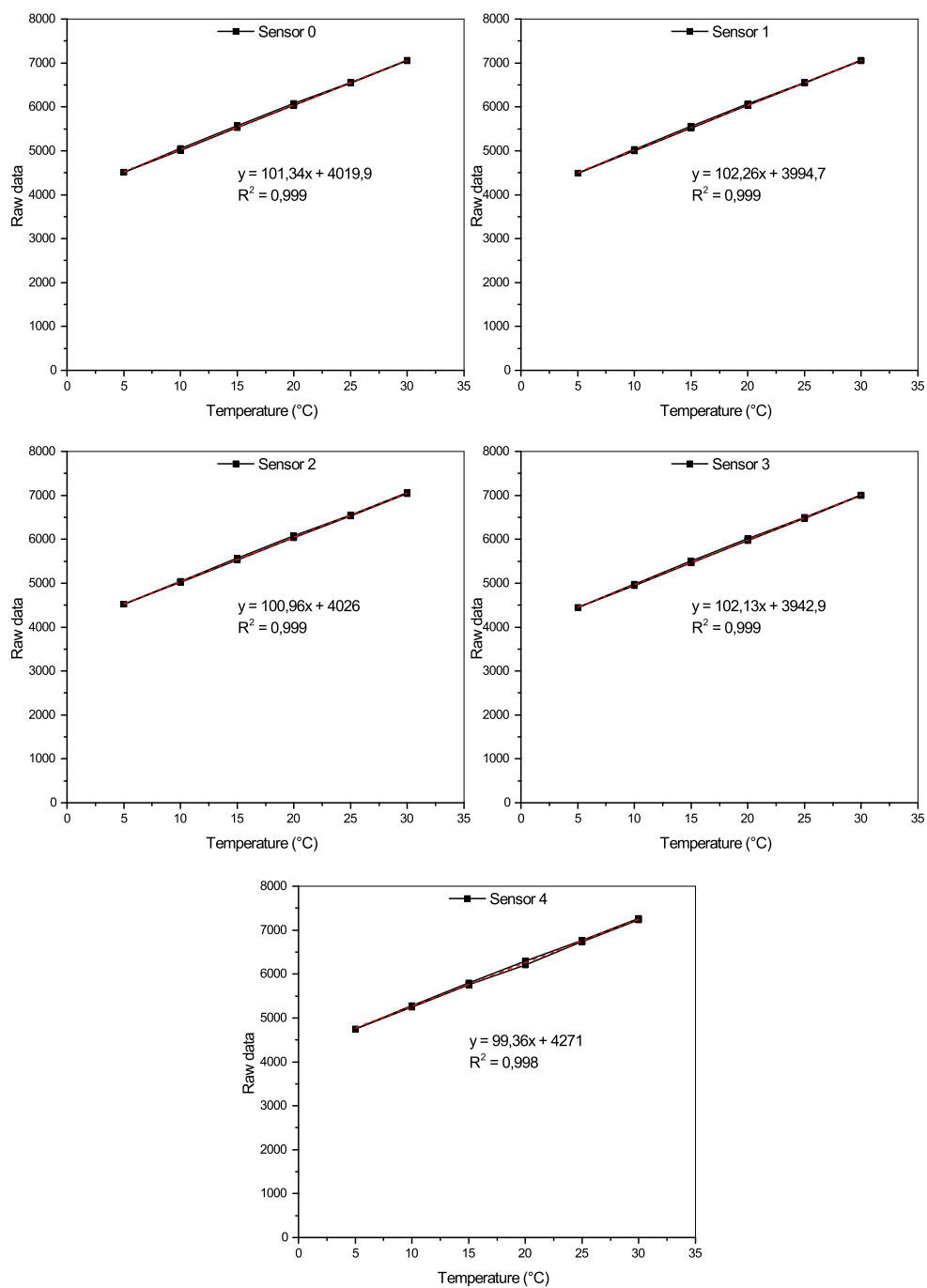


Figure D.3: Temperature calibration factors for SHT sensors 0-4

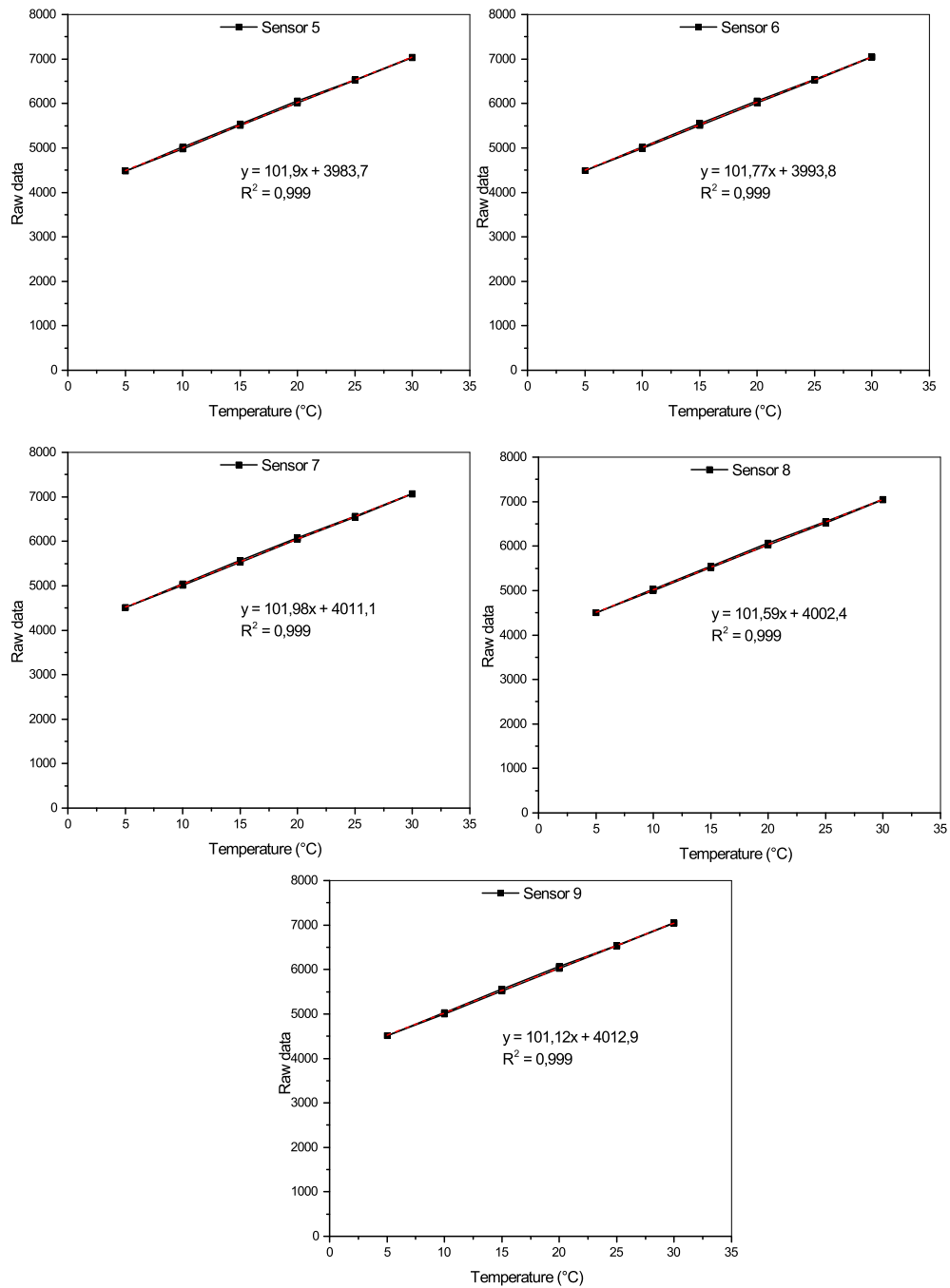


Figure D.4: Temperature calibration factors for SHT sensors 5-9

Appendix E: Calculation of vertical stress from subsequent floor construction (GBP Pisé, 2018)

In Guide de Bonnes Pratiques (GBP), Pisé [25], an example of stress calculation for subsequent floor is mentioned. The plan and elevation of the 2 floor building (Ground floor+1) is shown in figure E.1.

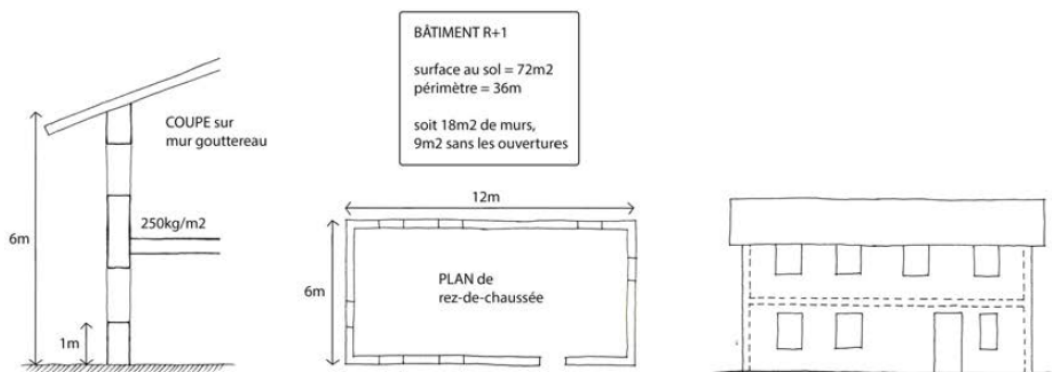


Figure E.1: Plan and elevation of the 2 floor building (ground floor+1) taken from GBP Pisé, 2018 [25] for the estimation of vertical stress

The building is 6 m high and the base is of dimensions 6 m x 12 m. The Perimeter (P) = 36 m and area (A) = 72 m^2 . The walls are taken 50 cm thick and 30% are considered 1 m from the ground surface. Considering the density of rammed earth as 2000 kg/m^3 , the load per meter length (W_d) of wall due to its self weight can be calculated as:

$$W_d = 6 \times 0.5 \times 2000 = 6000 \text{ kg/m}$$

The load from the roof and wooden floor including the roof and wooden floor (self-weight, operating, and climatic loads) are calculated here. It is considered that the load from floors and the frame are only taken by the gutter walls (2 x 12m). The vertical stress from the roof (w_r) is taken as 150 kg/m^2 , and from the wooden floor (w_f) is taken as 250 kg/m^2 . The total stress from this combination is $w_{r+f} = 400 \text{ kg/m}^2$. Thus load per meter length (W_l) can be calculated for for the gutter walls as follows:

$$W_l = \frac{400 \times (12 \times 6)}{12 \times 2} = 1200 \text{ kg/m}$$

The total load per meter length (w) can thus be determined:

$$W = W_d + W_l = 6000 + 1200 = 7200 \text{ kg/m}$$

One meter of wall which is 50 cm thick has a bearing surface of 5000 cm^2 . If 30% openings are considered, 1 m of wall has a bearing surface of 3500 cm^2 . The final resulting stress (σ_v) is taken as:

$$\sigma_v = 7200/3500 = 2.06 \text{ kg/cm}^2 = 0.2 \text{ MPa}$$

Bibliography

- [1] E. Hamard, B. Cazacliu, A. Razakamanantsoa, J.-C. Morel, Cob, a vernacular earth construction process in the context of modern sustainable building, *Building and Environment* 106 (2016) 103–119. doi:[10.1016/j.buildenv.2016.06.009](https://doi.org/10.1016/j.buildenv.2016.06.009).
- [2] M. Krayenhoff, Techno-economic analysis and environmental assessment of stabilized insulated rammed earth (sirewall) building, in: *Modern Earth Buildings*, Elsevier, 2012, pp. 735–748.
- [3] M. Hall, Y. Djerbib, Rammed earth sample production: context, recommendations and consistency, *Construction and Building Materials* 18 (4) (2004) 281 – 286. doi:<https://doi.org/10.1016/j.conbuildmat.2003.11.001>.
- [4] P. A. Jaquin, C. Augarde, C. Gerrard, Analysis of historic rammed earth construction, in: *Proceedings of the 5th international conference on structural analysis of historical constructions*, New Delhi, India, 2006, pp. 1091–1098.
- [5] T. T. Bui, Q. B. Bui, A. Limam, S. Maximilien, Failure of rammed earth walls: From observations to quantifications, *Construction and Building Materials* 51 (2014) 295–302. doi:[10.1016/j.conbuildmat.2013.10.053](https://doi.org/10.1016/j.conbuildmat.2013.10.053).
- [6] L. Miccoli, D. V. Oliveira, R. A. Silva, U. Müller, L. Schueremans, Static behaviour of rammed earth: experimental testing and finite element modelling, *Materials and Structures* 48 (10) (2015) 3443–3456. doi:[10.1617/s11527-014-0411-7](https://doi.org/10.1617/s11527-014-0411-7).
- [7] Q.-B. Bui, J.-C. Morel, A. E. Stéphane, H. Ae, N. Meunier, Compression behaviour of non-industrial materials in civil engineering by three scale experiments: the case of rammed earth, *Springer* 42 (8) (2009) 1101–1116. doi:[10.1617/s11527-008-9446-y](https://doi.org/10.1617/s11527-008-9446-y).
- [8] H. Houben, H. Guillaud, *Earth construction: a comprehensive guide*, bcin.ca.
- [9] F. Champiré, A. Fabbri, J. C. Morel, H. Wong, F. McGregor, Impact of relative humidity on the mechanical behavior of compacted earth as a building material, *Construction and Building Materials* 110 (2016) 70–78. doi:[10.1016/j.conbuildmat.2016.01.027](https://doi.org/10.1016/j.conbuildmat.2016.01.027).
- [10] O. Helson, A.-L. Beaucour, J. Eslami, A. Noumowe, P. Gotteland, Physical and mechanical properties of soilcrete mixtures: Soil clay content and formulation parameters, *Construction and Building Materials* 131 (2017) 775 – 783. doi:<https://doi.org/10.1016/j.conbuildmat.2016.11.021>.
- [11] J.-C. Morel, A. Pkla, P. Walker, Compressive strength testing of compressed earth blocks, *Construction and Building Materials* 21 (2) (2007) 303 – 309. doi:<https://doi.org/10.1016/j.conbuildmat.2005.08.021>.

- [12] C. Kouakou, J. Morel, Strength and elasto-plastic properties of non-industrial building materials manufactured with clay as a natural binder, *Applied Clay Science* 44 (1) (2009) 27 – 34. doi:<https://doi.org/10.1016/j.clay.2008.12.019>.
- [13] P. A. Jaquin, C. E. Augarde, D. Gallipoli, D. G. Toll, The strength of unstabilised rammed earth materials, *Géotechnique* 59 (5) (2009) 487–490. doi:[10.1680/geot.2007.00129](https://doi.org/10.1680/geot.2007.00129).
- [14] P. Gerard, M. Mahdad, A. Robert McCormack, B. François, A unified failure criterion for unstabilized rammed earth materials upon varying relative humidity conditions, *Construction and Building Materials* 95 (2015) 437–447. doi:[10.1016/j.conbuildmat.2015.07.100](https://doi.org/10.1016/j.conbuildmat.2015.07.100).
- [15] Q. B. Bui, J. C. Morel, S. Hans, P. Walker, Effect of moisture content on the mechanical characteristics of rammed earth, *Construction and Building Materials* 54 (2014) 163–169. doi:[10.1016/j.conbuildmat.2013.12.067](https://doi.org/10.1016/j.conbuildmat.2013.12.067).
- [16] The Effect of Relative Humidity and Temperature on the Unconfined Compressive Strength of Rammed Earth, in: *Unsaturated Soils: Research and Applications*, Springer Berlin Heidelberg, 2012, pp. 287–292. doi:[10.1007/978-3-642-31116-1_39](https://doi.org/10.1007/978-3-642-31116-1_39).
- [17] A. W. Bruno, D. Gallipoli, C. Perlot, J. Mendes, Mechanical behaviour of hyper-compacted earth for building construction, *Materials and Structures/Materiaux et Constructions* 50 (2) (2017) 1–15. doi:[10.1617/s11527-017-1027-5](https://doi.org/10.1617/s11527-017-1027-5).
- [18] P. A. Jaquin, C. E. Augarde, L. Legrand, Unsaturated characteristics of rammed earth, *Unsaturated Soils: Advances in Geo-Engineering (1995)* (2008) 417–422. doi:[10.1201/9780203884430.ch53](https://doi.org/10.1201/9780203884430.ch53).
- [19] L. Xu, F. Champiré, A. Fabbri, H. Wong, D. Branque, Hydro-Mechanical Triaxial Behaviour of Compacted Earth at Different Temperatures, in: *Poromechanics 2017 - Proceedings of the 6th Biot Conference on Poromechanics*, American Society of Civil Engineers (ASCE), 2017, pp. 164–171. doi:[10.1061/9780784480779.020](https://doi.org/10.1061/9780784480779.020).
- [20] Structural behaviour of unstabilized rammed earth constructions submitted to hygroscopic conditions, *Construction and Building Materials* 155 (2017) 164–175. doi:[10.1016/j.conbuildmat.2017.08.012](https://doi.org/10.1016/j.conbuildmat.2017.08.012).
- [21] J. Nelson, D. J. Miller, *Expansive soils: problems and practice in foundation and pavement engineering*, John Wiley & Sons, 1997.
- [22] N. P. López-Acosta, J. A. Mendoza-Promotor, Study of unsaturated soils by coupled numerical analyses of water flow-slope stability, *Groundwater: Contaminant and Resource Management* (2016) 163.

- [23] F. A. Marinho, W. A. Take, A. Tarantino, Measurement of matric suction using tensiometric and axis translation techniques, in: *Laboratory and Field Testing of Unsaturated Soils*, Springer Netherlands, 2009, pp. 3–19. doi:10.1007/978-1-4020-8819-3_2.
- [24] Y. Mualem, A new model for predicting the hydraulic conductivity of unsaturated porous media, *Water resources research* 12 (3). doi:10.1029/WR012i003p00513.
- [25] TERA, *Guide des bonne pratique de la construction en terre crue, pisé* (2018). URL <http://terre-crue-rhone-alpes.org/guides-de-bonnes-pratiques/>
- [26] L. Scholtès, P.-Y. Hicher, F. Nicot, B. Chareyre, F. Darve, On the capillary stress tensor in wet granular materials, *International Journal for Numerical and Analytical Methods in Geomechanics* 33 (10) (2009) 1289–1313. doi:10.1002/nag.767.
- [27] C. S. Costa, F. Rocha, A. L. Velosa, Sustainability in earthen heritage conservation, *Geological Society Special Publication* 416 (1) (2016) 91–100. doi:10.1144/SP416.22.
- [28] G. Minke, *Building with earth: design and technology of a sustainable architecture* (2004).
- [29] J. Vyncke, L. Kupers, N. Denies, Earth as building material—an overview of rilem activities and recent innovations in geotechnics, in: *MATEC Web of Conferences*, Vol. 149, EDP Sciences, 2018, p. 02001. doi:10.1051/mateconf/201814902001.
- [30] B. Pignal, *de l'article/du chapitre Terre crue. Techniques de construction et de restauration*, distributeur Eyrolles, 2005.
- [31] B. V. Venkatarama Reddy, P. Prasanna Kumar, Embodied energy in cement stabilised rammed earth walls, *Energy and Buildings* 42 (3) (2010) 380–385. doi:10.1016/j.enbuild.2009.10.005.
- [32] D. Gallipoli, A. Bruno, C. Perlot, N. Salmon, Raw earth construction: is there a role for unsaturated soil mechanics, *Proceedings of Unsaturated Soils: Research & Applications* (2014) 55–62.
- [33] J. Morel, A. Mesbah, M. Oggero, P. Walker, Building houses with local materials: means to drastically reduce the environmental impact of construction, *Building and Environment* 36 (10) (2001) 1119–1126. doi:10.1016/s0360-1323(00)00054-8.
- [34] B. Bossink, H. Brouwers, Construction waste: quantification and source evaluation, *Journal of construction engineering and management* 122 (1) (1996) 55–60. doi:10.1061/(ASCE)0733-9364(1996)122:1(55).
- [35] P. Gülkan, R. Langenbach, The Earthquake Resistance of traditional timber and masonry dwelling in Turkey, 13th World Conference on Earthquake Engineering (2297) (2004).

- [36] P. Walker, R. Keable, J. Martin, V. Maniatidis, *Rammed earth: design and construction guidelines*, BRE Bookshop Watford, UK (2005).
- [37] S. N. Zealand, NZS 4297:1998 Engineering design of earth buildings 4297 (1998) 60.
- [38] S. Australia, *The Australian earth building handbook*, Sydney, Australia (2002).
- [39] J. Tibbets, Emphasis on rammed earth—the rational, *Interaméricas Adobe Builder* 9 (2001) 4–33.
- [40] J. Lilley, D. M., & Robinson, Ultimate strength of rammed earth walls with openings, *International Journal of Rock Mechanics and Mining Sciences and Geomechanics Abstracts* 2 (33) (1996) 84A.
- [41] V. Maniatidis, P. Walker, A. Heath, S. Hayward, Mechanical and thermal characteristics of rammed earth, in: *International Symposium on Earthen Structures.*, 2007.
- [42] W. P. Maniatidis V, Structural capacity of rammed earth in compression, *Journal of Materials in Civil Engineering* 20 (3) (2008) 230–238. doi:[10.1061/\(asce\)0899-1561\(2008\)20:3\(230\)](https://doi.org/10.1061/(asce)0899-1561(2008)20:3(230)).
- [43] Q. Piattoni, E. Quagliarini, S. Lenci, Experimental analysis and modelling of the mechanical behaviour of earthen bricks, *Construction and Building Materials* 25 (4) (2011) 2067 – 2075. doi:<https://doi.org/10.1016/j.conbuildmat.2010.11.039>.
- [44] R. El-Nabouch, Q.-B. Bui, O. Plé, P. Perrotin, Characterizing the shear parameters of rammed earth material by using a full-scale direct shear box, *Construction and Building Materials* 171 (2018) 414–420. doi:[10.1016/j.conbuildmat.2018.03.142](https://doi.org/10.1016/j.conbuildmat.2018.03.142).
- [45] D. Ciancio, J. Gibbings, Experimental investigation on the compressive strength of cored and molded cement-stabilized rammed earth samples, *Construction and Building Materials* 28 (1) (2012) 294 – 304. doi:<https://doi.org/10.1016/j.conbuildmat.2011.08.070>.
- [46] J.-E. Aubert, A. Fabbri, J. Morel, P. Maillard, An earth block with a compressive strength higher than 45 mpa!, *Construction and Building Materials* 47 (2013) 366–369. doi:[10.1016/j.conbuildmat.2013.05.068](https://doi.org/10.1016/j.conbuildmat.2013.05.068).
- [47] P. Walker, Characteristics of pressed earth blocks in compression, in: *Proceedings of the 11th international brick/block masonry conference*, Shanghai, China, 1997, pp. 14–16.
- [48] H. Morris, New Zealand: Aseismic Performance-Based Standards, *Earth Construction, Research, and Opportunities*, Getty Seismic Adobe Project 2006 Colloquium, Los Angeles, US (Best 1974) (2003) 52–66.

- [49] D. Ciancio, P. Jaquin, P. Walker, Advances on the assessment of soil suitability for rammed earth, *Construction and Building Materials* 42 (2013) 40 – 47. doi:<https://doi.org/10.1016/j.conbuildmat.2012.12.049>.
- [50] V. Maniatidis, P. Walker, A review of rammed earth construction, Innovation Project “Developing Rammed Earth for UK Housing”, Natural Building Technology Group, Department of Architecture & Civil Engineering, University of Bath (2003) 12.
- [51] S. Burroughs, Recommendations for the selection, stabilization, and compaction of soil for rammed earth wall construction, *Journal of Green Building* 5 (1) (2010) 101–114. doi:[10.3992/jgb.5.1.101](https://doi.org/10.3992/jgb.5.1.101).
- [52] O. D. Martínez, Preservation and repair of rammed earth constructions., Universidade do Minho, Braga (2015).
- [53] J. E. Aubert, A. Fabbri, J. C. Morel, P. Maillard, An earth block with a compressive strength higher than 45 MPa!, *Construction and Building Materials* 47 (2013) 366–369. doi:[10.1016/j.conbuildmat.2013.05.068](https://doi.org/10.1016/j.conbuildmat.2013.05.068).
- [54] H. Nowamooz, C. Chazallon, Finite element modelling of a rammed earth wall, *Construction and Building Materials* 25 (4) (2011) 2112–2121. doi:[10.1016/j.conbuildmat.2010.11.021](https://doi.org/10.1016/j.conbuildmat.2010.11.021).
- [55] M. Olivier, Le matériau terre, compactage, comportement, application aux structures en bloc sur terre, Ph.D. thesis, Lyon, INSA (1994).
- [56] L. Miccoli, U. Müller, P. Fontana, Mechanical behaviour of earthen materials: A comparison between earth block masonry, rammed earth and cob, *Construction and Building Materials* 61 (2014) 327 – 339. doi:<https://doi.org/10.1016/j.conbuildmat.2014.03.009>.
- [57] M. Olivier, A. Mesbah, Constitutive equations for compacted soils, in: *Unsaturated Soils. Proc. 1st Int. Conf. on Unsaturated Soils (UNSAT 95)*, 1995, pp. 765–773.
- [58] D. Gallipoli, A. W. Bruno, C. Perlot, J. Mendes, A geotechnical perspective of raw earth building 12 (3) (2017) 463–478. doi:[10.1007/s11440-016-0521-1](https://doi.org/10.1007/s11440-016-0521-1).
- [59] R. Fisher, On the capillary forces in an ideal soil; correction of formulae given by wb haines, *The Journal of Agricultural Science* 16 (3) (1926) 492–505.
- [60] G. Mason, W. Clark, Liquid bridges between spheres, *Chemical Engineering Science* 20 (10) (1965) 859 – 866. doi:[https://doi.org/10.1016/0009-2509\(65\)80082-3](https://doi.org/10.1016/0009-2509(65)80082-3).
- [61] L. Fisher, J. Israelachvili, Direct experimental verification of the kelvin equation for capillary condensation, *Nature* 277 (5697) (1979) 548–549.

- [62] V. Mehrotra, K. Sastry, Pendular bond strength between unequal-sized spherical particles, *Powder Technology* 25 (2) (1980) 203 – 214. doi:[https://doi.org/10.1016/0032-5910\(80\)87031-8](https://doi.org/10.1016/0032-5910(80)87031-8).
- [63] C. Jommi, A. Sciotti, A study of the microstructure to assess the reliability of laboratory compacted soils as reference material for earth constructions, in: *Proceedings of the 2nd international conference on structural and construction engineering*, Vol. 3, Balkema, 2003, pp. 2409–2415.
- [64] Rupture energy of a pendular liquid bridge, *European Physical Journal B* 23 (1) (2001) 79–86. doi:[10.1007/s100510170084](https://doi.org/10.1007/s100510170084).
- [65] M. M. Kohonen, D. Geromichalos, M. Scheel, C. Schier, S. Herminghaus, On capillary bridges in wet granular materials, *Physica A: Statistical Mechanics and its Applications* 339 (1) (2004) 7 – 15, proceedings of the International Conference New Materials and Complexity. doi:<https://doi.org/10.1016/j.physa.2004.03.047>.
- [66] D. G. Fredlund, H. Rahardjo, *Soil Mechanics for Unsaturated Soils*, *Water Science Technologies* 30 (1) (1993) 205–210. arXiv:[worldcat.org/oclc/3519342](https://arxiv.org/abs/worldcat.org/oclc/3519342), doi:[10.1016/0267-7261\(93\)90011-F](https://doi.org/10.1016/0267-7261(93)90011-F).
- [67] Y. I. Rabinovich, M. S. Esayanur, B. M. Moudgil, Capillary forces between two spheres with a fixed volume liquid bridge: Theory and experiment, *Langmuir* 21 (24) (2005) 10992–10997. doi:[10.1021/la0517639](https://doi.org/10.1021/la0517639).
- [68] K. Murase, T. Mochida, Y. Sagawa, H. Sugama, Estimation on the strength of a liquid bridge adhered to three spheres, *Advanced Powder Technology* 19 (4) (2008) 349 – 367. doi:<https://doi.org/10.1163/156855208X314949>.
- [69] D. Toll, A framework for unsaturated soil behaviour, *Géotechnique* 40 (1) (1990) 31–44. doi:[10.1680/geot.1990.40.1.31](https://doi.org/10.1680/geot.1990.40.1.31).
- [70] W. Zhang, Y. Cai, *Continuum damage mechanics and numerical applications*, Springer Science & Business Media, 2010.
- [71] J. Mazars, *Application de la mecanique de l'endommagement au comportement non lineaire et a la rupture du beton de structure.*, Ph.D. thesis (1984).
- [72] P. NF, 94–051. soil: investigation and testing—determination of atterberg's limits—liquid limit test using casagrande apparatus—plastic limit test on rolled thread, *Association Française de Normalisation* (1993).
- [73] P. NF, 94–093. soil: Investigation and testing – determination of the compaction reference values of a soil type – standard proctor test and modified proctor test., *AFNOR* (1999).

- [74] Nf en 286-2, test methods for the determination of the laboratory reference volume density and water content. proctor-compaction.
- [75] L. Xu, K. K. Wong, A. Fabbri, F. Champiré, D. Branque, Loading-unloading shear behavior of rammed earth upon varying clay content and relative humidity conditions, *Soils and Foundations* 58 (4) (2018) 1001–1015. doi:10.1016/j.sandf.2018.05.005.
- [76] A. H. Narayanaswamy, Mechanical testing procedure for local building materials : rammed earth and laterite building stones, <http://www.theses.fr> (dec 2016).
- [77] B. Venkatarama-Reddy, K. Jagadish, The static compaction of soils, *Geotechnique* 43 (2) (1993).
- [78] J.-F. Daïan, *Equilibre et transferts en milieux poreux* (2013).
- [79] A. W. Bruno, D. Gallipoli, C. é. l. Perlot-Bascoules, J. Mendes, N. Salmon, *Briques de terre crue: procédure de compactage haute pression et influence sur propriétés mécaniques*, 2015.
- [80] A. Corbin, C. Augarde, Investigation Into the Shear Behaviour of Rammed Earth Using Shear Box Tests, *First International Conference On Bio-based Building Materials* (2015) 93–98doi:10.1371/journal.-pone.0018239.
- [81] J. S. J. Cheah, P. Walker, A. Heath, T. K. K. B. Morgan, Evaluating shear test methods for stabilised rammed earth, *Proceedings of the Institution of Civil Engineers - Construction Materials* 165 (6) (2012) 325–334. doi:10.1680/coma.10.00061.
- [82] S. K. Vanapalli, D. G. Fredlund, D. E. Pufahl, A. W. Clifton, Model for the prediction of shear strength with respect to soil suction, *Canadian Geotechnical Journal* 33 (3) (1996) 379–392. arXiv:arXiv:1011.1669v3, doi:10.1139/t96-060.
- [83] Determination of the shear strength parameters of an unsaturated soil using the direct shear test, *Canadian Geotechnical Journal* 25 (3) (1988) 500–510. doi:10.1139/t88-055.
- [84] D. G. Fredlund, A. Xing, M. D. Fredlund, S. L. Barbour, The relationship of the unsaturated soil shear to the soil-water characteristic curve, *Canadian Geotechnical Journal* 33 (3) (1996) 440–448. doi:10.1139/t96-065.
- [85] [ASTM D2850 - 15 Standard Test Method for Unconsolidated-Undrained Triaxial Compression Test on Cohesive Soils.](#)
URL <https://www.astm.org/Standards/D2850.htm>
- [86] NF P94-074, 1994. Sols: reconnaissance et essais - Essais à l'appareil triaxial de révolution - Appareillage - Préparation des éprouvettes e Essai (UU) non consolidé non drainé - Essai (Cu + U) consolidé non drainé avec mesure de pression interstitielle - Essai (CD) consolidé drainé.

- [87] ASTM D 4767-95: Standard Test Method for Consolidated Undrained Triaxial Compression Test for cohesive soils.
- [88] L. Miccoli, A. Drougkas, U. Müller, In-plane behaviour of rammed earth under cyclic loading: Experimental testing and finite element modelling, *Engineering Structures* 125 (2016) 144–152. doi:10.1016/j.engstruct.2016.07.010.
- [89] T.-T. Bui, Q.-B. Bui, A. Limam, J.-C. Morel, Modeling rammed earth wall using discrete element method, *Continuum Mechanics and Thermodynamics* 28 (1-2) (2016) 523–538. doi:10.1007/s00161-015-0460-3.
- [90] A. W. Bishop, The principal of effective stress, *Norwegian Geotechnical Institute* 32 (1960) 1–5.
- [91] A. Penman, Shear characteristics of a saturated silt, measured in triaxial compression, *Geotechnique* 3 (8) (1953) 312–328. doi:10.1680/geot.1953.3.8.312.
- [92] J. Atkinson, Stress path tests to measure soil strength parameters for shallow landslides, Proc. 11th ICSMFE, AA Balkema, Brookfield, VT, 1985 2 (1985) 983–986.
- [93] B. Shen, J. Shi, N. Barton, Journal of Rock Mechanics and Geotechnical Engineering An approximate nonlinear modified Mohr-Coulomb shear strength criterion with critical state for intact rocks, *Journal of Rock Mechanics and Geotechnical Engineering* (4) (2018) 645–652. doi:10.1016/j.jrmge.2018.04.002.
- [94] E. E. Alonso, A. Gens, A. Josa, A constitutive model for partially saturated soils, *Géotechnique* 40 (3) (1990) 405–430. doi:10.1680/geot.1990.40.3.405.
- [95] C. JOMMI, C. G. DI PRISCO, A simple theoretical approach for modeling the mechanical behavior of partially saturated granular soils, in: *The role of fluids in geotechnical engineering problems*, 1994, pp. 167–188.
- [96] G. Bolzon, B. A. Schrefler, O. C. Zienkiewicz, Elastoplastic soil constitutive laws generalized to partially saturated states, *Géotechnique* 46 (2) (1996) 279–289. doi:10.1680/geot.1996.46.2.279.
- [97] B. Loret, N. Khalili, A three-phase model for unsaturated soils, *International Journal for Numerical and Analytical Methods in Geomechanics* 24 (11) (2000) 893–927. doi:10.1002/1096-9853(200009)24:11<893::AID-NAG105>3.0.CO;2-V.
- [98] D. Karube, K. Kawai, The role of pore water in the mechanical behavior of unsaturated soils, *Geotechnical and Geological Engineering* 19 (3-4) (2001) 211–241. doi:10.1023/A:1013188200053.
- [99] N. P. 94-057, *Soils: Recognition and testing, soil granulometric analysis, separation method* (1992).

- [100] S. Olivella, A. Gens, J. Carrera, E. E. Alonso, Numerical formulation for a simulator (CODE_BRIGHT) for the coupled analysis of saline media, *Engineering Computations* (Swansea, Wales) 13 (7) (1996) 87–112. doi:10.1108/02644409610151575.
- [101] M. T. van Genuchten, A Closed-form Equation for Predicting the Hydraulic Conductivity of Unsaturated Soils, *Soil Science Society of America Journal* 44 (5) (1980) 892–898. doi:10.2136/sssaj1980.03615995004400050002x.
- [102] D. Fredlund, N. R. Morgenstern, R. Widger, The shear strength of unsaturated soils, *Canadian geotechnical journal* 15 (3) (1978) 313–321.
- [103] N. Mendes, P. C. Philippi, R. Lamberts, A new mathematical method to solve highly coupled equations of heat and mass transfer in porous media, *International Journal of Heat and Mass Transfer* 45 (3) (2001) 509–518. doi:10.1016/S0017-9310(01)00172-7.
- [104] T. Kusuda, Indoor humidity calculations, *ASHRAE transactions* 89 (1983) 728–740.
- [105] R. H. Howell, W. J. Coad, H. J. Sauer, Principles of heating ventilating and air conditioning, American Society of Heating, Refrigerating and Air-Conditioning Engineers (ASHRAE), 2005.
- [106] D. Molle, P.-M. Patry, RT 2012 et RT Existant: réglementation thermique et efficacité énergétique, Editions Eyrolles, 2011.
- [107] Ademe, “se chauffer au bois,” (2015).